MANIPULATING PHOTOLUMINESCENT PROPERTIES VIA SPATIAL CONTROL OF OPTICALLY ACTIVE MEDIA WITHIN POLYMER MATRICES AND TEMPLATES

A Dissertation

Presented to

The Academic Faculty

by

Marcus James Smith

In Partial Fulfillment

of the Requirements for the Degree

Doctor of Philosophy in the

School of Materials Science and Engineering

Georgia Institute of Technology

August 2019

MANIPULATING PHOTOLUMINESCENT PROPERTIES VIA GUIDED ASSEMBLY AND CONTROL OF OPTICALLY ACTIVE MEDIA WITHIN POLYMER MATRICES AND TEMPLATES

Approved by:

Dr. Vladimir V. Tsukruk, Advisor
School of Materials Science and Engineering
Georgia Institute of Technology

Dr. Zhiqun Lin
School of Materials Science and Engineering
Georgia Institute of Technology

Dr. Dong Qin
School of Materials Science and Engineering
Georgia Institute of Technology

Dr. Wenshan Cai
School of Electrical and Computer Engineering,
School of Materials Science and Engineering
Georgia Institute of Technology

Dr. Timothy Bunning
School of Materials Science and Engineering
Georgia Institute of Technology
Materials and Manufacturing Directorate,
Air Force Research Laboratory

Date Approved: May 2, 2019

Dedicated to my family and friends for their support, in particular my parents, Ronnie and Jean Smith, who I am forever grateful for, as they have always given me freedom to chase my dream and have continued to pour into me as I chase those dreams.

ACKNOWLEDGEMENTS

First and foremost, I would like to thank God, through Him all things are made possible. I would like to take this opportunity to thank my advisor, Prof. Vladimir V. Tsukruk, for initially taking a chance on me and giving me the opportunity, additionally for his constant support, motivation, and guidance throughout my tenure at Georgia Tech. Without his oversight for the last five years I would not have evolved into the researcher I am today. I appreciate the financial support from the Science, Mathematics and Research for Transformation (SMART) scholarship funded by OSD-T&E, Defense – Wide/PE0601120D8Z National Defense Education Program (NDEP)/BA-1, N00244-09-1-0081, the Aerospace Systems Directorate (AFRL/RQ), and the Air Force Office of Scientific Research grant FA9550-14-1-0037 (Synthetic Photonics Multidisciplinary University Research Initiative). I want to thank my PhD dissertation committee members, Prof. Zhiquin Lin, Prof. Wenshan Cai, and Prof. Dong Qin, and Dr. Timothy Bunning for their recommendations and direction.

I would also like to thank my many collaborators including Dr. Evan Lafalce and Q. Zeng from Prof. Valy Vardeny's group at the University of Utah for providing useful suggestions, simulations, and lasing measurements. In addition, I want to thank Dr. Y.J. Yoon, Dr. J. Jung, and G. Biesold-Mcgee from Prof. Lin's group for providing various core and core-shell QDs. Further thanks go to my collaborators on the parity-time symmetry MURI project, Prof. T. Kottos (Wesleyan), and Prof. E. Thomas (Rice) for their practical suggestions and theoretical insights regarding lasing and PT-systems design. I also want to

thank all the SEMA group members who provided technical assistance and discussion, in particular Dr. Sid Malak, Dr. Chun Hao Lin, Dr. Shuaidi Zhang, and Shengtao Yu.

Finally, I am greatly appreciative of the support from my family and friends, in addition to the Georgia Tech faculty, specifically the Center for Engineering Education and Diversity (CEED) and Institute Diversity - OMED who have provided me with a second home and a constant source of support during my time at Georgia Tech.

TABLE OF CONTENTS

LIST OF TABLES

LIST OF FIGURES

LIST OF SYMBOLS AND ABBREVIATIONS

λ	wavelength
μCP	microcontact printing
μTM	microtransfer molding
3-MPA	3-mercaptopropionic acid
3DL	3D lithography
AFM	Atomic force microscope
BA	Butylamine
BODIPY	Boron-dipyromethane
DFB	distributed feedback
DIAH	1,7 diaminoheptane
DSC	Thermogravimetric analysis
EBL	Electron beam lithography
FDTD	Finite-difference time-domain
HDA	hexadecylamine
IR	Infrared
MIMIC	micromolding in capillaries
NA	Numerical aperture
NC	Nanocrystal
OA	oleic acid
ODE	octadecene

PDMS	polydimethysiloxane
PL	Photoluminescence
PLMA	poly (lauryl methacrylate)
PMMA	poly(methyl methacrylate)
PT	Parity-Time
Q	quality factor
QD	Quantum dot
QY	Quantum yield
REM	replica molding
SAMIM	solvent-assisted micromolding
SEM	Scanning electron microscope
TDPA	1-tetradecylphosphonic acid
TEM	Transmission electron microscope
TEOS	tetraethyl orthosilicate
TGA	thermogravimetric analysis
TOABr	tetra-n-octylammonium bromide
TOP	tri-n-octylphosphine -
TOPO	tri-n-octylphosphine oxide
UV	ultraviolet
V	mode volume
WGM	whispering gallery mode

SUMMARY

Fundamentally, light management plays a central role in industries such as life science, health, communication, energy, and agriculture. Research involving further understanding and control of light to the benefit of humankind continues to be a driving force for advancing society. Of particular interest is furthering our understanding of light-matter interactions. By controlling these interactions, intriguing optical phenomenon such as directional light modulation and lasing with low thresholds can be achieved, particularly with photonic assemblies of gain medium. This study focuses on understanding the fundamental aspect of light-matter interactions and propagation in gain medium such as organic dyes, quantum dots (QD), and QD-polymer nanocomposites. Specific emphasis is placed on understanding the QD-polymer interface to realize guided assembly in nanocomposites and on finding the parameters governing optical coupling between nanocomposite structures with particular focus on photonic cavity size, shape, position, and obtaining dynamic tunability.

To summarize, this research provides a scientific framework which demonstrates useful methodologies for designing photonic systems that require control of light-matter interactions including emission, mode activity, and resonator coupling. Major themes present in this work include:

- Understanding quantum dot architecture and the effect on dynamic photoluminescence properties. In addition, understanding UV polymerization schemes to design QD-polymer nanocomposites in which the polymer backbone

minimizes aggregation and provides a stable and robust support for the nanocomposite;

- Exploiting 3D lithography and template assisted directed assembly in order to realize assemblies of individual and coupled microsphere resonators. Unique system design ensures resolution is pushed beyond limits of instrumentation in order to achieve strong coupling between resonators;
- Utilizing photolithography to develop microdisk resonators offering precise spatial control over QD based photonic structures and developing approaches to tailor gain/loss contrast to achieve unique optical phenomenon in coupled resonator systems.

Specifically, Cd-based core and core/shell QDs with different interfacial architectures, including core sharp shell, and core alloyed shell, are investigated to understand dynamic photoluminescence behavior. Core/shell QDs with a CdSe/ZnS composition showed the most dynamic PL behavior with an emission signature that showed semi-reversible recovery behavior based on exposure conditions. Next, a crosslinking technique incorporating thiol-ene chemistry was used to realize QD-polymer nanocomposites with high loading, minimal aggregation, optical scattering, and tunable mechanical properties. As the QD loading is increased, the thiol and -ene conversion decreases, which translates to a nanocomposite with widely variable and tailorable mechanical properties, elastic modulus decreasing to 1 GPa with increased QD loading. Finally, lithographic techniques were used to fabricate high resolution templates for whispering gallery mode microsphere resonator assembly, and individual and coupled microdisk resonators with strong evanescent coupling due to the close proximity of adjacent resonators. Taking advantage of 3D lithography, with ~200nm resolution, and unique system design, we obtain microsphere resonators with sub-100nm gap spacing, equating to strong evanescently

coupled resonators. The knowledge obtained herein can be used to aid in the design of robust optical materials with added functionality and tunability for sensing and enhanced light modulation leading to unique optical phenomenon such as unidirectional directional lasing and enhanced single mode lasing.

CHAPTER 1. INTRODUCTION

Dating back to the Roman era (4th century) though likely accidental and not well understood at the time, artists demonstrated the importance of light-matter interactions and the effects of controlling the flow of light.[1] By inclusion of gold nanoparticles in glass, a dichroic effect was observed, having the Lycurgus cup appear different colors depending on the direction of illumination.[1] While simply dependent on the scattering properties of the gold nanoparticles, our understanding of light-matter interactions continues to evolve bringing forward ways to further develop and improve technologies for the betterment of humankind. From a fundamental standpoint, light is essential for the existence of life. Through photosynthesis, light is converted to chemical energy, then to fuel for sustainable plant life. In a similar manner, light has become fundamental in understanding and pushing technological advances. Applications such as lasers and fiber optics involving the control and manipulation of light continue to revolutionize society through medicine,[2] communications,[3] and entertainment[4]. A material's response to light or external fields is governed by Maxwell's equations, and more specifically, parameters such as refractive index, permittivity, and permeability. As shown in the diagram below various combinations of positive and negative permittivity and permeability lead to materials that can be transparent, negative index materials, and plasmas. (Figure 1.1).[5]

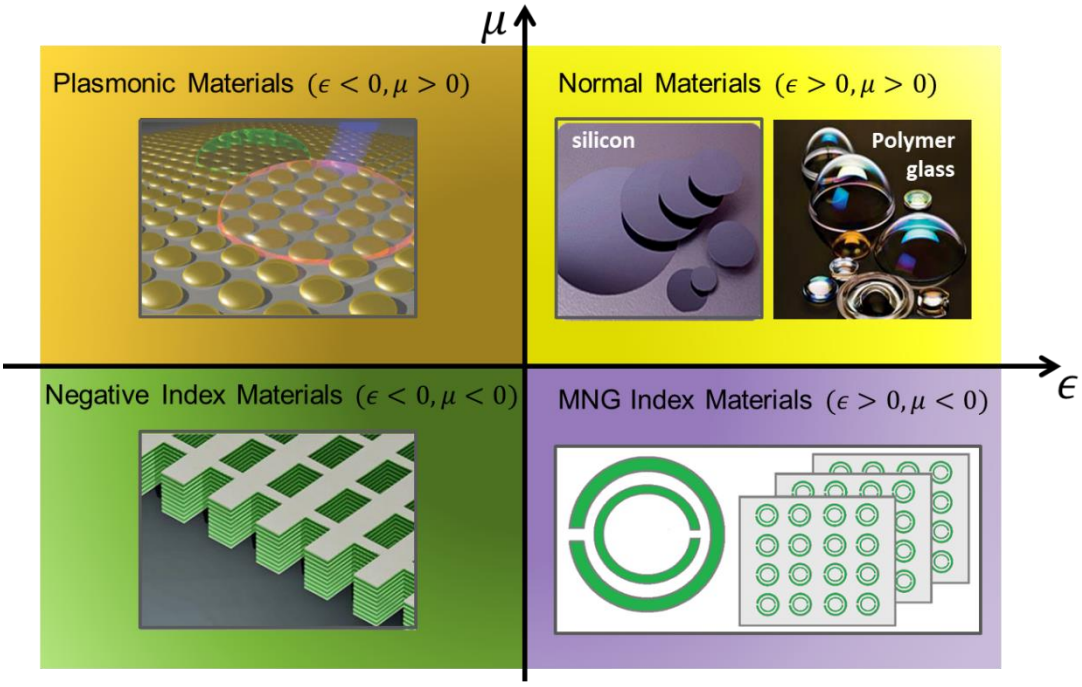

Figure 1.1: Real parts of permittivity and permeability and corresponding materials for each parameter space.

Even more appealing in terms of our understanding of light-matter interactions, due to the observation of phenomenon such as parity time symmetry in optical materials, such systems have garnered intense research interest over more recent years leading to technological breakthroughs for photonics applications.[6] Novel device functionalities such as unidirectional invisibility and coherent perfect absorption have been demonstrated experimentally.[6] Key requirements for such systems are optically active gain medium and their controlled assembly. For this reason, such materials rely judiciously on organic and inorganic semiconductor nanocrystals to provide refractive index contrast for manipulation and control of the flow of light.

The gamut of materials displaying unique optical phenomenon simply by exploiting the ability to control a material's properties such as refractive index, combined with precision patterning is far reaching, poised to have significant impacts on fields such as sensing, light amplification, and modulation.

1.1 Introduction to Organic Dyes

The investigation of many fundamental processes involving light typically involves the use of a fluorescent material to enhance or possibly probe light. Whether it be simple fluorescence imaging, sensing, or light amplification, fluorescent molecules have had a pivotal role in the evolution of these applications.[7,8] Traditional fluorescent molecules typically consist of several combined aromatic rings with a variety of terminal functionality or molecules with several π bonds. Some of the more common organic dyes, often used for probes as well as lasers, are the rhodamine, cyanine, and BODIPY dye families. They are characterized by narrow absorption and emission bands, high molar absorption coefficients, near unity quantum yields, and an emission spectrum that can be fine-tuned based on modifications of the structure.[7] As governed by the Joblanski diagram, the fluorescent dyes in an excited state can follow various relaxation pathways.[9] (Figure 1.2)

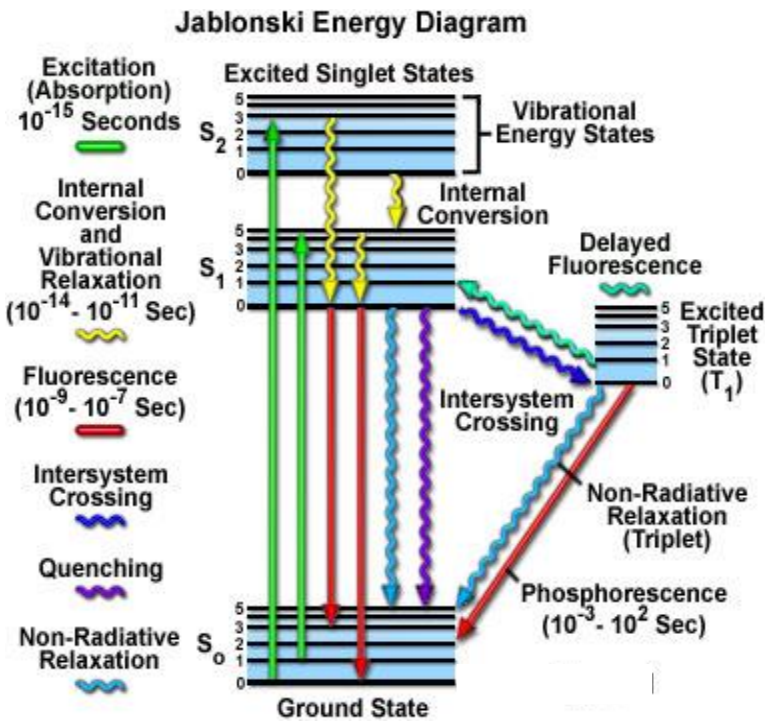

Figure 1.2: Jablonski energy diagram outlining the various radiative and non-radiative relaxation pathways and their typical lifetime for excited state electrons.

Although organic dyes offer an array of advantageous properties, they have several limitations. Due to the relatively small Stokes shift, the difference between the spectral position of the lowest energy absorption and luminescence from the same electronic transition, significant amounts of reabsorption or cross-talk can take place. Additionally, organic dyes tend to suffer from photobleaching, or irreversible degradation of the luminescence properties. Due to the above limitations, the use of organic dyes for some applications such as systems displaying optical gain has been severely limited.

1.2 Quantum confined systems

While there are a number of candidates that can be used to control light-matter interactions, an ideal candidate would have tunable emission ranging from the visible light to infrared (IR),

possess an ultrahigh gain coefficient and photostability, be solution processable, interface well with polymer matrices (demonstrating good wettability), and be readily patternable to enable precise control over light propagation and investigate interactions between neighboring assemblies. A judicious choice would be quantum dots, for reasons that will be discussed further below.

1.2.1 Fundamentals of Quantum Dots

Quantum dots (QDs) are semiconductor nanocrystals ranging in size from 1 to 10 nm, possessing excellent light absorption and emission characteristics. The optical properties can be tailored via precise control of synthetic parameters such as type and concentration of precursors, and duration of reaction. While there are many techniques to produce QDs, more recently, facile synthetic techniques allowing for more tunability, involve wet chemical processes (i.e. hot injection method).[10] QDs are quite advantageous in comparison to their organic dye counterparts, offering size and composition dependent energy band gaps (i.e. tunable absorption and photoluminescence), excellent photostability, and readily solution and aqueous processable based on surface chemistry.[11]

Prototypical QDs consist of post-transition metal cores mixed with metalloids or nonmetals (i.e. CdSe, CdS, CdTe, PbS, PbSe, InP). Due to some of the limitations afforded by core QDs, mainly non-unity quantum yield and non-radiative decay mechanisms dominating relaxation pathways, intense research has led to the evolution of QD architecture. Multicomponent QDs, both binary and ternary, consisting of precisely engineered core-shell architectures (Figure 1.3a), have overcome many of the shortcomings associated with core QDs.[12,13,14] These core-shell QD structures fall into one of three categories; Type I, quasi-type II, and type II, which describes the energy gap alignment of the core and shell (Figure 1.2b). Specifically, type-I structures consist of

a nested geometry in which the core bandgap is much smaller than that of the shell or the inverted arrangement in which the shell is the lower bandgap material. As depicted in Figure 1.3b, in one case, the valence band of the core is of higher energy than that of the shell and the conduction band is of lower energy. Similarly, for the inverted case, the shell has the higher valance band and lower conduction band in comparison to the core. Type-II structures demonstrate a more staggered bandgap, as illustrated the cores possess either lower or higher valence band and conduction band energies. Finally, in the case of quasi-Type II, the structure is similar to that of the nested type I structure; however the difference in the bandgap energies is much less. In summary, as the complexity of the QD core shell structure is enhanced, the delocalization of the electron and hole or the pair changes, typically resulting in suppression of non-radiative recombination pathways.

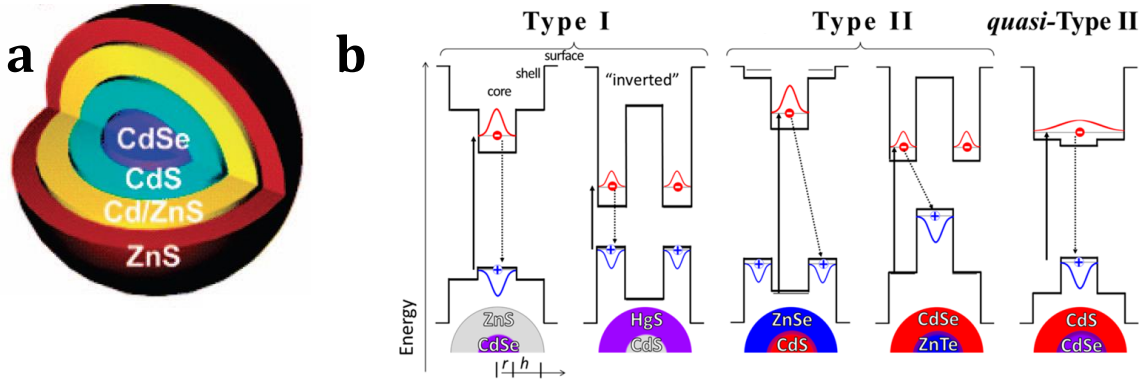

Figure 1.3: Schematic of core-shell QD architecture (a) and energy band-gap for type I, II and quasi-type II core-shell QDs (b).[11]

The versatility of colloidal synthetic techniques allows for very fine tailoring of the resulting QD size, shape, composition, surface chemistry, and thus the optical properties. The concept of alloying the core/shell interface was identified as a means to limit the detrimental effects on the QD electronic structure originating from lattice strain.[15] Type-I QDs composed of CdSe/ZnS have lattice mismatch as high as 12%, by providing an intermediate "strain alleviating"

layer in between the core and shell, resulting in a graded interface, the mismatch is significantly reduced. Consequently, a highly tunable QD with QYs near unity results.

Owing to the toxic nature of the above-mentioned post transition metal based QDs, metal halide colloidal nanocrystals (NCs) have been explored as an alternative for optoelectronic applications, specifically, cesium and lead based NCs, ($MAPbX_3$ (MA = CH_3NH_3, X = Cl, Br, and I) and ($CsPbX_3$, X = Cl, Br, I, and mixed Cl/Br and Br/I systems)).[16,17] In comparison to their transition metal based counterparts, metal halide QDs offer much higher QYs, narrow emission line widths, and ns lifetimes. Additionally, they are characterized by low bulk defect densities, ultra-high absorption coefficients, and slower Auger recombination (mentioned in the next section), making them ideal candidates for applications involving gain medium.

1.2.2 Quantum Confined Effect

Quantum dots are characterized by the fact that their dimensions are smaller than the exciton Bohr radius.[18] This gives way to a very interesting phenomenon called quantum confinement which can best be described by the particle in a box theory, suggesting the more confined a particle becomes, certain energy states become forbidden (i.e. the particle can only occupy certain energy levels). To further explain, it is first worth noting that upon excitation by electromagnetic radiation with energy larger than the semiconductor bandgap, excitons, or electron

hole pairs are generated, in which the electron is excited to the conduction band and the hole remains in the valence band (Figure 1.4).[18]

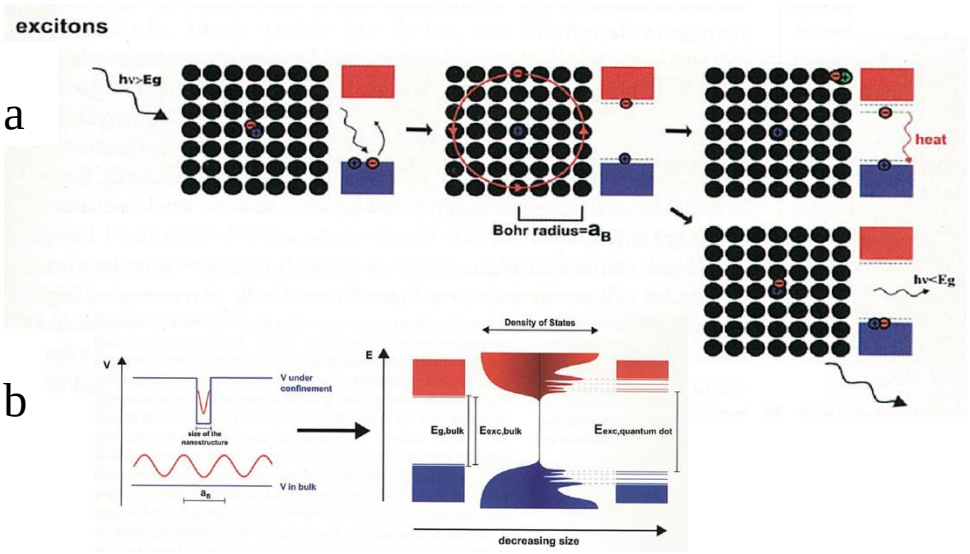

Figure 1.4: Process of excitation and generation of excitons within bulk semiconductor (a) and confinement in QD bandgap (b).[17]

The distance between the electron-hole pair is known as the exciton Bohr radius, a_b, ~5nm for the bulk CdSe exciton. As shown in Equation 1.1, the radius is influenced by several factors including the dielectric constant, and the masses of the electron and hole.[18]

$$a_b = a_e + a_h = \frac{4\pi\varepsilon_0\varepsilon n^2\hbar^2}{\mu q^2} \qquad (1.1)$$

Because the QD dimensions are smaller than the exciton Bohr radius, the system is said to be confined (Figure 1.4b). Traditionally speaking, in bulk semiconductors, electrons are treated as wave functions that fit within constraints determined by the crystal lattice. Given the constraints there are many allowed wave functions resulting in a continuous band structure. As the size of the crystal is reduced, so do the allowed wave functions, resulting in discrete quantum confined states

where the energy gap increases with decreasing nanocrystal size. (Figure 1.5a-b).[19,20] These discrete energy states lead to unique optical properties (i.e. tunable photoluminescence emission) based on QD size (Figure 1.5c).[21]

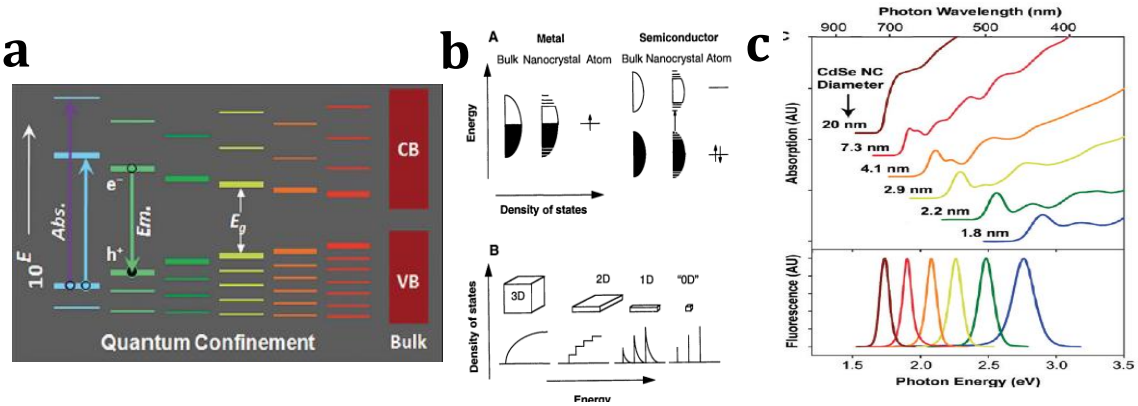

Figure 1.5: (a) and (b) formation of discrete energy states in seminconductor nanocrystal and[18,19,] (c) color tunability of QDs based on size.[20]

1.2.3 Radiative and non-radiative decay mechanisms

An interesting phenomenon associated with QD dynamics, and the strong carrier-carrier interactions, making QDs even more applicable as gain medium and applications such as lasing, is carrier multiplication, where absorption of a photon can result in the generation of many electron-hole pairs, enabling superior QYs above unity (Figure 1.6).[22]

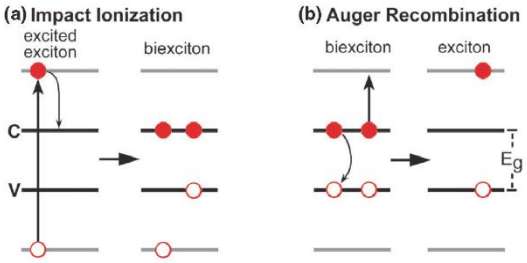

Figure 1.6: Illustration of carrier multiplication (a) biexciton generation and (b) Auger recombination in semiconductor nanocrystals.[21]

While single excitons typically display radiative recombination pathways, the introduction of multiple carriers and multiexciton generation results in completely different dynamics. Mainly due to strong carrier-carrier interactions, nonradiative recombination pathways become available.[12] There are several non-radiative decay mechanisms, which result in QDs with QY well below unity, consequently competing with QD applicability for areas such as lasing where radiative relaxation pathways should dominate.

One of the dominant non-radiative decay mechanisms associated with multiexcitons in QDs is Auger recombination, in which the energy of an exciton is used to excite another electron or hole to a higher energy level (Figure 1.5b).[13] The rate of the temperature-driven process can be expressed as:

$$r_A \propto e^{-\gamma_A E_g / k_B T} \tag{1.2}$$

where γ_A is a material dependent constant and E_g is the bandgap of the material.[13] Due to the ultrafast rates associated with Auger recombination, on the order of ps, the application of QDs specifically for lasing has only been realized more recently.

Intense research has focused on extending Auger recombination rates in order to see an appreciable impact in the field of photonics. Specifically, researchers have investigated suppression via control of the strength of the intraband transition (i.e. core/shell structure engineering via alloying), control of conduction and valence band mixing by introducing a much thicker shell, and finally controlling the overlap of the electron and hole wavefunctions via the heterostructure type.[13]

1.3 QD Polymer Nanocomposites

While nanoparticles, more specifically quantum dots, are quite diverse in their function, their application can be seen as quite limited owing to their limited processability. Providing a host matrix allows for nanoparticles to be used in more technologically exploitable forms such as fibers, and robust, mechanically and chemically stable films and patterns.[23] For such composite systems, inclusion of nanoparticles into polymer matrices typically results in improvements to thermal, mechanical, electrical, and optical properties of the system. For example, citrate-stabilized gold nanoparticles were embedded in a polyurethane matrix with ultra-high loading using a layer by layer (LbL) or vacuum assisted process. The resulting composite was flexible and stretchable, displaying excellent mechanical properties, maintaining its conductance even under significant mechanical strains.[24]

Of noteworthy importance is the incorporation of gain media, particularly QDs, into polymer matrices as it opens up opportunities for integrated materials with advantageous optical properties.[25] The controlled incorporation of QDs into polymer matrices is a particularly essential step because it allows for the fabrication of stable and functional optical materials with low optical losses, offering the ability to vary thickness (submicrometers to micrometers), relative ease in processing, and the controlled incorporation of significant quantities of QD gain medium into a matrix for potentially tunable emission strength and refractive index modulation.

Furthermore, optically active medium coupled with elastomeric supports/matrices not only provides for robust and mechanically stable optoelectronic devices,[26,27] but the ability to tune important photonic system parameters such as emission wavelength and coupling strength via external stimuli (i.e. stress, strain, temperature) has also been demonstrated.[28,29] While gain medium incorporated within flexible matrices and supports offer tremendous potential in terms of

photonics, their preparation remains challenging, primarily relating to large-scale phase separation, which results in QD aggregation due to the typically high interfacial energies and dominating enthalpic interactions,[30] thus resulting in high optical scattering and losses. In addition, nanoscale patterning of nanocomposites, with precise control and tunability using facile bench scale techniques remains an arduous task.

1.3.1 Understanding Ligand Chemistry

QD design has significantly evolved over the years, and precise control of processes has led to core-graded shell designs having very high quantum yield and greatly suppressed Auger recombination. [31] Of particular importance in terms of design of colloidal QDs and QD nanocomposites is ensuring they are readily processable. This requires that QDs interact favorably with the surrounding medium, enabling solubility in a variety of solvents and eventual controlled dispersion of nanoparticles within a polymer host matrix. As mentioned above, organic ligands are incorporated during synthesis of QDs to passivate the core-shell surface in order to control QD nucleation and growth, resulting in improved QD stability, limiting aggregation, and making them soluble in a number of solvents for easy processability.

Ligands can typically be categorized in three classes, based on the number of donor electrons involved and the identity of the electron donor and acceptor groups: L-type, X-type, and Z-type ligands.[32] L- and X- ligands such as Amines (RNH2) and carboxylates (RCOO-) bind to electron deficient surfaces while Z-type ligands, such as Pb(OOCR)2, are electron acceptors and bind through the metal atoms to electron rich sites.[32] In addition, use of metal free all-inorganic ions can serve as ligands and stabilize QDs in polar solvents.[33] Specifically, inorganic ions such as S^{2-}, HS^{-}, Se^{2-}, HSe^{-}, Te^{2-}, Hte^{-}, TeS_3^{2-},OH^{-},and NH_2^{-} can be exchanged with native organic ligands via a nucleophilic substitution, following a pseudo - dissociative reaction pathway. Use

of such smaller ligands significantly enhances charge transport among quantum dots making them even more ideal candidates for optoelectronics.

Left unbound, QD surfaces free of ligands can result in creation of surface-bond trapping sites, preventing the recombination of electron hole pairs, thus leading to degradation of QD optical properties. In contrast, certain ligands offer other benefits in addition to control of colloidal stability and aggregation. While amines and thiols are known to be hole scavengers, depending on the core-shell QD material, their use has resulted in enhanced quantum yield. For example, the controlled introduction of 3-mercaptopropionic acid (3-MPA) was demonstrated to quench band-edge emission and enhance deep trap state emission, displaying tunable QD emission across the visible spectrum based on the concentration of 3-MPA, and enhanced QY for deep trap states (**Figure 1.7**).[34]

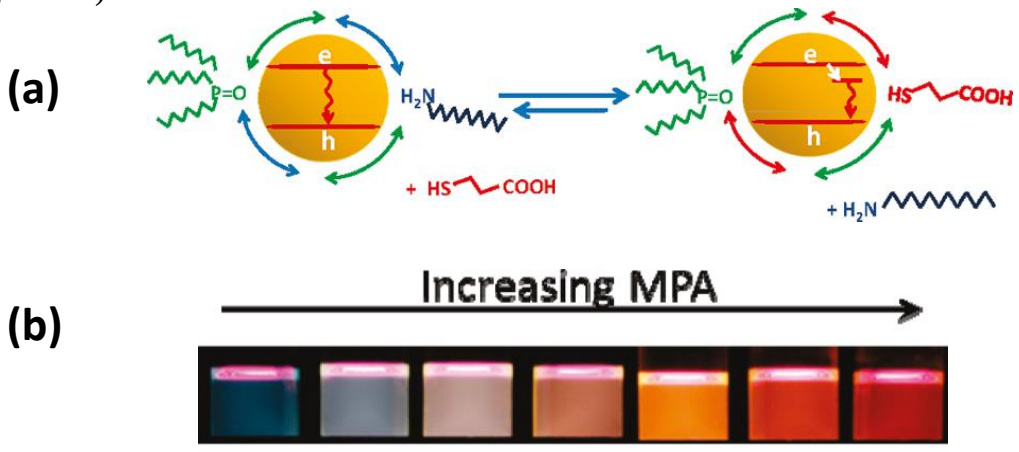

Figure 1.7: Ligand exchange using thiols showing change in exciton recombination (a) and tuning of PL emission via concentration of thiol ligand (b). Reproduced with permission [33] Copyright 2010, American Chemical Society.

In another study, amines, in comparison to their thiol counterparts, have demonstrated the ability to enhance QY, to nearly 80%, from 50% with thiol ligands.[35] This is due to the strong bond between the amine ligand and QD surface, eliminating potential surface traps. Some of the more common ligands used to stabilize these nanocrystals are TOPO, oleic acid (OA), and

hexadecylamine (HDA). While limited to organic solvents with these ligands, the QD surface has a strong affinity to a number of functional groups, making QDs readily soluble in a host of solvents following ligand exchange. Ligand exchange reactions are heavily influenced by ligand affinities to the nanocrystal surface, concentration of ligand, as well as solvent used. A thorough understanding of these effects will facilitate the design of stable QD nanocrystals that have solubility in a large gamut of solvents, and their incorporation in stable support matrices. Several schemes have been developed to passivate the QD surface, and expand their solubility range.[36,37]

Additionally, surface ligands can directly affect the optical and electrical properties of semiconductor nanocrystals. It has been established that these properties are heavily influenced by the QD size and ligand, moreover, induced surface dipoles present an opportunity to modify electronic structures. For example, based on the ligand treatment, energy levels of PbS can shift by 0.9 eV (**Figure 1.8**).[38]

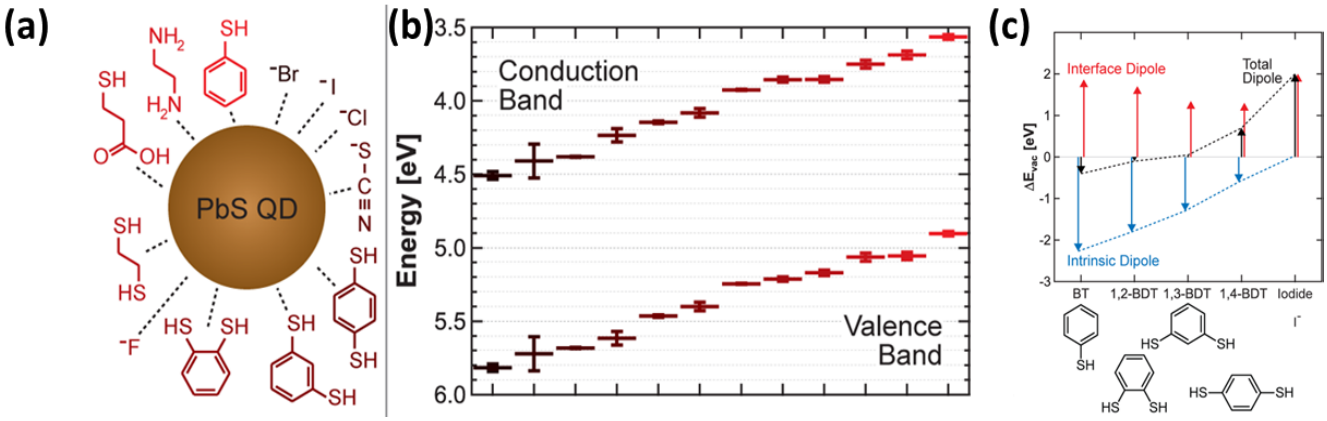

Figure 1.8: Ligand exchange on PbS QD surface using a variety of organic and inorganic ligands (a) and the resulting change in energy level (b). (c) effect of dipole moment of select ligands as well as the QD-ligand interface showing effect on total dipole moment. Reproduced with permission [37] Copyright 2014, American Chemical Society.

The resulting energy level set is a result of contributions from the QD-ligand dipole in addition to the dipole moment experienced by the ligand itself (**Figure 1.8c**).[38] For dipoles

pointing towards the QD surface, the resulting electric field potential shifts the energy levels down, in contrast for the opposite case, energy levels are shifted up.

Most important in understanding and exploiting the importance of QD surface chemistry is understanding the end use in terms of the requirements of the core constituents (i.e. solubility, polymer matrix compatibility). For example, the emissive properties of water-soluble QDs make them ideal candidates for biomedical imaging, diagnosis, and treatment, requiring the QDs to be dispersible in aqueous solutions. It is important to note that often times, initial ligands need to be

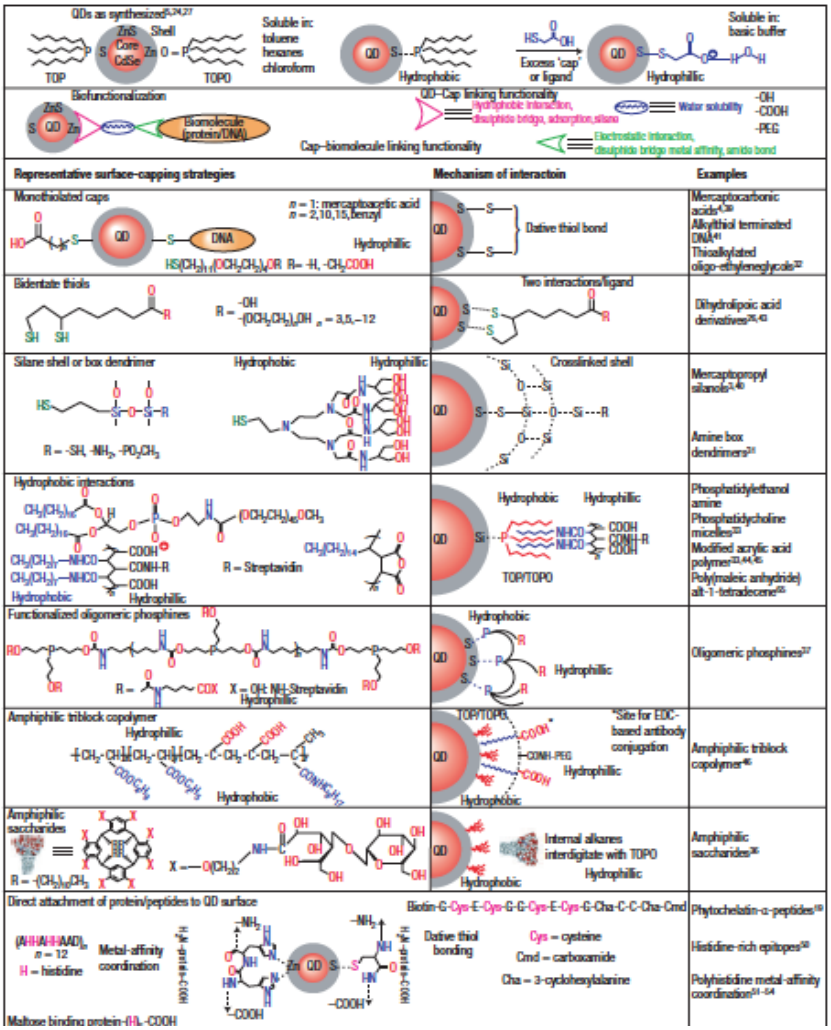

Figure 1.9: Various ligand exchange techniques making QDs readily soluble in a host of organic/inorganic medium and compatible with biological environments. Reproduced with permission.[38] Copyright 2017, Nature Publishing Group.

exchanged for bio related applications making the QDs compatible with biological environments and less toxic (**Figure 1.9**).[39]

For the fabrication of solid state materials and devices on the other hand, the requirements are quite different. Typically, native ligands are suitable for solid-state devices, as solution processability, stability, and excellent optical properties are most important. Solution processability affords QDs to be readily adaptable to facile and relatively low-cost deposition and patterning techniques such as spin-casting, ink-jet printing, photolithography, and soft lithography.

1.3.2 Current QD-polymer Nanocomposite systems

In order to realize fully functional devices a key hurdle to overcome is the fine dispersion of active gain nanostructures within a polymer matrix without significant phase separation. While still a challenging task, as mentioned above control of nanoparticle surface chemistry has been demonstrated to play a key role in fabricating well dispersed QD-polymer composites.

Initial efforts to develop QD−polymer composites have seen limited success since simple mixing of the two components typically led to significant QD aggregation.[40,41] Due to the strong particle-particle interactions and immiscibility of components, aggregation is favorable as a mechanism to reduce interfacial energy. For QD-polymer composites, the biggest concern is phase separation and the resulting QD aggregation leading to the deterioration of the QD optical properties due to excessive optical scattering and losses. As the concentration is increased, this leads to large-scale segregation of the components resulting in strong light scattering. In addition to aggregation, QD polymer composites often suffer in terms of post-fabrication processability due to increased viscosity. Ideally, for applications involving QDs, deposition/fabrication techniques

need to be extremely versatile, and offer ease of patterning in order to truly exploit the optical properties of QD composite materials.

To this end, Wang et al. developed microbubble composites via simple drop-casting of QD−poly(methyl methacrylate) (PMMA) solutions.[42] Loadings above 50% were achieved; however, this methodology is not easily adaptable to patterning, as structures are limited to hemispherical droplets. In addition to PMMA, similar polymer matrices have been used to develop QD composite materials.[43,44,45] Of notable interest is a methodology developed by Zhu et. al incorporating water soluble quantum dots at high concentrations (50 wt%) into cellulose nanofiber-based polymer matrices. By vigorously mixing oxidized cellulose nanofiber aqueous dispersions with glutathione capped QDs and degassing, the nanoscale separated phase within the cellulose nanofibers was exploited and composite films of micron thicknesses could be attained.[46]

In other studies, simple mixing of QDs with poly (lauryl methacrylate) (PLMA) have been exploited to fabricate QD polymer nanocomposites.[47,48] Going a few steps further, researchers have also initiated free radical polymerizations of monomer building blocks in the presence of QDs to fabricate QD composites.[49,50,51] Ehlert et al. demonstrated QD−polymer composites by grafting polymer brushes onto the QD surface and subsequently mixing with like polymers.[52] Additionally the importance of the ligand chemistry was demonstrated in fabricating polymer composites for photovoltaics.[53] But again, manipulation of such complex chemistries for composite patterning is all but facile.

Proposed complex reaction schemes have resulted in inclusion of QDs at very low weight percentages, however, these complex schemes can compromise the optical properties of the QD composites.[54] Specifically, aggregation of QDs typically leads to nonradiative decay mechanisms such as quenching[7] as well as optical losses from scattering.[55] In addition, while QD photopatterns

of micron resolution have been generated utilizing TEM grids as a mask, a scalable approach that allows for the fabrication of high-resolution submicron patterns in highly loaded QD composites have not yet been developed.[56]

A proposed method for combating large QD aggregation would be the utilization of a fast cross-linking mechanism that takes place on time scales faster than phase separation of relatively large nanoparticles and aggregates. [57] This methodology of fast crosslinking of photocurable polymers has proven to be efficient technique for producing dental composites. Furthermore, it has been demonstrated that crosslinked nanoparticles from polymer constituents can be dispersed within a polymer matrix provided the size of the nanoparticle is smaller than the radius of gyration of the polymer matrix.[58] In addition, it has been suggested that cross-linking of QDs during polymerization can reduce aggregation and control energy transfer mechanisms, resulting in enhanced light emission in comparison to the non-cross-linked counterparts.[59,60]

1.3.3 Photopolymerization

While there are a number of unique polymerization methods, a very attractive polymerization scheme due to its versatility is the thiol−ene reaction. This photopolymerization reaction produces cross-linked networks,[61] occurs rapidly, is highly efficient,[62,63] and is largely insensitive to ambient environments.[61, 64] Given the weak nature of the sulfur − hydrogen bonding, a free-radical initiating species will abstract a hydrogen from the thiol precursor. Subsequently, the thiyl radical will efficiently attack an electron-deficient terminal carbon−carbon double bond, forming a cross-linked network similar to the reaction that proceeds with the vulcanization of rubber.[61, 64]

The cross-linking density of thiol−ene photopolymerization can be readily tailored for tunability of the thermal and mechanical properties of the host matrix,[65, 66] leading to potentially robust and flexible networks with uniform distribution of components. Moreover, thiol−ene chemistries come in a variety of mixtures depending on the desired properties, including commercially available thiol−ene based optical adhesive mixtures,[67] i.e., Norland Optical Adhesives, which typically consists of a triene (i.e., 1,3,5-triallyl-1,3,5-triazine2,4,6(1H,3H,5H)-trione) and a multifunctional mercapto-ester (i.e., pentaerythritol tetrakis(3-mercaptopropionate)), with a urethane-based component, and a benzophenone photoinitiator (**Figure 1.10**).[64] In terms of nanocomposite fabrication, nanoparticles can readily be functionalized with ligands having terminal thiols or -enes to participate in the thiol-ene reaction.

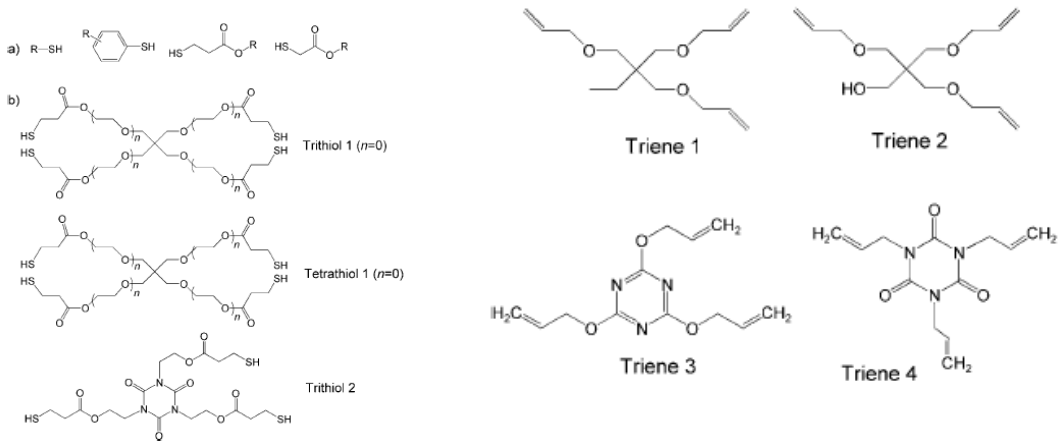

Figure 1.10: Thiols (a) and alkenes (b) used in thiol-ene click type chemistry.[63]

The thiol−ene mechanism has been utilized as a "click" reaction to generate QD−polymer composites via a "graft from" mechanism where the nanoparticle ligands serve as anchoring sites that participate in the step growth thiol−ene polymerization, producing various cross-linked polymer composites in which the nanoparticles can serve as cross-link or anchor sites.[67,68,69,70] For

instance, Lüet al. grafted thiolated styrene and phenol onto ZnS QDs, followed by a UV-initiated free radical polymerization to form a poly(urethane−methacrylate macromer) composite in which QDs were immobilized in the polymer network, taking advantage of thiol−ene based click chemistry.[71] Similarly, Kim et al. functionalized the surface of QDs with a complex norbornene compound and generated a QD−polymer composite by photopolymerizing the tethered -ene with a multifunctional thiol. Loading did not exceed 0.2 wt % as they were only interested in displaying photoluminescent QD patterns.[54] While the above-mentioned methods have mostly demonstrated the feasibility and benefits of thiol-ene chemistry, it's versatility expands beyond what has been reported. In order to realize the full potential of QD composites, subsequent work should focus on increasing loading while minimizing the potential for phase separation, as well as demonstrating high resolution patterning capabilities.

1.4 Individual Assemblies of QDs for Photonic Systems

To realize optimal control of light-matter interactions it is necessary to precisely control and pattern assemblies of gain medium. QDs are the prudent choice because they are very advantageous in comparison to their counterparts.[72] To summarize, QDs offer composition and size dependent absorption and photoluminescence ranging from ultraviolet (UV) to infrared (IR) regions, large absorption coefficients, solution processability via altering of the ligand chemistry, and extended photoluminescence lifetimes.[7] The chemical flexibility of QD surface chemistry makes them easily adaptable to surrounding environments/matrices. An ideal host matrix, particularly for photonic systems, would be robust and flexible, providing functional materials that are readily integrated and potentially tunable.

Patterning of QDs typically results in the formation of photonic cavities. Photonic systems are often times periodic in nature, providing repeating regions of high and low dielectric constant (refractive index) leading to coherent scattering of the light. (Figure 1.11)[73] As described by

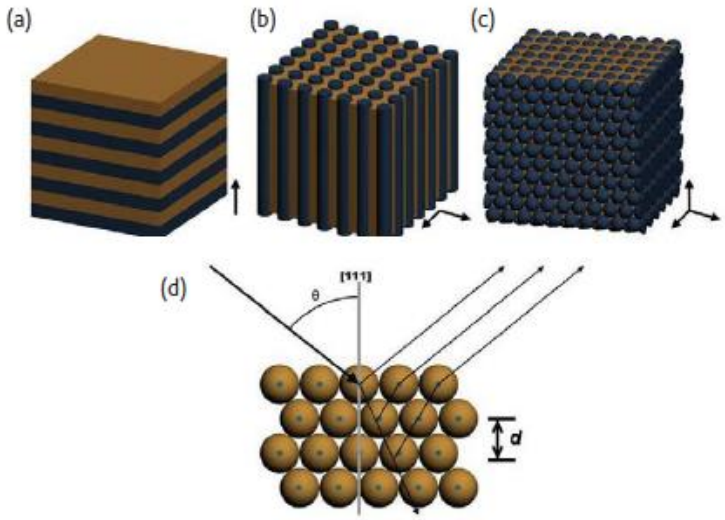

Figure 1.11: Structure for 1D (a) 2D (b) and 3D (c) photonic crystal with typical interference pattern generated (d).[76]

Maxwell's electric and magnetic field propagation equations, the response of a material to an external field, is largely governed by material properties such as refractive index, permeability, and permittivity. Their relationship to each other being $n = \sqrt{\varepsilon\mu}$, with the permeability of most optical materials being unity.

Photonic structures can be as simple as 1D waveguides and disk resonators, or as complex as 3D photonic crystals. The simpler case operating off the principal of total internal reflection, in which a wave strikes a medium boundary and the angle (Θ_i) is larger than a critical angle, and the refractive index contrast is significant (i.e. n is greater in the resonator cavity (gain medium)) the light will be completely reflected. [74] This can be described via Snell's law:

$$\theta_i > \sin^{-1}(n_2/n_1) \qquad (1.3)$$

Photonic assemblies have led to very interesting phenomena and applications including Bragg mirrors,[75] waveguides,[76] lasing,[77] filters,[78] and prisms[79].

Since the introduction of the vertical-cavity surface-emitting laser (VCSEL) in the late 1980s the trend towards smaller has opened avenues for new and exciting applications that were once unattainable.[80] Miniaturized lasers could potentially allow for on-chip optical communications and data processing, as well as next generation medical imaging and sensing. QDs are ideal candidates for next generation miniaturized photonic systems, as they are an optically active material showing high material gain values. Furthermore, their encapsulation and/or arrangement in/on periodic polymer matrices allows for a widely tunable photonic system taking advantage of the optical properties of the QDs and the transparency, low refractive index, and tunable mechanical properties of the polymers.

Polymers are easily processable, often times providing a mechanically tunable matrix, and are compatible with a number of patterning techniques, making them ideal candidates for producing photonic system templates. A number of polymer photonic crystals have been previously fabricated using a variety of techniques including self-assembly, microfabrication, and template assisted assembly.[73] For example, polymer photonic systems have been demonstrated via the self-assembly of polystyrene beads [81] and block copolymers.[82] The polymer matrix can provide the refractive index contrast and thereby total internal reflection to realize the cavity like structure and the inclusion of QDs as gain medium could lead to precisely tunable photonic laser cavities.[83]

Examples of the four most common photonic microcavity configurations, allowing for light to be confined within the gain medium, can be seen in Figure 1.12.[84]

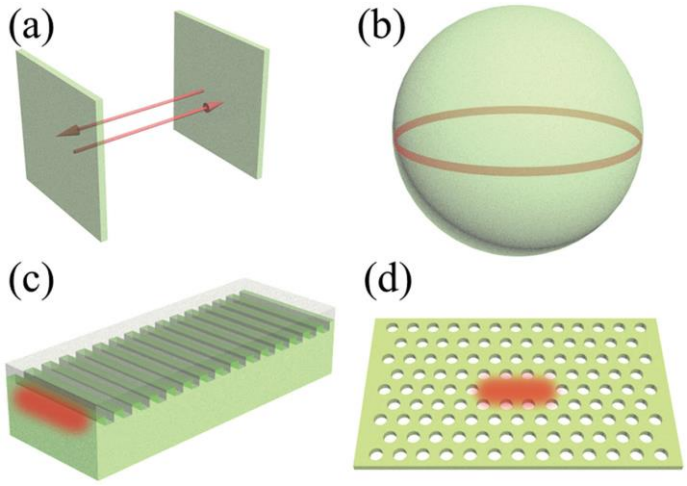

Figure 1.12: Various resonator cavities used to demonstrate lasing. [87]

They include Fabry–Perot microcavities, whispering gallery mode (WGM) microcavities, distributed feedback (DFB) microcavities, and photonic crystal defect microcavities.

1.4.1 WGM Resonators

WGM mircocavities have garnered the most attention due to their ease of fabrication as well as their high quality factor, low mode volume, and large optical density.[85] In such cavities, the majority of the light is confined within the structure via continuous total internal reflection.

1.4.1.1 Dielectric Spheres

One of the most unique WGM resonators, are microspheres, as light travels and can be confined in all directions, enabling ultra-low mode volumes and ultrahigh quality factors.

Additionally, their ease of fabrication, discussed in detail below, in a variety of sizes, and simplistic post fabrication modification makes them quite attractive optical components. Using the Stöber method, silica microspheres ranging in size from sub-500nm to tens of microns have been fabricated.[86] In addition, with the aid of surface hydroxyl groups, researchers have readily demonstrated the ability to functionalize the silica microsphere surface with metals and quantum dots.[87, 88] Similarly, polymeric microspheres, typically consisting of polystyrene, can be fabricated via emulsion polymerizations.[89, 90] Due to their crosslinked nature, post modification can be more simplified in comparison to their silica counterparts, merely by swelling using an appropriate solvent and introducing metals, quantum dots, etc., and deswelling, polystyrene beads can be easily embedded with nanomaterials.[90]

1.4.1.2 Synthesis

As mentioned above, a host of materials can be used in the formation of dielectric microspheres, referred to as WGM resonators going forward. For example, microspheres have been demonstrated using silica, traditional polymers such as polystyrene and PMMA, as well as conjugated polymers.[86, 89, 91]

Focusing on silica, in a traditional synthesis, spherical particles of uniform size can be fabricated via a hydrolysis reaction. Specifically, alkyl silicates from tetraethyl orthosilicate (TEOS) are hydrolyzed followed by the condensation of silicic acid, in the presence of morphological catalyst, ammonia, and alcoholic solvents.[86] Control of size is afforded by control of the ratio between TEOS and water/ammonia. Synthesis results in hydroxyl (-OH) surface chemistries, which are readily amenable via simplistic post modification of surface chemistry. While microsphere fabrication is fairly straightforward, and uniform size distribution results, the

coefficient of variation can be quite broad ranging from 5-10%. In terms of WGM resonators, these size variations can translate to large shifts of the resonant peaks in the WGM spectra.[92]

1.4.1.3 Optical modes in WGM Resonators

Resonance behavior of spheres has been studied for decades. They were first discovered by Lord Rayleigh to describe the phenomenon of the whispering gallery at St. Paul's cathedral in London, England.[93] Via total internal reflection waves at the sphere circumference form standing waves after one round trip, as shown in Figure 1.13. Comprehensive overviews has been conducted by several authors.[94, 95] A simple method for approximation of high-order WGMs

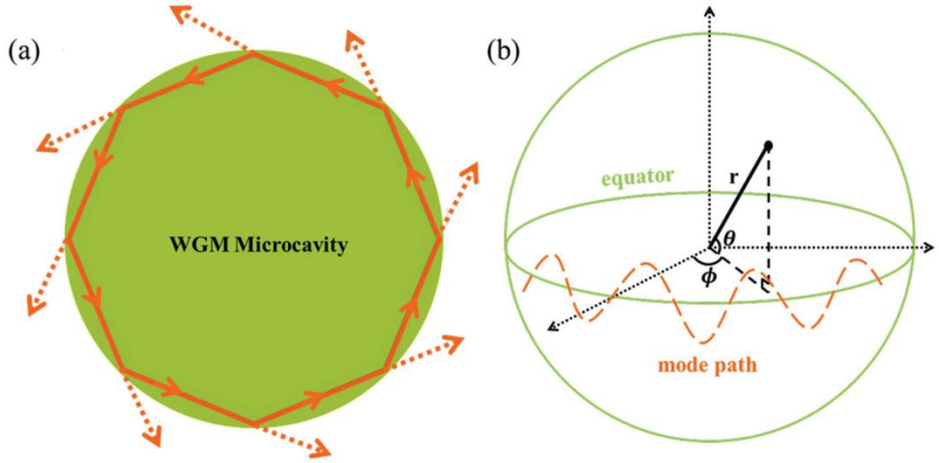

Figure 1.13: WGM cavity demonstrating total internal reflection and mode path at equator of resonator.

can be calculated by solving for Helmholtz equations in spherical coordinates.[95,96] The Helmholtz equation can be seen below:

$$(\nabla^2 - k^2)\psi = 0 \qquad (1.4)$$

where $k = n\frac{\omega}{c}$. In spherical coordinates the Laplace equations becomes:

$$\frac{1}{r^2}\frac{\partial^2\psi}{\partial r}+\frac{1}{r^2\sin\theta}\frac{\partial}{\partial\theta}\left(\sin\theta\frac{\partial\psi}{\partial\theta}\right)+\frac{1}{r^2\sin^2\theta}\frac{\partial^2\psi}{\partial\varphi^2}+k^2\psi=0 \qquad (1.5)$$

By assuming a homogeneous microsphere having constant polarization, a simplification occurs allowing for the optical modes to be solved by the scalar wave equation approximation. The field components can now be expressed in terms of a single component (E_φ (TM-case) or H_φ (TE-case)), solutions for which can be found by solving the above scalar wave equation for either E_φ or H_φ by using the separation of variables approach obtaining a product form of the potential:

$$\psi \text{ (i.e. } E_\varphi \text{ or } H_\varphi = \psi(\varphi,\theta,r) = \psi_\varphi(\varphi)\psi_\theta(\theta)\psi_r(r)\text{)} \qquad (1.6)$$

where r is the radial coordinate, θ is the polar angle, and φ is the azimuthal angle as shown in Figure 1.13b. The introduction of the eigenfunctions associated with the radial, polar, and azimuthal fields are directly related to the radial mode number (q), the polar/angular mode number (l), the azimuthal mode number (m), and the polarization (p).

The separation of variables leads to the introduction of the azimuthal and angular mode number as follows:

$$\frac{1}{\psi_\varphi}\frac{\partial^2\psi_\varphi}{\partial\varphi^2}=-m^2 \qquad (1.7)$$

$$\frac{r}{\psi_r}\frac{d^2\psi_r}{dr^2}=l(l+1) \qquad (1.8)$$

Based on the separation of variables, the following solutions can be gathered. The azimuthal dependence is given by:

$$\psi_{\varphi} = \frac{1}{\sqrt{2\pi}} \exp(\pm im\varphi) \tag{1.9}$$

The polar dependence satisfies the equation:

$$\frac{1}{sin\theta}\frac{d}{d\theta}\left(\sin\theta \frac{d}{d\theta}\psi_{\theta}\right) - \frac{m^2}{sin^2\theta}\psi_{\theta} + l(l+1)\psi_{\theta} = 0 \tag{1.10}$$

and the radial field has to obey:

$$\frac{\partial^2\psi_r}{\partial r^2} + \frac{2}{r}\frac{\partial\psi_r}{\partial r} + \left(k^2 - \frac{l(l+1)}{r^2}\right)\psi_r = 0 \tag{1.11}$$

Both equations 1.10 and 1.11 have exact solutions in the form of the Legendre Polynomials $P_l^m(\cos\theta)$ for $\psi_{\theta}(\theta)$ and the spherical Bessel function $j_l(kr)$ for $\psi_r(r)$. The component of the amplitude of either field in the field can be expressed as follows:

$$\begin{bmatrix} B(\psi)_r^{in} \\ B(\psi)_{\theta}^{in} \\ B(\psi)_{\phi}^{in} \end{bmatrix} = \begin{pmatrix} b_r \\ b_{\theta} \\ b_{\psi} \end{pmatrix} j_l(k_{in}r) P_l^m(\cos\theta) e^{im\varphi} \tag{1.12}$$

In order to determine the field distribution and resonance positions of the resonator, it is required to match the solution of the system inside the sphere with that outside the sphere at the dielectric-air boundary. While the interior of the sphere is best described by the Bessel function, the outside of the sphere, possessing a wave that is evanescent in nature, should have the asymptotic form of

a runaway wave, or the Hankel function, $H_l(k_0 r)$. Similar to the solution of the system inside the sphere, the amplitude of the evanescent field outside the cavity can be described as follows:

$$\begin{bmatrix} B(\psi)_r^{in} \\ B(\psi)_\theta^{in} \\ B(\psi)_\phi^{in} \end{bmatrix} = \begin{pmatrix} x_r \\ x_\theta \\ x_\psi \end{pmatrix} h_l(k_{out} r) P_l^m(\cos\theta) e^{im\varphi} \tag{1.13}$$

The characteristic equation matching the two functions at the boundary is as follows:

$$x \cdot \frac{j_l'(ka)}{j_l(ka)} = \frac{h_l'(ka)}{h_l(ka)} \quad \text{where } x = \begin{bmatrix} \left(\frac{\mu}{\varepsilon}\right)^{1/2} & for\ TM \\ \left(\frac{\varepsilon}{\mu}\right)^{1/2} & for\ TE \end{bmatrix} \tag{1.14}$$

This characteristic equation determines the relationship between the wave number, k, and the sphere radius, a. The roots of these characteristic equations give the theoretical approximations of the WGM resonances. The resonant positions are dependent on the TE and TM modes as well as the angular mode number (l), equivalent to the number of fields along the boundary of the microcavity, the azimuthal mode number (m), where l-m+1 indicated the number of resonances in the azimuthal direction, and the radial mode number q, indicating the number of modes in the radial direction. The allowed azimuthal mode numbers are in the range $-l < m < l$, resulting in

2l+1 degeneracy of the azimuthal modes. Simulations showing how each mode number affects whispering gallery mode formation can be seen in Figure 1.14.[84]

Asymptotic expansion of the above characteristic equations leads to approximate resonance locations. More specifically, the mode spectrum can be determined by implementing

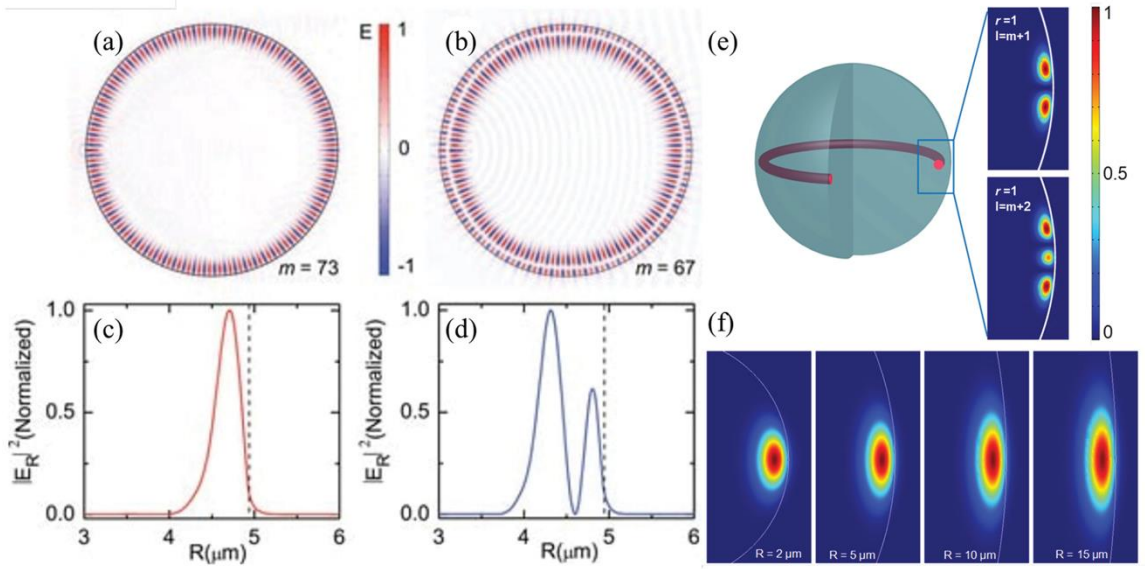

Figure 1.14: Illustration showing mode profile for different radial and azimuthal mode numbers.[84]

the following boundary conditions: $\Psi(r) \to 0$ for $r \to \infty$ and $r \to 0$. For both TE and TM high order modes ($\nu \gg 1$) the wave vector can be approximated:[95]

$$k_{\nu,q} \cong \frac{1}{a\sqrt{\varepsilon}}\left[\nu + \alpha_q \left(\frac{\nu}{2}\right)^{1/3} - \sqrt{\frac{\varepsilon}{\varepsilon - 1}} + \frac{3\alpha_q^2}{20}\left(\frac{2}{\nu}\right)^{1/3} + O\left(\nu^{-2/3}\right)\right] \qquad (1.15)$$

$$k_{\nu,q} \cong \frac{1}{a\sqrt{\varepsilon}}\left[\nu + \alpha_q \left(\frac{\nu}{2}\right)^{1/3} - \sqrt{\frac{1}{\varepsilon(\varepsilon - 1)}} + \frac{3\alpha_q^2}{20}\left(\frac{2}{\nu}\right)^{1/3} + O\left(\nu^{-2/3}\right)\right] \qquad (1.16)$$

where α_q is the qth root of the Airy function, and a is the radius of the resonator, and ν = l+1/2. Solving for the first root of the Airy function and simplifying in terms of wavelength gives the following approximation of resonance positions:

$$\lambda_{TE} \approx \frac{2\pi a n_1}{\nu + 1.856\nu^{1/3} + \left(\frac{1}{2} - \frac{n_1}{\sqrt{n_1^2 - 1}}\right)} \tag{1.17}$$

$$\lambda_{TM} \approx \frac{2\pi R n_1}{\nu + 1.856\nu^{1/3} + \left(\frac{1}{2} - \frac{1}{n_1\sqrt{n_1^2 - 1}}\right)} \tag{1.18}$$

where R is the sphere radius, $n_1 = \sqrt{\varepsilon\mu}$ and is the spherical cavity refractive index, and μ=1.

1.4.1.4 Quality Factor, Free Spectral Range, and Mode Volume of WGMs

There are several parameters used to characterize the efficiency of whispering gallery mode resonators. Two of the most important parameters are quality factor (Q) and mode volume (V). Due to the lossy nature of WGM resonators, typically caused by reabsorption as well as scattering losses, the resonance behavior eventually decays, suggesting the WGMs are best described as quasi-modes. In order to characterize the dissipative nature of the WGMs, the Quality-factor or Q-factor is used. It is defined as the energy storage time normalized by the period of oscillation.

$$Q = \omega\tau \tag{1.19}$$

Specifically, in terms of optical cavities the Q-factor describes the photon optical lifetime inside a cavity mode or how well a cavity mode stores/confines light. As mentioned above, any deviations from ideal result in losses for the resonator, contributing to a reduction in Q-factor. The loss mechanisms include materials absorption, scattering losses, surface absorption losses, whispering gallery mode losses, and external coupling losses.[96,97]

$$Q_{tot}^{-1} = Q_{mat}^{-1} + Q_{scatt}^{-1} + Q_{surf}^{-1} + Q_{WGM}^{-1} + Q_{ext}^{-1} \quad (1.20)$$

Of most importance when considering WGM resonators are the material used and fabrication techniques in order to minimize inhomogeneities on the surface causing scattering losses, and finally the material and gain medium to minimize losses that arise from a materials intrinsic properties. Also of importance is the WGM losses, typically associated with the curvature of the circular boundary. Though this is inevitable, generally the smaller the resonator the larger the curvature/bending losses reducing the efficiency of light confinement. Theoretical calculations show that spherical WGM resonators can possess Q-factors larger than 10^9.

The free spectral range (FSR) of a resonator is defined as the distance between two adjacent angular mode numbers.

$$\Delta\lambda = \frac{\lambda^2}{2n\pi R} \quad (1.21)$$

Generally speaking, the smaller your resonator the larger the FSR. Finally, the mode volume (V) of a resonator describes how well a resonator can spatially confine light.

$$V = \frac{Total\ Energy}{\max(Energy\ Density)} \tag{1.22}$$

Specifically, in terms of microlasers the spontaneous emission and stimulated emission rates are proportional to V^{-1} and the lasing threshold is proportional to V. To date mode volumes for spherical WGMs have exceeded 3000.[98] A host of WGM resonators have been demonstrated, including droplets, rings, microdisks, and microspheres.[84, 99] In order to excite whispering gallery modes in a resonator evanescent coupling is required. When there is a gain medium embedded in the resonator the scattering from the gain medium can serve as a local excitation source for the modes, however.

1.5 Coupled Assemblies of QDs for Photonic Systems

For WGM resonators, nearly 99% of light is confined within the cavity via total internal reflection, the remaining 1% manifest itself as an evanescent field just outside the cavity. As a result of the evanescent wave that extends hundreds of nanometers outside of the circumference of WGM cavities, interesting coupling phenomena can be observed and exploited when microcavities are fabricated in close proximity to one another. It is well understood and very important to note that the strength of the evanescent field decays exponentially as the distance from the cavity edge increases, as described in the following equation, (Figure 1.15)[100]

:

$$I(z) = I(0)e^{-z/d} \tag{1.23}$$

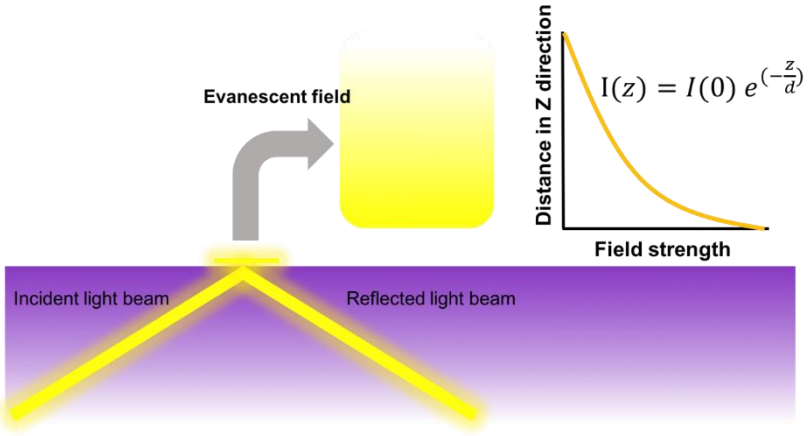

Figure 1.15: Illustration of evanescent field in optical cavities and decay of field with distance.[96]

In the above equation, z is the distance from the surface, I is the field strength at distance z, I(0) is the field strength at the surface, and d is the penetration depth, which describes the decay of the electromagnetic wave, and is linearly proportional to the emission wavelength of the material: [74]

$$d = \frac{\lambda}{2\pi\sqrt{n_1^2 \sin^2\theta - n_2^2}} \qquad (1.24)$$

When z=d, the strength falls to 1/e (about 37%) of its original value I(0). The field decays with increasing distance, therefore, the cavities need to be in very close proximity of each other to realize overlap of the evanescent fields. Such coupling phenomenon is the basis for on-chip signal processing, in addition to wavelength selective amplification, switching, and modulation.[101]

Resonator to resonator coupling has been demonstrated in a host of geometries, for example microdisks, microtoroids, and microspheres. Traditionally this is accomplished by taking advantage of precision patterning techniques, such as EBL, in the case of microring resonators or via micromanipulators in the case of microsphere resonators. When coupling between neighboring

resonators is observed, high Q resonant modes of individual resonators split into distinct broad features. This can best be described via the classical physics example of the coupled pendulum. When two identical pendulums are coupled via a spring, eigenmodes will be observed in two cases: when the pendulums swing in phase with each other and when they swing alternatively towards and away from one another. The mode splitting is due to the coupling of the systems, resulting in the pendulums oscillating at a slower rate when in phase, and slightly faster when out of phase. In terms of optical coupling these two phases are considered the bonding and antibonding state.[102] The distance between the peaks dictates the strength of the coupling, showing an inverse relationship. Sophisticated patterning techniques are generally required to achieve strong optical coupling and mode splitting among resonators. Techniques to fabricate such coupled resonators will be discussed below.

1.5.1 Nanofabrication of Photonic Arrangements

Advancements in fields such as micro/nanofabrication and nanoparticle synthesis have pushed the limits of the field of nanophotonics leading to new and exciting functional devices. As was demonstrated in the examples provided above, precise patterning of structures on the nanoscale is essential to realize photonic cavity/crystals and the unique optical phenomenon associated with them. Traditionally, the formation of photonic cavities and crystals is done by electron beam lithography,[103,104] although more recently they have been fabricated using soft-lithography.[105] Generally, the patterning of QD falls into one of four categories: inkjet printing, electron beam lithography, template stripping, and soft lithography. To briefly summarize the deposition/patterning techniques, ink-jet printing is a technique used to print large area arrays, however conductive inks are typically required, and resolution is limited to tens of micrometers.[106]

E-beam lithography is capable of sub 10-nm resolution but is very limited in throughput and costly given the clean room requirements for fabrication.[107] Finally templated stripping utilizes a combination of e-beam lithography with a transfer technique to generate submicron QD patterns. Unfortunately, the low throughput and costly e-beam lithography step is required.[108] The above techniques suffer from all or some of the following limitations: high cost, limited selection of materials to use, and low resolution. Ideally a patterning technique would be readily scalable, offer high resolution patterns, and offer post processing tunability and flexibility. Soft lithography is the judicious choice for reasons that will be discussed in the following sections.

1.5.1.1 Soft-lithography

Soft-lithography is a technique by which an elastomeric stamp is used to pattern micron to nanoscale features on a substrate. [109] Briefly, using a patterned stamp typically made of polydimethysiloxane (PDMS), the features of the stamp are replicated on a substrate using a photo or thermally polymerizable monomer solution. It is a versatile technique, offering the ability to fabricate structures and patterns ranging from tens of nanometers to hundreds of microns. While proposed to be an alternative to photolithography, it is more complementary as initial fabrication of the master used to develop the elastomeric stamp/mold typically requires photolithography.

Limitations associated with photolithography, mainly the limited resolution, set by the optical resolution equation:

$$R = \frac{\lambda}{2NA} \tag{1.25}$$

where λ is the wavelength of light, and NA is the numerical aperture of the lens system, suggest that the minimum feature size obtainable is approximately ½ the wavelength of light used, while in reality the true achievable resolution due to instrument limitations is approximately the wavelength of light.[110]

Using deep and extreme ultraviolet (DUV and EUV) light, the resolution of photolithography has been pushed to sub-10 nm.[111,112] However, complex and expensive equipment and setups are required. Soft lithography, on the other hand, through unique design and

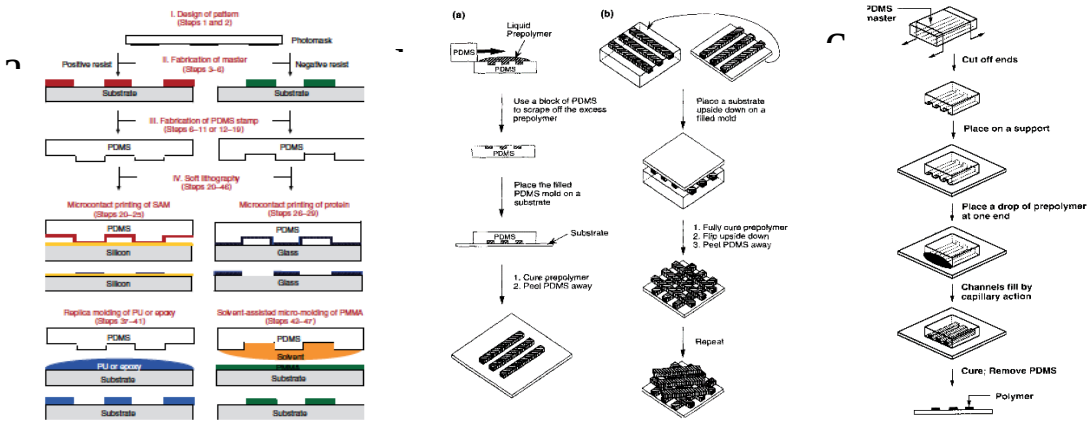

Figure 1.16: Illustration of various patterning techniques using soft lithography (a)109 microtransfer molding (b)110 and micromolding in capillary (c)[111].

offers a facile method for obtaining sub-100 nm resolution, with high throughput and low cost.[109] Within soft lithography, patterning techniques include microcontact printing (μCP),[113] replica molding (REM),[113] microtransfer molding (μTM),[114] micromolding in capillaries (MIMIC),[115] and solvent-assisted micromolding (SAMIM),[116] illustrated in Figure 1.16. Each technique has its advantages based on the resulting application.

Zhao et. al successfully demonstrated the feasibility of obtaining polymeric waveguides using a host of UV curable polymers in tandem with MIMIC.[117] Polymers used included epoxies,

polyurethanes, and polyacrylates. Though there were several limitations noted, single mode waveguiding was achieved using visible light.

This highly adaptable technique has seen very limited used in terms of patterning of QD composites. Mentioned briefly above, Kim et. al took advantage of thiol-ene chemistry and its compatibility with soft lithography to attain micron scale patterns as shown in Figure 1.17.[54] Beautiful luminescent patterns were fabricated but the loading was negligible, with a maximum of 0.2 wt. % QDs.

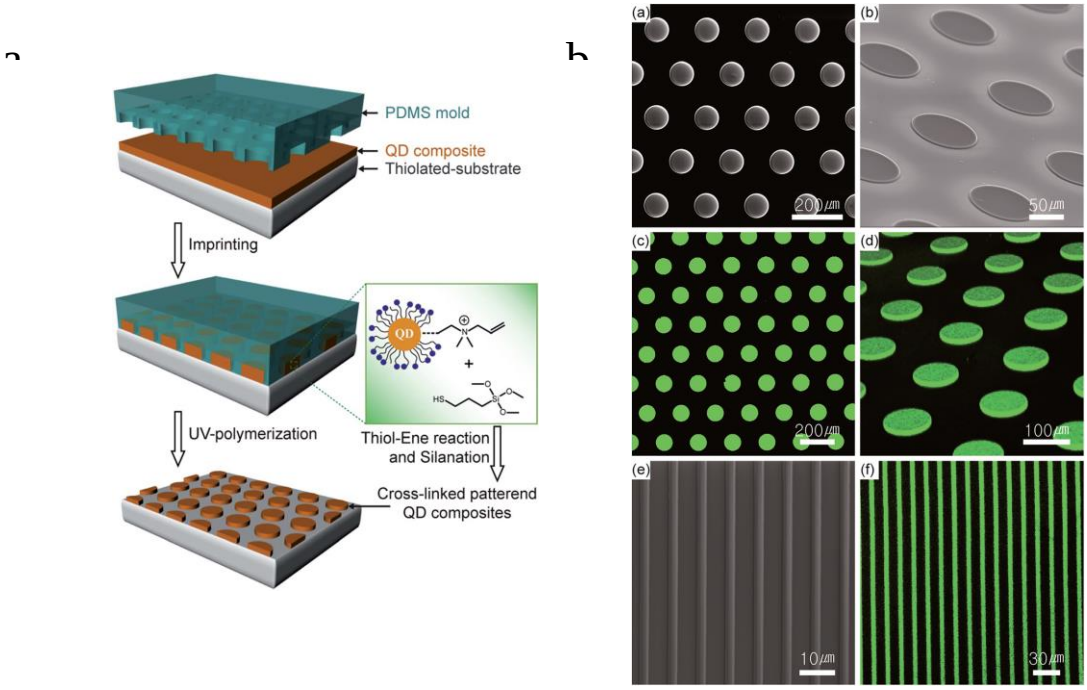

Figure 1.17: Schematic of patterning using thiol-ene chemistry (a) and corresponding SEM and photolumiscence imaging (b).[53`]

A prototypical host matrix for QDs would maintain the properties that make polymers attractive (i.e. robust, stable, elastic, and malleable) while being able to enhance optical properties of colloidal QDs via the inherent polymer properties. Ideally QD based nanocomposites result in fully functional materials that are robust, chemically and environmentally stable, and readily processable to yield desired planar films and patterns that can be readily integrated for an

application. Current host matrices are often lacking in that they are often not multifunctional, offering no added benefit to QD systems. Nanocomposite systems are thought to offer enhanced functionality, processability, in addition to potential tunability. Similar benefits should be realized with a QD-polymer nanocomposite system. While current patterning has yielded high-resolution patterns of QDs, here we aim for patterning with diverse material selection resulting in synergistic effects for the composite system. Desired properties include robust and stable composites with uniformly distributed QDs, with potentially tunable properties. Via precise ligand and monomer engineering we propose composites with good mechanical and optical properties. In addition, the precise selection of chemistries yields integration with patterning techniques as well as post fabrication manipulation and tunability. Lithographic techniques, including soft-lithography, are ideal for high-resolution sub-micron patterning of QD composites, however, it has yet to be done and furthermore exploited for photonics-based applications.

1.5.1.2 Lithography Patterned Photonic Systems

As mentioned above, photolithography generally suffers in terms of limited resolution. The above optical resolution equation suggesting a theoretical resolution of ½ λ, while in reality the resolution is much less. Nonetheless, several researchers have exploited photolithography to

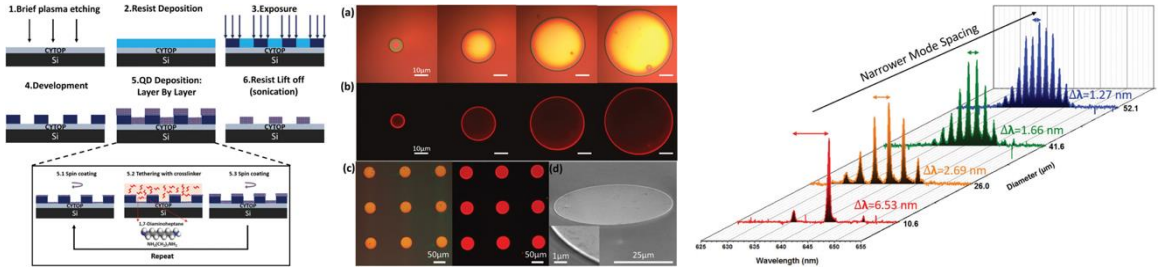

Figure 1.18: Colloidal QD microdisks resonators fabricated via photolithography and their lasing behavior.

achieve unique photonic systems. For example, Lin et. al fabricated colloidal quantum dot microdisks via photolithography combined with a layer-by-layer crosslinking approach to provide long-term stability to the crosslinked patterns.[118] (Figure 1.18)

By controlling the size of the microdisk resonators they offered control over important lasing parameters including Q-factor, FSR, and the number of cavity modes, achieving higher Q-factors with larger microdisks and near single mode lasing with the smallest microdisk. Additionally, taking advantage of photolithography an array style format of microlasers could be achieved potentially, providing robust, on-chip, arrays of tunable lasing.

Optimal resolution is generally achieved with electron beam lithography (EBL), however, unlike photolithography, large scale array fabrication is fairly difficult, giving very limited practicality. Generally, device fabrication is afforded via template development in a resist using EBL, followed by backfilling and etching/stripping to remove any excess buildup, resulting in prestine cavities with sub-500nm resolution. Among recent efforts, Xie et. al developed varying

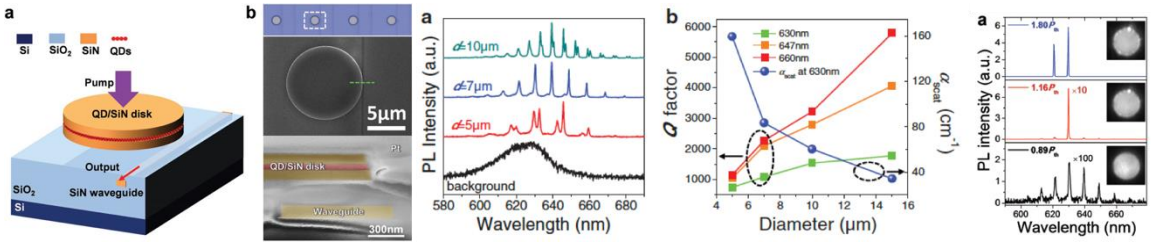

Figure 1.19: EBL fabricated microdisk and their Q-factor, and lasing behavior.

diameter, on-chip integrateable microdisk lasers using a multistep EBL process, in which colloidal QDs were sandwiched in between SiN microdisk to form a cavity.

Due to the high resolution of EBL, microdisk emission could be out coupled to a waveguide which was implanted hundreds of nanometers from the base of the resonator. Similar to examples provided above, they were able to achieve low threshold WGM lasing with Q-factors that scaled with the microdisk diameter.

1.5.1.3 Microsphere, Microdroplet, and Microtoroid WGM Lasers

In addition to the high-resolution mechanisms mentioned, a number of QD polymer WGM photonic cavity lasers have been fabricated to date, simply by taking advantage of the cavity itself. Among recent examples, Wang et al. developed microbubble lasers via simple drop-casting of QD−poly(methyl methacrylate) (PMMA) solutions with loadings above 50%.[119] Tunable laser emission was demonstrated via control of microbubble size (Figure 1.20a).

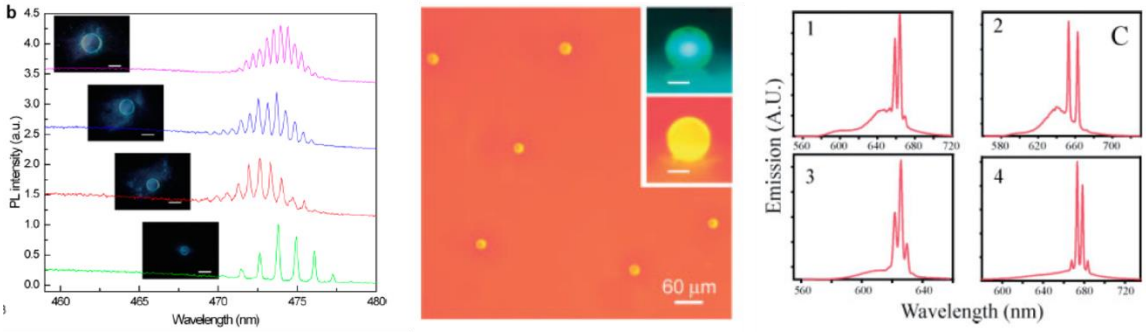

Figure 1.20: WGM droplet and sphere resonators and their lasing behavior.

Other WGM geometries have also been explored, for example, Gomez et al decorated the surface of silica microspheres with QDs to realize tunable WGM formation via control of the shell thickness.[120] Similarly, simply by depositing colloidal QD solutions over the top of microspheres Snee et. al realized controlled lasing emission based on the diameter of the microspheres used (Figure 1.20b-c). In addition, other gain medium has been explored. Siegle et al. fabricated dye doped WGM resonators via direct laser writing on top of PDMS.[121] Exploiting the elasticity of the PDMS host matrix, they were able to demonstrate a tunable inter-cavity gap to realize coupling between the microresonators. It would be quite advantageous to realize array style tunable QD based resonators.

1.5.1.4 Template Assisted, Directed Assembly of Microspheres

One unique, largely unexplored area to fabricate photonic devices, particularly photonic arrays of microspheres, is that of directed assembly. Directed assembly involves using a patterned substrate or simply a flow cell to assemble nano or microparticles. The first attempts at directed assembly were exploited to realize opals, inverse opals, and photonic bandgap structures.[122] This technique was further developed to achieve unique assemblies of microspheres.[123] (Figure 1.21)

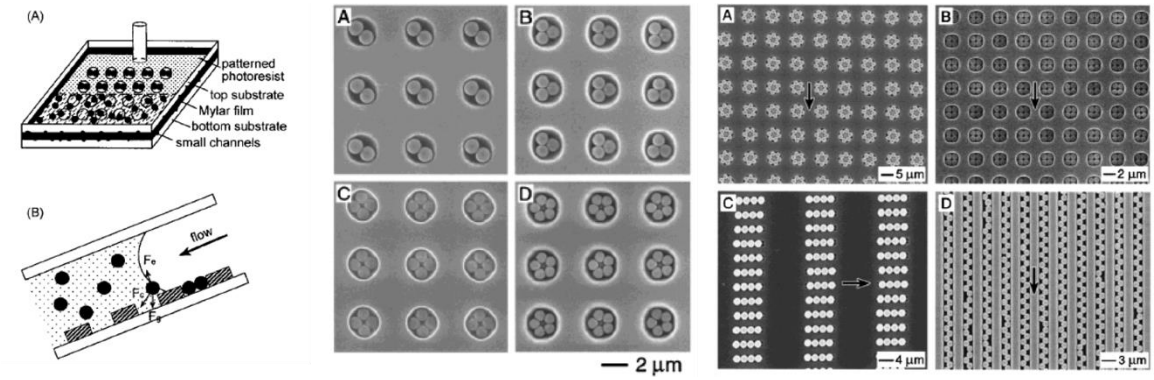

Figure 1.21: Template assisted, directed assembly and resulting patterns.

In a typical assembly, an aqueous suspension of microspheres is injected into a flow cell in which the bottom substrate is patterned with various relief structures. Several forces act upon the liquid slug of microspheres as the solution evaporates through the flow cell. Specifically, the microspheres are acted upon by capillary, electrostatic, and gravitational forces. The number of microspheres that deposits in each relief structure is determined by the ratio of the diameter of the relief structure to the diameter of the microsphere. Directed assembly could be a very unique mechanism to achieve coupling between microspheres.

1.5.1.4.1 Current Attempts at Microsphere Coupling

Coincidentally, though it offers advantageous optical properties, coupling between neighboring spherical resonators is seldom explored. Researchers who have explored this field often require quite complicated setups to do so. Attempts at microsphere coupling usually involve micromanipulator setups[124] or investigation of the random assembly of microsphere aggregates in which microspheres are typically touching.[125]

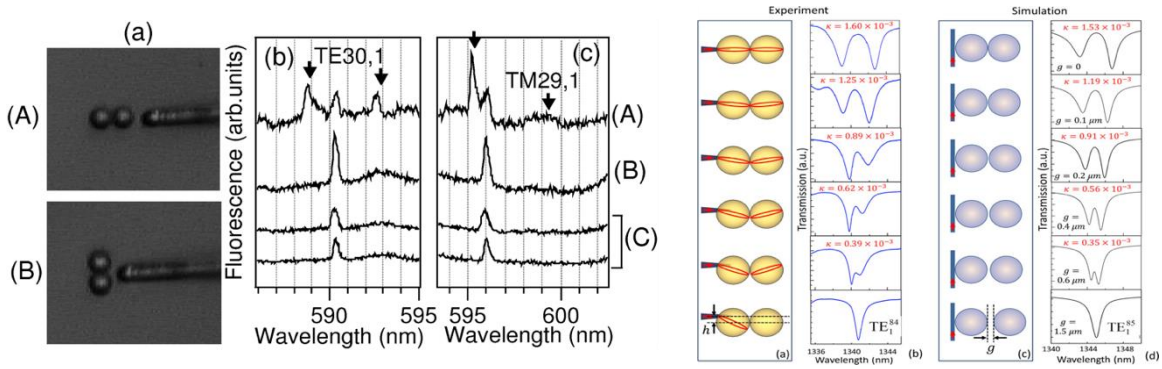

Figure 1.22: Coupled resonators achieved via micromanipulator (a) and position of coupling fiber (b).

Li et. al demonstrated WGM coupled microspheres theoretically and experimentally in linear chains and planar geometries. Microspheres were touching, however; by controlling the location of the coupling microfiber, the equatorial WGM plane could be adjusted, thereby displaying control over the coupling distance between neighboring resonators. Others have demonstrated the ability to control coupling by moving the resonators via an elastomeric substrate,[126, 127] or by control of one resonator via a piezo-positioner.[128] While coupling was demonstrated in these systems, an ideal system with practical realization would have a more simplistic setup with less moving parts and be readily integrateable. In addition, these techniques are excellent for bench scale testing, however they are not practical and readily implementable.

It is important to note that, traditionally, for coupled resonator systems in which identical resonators are placed side by side and both excited, their degeneracy is broken, which gives rise to the mode splitting.[129] It is however possible to observe intra-resonator mode splitting. For example, by introducing nanoscale defects on the surface of resonantors, Rayleigh scattering was shown to induce coupling between the two degnerate clockwise and counterclockwise modes within the WGM resonator.[130] For this reason it is essential to fabricate pristine, defect free resonators to avoid breaking the degeneracy.

1.5.1.4.2 2 Photon Polymerization (3D lithography) for Template Fabrication

A relatively new and high-resolution technique taking advantage of two photon polymerization has been widely explored. Also termed 3D lithography, this maskless technique takes advantage of intensity driven polymerization events. Traditional photo-initiators used are sensitive to UV and transparent in near IR, enabling pulsed IR lasers to penetrate photoresists and only polymerize regions in which high photon densities are injected, basically initiating two photon polymerization reactions above a threshold.[131] Due to this threshold behavior, sub-200nm resolution, well below the diffraction limit, can be achieved simply by controlling the laser pulse energy and number of pulses. The technique offers maskless lithography enabling the fabrication of any arbitrary structure, which could have applicability for deriving templates for assembly of photonic arrays of microspheres. Examples of the structures that have been fabricated can be seen below in Figure 1.23.[132, 133, 134]

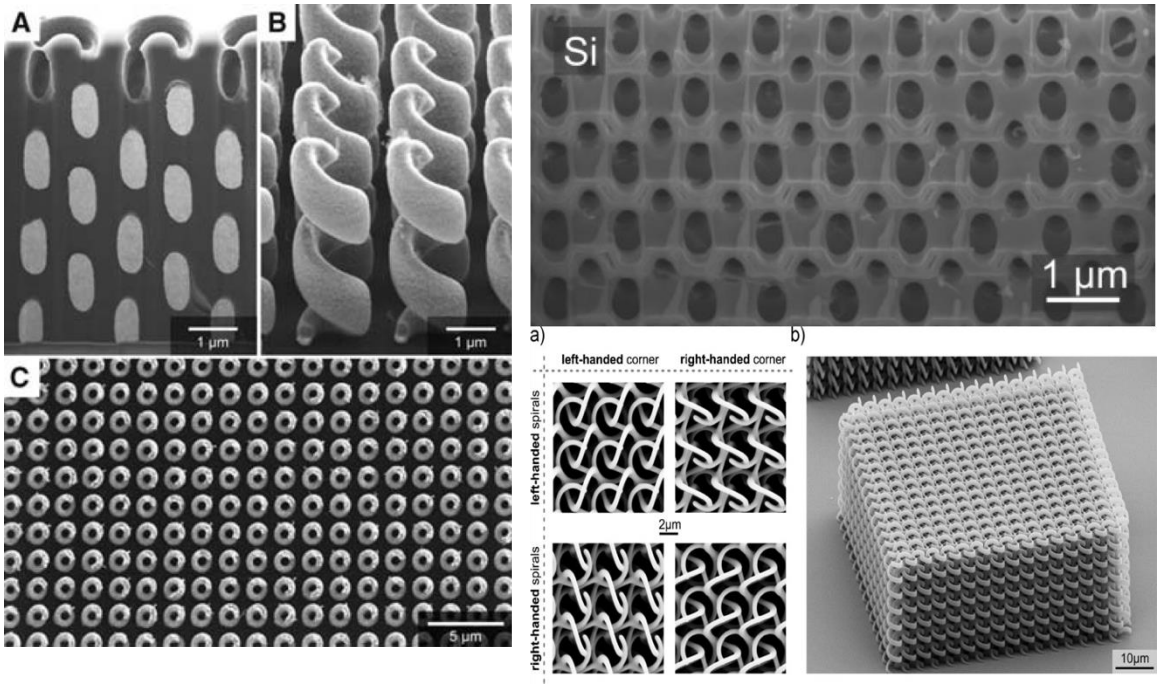

Figure 1.23: High resolution patterns fabricated via 3D lithography.

1.5.2 Patterning Gain/Loss systems with parity-time symmetry

Even more exciting phenomenon can be realized when exercising controlled fabrication of microresonator cavities. One example of the result of controlled assembly and coupling of gain medium is the realization of parity-time (PT) symmetric optical systems. PT symmetry is a physics phenomenon in which systems are described by a Hamiltonian (H) that commutes with the combined PT operator. [135] Optical systems are ideal candidates to experimentally realize PT related concepts, due to the equivalence between the quantum mechanical Schrodinger equation and the optical wave equation. In addition optical systems offer the ability to precisely tune/manipulate gain and loss via refractive index.[135] In terms of optical materials, this complex potential manifests itself in the form of a complex refractive index:

$$n(x) = n_R(x) + in_I(x) \tag{1.26}$$

where $n_R(x)$ represents the real refractive index and $n_I(x)$ represents the periodic distribution of gain and loss. In order for a system to display PT symmetry the following criteria must be met: $n(x) = n^*(-x)$, that is $n_R(x) = n_R(-x)$ and $n_I(x) = -n_I(-x)$ (i.e. the real component of the refractive be an even function while the imaginary component be odd).[136] The imaginary component is directly related to the gain (g) and loss (α) of a system via the following equation:

$$(\alpha, g) = 2k_0 n_I \tag{1.27}$$

where $k_0 = {}^{2\pi}/_{\lambda}$. In its simplest form, in the case of two coupled waveguides, this can be manifested as follows: Having two coupled waveguides of gain (red) and loss (green) initially pumped via the left waveguide (left column) and right waveguide (right column) (Figure 1.24).[135,137]

When the gain/loss parameter is below the critical value ($\gamma < \gamma_{PT}$), systems demonstrate reciprocal propagation, however when this parameter exceeds the critical value ($\gamma > \gamma_{PT}$), PT symmetry is broken and nonreciprocal propagation is observed with exponential amplification of the beam. In other words, while for conventional wave propagation, light is reciprocal, for the PT symmetric system below and above the threshold that is not the case.

Systems meeting this PT symmetry requirement have exhibited unique optical phenomena such as unidirectional invisibility,[138] unidirectional reflection,[139] directional optical manipulation,[139] and transitions from ballistic to diffusive transport.[140] As was emphasized before,

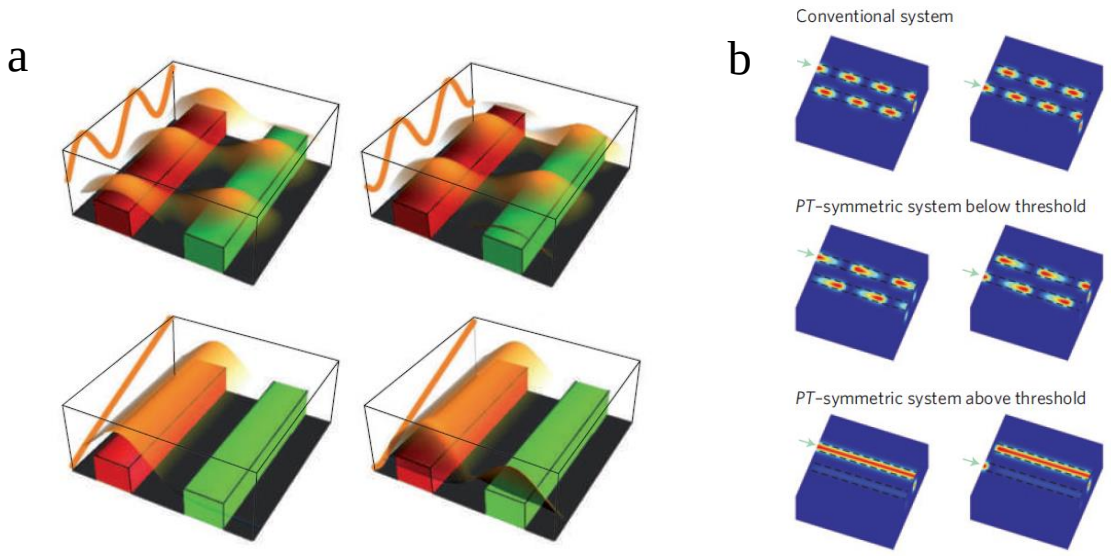

Figure 1.24: (a) Coupled waveguide schematic demonstrating conventional system and PT symmetric systems below and above threshold[131] along with (b) modeling[133].

specifically in terms of whispering gallery mode photonic cavities, they can provide valuable platforms for achieving lasing and manipulating light. In terms of PT symmetric systems, the evanescent field is critical to achieve the desired phenomenon. For example, coupled microring disks were utilized to demonstrate single mode lasing with the strongest coupling occurring for coupled rings with a 50 nm gap distance.[141]

In this particular case, the cavity spacing was 200 nm, with the coupling strength κ, increasing with decreased gap distances **(Figure 1.25).** [142]

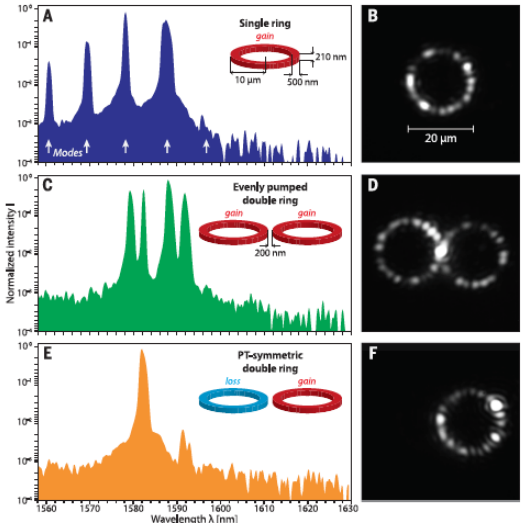

Figure 1.25: Single and coupled microring resonator showing transition to PT-symmetric behavior.[138]

Additionally, to observe the phenomenon the gain/loss of the systems must be easily modulated. Traditionally this has been demonstrated by selective pumping of cavities. According to coupled mode theory:[142]

$$\omega_n^{(1,2)} = \omega_n + i\frac{\gamma_{a_n}+\gamma_{b_n}}{2} \pm \sqrt{\kappa_n^2 - \left(\frac{\gamma_{a_n}-\gamma_{b_n}}{2}\right)^2} \qquad (1.28)$$

where $\omega_n^{(1,2)}$ represents the eigenfrequencies of the two supermodes of this system, ω_n is the nth longitudinal resonance frequency of an isolated passive ring, γ_{a_n} is the net gain/loss in cavity a, γ_{b_n} is the net gain/loss in cavity b, and κ_n is the coupling strength between cavities. In order to break PT symmetry the system must reach the exceptional point, in which $\left|\gamma_{a_n}-\gamma_{b_n}\right| = 2\kappa_n$, in other word the coupling strength of the two cavities must be equal to the gain/loss contrast between the two. [142]

These findings are clear evidence that exploiting PT symmetry as well as strong coupling with nanoscale dimensions offer extreme benefits such as nonconventional light propagation. The utilization of colloidal QDs as the active gain medium for such PT systems could have important practical implications since they offer tunable emission wavelengths. Additionally, coupling these solution processable nanocrystals with elastomeric matrices offers potentially flexible gain/loss systems, suggesting the possibility of additional control and tuning of the system via external stimuli.[143]

1.6 Summary of Critical Issue

Over the last several decades, dating back to their inception, a significant amount of theoretical and experimental work has been conducted on photonic nanostructures, from developing schemes to encapsulate quantum dots into polymer matrices, imparting long term stability and more functionality, to utilizing photoluminescent materials as gain medium and for lasing. Colloidal QDs have proven to be beneficial building blocks for next generation photonics applications. While several advances have been made in attempt to understand the dynamics of photonics systems, starting from the emissive components, specifically quantum dots, evolving to polymeric host and templates, there is still plenty to be explored.

In understanding the stability and dynamic emission characteristics of different architecture quantum dots, studies traditionally involve response to different exposure conditions, including chemicals, gaseous environments, polyelectrolyte matrices, substrates, and light. Additionally, mechanisms have been proposed for combatting the unstable emission behavior that is sometimes exhibited by various architecture QDs. Prevention of the unfavorable emission characteristics is

typically afforded via incorporation of an inorganic passivation layer. However, the exploitation of the dynamic emission behavior to realize potential reversible behavior has yet to be explored. Understanding how the photo-responsive behavior can be engineered could be critical for various applications where reversible emission behavior is required.

The inclusion of quantum dots into polymer matrices is an essential step in developing more functional materials that are mechanically robust, chemically inert, and stable over long periods of time. To date inclusion of emissive materials into ideal matrices has been quite limited. Typically, QD nanocomposite fabrication results in inclusion of QDs at very low wt. fractions, making their end use quite limited. Additionally, several studies involve the simple mixing of QD and polymer to produce a composite material. Generally, this leads to significant phase separation, again limiting the end use application, as phase separation and aggregation can lead to detrimental optical properties such as scattering and losses. A proposed method for combating large QD aggregation would be the utilization of a fast cross-linking mechanism that takes place on time scales faster than phase separation of relatively large nanoparticles and aggregates. Further, it has been suggested that in situ cross-linking of QDs to form nanocomposites can reduce significantly aggregation and prevent unwanted energy transfer mechanisms, resulting in enhanced light emission in comparison to the non-cross-linked counterparts. Such a unique polymerization scheme, involving fast crosslinking polymerizations, resulting in highly loaded QD-polymer nanocomposites is yet to be realized.

Finally, to realize the potential of QDs and other emissive components, a significant amount of QD applications are patterned into various cavities such as waveguides and microdisk resonators. To date most solution based photonic resonators filled the outer layer of microspheres or the interior of microcapillary tubes with QDs. While this results in typically high quality WGM

resonators, such cavities can be quite difficult to integrate into on-chip photonic circuits, or large-scale arrays. Additionally, the coupling of such photonic structures is seldom explored and require rather complex setups using micromanipulators, which again are not readily integratable.

Other photonic structure patterning techniques involve techniques with limited scalability, such as EBL. Ideally, fabrication methods to realize photonic structures would be readily scalable, offering flexibility of control of the emission characteristics, and still able to preserve high resolution, required to achieve unique coupling systems such as PT-symmetry.

1.7 References (Chapter 1)

[1] Leonhardt, U., *Nat. Photonics* **2007**, 1, 207.

[2] Dolmans, D. E. J. G. J.; Fukumura, D.; Jain, R. K., *Nat. Rev. Cancer* **2003**, 3, 380.

[3] VanWiggeren, G. D.; Roy, R., *Science* **1998**, 279, 1198.

[4] Nakamura, S.; Mukai, T.; Senoh, M., *Appl. Phys. Lett.* **1994**, 64, 1687.

[5] Cai, W.; Shalaev, V.; Optical Metamaterials: Fundamentals and Applications, 1set ed.; Springer-Verlag: New York, 2010

[6] Feng, L.; El-Ganainy, R.; Ge, L., *Nat. Photonics* **2017**, 11, 752.

[7] Resch-Genger, U.; Grabolle, M.; Cavaliere-Jaricot, S.; Nitschke, R.; Nann, T. *Nat. Methods* **2008**, 5, 763.

[8] Soffer, B. H.; McFarland, B. B., *Appl. Phys. Lett.* **1967**, 10, 266.

[9] Herman, B., Frohlich, V.E., Lakowicz, J.R., Murphy, D.B., Spring, K.R., Davidson, M.W., Fluorescence microscopy: Basic concepts in fluorescence microscopy. National High Magnetic Field Laboratory, Florida State University, 2013.

[10] Peng, X.; Manna, L.; Yang, W.; Wickham, J.; Scher, E.; Kadavanich, A.; Alivisatos, A. P., *Nature* **2000**, 404, 59.

[11] Michalet, X.; Pinaud, F. F.; Bentolila, L. A.; Tsay, J. M.; Doose, S.; Li, J. J.; Sundaresan, G.; Wu, A. M.; Gambhir, S. S.; Weiss, S., *Science* **2005**, 307, 538.

[12] Talapin, D. V.; Lee, J.-S.; Kovalenko, M. V.; Shevchenko, E. V., *Chem. Rev.* **2010**, 110, 389.

[13] Pietryga, J. M.; Park, Y.-S.; Lim, J.; Fidler, A. F.; Bae, W. K.; Brovelli, S.; Klimov, V. I., *Chem. Rev.* **2016**, 116, 10513.

[14] Dabbousi, B. O.; Rodriguez-Viejo, J.; Mikulec, F. V.; Heine, J. R.; Mattoussi, H.; Ober, R.; Jensen, K. F.; Bawendi, M. G., *J Phys. Chem. B* **1997**, 101, 9463.

[15] Jung, J.; Lin, C. H.; Yoon, Y. J.; Malak, S. T.; Zhai, Y.; Thomas, E. L.; Vardeny, V.; Tsukruk, V. V.; Lin, Z., *Angew. Chem., Int. Ed.* **2016**, 55, 5071.

[16] Kojima, A.; Teshima, K.; Shirai, Y.; Miyasaka, T., *J Am. Chem. Soc.* **2009**, 131, 6050.

[17] Protesescu, L.; Yakunin, S.; Bodnarchuk, M. I.; Krieg, F.; Caputo, R.; Hendon, C. H.; Yang, R. X.; Walsh, A.; Kovalenko, M. V., *Nano Lett.* **2015**, 15, 3692.

[18] Cadwmartiri, L.; Ozin, G.G.; Concepts of Nanochemistry, WILEY-VCH, 2009

[19] Algar, W. R.; Susumu, K.; Delehanty, J. B.; Medintz, I. L., *Anal Chem.* **2011**, 83, 8826.

[20] Alivisatos, A. P., *Science* **1996**, 271, 933.

[21] Smith, A. M.; Nie, S., *Acc. Chem. Res.* **2010**, 43, 190.

[22] Schaller, R. D.; Klimov, V. I., *Phys. Rev. Lett*. **2004**, 92, 186601.

[23] Beecroft, L. L.; Ober, C. K., *Chem. Mater.* **1997**, 9, 1302.

[24] Kim, Y.; Zhu, J.; Yeom, B.; Di Prima, M.; Su, X.; Kim, J.-G.; Yoo, S. J.; Uher, C.; Kotov, N. A., *Nature* **2013**, 500, 59.

[25] Balazs, A. C.; Emrick, T.; Russell, T. P., *Science* **2006**, 314, 1107.

[26] Kwon, Y. K.; Han, J. K.; Lee, J. M.; Ko, Y. S.; Oh, J. H.; Lee, H.-S.; Lee, E.-H., *J Mater. Chem.* **2008**, 18, 579.

[27] Li, L.; Lin, H.; Qiao, S.; Zou, Y.; Danto, S.; Richardson, K.; Musgraves, J. D.; Lu, N.; Hu, J., *Nat. Photonics* **2014**, 8, 643.

[28] Shih, M. H.; Hsu, K. S.; Kunag, W.; Yang, Y. C.; Wang, Y. C.; Tsai, S. K.; Liu, Y. C.; Chang, Z. C.; Wu, M. C., *Opt. Lett.* **2009**, 34, 2733.

[29] Yu, C. L.; Kim, H.; de Leon, N.; Frank, I. W.; Robinson, J. T.; McCutcheon, M.; Liu, M.; Lukin, M. D.; Loncar, M.; Park, H., *Nano Lett.* **2013**, 13, 248.

[30] Hooper, J. B.; Schweizer, K. S., *Macromolecules* **2006**, 39, 5133.

[31] Jung, J.; Lin, C. H.; Yoon, Y. J.; Malak, S. T.; Zhai, Y.; Thomas, E. L.; Vardeny, V.; Tsukruk, V. V.; Lin, Z., *Angew. Chem.* **2016**, 128, 5155.

[32] Boles, M. A.; Ling, D.; Hyeon, T.; Talapin, D. V., *Nat. Mater.* **2016**, 15, 141.

[33] Nag, A.; Kovalenko, M. V.; Lee, J.-S.; Liu, W.; Spokoyny, B.; Talapin, D. V.; *J. Am. Chem. Soc.* **2011**, 133, 10612.

[34] Baker, D. R.; Kamat, P. V.; *Langmuir* **2010**, 26, 11272.

[35] Xie, R.; Kolb, U.; Li, J.; Basché, T.; Mews, A., *J. Am. Chem. Soc.* **2005**, 127, 7480.

[36] Dubois, F.; Mahler, B.; Dubertret, B.; Doris, E.; Mioskowski, C., *J. Am. Chem. Soc*. **2007**, 129, 482.

[37] Kim, S.; Bawendi, M. G., *J. Am. Chem. Soc.* **2003**, 125, 14652.

[38] Brown, P. R.; Kim, D.; Lunt, R. R.; Zhao, N.; Bawendi, M. G.; Grossman, J. C.; Bulović, V., *ACS Nano* **2014**, 8, 5863.

[39] Medintz, I. L.; Uyeda, H. T.; Goldman, E. R.; Mattoussi, H., *Nat. Mater.* **2005**, 4, 435.

[40] Liu, Z.; Sun, Y.; Yuan, J.; Wei, H.; Huang, X.; Han, L.; Wang, W.; Wang, H.; Ma, W., *Adv. Mater.* **2013**, 25, 5772.

[41] Coe-Sullivan, S.; Steckel, J. S.; Woo, W. K.; Bawendi, M. G.; Bulović, V., *Adv. Funct. Mater.* **2005**, 15, 1117.

[42] Wang, Y.; Ta, V. D.; Leck, K. S.; I. Tan, B. H.; Wang, Z.; He, T.; Ohl, C.-D.; Demir, H. V.; Sun, H.; *Nano Lett.* **2017**, 17, 2640.

[43] Malak, S. T.; Smith, M. J.; Yoon, Y. J.; Lin, C. H.; Jung, J.; Lin, Z.; Tsukruk, V. V.; *Adv. Opt. Mater.* **2017**, 5, 1600509.

[44] Geiregat, P.; Houtepen, A. J.; Sagar, L. K.; Infante, I.; Zapata, F.; Grigel, V.; Allan, G.; Delerue, C.; Van Thourhout, D.; Hens, Z., *Nat. Mater.* **2017**, 17, 35.

[45] Tamborra, M.; Striccoli, M.; Comparelli, R.; Curri, M. L.; Petrella, A.; Agostiano, A., *Nanotechnology* **2004**, 15, S240.

[46] Zhu, M.; Peng, X.; Wang, Z.; Bai, Z.; Chen, B.; Wang, Y.; Hao, H.; Shao, Z.; Zhong, H., *J. Mater. Chem. C* **2014**, 2, 10031.

[47] Geldmeier, J.; Rile, L.; Yoon, Y. J.; Jung, J.; Lin, Z.; Tsukruk, V. V., *Langmuir* **2017**, 33, 14325.

[48] Walker, G. W.; Sundar, V. C.; Rudzinski, C. M.; Wun, A. W.; Bawendi, M. G.; Nocera, D. G., *Appl. Phys. Lett.* **2003**, 83, 3555.

[49] Hongjoo, S.; Seonghoon, L.; *Nanotechnology* **2007**, 18, 055402.

[50] Meinardi, F.; Colombo, A.; Velizhanin, K. A.; Simonutti, R.; Lorenzon, M.; Beverina, L.; Viswanatha, R.; Klimov, V. I.; Brovelli, S.; *Nat. Photonics* **2014**, 8, 392.

[51] Wood, V.; Panzer, M. J.; Chen, J.; Bradley, M. S.; Halpert, J. E.; Bawendi, M. G. Bulović, V., *Adv. Mater.* **2009**, 21, 2151.

[52] Ehlert, S.; Stegelmeier, C.; Pirner, D.; Förster, S., *Macromolecules* **2015**, 48, 5323.

[53] Draaisma, G. J. J.; Reardon, D.; Schenning, A. P. H. J.; Meskers, S. C. J.; Bastiaansen, C. W. M.; *J. Mater. Chem. C.* **2016**, 4, 5747.

[54] Kim, C.-H.; Bang, J.-H.; Hong, K. B.; Park, M.-H., *RSC Adv.* **2016**, 6, 96700.

[55] Noh, M.; Kim, T.; Lee, H.; Kim, C.-K.; Joo, S.-W.; Lee, K., *Colloids Surf. A* **2010**, 359, 39.

[56] Wang, Y.; Li, X.; Sreejith, S.; Cao, F.; Wang, Z.; Stuparu Mihaiela, C.; Zeng, H.; Sun, H., *Adv. Mater.* **2016**, 28, 10637.

[57] Stansbury Jeffrey, W., *J Esthet. Restor. Dent.* **2007**, 12, 300.

[58] Mackay, M. E.; Tuteja, A.; Duxbury, P. M.; Hawker, C. J.; Van Horn, B.; Guan, Z.; Chen, G.; Krishnan, R. S.; *Science* **2006**, 311, 1740.

[59] Vaidya, S. V.; Couzis, A.; Maldarelli, C., *Langmuir* **2015**, 31, 3167.

[60] Raja, S. N.; Luong, A. J.; Zhang, W.; Lin, L.; Ritchie, R. O.; Alivisatos, A. P.; *Chem. Mater.* **2016**, 28, 2540.

[61] Kade, M. J.; Burke, D. J.; Hawker, C. J., *J. Polym. Sci., Part A: Polym. Chem.* **2010**, 48, 743.

[62] Lowe, A. B., *Polym. Chem.* **2014**, 5, 4820.

[63] Chan, J. W.; Hoyle, C. E.; Lowe, A. B.; *J. Am. Chem. Soc.* **2009**, 131, 5751.

[64] Hoyle, C. E.; Bowman, C. N., *Angew. Chem. Int. Ed.* **2010**, 49, 1540.

[65] Carioscia, J. A.; Schneidewind, L.; O'Brien, C.; Ely, R.; Feeser, C.; Cramer, N.; Bowman, C. N., *J. Polym. Sci., Part A: Polym. Chem.* **2007**, 45, 5686.

[66] Senyurt, A. F.; Wei, H.; Hoyle, C. E.; Piland, S. G.; Gould, T. E., *Macromolecules* **2007**, 40, 4901.

[67] https://www.norlandprod.com/adhesiveindex2.html.

[68] Khire, V. S.; Benoit, D. S. W.; Anseth, K. S.; Bowman, C. N., *J. Polym. Sci., Part A: Polym. Chem.* **2006**, 44, 7027−7039.

[69] Phillips, J. P.; Mackey, N. M.; Confait, B. S.; Heaps, D. T.; Deng, X.; Todd, M. L.; Stevenson, S.; Zhou, H.; Hoyle, C. E., *Chem. Mater.* **2008**, 20, 5240−5245.

[70] van Berkel, K. Y.; Hawker, C. J., *J. Polym. Sci., Part A: Polym. Chem.* **2010**, 48, 1594.

[71] Lü, C.; Cui, Z.; Wang, Y.; Li, Z.; Guan, C.; Yang, B.; Shen, J., *J. Mater. Chem.* **2003**, 13, 2189− 2195.

[72] Hill, M. T.; Gather, M. C., *Nat. Photonics* **2014**, 8, 908.

[73] Paquet, C.; Kumacheva, E., *Materials Today* **2008**, 11, 48.

[74] de Fornel, F., Evanescent Waves: From Newtonian Optics to Atomic Optics, Springer, Berlin 2001

[75] Akahane, Y.; Asano, T.; Song, B.-S.; Noda, S., *Nature* **2003**, 425, 944947.

[76] Vlasov, Y. A.; O'Boyle, M.; Hamann, H. F.; McNab, S. J., *Nature* **2005**, 438, 65.

[77] Park, H.-G.; Kim, S.-H.; Kwon, S.-H.; Ju, Y.-G.; Yang, J.-K.; Baek, J.-H.; Kim, S.-B.; Lee, Y.-H., *Science* **2004**, 305, 1444.

[78] Qiang, Z.; Zhou, W.; Soref, R. A., *Opt. Express* **2007**, 15 (4), 1823.

[79] Parimi, P. V.; Lu, W. T.; Vodo, P.; Sridhar, S., *Nature* **2003**, 426, 404.

[80] Koyama, F.; Kinoshita, S.; Iga, K., *Appl. Phys. Lett.* **1989**, 55, 221.

[81] Yoon, J.; Lee, W.; Thomas, E. L., *Nano Lett.* **2006**, 6, 2211.

[82] Paquet, C.; Yoshino, F.; Levina, L.; Gourevich, I.; Sargent, E. H.; Kumacheva, E., *Adv. Funct. Mater.* **2006**, 16 (14), 1892-1896.

[83] Chen, R.; Ta, V. D.; Sun, H., *ACS Photonics* **2014**, 1, 11.

[84] Yang, S.; Wang, Y.; Sun, H., *Adv. Opt. Mater.* **2015**, 3, 1136.

[85] Matsko, A. B.; Ilchenko, V. S., *IEEE J. Sel. Top. Quantum Electron.* **2006**, 12, 3.

[86] Stöber, W.; Fink, A.; Bohn, E., *J. Colloid Interface Sci.* **1968**, 26, 62.

[87] Pastoriza-Santos, I.; Gomez, D.; Pérez-Juste, J.; Liz-Marzán, L. M.; Mulvaney, P., *Phys. Chem. Chem. Phys.* **2004**, 6, 5056.

[88] Gómez, D. E.; Pastoriza-Santos, I.; Mulvaney, P., *Small* **2004**, 1, 238.

[89] Shim, S.-E.; Cha, Y.-J.; Byun, J.-M.; Choe, S., *J. Appl. Polym. Sci.* **1999**, 71, 2259.

[90] Han, M.; Gao, X.; Su, J. Z.; Nie, S., Nat. Biotechnol. **2001**, 19, 631.

[91] Tabata, K., Braam, D., Kushida, S., Tong, L., Kuwabara, J., Kanbara, T., Beckel, A., Lorke, A., Yamamoto, Y., *Sci. Rep.* **2014**, 4, 5902

[92] Weller, A.; Liu, F. C.; Dahint, R.; Himmelhaus, M., *Appl. Phys. B: Lasers Opt.* **2008,** *90*, 561.

[93] Rayleigh L. CXII. *The London, Edinburgh, and Dublin Philosophical Magazine and Journal of Science.* **1910**, 20, 1001.

[94] Matsko, A. B., Ilchenko, V. S., *IEEE JSTQE* **2006**, 12, 3.

[95] Oraevsky, A. N., Whispering-gallery waves. *Quantum Electron.* **2002,** *32*, 377.

[96] Kippenberg, T. J. A., *Nonlinear Optics in Ultra-high Q Whispering-Gallery Optical Microcavities. Dissertation (Ph.D.),* **2004** California Institute of Technology.

[97] Buck, J. R.; Kimble, H. J., *Phys. Rev. A* **2003**, 67, 033806.

[98] Vahala, K. J., *Nature* **2003**, 424, 839.

[99] Smith, M. J.; Lin, C. H.; Yu, S.; Tsukruk, V. V., *Adv. Opt. Mater.* **2019**, 7, 1801072

[100] Wangsness, R. K., Electromagnetic fields. Electromagnetic Fields, 2nd Edition, by Roald K. Wangsness, pp. 608. ISBN 0-471-81186-6. Wiley-VCH, July 1986, 608.

[101] Choi, J. M.; Lee, R. K.; Yariv, A., *Opt. Lett.* **2001**, 26, 1236.

[102] Rakovich, Y. P.; Donegan, J. F.; Gerlach, M.; Bradley, A. L.; Connolly, T. M.; Boland, J. J.; Gaponik, N.; Rogach, A., *Phys. Rev. A* **2004**, 70, 051801.

[103] Ganesh, N.; Zhang, W.; Mathias, P. C.; Chow, E.; Soares, J. A. N. T.; Malyarchuk, V.; Smith, A. D.; Cunningham, B. T., *Nature Nanotech.* **2007**, 2, 515.

[104] Wu, Z.; Mi, Z.; Bhattacharya, P.; Zhu, T.; Xu, J., *Appl. Phys. Lett.* **2007**, 90, 171105.

[105] Pisignano, D.; Persano, L.; Gigli, G.; Visconti, P.; Stomeo, T.; Vittorio, M. D.; Barbarella, G.; Favaretto, L.; Cingolani, R., *Nanotechnology* **2004**, 15, 766.

[106] Wood, V.; Panzer, M. J.; Chen, J.; Bradley, M. S.; Halpert, J. E.; Bawendi, M. G.; Bulović, V., *Adv. Mater.* **2009**, 21, 2151.

[107] Xie, W.; Gomes, R.; Aubert, T.; Bisschop, S.; Zhu, Y.; Hens, Z.; Brainis, E.; Van Thourhout, D., *Nano Lett.* **2015**, 15, 7481.

[108] Prins, F.; Kim, D. K.; Cui, J.; De Leo, E.; Spiegel, L. L.; McPeak, K. M.; Norris, D. J., *Nano Lett.* **2017**, 17, 1319.

[109] Xia, Y.; Whitesides, G. M., *Angew. Chem., Int. Ed.* **1998**, 37, 550.

[110] Madou, M.J.; Fundamentals of Microfabrication,. The Science of Miniaturization,. 2nd edition. By, CRC Press, 2002. ISBN 0-8493-0826-7

[111] Dong, J.; Liu, J.; Kang, G.; Xie, J.; Wang, Y., Pushing the resolution of photolithography down to 15nm by surface plasmon interference. Sci Rep 2014, 4, 5618.

[112] Park, W.; Rhie, J.; Kim, N. Y.; Hong, S.; Kim, D.-S., *Sci. Rep.* **2016**, 6, 23823.

[113] Qin, D.; Xia, Y. N.; Whitesides, G. M., *Nat. Protoc.* **2010**, 5, 491.

[114] Zhao, X. M.; Xia, Y.; Whitesides, G. M., *Adv. Mater.* **2004**, 8, 837.

[115] Kim, E.; Xia, Y.; Whitesides, G. M., *Nature* **1995**, 376, 581.

[116] Bernard, A.; Renault, J. P.; Michel, B.; Bosshard, H. R.; Delamarche, E., *Adv. Mater.* **2000**, 12, 1067.

[117] Zhao, X. M.; Stoddart, A.; Smith, S. P.; Kim, E.; Xia, Y.; Prentiss, M.; Whitesides, G. M., *Adv. Mater.* **2004**, 8, 420.

[118] Lin, C. H.; Zeng, Q.; Lafalce, E.; Smith, M. J.; Malak, S. T.; Jung, J.; Yoon, Y. J.; Lin, Z.; Vardeny, Z. V.; Tsukruk, V. V., *Adv. Opt. Mater.* **2017**, 5, 1700011.

[119] Wang, Y.; Ta, V. D.; Leck, K. S.; Tan, B. H. I.; Wang, Z.; He, T.; Ohl, C.-D.; Demir, H. V.; Sun, H., *Nano Lett.* **2017**, 17, 2640.

[120] Gómez Daniel , E.; Pastoriza-Santos, I.; Mulvaney, P., *Small* **2004**, 1, 238.

[121] Siegle, T.; Schierle, S.; Kraemmer, S.; Richter, B.; Wondimu, S. F.; Schuch, P.; Koos, C.; Kalt, H., *Light: Sci. Appl.* **2017**, 6, e16224.

[122] Xia, Y.; Gates, B.; Yin, Y.; Lu, Y., *Adv. Mater.* **2000,** *12*, 693.

[123] Yin, Y.; Lu, Y.; Gates, B.; Xia, Y., *J. Am. Chem. Soc.* **2001,** *123*, 8718.

[124] Mukaiyama, T.; Takeda, K.; Miyazaki, H.; Jimba, Y.; Kuwata-Gonokami, M., *Phys. Rev. Lett.* **1999,** *82*, 4623.

[125] Li, Y.; Abolmaali, F.; Allen, K. W.; Limberopoulos, N. I.; Urbas, A.; Rakovich, Y.; Maslov, A. V.; Astratov, V. N., *Laser Photonics Rev.* **2017**, 11, 2.

[126] Ashili, S. P.; Astratov, V. N.; Sykes, E. C. H., *Opt. Express* **2006**, 14, 9460.

[127] Huang, F.; Baumberg, J. J., *Nano Lett.* **2010**, 10, 1787.

[128] Ilchenko, V. S.; Gorodetsky, M. L.; Vyatchanin, S. P., *Opt. Commun.* **1994**, 107, 41.

[129] Oraevsky, A. N., *Quantum Electron.* **2002**, 32, 377.

[130] Mazzei, A.; Götzinger, S.; de S. Menezes, L.; Zumofen, G.; Benson, O.; Sandoghdar, V., *Phys. Rev. Lett.* **2007**, 99, 173603.

[131] Serbin, J.; Egbert, A.; Ostendorf, A.; Chichkov, B. N.; Houbertz, R.; Domann, G.; Schulz, J.; Cronauer, C.; Fröhlich, L.; Popall, M., *Opt. Lett.* **2003**, 28, 301.

[132] Gansel, J. K.; Thiel, M.; Rill, M. S.; Decker, M.; Bade, K.; Saile, V.; von Freymann, G.; Linden, S.; Wegener, M., *Science* **2009**, 325, 1513.

[133] Hermatschweiler, M.; Ledermann, A.; Ozin, G. A.; Wegener, M.; von Freymann, G., *Adv. Funct. Mater.* **2007,** *17*, 2273.

[134] Thiel, M.; Rill, M. S.; von Freymann, G.; Wegener, M., Three-Dimensional Bi-Chiral Photonic Crystals. *Adv. Mater.* **2009,** *21*, 4680.

[135] Kottos, T., *Nat. Phys.* **2010**, 6, 166-167.

[136] Makris, K. G.; El-Ganainy, R.; Christodoulides, D. N.; Musslimani, Z. H., *Phys. Rev. Lett.* **2008**, 100, 103904.

[137] Rüter, C. E.; Makris, K. G.; El-Ganainy, R.; Christodoulides, D. N.; Segev, M.; Kip, D., *Nat. Phys.* **2010**, 6, 192.

[138] Lin, Z.; Ramezani, H.; Eichelkraut, T.; Kottos, T.; Cao, H.; Christodoulides, D. N., *Phys. Rev. Lett.* **2011**, 106, 213901.

[139] Feng, L.; Xu, Y.-L.; Fegadolli, W. S.; Lu, M.-H.; Oliveira, J. E. B.; Almeida, V. R.; Chen, Y.-F.; Scherer, A., *Nat. Mater.* **2012**, 12, 108.

[140] Eichelkraut, T.; Heilmann, R.; Weimann, S.; Stützer, S.; Dreisow, F.; Christodoulides, D. N.; Nolte, S.; Szameit, A., *Nat. Commun.* **2013**, 4, 2533.

[141] Hodaei, H.; Miri, M.-A.; Heinrich, M.; Christodoulides, D. N.; Khajavikhan, M., *Science* **2014**, 346, 975.

[142] Hodaei, H.; Miri, M. A.; Hassan, A. U.; Hayenga, W. E.; Heinrich, M.; Christodoulides, D. N.; Khajavikhan, M., *Opt. Lett.* **2015**, 40, 4955.

[143] Pryce, I. M.; Aydin, K.; Kelaita, Y. A.; Briggs, R. M.; Atwater, H. A., *Nano Lett.* **2010**, 10, 4222.

CHAPTER 2. RESEARCH GOALS, TECHNICAL OBJECTIVES, AND DISSERTATION OVERVIEW

2.1 Research Goals

The overarching goal for this research is to understand, control, and manipulate light-matter interactions of hierarchical hybrid, organic/ inorganic spatially arranged photonic systems. Specifically, we focused on controlling and understanding local assemblies of highly emissive QDs in polymer matrices, individual/coupled photonic hybrid microfabricated resonators, and template assembled individual/coupled photonic microsphere resonators. This study provides a framework for the design of optimum optical systems for sensing and enhanced light modulation (i.e. lasing) applications.

Specific focus of this research will be on composite nanostructures, individual local nanocomposite structure assemblies and coupled local nanocomposite structures in polymer host matrices and templates. We aim to utilize quantum confined nanostructures as well as other emissive components as the optically active component to develop robust local assemblies (films) as well as photonic structures with tunable mechanical and optical properties such as lasing threshold, coupling strength, and mode activity. A fundamental understanding of the above-mentioned properties allows for the design of advanced flexible photonic systems, such as those obeying PT-symmetry and supersymmetry. This first requires, a thorough understanding of the emissive components being used for such photonic systems as well as understanding the role of host matrices, which are essential for imparting advanced functionalities to photonic systems. In addition to understanding the optical properties, promising and reliable methods to fabricate robust

array style optical cavities will be explored, with control over dimension and spatial locations. The final focus will be placed on fabricating coupled optical resonators to achieve desired coupling phenomenon, which is essential for realizing the above mentioned advanced photonic systems.

2.2 Technical Objectives

Of particular importance is understanding how the organic surrounding the emissive nanostructures (i.e. polymer matrix or template) can be used to influence and manipulate the light-matter interactions. The aim is to use knowledge of quantum confined nanostructures and properties of polymers and templates to fabricate nanophotonic systems displaying unique optical properties such has enhanced photoluminescence, lasing with mode selection, directional lasing, and enhanced coupling strength for signal processing and modulation. To do a thorough investigation of emissive components to include QD and dyes and QD-polymer nanocomposite optical properties, the research includes three main objectives (Figure 2.1).

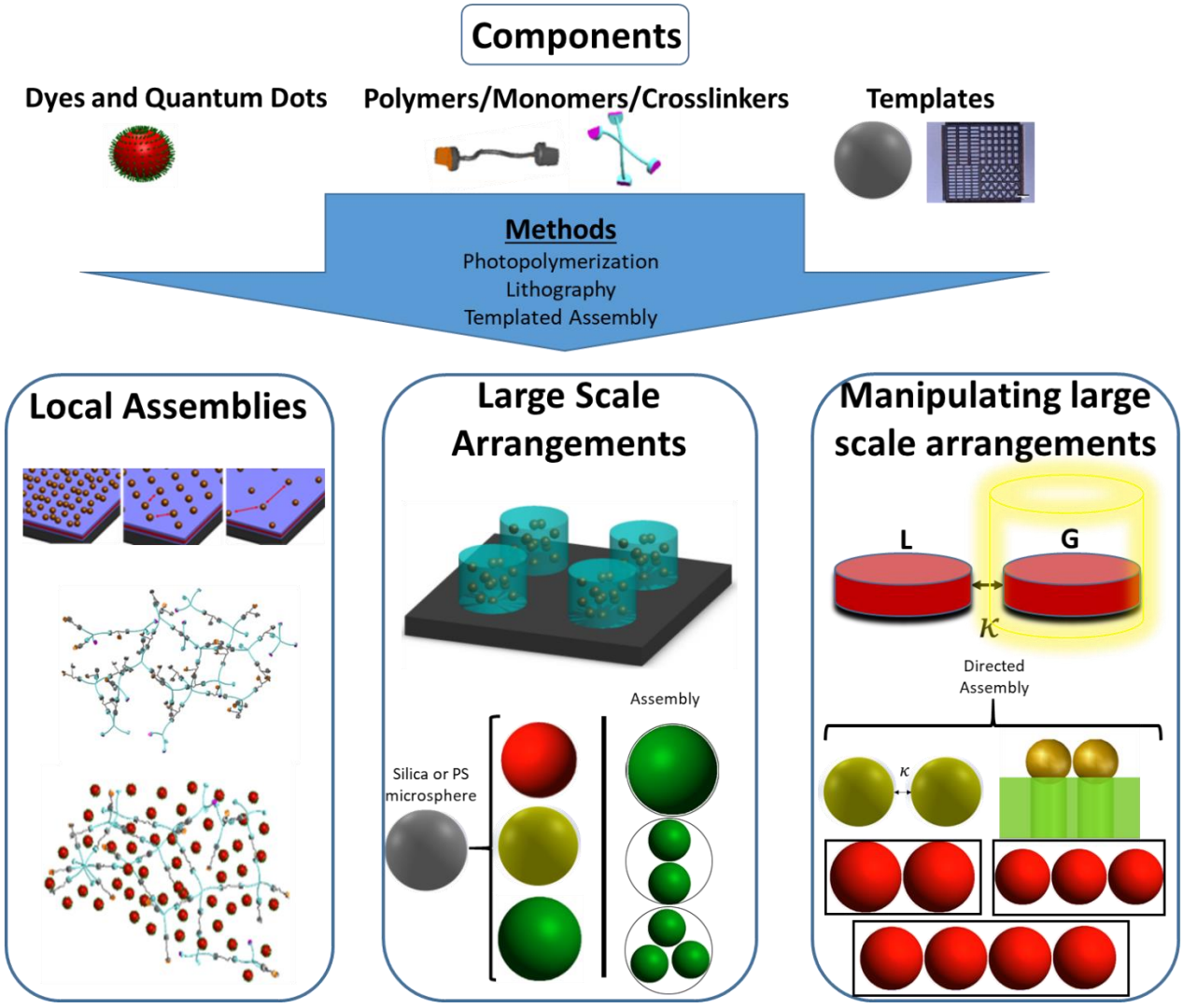

Figure 2.1: Research tasks at different hierarchical levels that are investigated in this research work to understand fundamental light-matter interactions at each level of QD assemblies from individual local assembled nanostructure to individual and coupled photonics cavities

Task one focuses on first understanding the quantum dot architecture and the role of various polymer matrices. Controlling the optical properties of QD-polymer composites by investigating monomer chemistries that are photopolymerizable and compatible with QD surface chemistry is the focus. Particular attention is paid to understanding the QD-polymer interfaces to control QD aggregation and phase separation. Ligand engineering is used as a means to exploit

favorable interactions between the QDs and polymer matrices, influencing QD particle behavior, and ideally enhancing spatial distribution. Thiol-ene chemistries are explored to fabricate polymeric host matrices to optimize QD dispersion while simultaneously maintaining the QD optical properties.

Task two utilizes lithographies, in addition to various templates, to fabricate well defined functional microstructures (i.e. waveguides, microdisk, and microspheres) embedded with QDs and organic dyes. Well defined and organized arrays of optical structures are used to understand unique optical phenomenon such as enhanced photoluminescence, lasing, and whispering gallery mode formation.

In Task three, the templated patterns generated in Task two are used to realize tunable optical phenomenon on demand such as mode selectivity, directional lasing output, and coupling strength of coupled assemblies for enhanced light modulation. We take advantage of various spatial pumping schemes to realized unique optical phenomenon including PT-symmetry. Additionally, templates fabricated from photolithography and 3D lithography, are used to realize unique coupled assemblies with high resolution to control light-matter interactions. Particular focus is placed on the ability to precisely tune coupled resonator microparticles to achieve desired coupling strength.

Specific objectives:

Task 1: Understanding QD core/shell architecture and design of polymer support matrix.

Focus will be placed on:

- Interrogate QD PL properties as a function of polymer matrix, surrounding medium, and various light exposure conditions.
- Assemble quantum dots into polymer matrices at controlled loadings with minimal aggregation by taking advantage of fast UV initiated thiol-ene chemistries.
- Examine the interface of the QD-polymer composite, specifically the effect of ligand chemistry and choice of monomers on nanoparticle aggregation and spatial distribution within the matrix.
- Study how increased loading of QDs into a polymer matrix affects optical properties and structure-property relationships in composite materials.
- Examine how the inclusion of QDs into the polymer host matrix effects QD and polymer properties including absorption, photoluminescence, quantum yield, glass transition temperature, thermal degradation temperature, and Young's modulus.
- Study polymerization kinetics and understand how QD loading and conversion affects properties including photoluminescence and mechanical properties.

Task 2: Use lithography and templates to formulate photonic systems and supports for quantum dots and emissive dyes, to study light-matter interactions. Focus is placed on:

- Develop a microfabrication technique that allows for the fabrication of QD-based cavities with controllable dimensions and lasing properties combined with long-term photostability.

- Fabricate nanoscale QD patterns via a templated approach focusing on the assembly of silica microbeads to take advantage of its resonator structure.
- Exploit directed assembly to achieve robust arrays of whispering gallery mode resonators.
    - Refine technique to obtain QD decorated silica microbeads, by focusing on appropriate ligand selection and silica surface chemistry to promote favorable interactions between components as well as high loading of QDs on silica surface.
- Establish characterization methods to examine the properties of fabricated assemblies including quality factor, whispering gallery mode activity, free spectral range, and effective refractive index.

Task 3: Take advantage of high-resolution lithographic techniques to influence optical properties such as enhanced photoluminescence, resonator coupling, and directional lasing. Focus is placed on:

- Utilize the sub-500nm resolution of photolithography to achieve coupled photonic structures.
- Study how the spatial modulation of the excitation pump can affect light-matter interactions. Selective introduction of gain/loss to a coupled system can exhibit novel phenomenon focusing on PT-symmetry.
- Utilize directed assembly to achieve stronger coupling between WGM resonators. Resolution will be pushed to sub-100nm.
- Fabricate large scale arrays by taking advantage of lithographic processes and template assisted, directed assembly.

- Establish templated assembly as a modular technique for realizing coupling between unique assemblies (i.e. resonators of variable size, color, etc.)

Overall, this work provides a framework for realizing structures, arrays, patterns, and eventually prototypes in which controlling light-matter interactions are important. Each level of the hierarchical system is investigated, from individual QD (and other emissive components) nanostructures, to QD composite structures, and finally coupled QD composite structures. This work focuses on the control of the local and large-scale assembly of quantum dots via precise engineering and manipulation of host matrices and templates. Specific emphasis is placed on implementing strategic designs with common fabrication methods (i.e. hybrid microfabrication using photolithography and unique template design using 3D lithography) to realize local photonic assemblies to demonstrate enhanced light propagation for applications including sensing, lasing, and signal processing.

Furthermore, different strategies to exploit lithographic techniques are explored and adopted to push the limits of the resolution of templates and photonic structures to truly realize robust, tunable QD-polymer composites with controlled optical and lasing properties. Finally, high-resolution lithographic techniques and templated patterning approaches are explored to fabricate large-scale patterns with controlled modulation of gain, loss, and refractive indices, taking advantage of both optical properties of quantum dots and other emissive components as well as mechanical properties of polymer host in attempt to demonstrate unique photonic systems with tunable lasing emission, controlled coupling, and potentially PT-symmetric like behavior.

2.3 Dissertation Overview

Chapter 1 provides a comprehensive review of literature which involves emissive components, with particular focus on QDs. Synthesis routes including core/shell engineering as well as the fundamental exciton dynamics of QDs are discussed. Different aspects of QD assembly including optical gain systems, deposition, patterning and microfabrication techniques, focusing on whispering gallery mode resonators, are also detailed. The introduction is concluded with an overview of the PT symmetric photonic system.

Chapter 2 outlines the research goals and technical objectives of this dissertation. A brief description of the organization and each chapter of this dissertation are also provided.

Chapter 3 outlines all different experimental techniques used in this dissertation including materials, synthesis of QDs, ligand exchange process, film deposition, photopolymerization of nanocomposites, microfabrication of QD patterns and templates, templated assembly, FDTD modeling, and various characterization methods.

Chapter 4 outlines a methodological way to understand the dynamic properties of QDs of various architectures. Focusing on core, core/shell, and core gradient shell QDs, we thoroughly investigate the effects of the polymer matrix as well as surrounding medium to understand the dynamic emission properties. A general framework is provided for appropriate selection of QD based on application.

Chapter 5 outlines a unique polymerization scheme to fabricate a highly QD-polymer nanocomposite. By taking advantage of thiol-ene chemistry providing a fast crosslinking mechanism to encapsulate QDs we provide a nanocomposite with minimal phase separation and tunable mechanical properties based on QD loading. Furthermore, we demonstrate patterning of the QD-polymer nanocomposite by taking advantage of soft lithography.

Chapter 6 reports a method that utilizes template assisted directed assembly to realize arrays of coupled whispering gallery mode resonators. Using a clever design of the template we achieve microspheres which rest atop the template and not embedded within to achieve resonator gap distances below 100nm. In addition, we demonstrate the ability to control the coupling strength of coupled resonators based on the gap distance.

Chapter 7 studies the effect of gain/loss modulation in evanescently coupled microdisks of solution-processed quantum dots. Defect formation on cavities leads to the formation of coupled intra-cavity modes. Varying the gain differential between such disks by optical modulation leads to coalescence of parasitic intra-cavity modes that result from material inhomogeneity.

Chapter 8 summarizes the general results and conclusions discussed in chapter 4-7. In addition, the scientific significance in the field and the impact to the future development of potential applications are also provided.

CHAPTER 3. EXPERIMENTAL TECHNIQUES AND MATERIALS

3.1 Chemicals and Materials

Cadmium oxide, tri-n-octylphosphine (TOP, 90%), selenium powder, 1,7 diaminoheptane (DIAH, 98%), ethyl lactate, were obtained from Sigma Aldrich. 1-tetradecylphosphonic acid (TDPA, 98%), tri-n-octylphosphine oxide (TOPO, 90%), diethylzinc (15 weight% in hexane), cesium acetate (99.9%), lead acetate trihydrate (99.995%) and tetra-n-octylammonium bromide (TOABr) (98+%) were obtained from Alfa Aesar. 1-octadecene (ODE, 90%), hexadecylamine (HDA, 90%), butylamine (BA, 98%), oleic acid (OA, 97%), and bis(trimethylsilyl) sulfide (95%) were obtained from TCI. Hexane, acetone, toluene (ACS reagent grade) and heptane were obtained from BDH Chemicals. All chemicals were used as received.

3.2 Quantum Dots

3.2.1 Synthesis of CdSe/$Cd_{1-x}Zn_xSe_{1-y}S_y$ core/graded shell QDs

Chemical composition gradient CdSe/$Cd_{1-x}Zn_xSe_{1-y}S_y$ core/graded-shell QDs were synthesized by modifying reported methods and provided by collaborators (Prof. Lin's group, School of Materials Science and Engineering, Georgia Institute of Technology).[1] Briefly, 0.2 mmol of CdO, 4 mmol of $Zn(acetate)_2$, 5 ml of oleic acid, and 15 ml of 1-octadecene (ODE) were placed in a three-neck flask and degassed at 150°C for 1 hr. The reaction was heated to 300°C under Ar. At the elevated temperature (300°C), 1 mmol of Se and 4 mmol of S in 2 ml of TOP were rapidly injected into the reaction vessel. The reaction was allowed to proceed at 300°C for 10 minutes, and then the heating

mantle was removed to stop the reaction. 5 ml of hexane was added to the solution once the temperature reached 70°C.

3.2.2 Ligand Exchange Process

The oleic acid-capped CdSe/$Cd_{1-x}Zn_xSe_{1-y}S_y$ QDs were centrifuged with acetone three times to remove excess oleic acid and ODE. Subsequently, purified oleic acid-capped CdSe/$Cd_{1-x}Zn_xSe_{1-y}S_y$ QDs were re-dispersed in hexane and an excess amount of hexadecylamine, octylamine, butylamine (BA) was added to perform the solution-phase ligand exchange. The ligand exchange reaction was allowed to proceed at 45℃ for 1 day. The solution was then precipitated using methanol and re-dispersed in a mixture of hexane and an excess ligand amount. This procedure was repeated three times.[2]

The solid-state exchange is performed by soaking the prepared butylamine-capped QD films in a 0.1 M methanol solution of 1,7 diaminoheptane (DIAH) for 1 hour. After soaking, the films are washed with methanol 3 times to remove any excess 1,7 diaminoheptane. It was observed that the QD loading did not significantly change during the networking step (53% to 49%), which may be due to the similar length of the two BA ligands and the length of one DIAH ligand if the ligands are fully extended between adjacent QD surfaces.[2]

3.3 Film Deposition and Patterning

Neat or composite QD films were fabricated by spincoating a concentrated QD solution in chloroform or heptane with or without a 5 wt. % thiol-ene monomer mixture. The film thicknesses ranged from 150-250nm.

3.4 Scanning Electron Microscopy (SEM) / Transmission Electron Microscopy (TEM)

SEM characterization was performed on a Hitachi S-3400N SEM with a backscattered electron detector with an accelerating voltage in the range of 5-15kV. If necessary, samples were sputtered with a gold/palladium mixture using a Hummer VI instrument. The interparticle distance and size of CdSe/Cd1-xZnxSe1-ySy QDs was studied using a high-resolution transmission electron microscope (Tecnai F30). An accelerating voltage of 300 keV was used. TEM samples were prepared by diluting the original QD solution of ~6 mg/mL 30 times. 5-10 µL of the diluted solution was then drop-cast on the TEM grid and allowed to dry completely. The DIAH-tethered QD sample was prepared by making the BA-capped QD sample and then subsequently performing the crosslinking process for 1 hour.

3.5 Atomic Force Microscopy (AFM)

Atomic force microscopy (AFM) images were collected using an Icon microscope (Bruker) in tapping mode according to usual procedure.[3] MikroMasch pyramidal silicon tips were used with a height of 15 µm and a cantilever length of 150 µm. Scan sizes ranging from 1 µm to 60 µm (on a side) with a scan rate in the range of 0.3-0.8 Hz.

3.6 Optical Microscopies (brightfield, darkfield, and photoluminescence imaging)

Darkfield, brightfield, and photoluminescence images were collected using a CytoViva hyperspectral system equipped with either a Dagexcel-M Digital Firewire camera (cooled) or a R1 Retiga installed on optical microscope (Olympus BX51) and a 50x objective. PL imaging was performed using photoluminescence excitation from a blue bandpass filter (450-490 nm) with a dichroic mirror that reflects optical wavelengths below 495 nm, and with a longpass emission filter that passes optical wavelengths above 500 nm. The light source is a quartz halogen lamp with an aluminum reflector providing a wavelength range of 420−850 nm and a power of 150 W of

unpolarized light. All filters and the dichroic mirror are from Chroma Technology Corp. The light source was a quartz halogen lamp with an aluminum reflector providing an emission range of 420-850 nm and a maximum power of 150 Watts.

3.7 Spectroscopic Ellipsometry

The QD films were examined using a spectroscopic ellipsometer from Woollam (model M2000) with a wavelength range of 245-1000 nm and a rotating compensator configuration. Film thickness was determined by applying a cauchy model to the transparent region of the optical spectrum. The refractive index at 650 nm (also in the transparent region) was estimated using the cauchy model. QD-loading (volume fraction) was determined by applying the effective medium approximation Bruggeman model to the refractive index at 650 nm to fit for the volume fraction of QDs in the film (with thickness treated as a constant). The refractive index of CdSe/$Cd_{1-x}Zn_xSe_{1-y}S_y$ QD was approximated using the refractive index of bulk CdSe (n_{bulk} = 2.4), and the refractive index value of the ligand at 650 nm was adjusted according to the ligand content.[4]

3.8 UV-vis and Fluorescence Spectroscopy

UV-vis extinction spectra of QD solutions (quartz cuvette) from 350-900 nm (1 nm intervals) were collected using a Shimadzu UV-vis 2450 spectrometer with D2 and tungsten lamps offering a wavelength range of 300-1100 nm. The QD extinction spectra were corrected against the pure solvent background and the same quartz cuvette. Photoluminescence spectra of QD solutions were collected using a Shimadzu RF-5301PC spectrofluorophotometer with the excitation wavelength of 525 nm.

3.9 Quantum Yield Measurements

Quantum yields of QDs dispersed in hexane and chloroform are determined by the relative quantum yield method.[5] Standard samples, rhodamine 101 (QY = 91.5%), dissolved in ethanol was used to determine QDs emitting at red regions while rhodamine 6G (QY = 95%) dissolved in ethanol was used to determine QDs emitting at green regions. UV−vis extinction spectra of QD solutions (quartz cuvette) from 350 to 900 nm (1 nm intervals) were collected using a Shimadzu UV− vis-2450 spectrometer with D2 and tungsten lamps offering a wavelength range of 300−1100 nm. The QD extinction spectra were corrected against the pure solvent background and the same quartz cuvette. Photoluminescence spectra of QD solutions were collected using a Shimadzu fluorescent RF- 5301PC spectrofluorophotometer with the excitation wavelengths of 525 nm for red emitting QDs while 480nm was used for green emitting QDs. All the extinction values of solutions are diluted to be less than 0.1 before measurement in order to avoid the reabsorption effect.

3.10 Collaborative Efforts

A great amount of the work described in this thesis was done in collaboration with Professor Z. Lin's research group in Georgia Institute of Technology and Professor Vardeny's research group in University of Utah. Synthesis of QDs were all done and obtained from Professor Z. Lin's research group. The confocal micro-photoluminescence measurement were done by Professor Vardeny's research group (University of Utah).

3.11 References (Chapter 3)

[1] Bae, W. K.; Char, K.; Hur, H.; Lee, S.; *Chem. Mater.* **2008**, 20, 531.

[2] Lin, C. H.; Lafalce, E.; Jung, J.; Smith, M. J.; Malak, S. T.; Aryal, S.; Yoon, Y. J.; ZhY.;Lin, Z.; Vardeny, Z. V.; Tsukruk, V. V. *ACS Photonics* **2016**, 3, 647.

[3]McConney, M. E.; Singamaneni, S.; Tsukruk, V. V.; *Polymer Reviews* **2010**, 50, 235.

[4]Sigma-Aldrich. Butylamine, 1,7 diaminoheptane, & oleic acid.

[5]Wurth, C.; Grabolle, M.; Pauli, J.; Spieles, M.; Resch-Genger, U. *Nature Protocols* **2013**, 8, 1535.

CHAPTER 4. DECAY-TO-RECOVERY BEHAVIOR AND ON−OFF RECOVERY OF PHOTOLUMINESCENCE INTENSITY FROM CORE/SHELL QUANTUM DOTS

4.1 Introduction

Quantum dots have gained significant interest in the area of photonics due to their tunable emission across the visible spectrum, narrow emission bands, and high quantum yields.[1] In addition, these small semiconductor nanoparticles are compatible with many surface functionalization schemes,[1] deposition approaches,[2,3] and patterning techniques,[4,5] making them ideal candidates for a variety of technologies including LEDs,[6,7] solar cells,[8,9,10,11] lasing media[2,3] and cell tracking.[12]

The wide range of applications for QDs have, therefore, resulted in intense research examining how the compositional profile (core, core/shell, and core/graded shell) can be used to tune their optical properties in a controllable manner.[13,14,15,16,17] Typically, the introduction of a protective inorganic shell around a QD core improves their optoelectronic properties, with graded or alloyed core/shell interfaces providing the greatest improvements.[16,17] QDs are commonly evaluated by considering steady-state characteristics like quantum yield, emission full-width half-maximum (FWHM), photoluminescence lifetime, and Auger relaxation dynamics.[13-18] The formation and dynamics of excitons and multiexcitons have also been shown to depend on the presence (and type) of inorganic shell.[19,20]

However, one of the most critically important metrics of evaluation is the stability of emission characteristics like spectral position, FWHM, and intensity since they play such a critical role in

device lifetime and scientific investigation. For example, the issue of QD emission stability is very important to consider for characterization techniques like the variable strip length method (for optical gain) and fluorescence lifetime imaging (for cellular and nanoparticle imaging/tracking) where stable emission is required to obtain meaningful results.[12,21,22] Additionally, QD stability is critically important in photonic systems that need to have a long lifetime when it experiences a variety of environmental conditions (QD LEDs, displays, and lasers).[6,23,24] Deviations from perfect emission stability can therefore introduce unstable emission but can be valuable for dynamic, light-intensity dependent photonic systems. Indeed, controllably variable emission is actually necessary, as in the case of dynamic photopatterning.[25]

Various studies have examined how the emission of QDs evolve in response to chemicals, gaseous environments, polyelectrolyte matrices, substrates, and light exposure.[26,27,28,29,30] Blue shifting is a very common phenomenon and is caused by an increase of quantum confinement of the exciton due to a reduction of QD size. Typically, size reduction is attributed to chemical or photochemical oxidation and corrosion of the QD surface,[31,32,33,34] since it can be significantly reduced by placing QDs in a nitrogen environment or vacuum.[34,35,36] Blue shifting of PL can vary from a few nanometers in dark environments (i.e. oxidation)[35] to 15-20 nm under light exposure (i.e. photooxidation).[31,34,35] Changes of QD emission intensity (decreases and increases) have also been observed. In general, intensity is altered by modifying non-radiative trap states, which includes bypassing (via a more efficient recombination pathway), saturating (by ligand, H_2O, or charge carriers), or removing these pathways (shelling, photo-restructuring/annealing of the QD surface). The variety of mechanisms that affect emission makes the evaluation and understanding of the situation complex. In general, a PL intensity increase is much more common in the literature than

a decrease. For example, increasing intensity upon light exposure have been attributed to photoactivation (in vacuum),[35] photo-induced H_2O defect passivation,[31] increased coordination of ligands with the QD surface via pH changes or light,[37,38] and photo-induced surface annealing/restructuring.[34] On the other hand, the decreases of PL intensity have been credited to the formation of surface quenching states during photooxidation as a result of photobleaching.[35,36] Interestingly, photobleaching has been shown to still occur in a nitrogen environment, so it has been suggested that the formation of lattice defects in the CdSe/ZnS QD likely leads to non-radiative recombination pathways.[39]

Additional complexity is added by the fact that some of these changes are reversible and others irreversible. For example, reversible changes to intensity were demonstrated by heat cycling due to photoinduced surface transformation,[40] pressure cycling due to adsorption/desorption of H_2O,[31] and light exposure cycling due to light-activated rearrangement of surfactant molecules.[38] Additional complications include the variety of rates over which these changes can occur (seconds versus minutes versus hours). For example, studies that utilized PL integration times on the order of 20 seconds to 2 minutes might have missed changes occurring within the first seconds of light exposure.[41,42]

Different studies have presented routes for mediating these changes to emission, typically involving the introduction of an inorganic protective shell around the QD core where the exciton is located.[34,35,38] For example, previous studies have compared bare CdSe core QDs to CdSe/ZnS core/shell QDs in a variety of environments.[35] However, these measurements were performed

either under continuous darkness or continuous light exposure without checking for reversibility and, therefore, did not observe the unique light-mediated on-off (reversible) PL intensity recovery.

In this work, we examine how the emission from QD-polymer composite films with different green-emitting QD architectures (core, core/shell, core/graded shell) evolve when in darkness, when exposed to light, and when undergoing light-dark-light cycles. The photo-responsive behavior can be engineered into a QD by ensuring that the CdSe core (where the exciton is located) is exposed to the environment, either upon synthesis or through chemical/physical modification/degradation of the protective inorganic shell by light, oxygen, and water. We suggest that the competition between reversible and irreversible mechanisms can lead to unique decay-to-recovery behavior for intensity, meta-stable bright states that can be turned on and off many times, and decoupled optical changes (reversible intensity changes versus irreversible spectral shifts). Furthermore, there is a large rate difference between the decay and recovery mechanisms (seconds versus many minutes), suggesting the presence of fast processes (i.e. immediate decay upon light exposure) under certain conditions. The distinct response of each green-emitting QD architecture arises from how the core and shell material interact with each other (crystal lattice mismatches) and the environment.

4.2 Experimental methods

Chemicals and materials: Cadmium oxide, tri-n-octylphosphine (TOP, 90%), and selenium powder, were obtained from Sigma Aldrich. 1-tetradecylphosphonic acid (TDPA, 98%), tri-n-octylphosphine oxide (TOPO, 90%), diethylzinc (15 weight% in hexane), and hexane were obtained from Alfa Aesar. 1-octadecene (ODE, 90%), hexadecylamine (HDA, 90%), butylamine

(BA, 98%), oleic acid (OA, 97%), and bis(trimethylsilyl) sulfide (95%) were obtained from TCI. Poly(methyl methacrylate) (PMMA) (MW = 120000) was obtained from Sigma Aldrich. Toluene was obtained from BDH Chemicals. All chemicals were used as received.

Synthesis, unstable green CdSe QDs & CdSe/ZnS QDs: Green-emitting CdSe QDs were synthesized following a literature procedure.[25,44] Initially, 50 mg of CdO, 300 mg of TDPA, and 4 g of TOPO were inserted into a three neck flask. The mixture was heated to 120°C and degassed for 1 hour. Subsequently, the temperature was increased to 290°C under Argon. After the solution became clear and transparent, 1 ml of 1 M Se/TBP solution was quickly injected in order to initiate nucleation and growth. CdSe QDs were grown at 290°C for 10 sec. The heating mantle was then removed to stop the reaction. Afterwards, once the temperature reached 70°C, 5 ml of hexane was added to the solution.

The ZnS shell for the unstable CdSe/ZnS core/shell QDs was synthesized following a procedure reported in literature.[15,25] Initially, 2 g of TOPO and 1 g of hexadecylamine (HDA) were inserted into a three-neck flask and degassed at 120°C for 1 hour. Afterwards, 5 ml of plain CdSe core QDs were added and the temperature was increased to 220°C under Argon. Following this, precursor solution (0.15 ml of diethylzinc and 0.05 ml of bis(trimethylsilyl) sulfide in 1 ml of trioctylphosphine) was injected dropwise to the vigorously stirring reaction mixture. The reaction proceeded for 30 min to grow the ZnS shell. The heating mantle was then removed to stop the reaction. 5 ml of hexane was added to the solution once the temperature reached 70°C.

Sample preparation: QD-polymer films of thickness 270 nm (±50 nm) (as evaluated by ellipsometry) were prepared by spin-casting a QD-polymer mixture at 2500 rpm for 1 min, as outlined previously.[25] Films had a QD-loading of approximately 1% (volume fraction) which was estimated via fitting of refractive indices derived from ellipsometry data with the Bruggeman model.[43] The QD-polymer mixture was made by mixing equal volumes of QD (toluene) solution with a 10-12% PMMA (toluene) solution, which was then vortexed. Films were deposited on silicon with a ≈290 nm surface layer of SiO_2.

4.3 Results and discussion

4.3.1 QD optical characteristics

Colloidal green-emitting plain CdSe core QDs were synthesized following a seeded-growth procedure,[25,44] while the ZnS shell for the CdSe/ZnS core/shell QDs was synthesized following a procedure reported in literature.[15,25] Green core/graded shell CdSe/$Cd_{1-x}Zn_xSe_{1-y}S_y$ QDs were synthesized by modifying a reported method.[45,46] TEM micrographs show an outer diameter of 3.9±0.3 nm (shell thickness ~0.5 nm) for the CdSe/ZnS QDs, while the CdSe/$Cd_{1-x}Zn_xSe_{1-y}S_y$ QDs have diameter of 7.6±0.5 nm (shell thickness ~2.7 nm) (**Figure A.1**). The thicker shell for the core/graded shell QD could be synthesized due to the reduce crystal lattice mismatch between the CdSe core and graded composition shell. Core only, core/shell, and core/graded shell QDs were used to examine how the compositional profile affects the general optical characteristics in the solution state (**Table 4.1**). Each QD type displays a broadband absorbance down to the UV and narrowband emission in the green region (**Figure A.2**).

Table 4.1: Optical characteristics of plain CdSe core, CdSe/ZnS core/shell, and CdSe/$Cd_{1-x}Zn_xSe_{1-y}S_y$ core/graded shell QDs in the solution state.

Quantum Dot	Composition	Absorption Peak (nm)	PL Peak (nm)	Stokes Shift (nm)	FWHM (nm)	Quantum Yield (%)
Core	CdSe	553	560	7	26	3
Core/shell	CdSe/ZnS	546	554	8	28	16
Core/graded shell	$CdSe/Cd_{1-x}Zn_xSe_{1-y}S_y$	492	508	16	33	73

In addition, the FWHM of all QD types is narrow, under 35 nm, indicating a relatively homogeneous size distribution. The quantum yield (QY) shows a strong dependence on QD composition profile, with the plain core CdSe QDs having the lowest QY and the core/graded shell $CdSe/Cd_{1-x}Zn_xSe_{1-y}S_y$ QDs possessing the highest QY. The significant increase of QY for the core/shell and core/graded shell QDs can be attributed to the passivation of the CdSe core surface states.[17,18,47,48] In addition, core/shell alloying provides more effective surface passivation via the removal of defect sites that arise from the crystal lattice mismatch (12%) between CdSe and ZnS.[17,48] These trends are consistent with previous studies examining how QD shelling can influence the optical characteristics.[17,48,49]

4.3.2 Emission Evolution: Darkness

In addition to QY, the QD composition profile should also strongly influence the optical stability (intensity and spectral position) of QDs since the environment can lead to changes in the QD surface composition (oxidation, corrosion, etc.) which in turn affects surface passivation and the relaxation pathways available to the exciton (trap states and non-radiative relaxation pathways).

The QD composition profile and shell thickness become particularly important for type-I QD designs since the exciton can be localized to the QD core and, therefore, isolated from the environment. Furthermore, QD composition profile and shell thickness are very important when QDs are deposited into films since the QDs are in close contact with a variety of additional factors (oxygen, moisture, and surrounding materials) that have been shown to cause changes of the spectral position and QY of QDs.[25,35,36]

To examine how QD composition profile and shell thickness affect PL stability in a dark environment (ambient atmosphere, temperature, pressure), each type of QD (plain core, core/shell, core/graded shell) was deposited into a poly(methyl methacrylate) (PMMA) film. QD-polymer films of thickness 270 nm (±50 nm) were prepared by spin-casting a QD-PMMA mixture at 2500 rpm for 1 min, as outlined previously.[25] All QD-polymer films uniformly covered the substrate, exhibiting minimum scattering, and displayed uniform PL emission (**Figure A.3**). The PL intensity and spectral position of QD emission were then monitored while the films were in a dark environment. The composition profile and shell thickness of QDs were found to strongly influence how the intensity and spectral position evolve during this period of darkness (**Figure 4.1**). The core CdSe QDs display a large decrease in intensity (a 95% decrease) and moderate blue shift (5 nm), which results from oxidation and corrosion of the CdSe surface to $CdSeO_2$, and activates non-radiative surface quenching states (**Figure A.4**).[35,36]

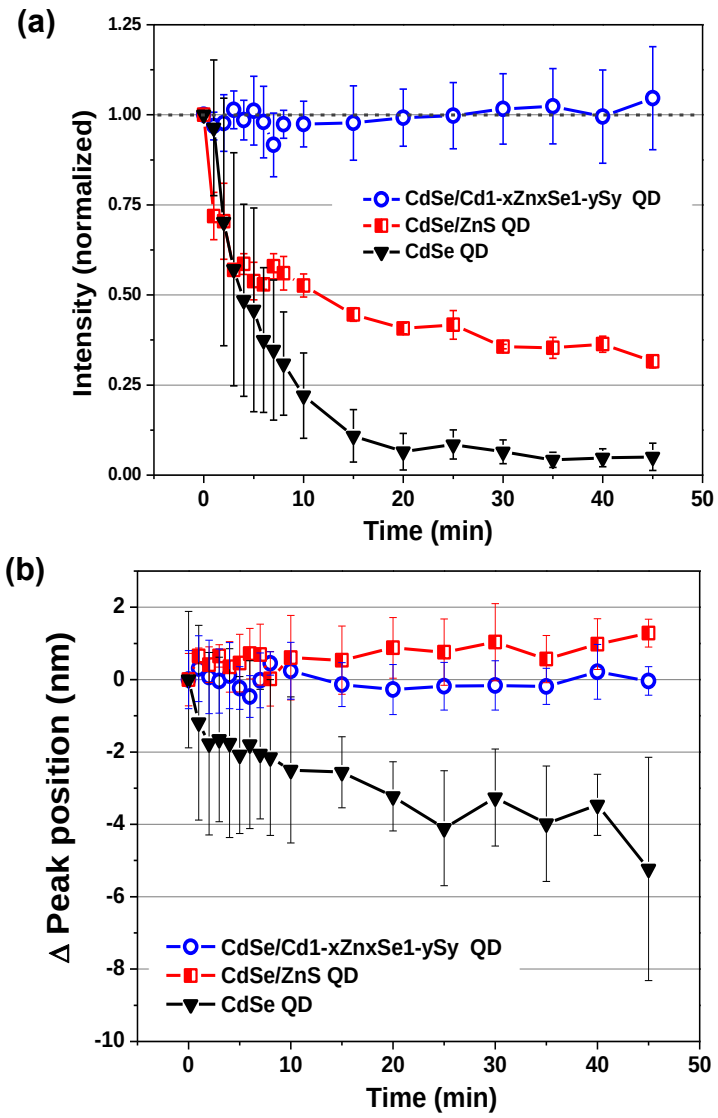

Figure 4.1: Evolution of the PL intensity (a) and spectral shift ($\lambda_t - \lambda_0$) (b) of QD-PMMA films using the CdSe core, CdSe/ZnS core/shell, or CdSe/$Cd_{1-x}Zn_xSe_{1-y}S_y$ core/graded shell QDs under darkness.

The core/shell CdSe/ZnS QD undergoes a less pronounced decrease of intensity (a 60% decrease) and a small red-shift ($\Delta\lambda \approx 1$nm) over the same period. The reduction of intensity indicates a decreased passivation of the CdSe core by the thin ZnS shell (~0.5 nm). The very small red shift

could be due to a reduction of quantum confinement on the CdSe core due to removal of the compressive ZnS shell.[50,51,52] However, in general the very weak spectral shift indicates quantum confinement of the exciton is not significantly altered, which means the core undergoes minimal physical change in size since the CdSe/ZnS QD is type-I with the exciton confined to the CdSe core. In short, these results show that the CdSe/ZnS QD experiences degradation of the 0.5 nm thick ZnS shell by oxidation and corrosion with little modification to the CdSe core (**Figure A.4**). Modification of the ZnS shell is not surprising since the ZnS shell is the material in direct contact with the environment.

Finally, the core/graded shell CdSe/$Cd_{1-x}Zn_xSe_{1-y}S_y$ QD shows no clear changes of intensity ($\Delta I < 5\%$) or spectral position ($\Delta\lambda < 1$nm) over the same period. Although oxidation of the outer graded shell is likely occurring, its effects do not directly affect the CdSe core due to the thickness (2.7 nm) and thermodynamic stability of the graded $Cd_{1-x}Zn_xSe_{1-y}S_y$ shell. Both the thicker shell and thermodynamic stability result from the graded shell composition profile imparted during synthesis, which reduces the strain energy from the crystal lattice mismatch between CdSe and ZnS allowing for thicker epitaxial shells to be grown (compared to sharp transition core/shell QDs).[48,50]

These distinct emission trends clearly show that the composition profile and shell thickness of the QD composition affect how the optical properties evolve in a dark environment under ambient temperature and gaseous composition. The proposed physical changes underlying these PL trends are shown in **Figure A.4**. The consideration of these trends is very relevant for improving the lifetime and storage of QD devices and systems during storage. The proposed physical

mechanisms leading to this distinct behavior are based on the indirect evidence from PL emission. Direct verification of reduced QD size or crystal lattice due to oxidation and corrosion via high-resolution TEM is extremely difficult due to the very small physical changes that are likely occurring (<1 nm change) and exposure to e-beam at high-resolution TEM could alter the QDs.

4.3.3 Emission Evolution: Continuous Light Exposure

In the next step, compared to darkness as noted above, we examined whether continuous light exposure elicits additional mechanisms within the QDs that alter how the emission evolves, which is particularly important to know when developing QD devices and systems that experience constant harsh light excitation and exposure. In this case, the QD-polymer films are continuously exposed to light (24-32 mW, 450-490 nm) over a period of 45 minutes, while their PL intensity and spectral position are monitored.

Similarly, the QD composition profile and shell thickness profoundly impact how the intensity and spectral position of the emission evolves. Furthermore, continuous light exposure leads to more pronounced shifts in some instances compared to when in darkness. For example, the core CdSe QDs undergo a much larger blue shift (16 nm) compared to when in darkness (5 nm), indicating an accelerated oxidation and corrosion of the CdSe core that reduces the diameter and increases quantum confinement. The intensity follows a similar decay rate and magnitude presumably due to a saturation of non-radiative surface quenching states. The decay of PL intensity was corroborated with PL imaging (**Figure A.5**). The decay of PL intensity upon light exposure for plain CdSe core QDs is interesting since some previous studies have shown that CdSe QDs can experience an increase of PL intensity upon light exposure.[31] This variance could be due to the

different environmental and exposure conditions (toluene vs hexane/H_2O), deposition approach (spin-casting vs Langmuir-Blodgett), film type (QD-polymer vs purely QD), as well as differences in the available QD surface states caused by the different specific CdSe QD synthesis approaches that were used.[31]

Light exposure for the core/shell CdSe/ZnS QDs leads to more pronounced shifts and new behavior, signifying the emergence of photo-mediated mechanisms. For example, a large continuous spectral blue shift occurs (16 nm) throughout the 45 minutes of light exposure (instead of a red shift). Furthermore, upon exposure to light, the intensity decreases more rapidly than in the darkness case, and then undergoes a recovery of intensity. The convolution of the competing decay and recovery mechanisms leads to a decay-to-recovery evolution of intensity (**Figure 4.2a-4.2b**). Interestingly, the decay occurs much more quickly (seconds-to-minutes) than the recovery step (tens of minutes).

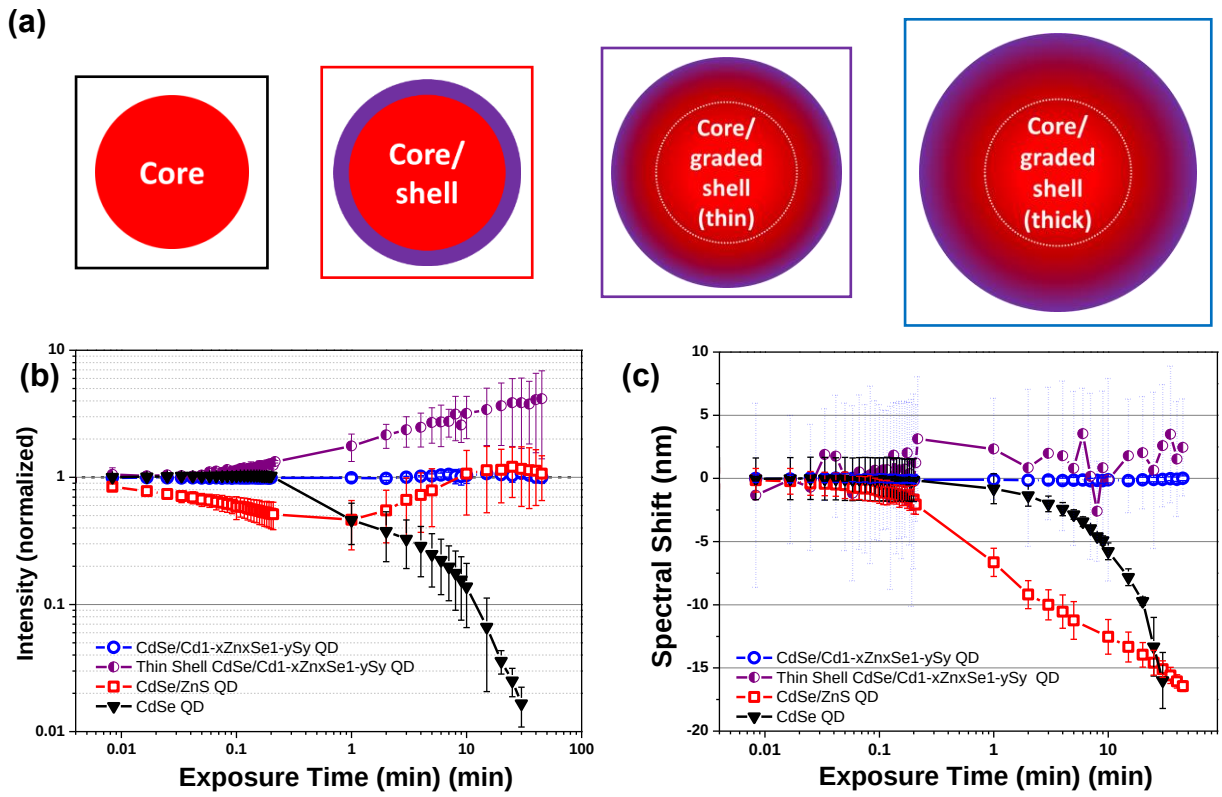

Figure 4.2: Examination of the photoluminescence stability of QD-PMMA films with different types of QD design (CdSe core, CdSe/ZnS core/shell, or CdSe/$Cd_{1-x}Zn_xSe_{1-y}S_y$ core/graded shell). (a) Schematic of the different QDs that were examined. Evolution of (b) PL intensity and (c) spectral shift ($\lambda_t - \lambda_0$) under continuous light exposure (blue light: 450-490 nm, 24-32 mW).

As in the darkness case, the intensity and spectral position of the core/graded shell CdSe/$Cd_{1-x}Zn_xSe_{1-y}S_y$ QDs show minimal change under continuous light exposure (verified with PL imaging in **Figure A.6**). In addition to the thick graded shell QD, thinner graded shell QDs (1 nm shell thickness) were examined to provide a more direct comparison to the CdSe/ZnS QDs with 0.5 nm

shell thickness. The thin graded shell QDs have very different behavior, showing no initial decay step and instead a PL intensity enhancement by a factor of 2-4 over the 45 min light exposure period (32 mW, 450-490 nm). This behavior indicates that a thinner graded shell is not sufficient to completely stabilize the QD against light exposure. However, the thin graded shell appears to prevent decay during initial light exposure, in contrast to the sharp ZnS shell of the CdSe/ZnS QDs. Therefore, the compositional gradient and thickness of the QD shell has the potential to lead to unique PL intensity behavior upon light exposure.

Continuous exposure experiments of the core, core/shell, and thin core/graded shell QDs in solution show an increase of PL intensity upon light exposure (55%, 16%, and 25% increase, respectively), while the thick core/graded shell QD show minimal change ($\Delta < 5\%$) (**Figure A.7a**). However, no clear indication of spectral shifting is observed during light exposure for any of the QDs in solution ($\Delta < 1$ nm) **Figure A.7b**). The absence of PL intensity decay and presence of PL enhancement indicates that it is exposure to the ambient environment and deposition into a solid film state that leads to the PL decay behavior via a photooxidative effect. Furthermore, the increase of PL intensity with no concurrent spectral (blue) shift indicates that the PL recovery/enhancement mechanism is due to a unique mechanism that does not cause spectral blue shifting. This provides additional evidence that more than one mechanism underlies the evolution of QD PL upon light exposure.

4.3.4 Emission Evolution: Decay-to-recovery behavior (CdSe/ZnS QDs)

As mentioned, the decay-to-recovery evolution of intensity for the CdSe/ZnS QDs arises from a combination of competing decay and recovery mechanisms. However, there are a variety of

mechanisms that lead to decay and recovery (reversible or irreversible) in QDs so additional information is required before a conclusive determination can be made.

Continuous light exposure of different power

PL intensity recovery only occurs with continuous light exposure so it is likely that the characteristics of recovery depend on the exposure power. However, it is also possible that light exposure also affects the decay mechanism. Therefore, the relative strength of each effect and its dependence on exposure power needs to be compared. The time-to-recovery is an ideal parameter to consider for this comparison as it represents the time required for the effects of the recovery mechanism to overcome those from the decay mechanism. The results show that the decay-to-recovery behavior is affected by the exposure power, where an increase of exposure power from 3 mW to 32m W (450-490 nm) reduces the time required for the CdSe/ZnS QDs to enter the recovery stage ($\tau_{recovery}$) from ~3.5 min to 1 min (**Figure 4.3a-4.3b**).

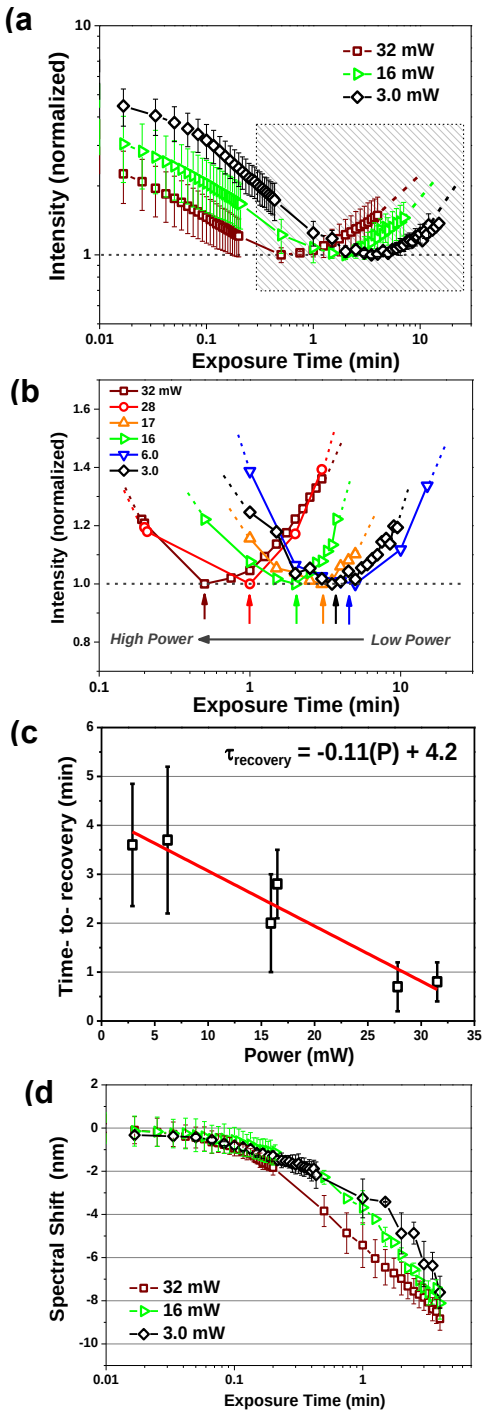

Figure 4.3: Evolution of the (a) PL intensity for core/shell CdSe/ZnS QD-PMMA films at three different exposure powers (continuous exposure), and (b) a narrowed viewing range of the time-to-recovery for additional exposure powers (dashed lines are guides only). (c) The

time-to-recovery of PL intensity versus incident exposure power. (d) Spectral shift ($\lambda_t - \lambda_0$) of the emission peak at three different exposure powers (continuous exposure).

This indicates that the recovery mechanism has a stronger dependence on (and is proportional to) the number of incident photons than the decay mechanism since recovery overcomes decay eventually (for the power range examined). Next, the time-to-recovery follows a downward linear relationship with exposure power (**Figure 4.3c**).

This suggests that the rate of the recovery is linearly proportional to the number of incident photons, or that the ratio of the rates of the recovery and decay mechanism is linear. Then, the rate of blue shifting increases with higher exposure power (**Figure 4.3d**), which shows that photooxidation and corrosion of the CdSe core scales with the number of incident photons. In order for photooxidation and corrosion to reduce the CdSe core size, the ZnS shell must either be removed or significantly degraded during this period. However, removal and degradation of the ZnS shell should reduce surface passivation (and the intensity). Therefore, we can speculate that the blue shifting is a result of the decay mechanism, which means the decay mechanism also is proportional to the exposure power.

Continuous light exposure of pure QD films exposed to water

The surrounding environment of the QD can have a strong impact on the surface of the QD which directly affects the relaxation pathways available to the QD exciton. Therefore, we cast pure CdSe/ZnS QD films to examine the role of the polymer matrix and examined the PL evolution upon continuous light exposure (450-490 nm). The removal of the protective polymer matrix leads to the emergence of unique PL evolution, specifically the presence of PL enhancement followed by decay (**Figure 4.4a**). In this case, the eventual decay indicates that the mechanism causing decay eventually overwhelms (or removes) the PL enhancement mechanism, essentially

transforming the CdSe/ZnS QDs into the CdSe QDs. Soaking the pure CdSe/ZnS QD film in water before light exposure increased the magnitude of PL enhancement compared to the dry state. However, the eventual decay was not prevented and the intensity eventual returned to a similar dark state as seen with the dry film state.

Both films underwent spectral shifting, with the H_2O soaked QD film showing slightly more blue shifting (**Figure 4.4b**). These results clearly show that the polymer matrix does play a role in the PL dynamics of unstable CdSe/ZnS QDs. In this case, removing the protective polymer matrix does not prevent PL recovery but does lead to the emergence of a post-enhancement decay

mechanism. Furthermore, H_2O clearly plays a role in the PL enhancement, and possibly the photooxidation (although not as pronounced).

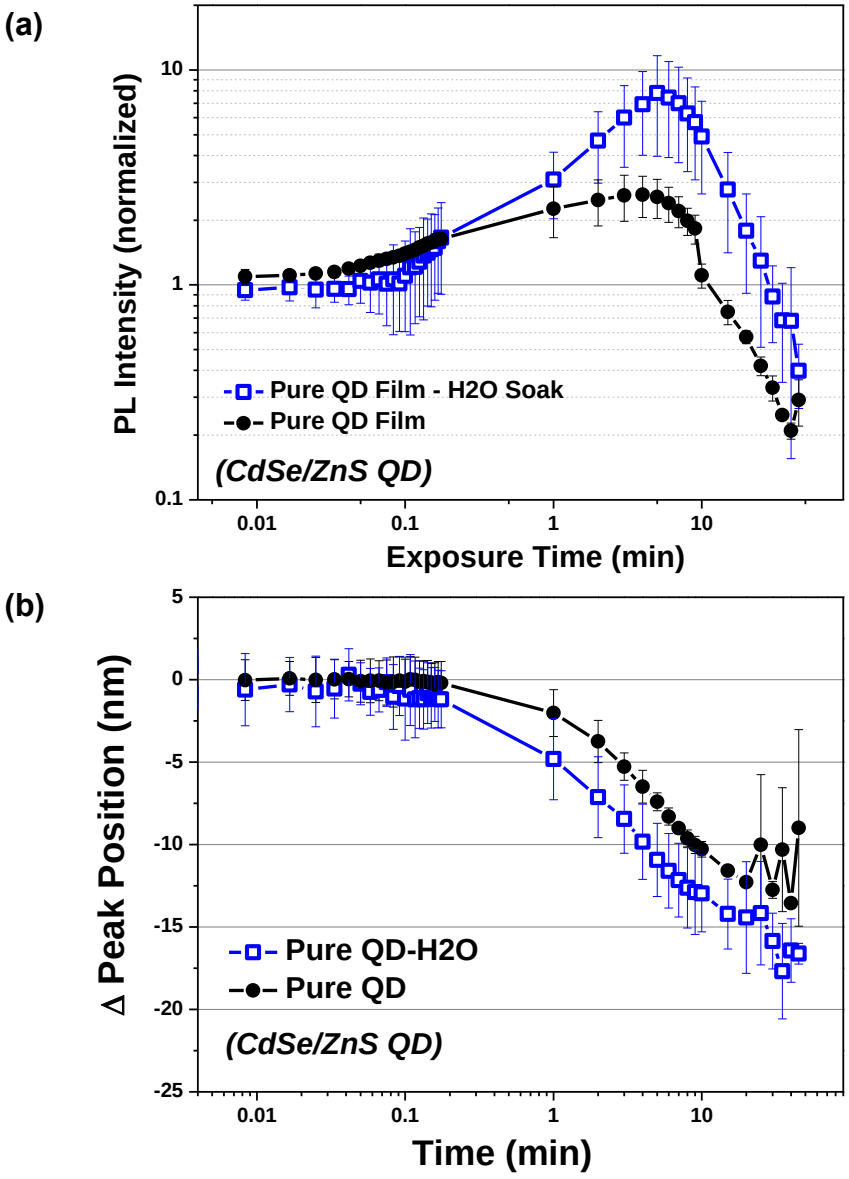

Figure 4.4: Evolution of the (a) PL intensity and (b) spectral shift ($\lambda_t - \lambda_0$) of pure CdSe/ZnS QD films in the dry and wet state upon continuous light exposure (450-490 nm).

Cyclic light exposure (light exposure-darkness-light exposure)

A variety of mechanisms have been presented in the literature to explain the recovery/enhancement of emission upon light exposure. These include irreversible options like photoinduced surface annealing/restructuring and photoactivation,[34,35] which remain upon removal of light. However, reversible mechanisms have also been presented including photoinduced surface transformation (via heat cycling),[40] adsorption/desorption of H_2O (via pressure cycling),[31] and light-activated rearrangement of surfactant molecules in solution (via light exposure cycling of QDs in solution).[38] However, so far, reversibility has either required the external modification of the surrounding environment or focused on QDs in solution (neither of which applies to this study). The identification of whether the recovery of PL intensity is irreversible of reversible will help identify the underlying mechanisms behind this behavior.

Therefore, the core/shell CdSe/ZnS QD-polymer films (which evolve very differently depending on whether they are in darkness or being exposed to light) were exposed to a cyclic light exposure regime to determine how the recovered PL state responds to a period of darkness (i.e. the removal of electromagnetic energy). A single cycle involves a period of light exposure, followed by a period of darkness, and then a resumption of light exposure. This sequence is designated an exposure-darkness-exposure cycle. Exposure-darkness-exposure cycling will determine whether the recovered PL state requires continuous light exposure to be maintained (indicating a reversible dynamic process that requires continuous input of energy to occur), or is not affected by the removal of light (indicating an irreversible process).

The results of a single exposure-darkness-exposure cycle are shown in **Figure 4.5a**. The QD-polymer film was continuously exposed to light for 10 minutes (~19 mW, 450-490 nm) during which a continuous recovery of emission occurred as expected. After 10 minutes of continuous light exposure, the light is removed for 20 minutes (a 20 min darkness step). Light exposure is then resumed (same intensity and wavelength) and a measurement is collected immediately to determine whether the period of darkness affected the PL recovery. It is clear from **Figure 4.5a** (images and spectral intensity data) that removal of light for 20 minutes leads to a drastic decrease in intensity of the recovered PL state (more than 85% reduction). Subsequent continuous light exposure leads to a gradual increase of PL intensity back to the initial recovered state (larger PL images of the film during this process provided in **Figure A.8**). Repeated exposure-darkness-exposure cycles at different times throughout the recovery process leads to a similar response (**Figure 4.5b**) (a 5 min darkness period).

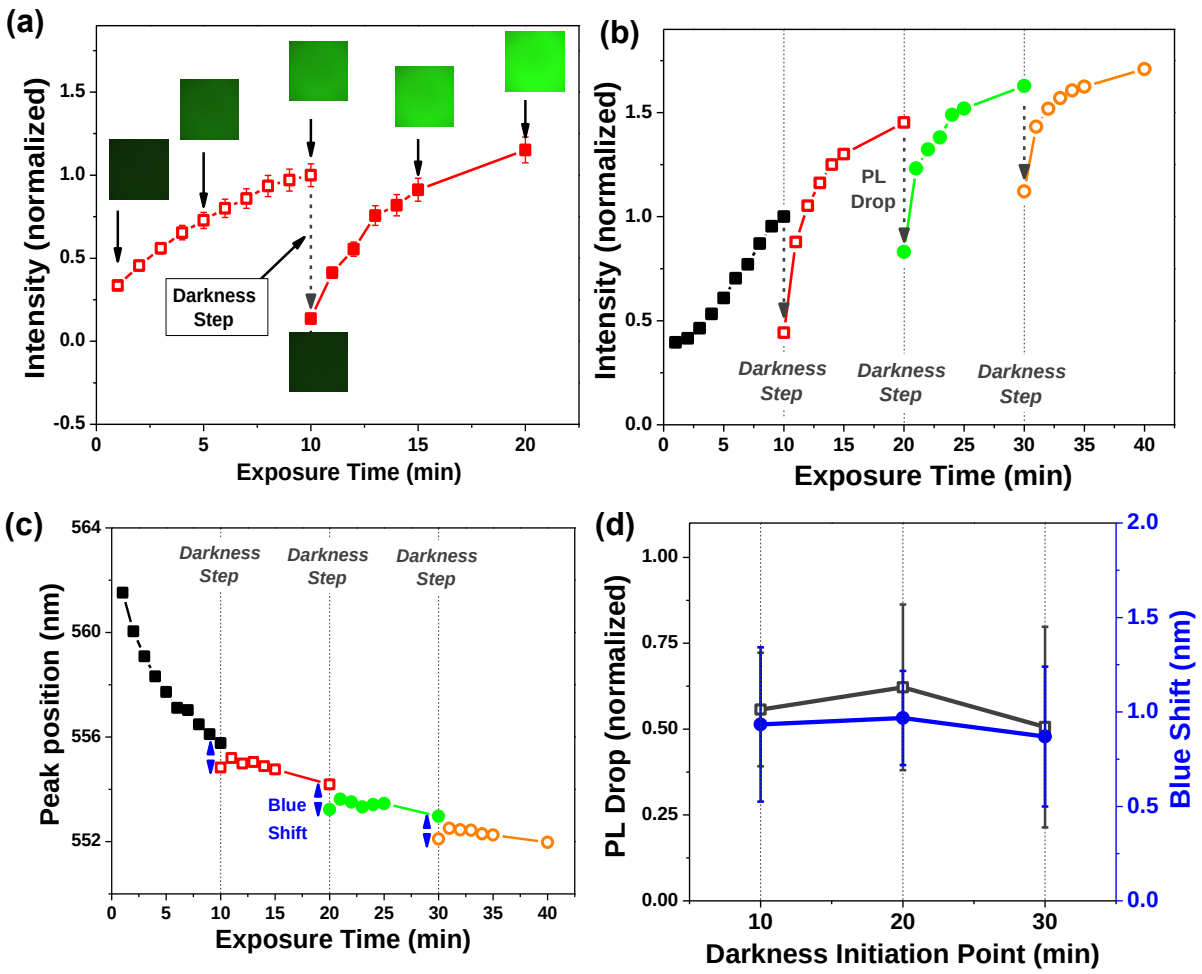

Figure 4.5: Examination of the charge-discharge effect observed upon light exposure and removal for a CdSe/ZnS QD-PMMA film. (a) The evolution of PL intensity during a exposure-darkness-exposure trial (darkness period: 20 minutes) (exposure: 450-490nm, ≈19mW). The (b) PL intensity and (c) PL spectral position during exposure-darkness-exposure cycling (5 min darkness periods). (d) The drop of PL intensity and spectral shift after each darkness period.

These results indicate that the PL recovery is a reversible process (or partially reversible). However, the spectral blue shift that occurred during the continuous exposure step does not

disappear during a darkness step (it actually continues to a small extent) (**Figure 4.5c**). The irreversibility indicates that the blue shifting of emission is not directly tied to the PL recovery mechanism, but more likely to the photooxidative decay process. The independence of PL recovery from spectral blue shifting agrees with the exposure study on QD solutions discussed earlier. The independence of the decay and recovery mechanisms is also supported by the fact that the intensity drop and blue shift that occur after a darkness step appear independent of when the darkness step is initiated over the recovery period (**Figure 4.5d**).

The PL intensity drop and blue shift are directly related to the duration of the darkness step, with longer darkness periods leading to greater intensity drops and blue shifts (**Figure 4.6**). The PL intensity drop follows an exponential trend (negative time constant) (**Figure 4.6c**). The blue shift also appears to scale with darkness time, matching closely with the blue shift observed in previous darkness studies (**Figure 4.6d**). It is interesting to note that a slight red-shift occurs within the first minute of resuming light exposure after a darkness step (**Figure A.9**), which could be due to an increase in the dielectric constant of the immediate surroundings.[38,53] Similar exposure-darkness-exposure studies were performed on thin shell core/graded shell CdSe/$Cd_{1-x}Zn_xSe_{1-y}S_y$ QDs. The behavior is similar to the CdSe/ZnS QDs, with the thin shell CdSe/$Cd_{1-x}Zn_xSe_{1-y}S_y$ QDs showing a discharge or the PL recovery that scales with time (**Figure 4.6c**)(**Figure A.10**). However, the amount of PL recovery discharge and degree of blue shifting were less extreme than the CdSe/ZnS QDs, presumably due to the thicker 1 nm graded $Cd_{1-x}Zn_xSe_{1-y}S_y$ shell. An opposite cycling approach can be performed as well (darkness-exposure-darkness cycle), which also leads to jumps of PL intensity and spectral position and corroborates the reversible PL recovery behavior just discussed (**Figure A.11**).

The results from the exposure-darkness-exposure experiments indicate a number of things: First, the results from the exposure-darkness-exposure experiments indicate that the recovery of PL intensity and spectral blue shift are not coupled, which means at least two mechanisms are present. Second, the process causing recovery of the PL intensity is (at least partially) reversible since it requires a constant input of electromagnetic energy to be maintained. Third, the mechanism underlying PL intensity recovery may be diffusion-based since it dissipates with time after light is removed. Finally, whatever mechanism underlies the PL intensity recovery process also leads to a small immediate red-shift upon resuming the input of electromagnetic energy (after a darkness period).

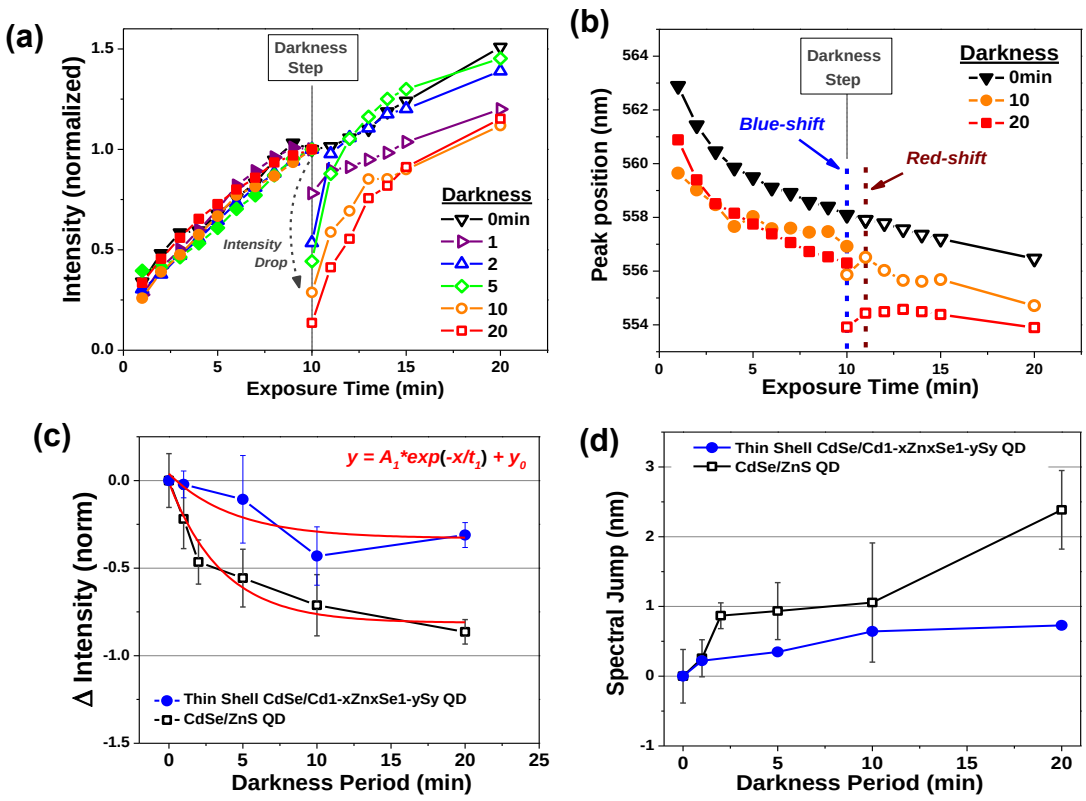

Figure 4.6: Examination of how periods of darkness affect the PL intensity of CdSe/ZnS core/shell QDs exposed to light (exposure: 450-490nm)(QD-PMMA films). (a) PL intensity decay dip and (b) spectral shift for different periods of darkness (10 min into light exposure regime). Magnitude of the (c) PL decay dip and (d) spectral shift versus the duration of the darkness step for the core/shell QD and thin core/graded shell QD.

4.3.5 Underlying mechanisms of dynamic changes

There are a variety of mechanisms that could be present in each of the QD architectures that could account for the corresponding evolution of PL emission.[35,38,54] A summary of the evolutionary

trends for the core, core/shell, and core/graded shell QD-polymer films under various external factors is provided in **Table 4.2**.

As noted previously, direct confirmation of physical (diameter) and material (surface oxidation/corrosion and H_2O passivation) changes to QDs via techniques like high-resolution TEM or NMR are very difficult due to the scale of the physical changes (<1 nm), the complexity in identifying different crystal structures over these small scales, the rate of the changes, and the reversibility of some mechanisms. Therefore, the following discussion of mechanisms is based on evidence from the evolution of optical emission under the various external factors, since these characteristics exhibit shifts that can be observed real time, with high accuracy, and require no cleaning steps that could modify the QD-polymer films.

The core/shell CdSe/ZnS QDs are the initial focus since they exhibit the most complex and interesting shifts of intensity and spectral position. To recap, the following phenomena need to be explained. First, continuous light exposure causes a decay-to-recovery behavior for intensity (**Figure 4.2b**). Second, the decay step is much faster than the recovery step (by an order of magnitude) **(Figure 4.2b)**. Third, the recovery phase occurs earlier for high exposure power **(Figure 4.3c)**. Fourth, there is a continuous blue shift throughout the decay-to-recovery evolution (most pronounced during the recovery step) (**Figure 4.2c)**. Fifth, the recovery of intensity is semi-reversible, requiring continuous light input to be maintained (**Figure 4.5a).**

Moreover, the blue shift is largely irreversible but the PL intensity recovery process can be "discharged" and "recharged" multiple times (**Figure 4.5c** and **4.5b, respectively)**. The

"discharge" of recovery upon darkness is proportional to the darkness period (**Figure 4.6c**). Finally, a small red-shift occurs immediately after light exposure during "intensity recharging" (**Figure 4.6b** and **4.6d**). Therefore, mechanisms need to be identified that alter quantum confinement and quantum yield, with one or more mechanisms being semi-reversible and one or more mechanisms being irreversible.

The core/shell CdSe/ZnS QDs likely have at least two competing mechanisms to explain all the phenomena. The continuous irreversible blue shift that occurs during light exposure indicates an increase of quantum confinement of the exciton caused by a reduction in size of the CdSe core. Size reduction is typically attributed to an irreversible photooxidation and corrosion of the QD surface, which is reasonable since the QD-polymer film is exposed to an environment with oxygen.[35] The rate of spectral blue shifting also slightly increases with exposure power which is expected since photons cause the process to occur.

Table 4.2: Evolution of the optical characteristics of the CdSe core, CdSe/ZnS core/shell, and CdSe/$Cd_{1-x}Zn_xSe_{1-y}S_y$ core/graded shell QD-polymer films in a dark environment (top frame) and under continuous light exposure (middle frame) (blue light: 450-490 nm). PL evolution of CdSe/ZnS QD-polymer film under cyclic light exposure (exposure-darkness-exposure) (bottom frame). The proposed mechanisms causing this behavior are noted as well.

Darkness (Continuous)				
Design	**Composition**	**Intensity**	**Peak Position**	**Proposed Mechanism**
Core	CdSe	Decay *(↓96%)*	Blue shift *(5nm)*	Oxidation
Core/shell	CdSe/ZnS	Decay *(↓68%)*	Red shift *(1nm)*	Oxidation
Core/thick graded shell	CdSe/Cd1-xZnxSe1-ySy	Stable *(±10%)*	Stable *(±0.5nm)*	NA

Light Exposure (continuous)				
Design	**Composition**	**Intensity**	**Peak Position**	**Proposed Mechanism**
Core	CdSe	Decay *(↓98%)*	Blue shift *(16nm)*	Oxidation, photooxidation
Core/shell	CdSe/ZnS	Decay-to-recovery	Blue shift *(16nm)*	Photooxidation, light-mediated H_2O passivation
Core/thin graded shell	CdSe/Cd1-xZnxSe1-ySy	Enhancement *(↑300%)*	Red shift *(2.5nm)*	Light-mediated H_2O passivation
Core/thick graded shell	CdSe/Cd1-xZnxSe1-ySy	Stable *(±8%)*	Stable *(±0.5nm)*	NA

Cyclic Light Exposure (exposure-dark-exposure)				
Design	**Composition**	**Intensity**	**Peak Position**	**Proposed Mechanism**
Core/shell CdSe/ZnS	Initial Light Exposure	Recovery	Blue shift *(Varies)*	Photooxidation, light-mediated H_2O passivation
	Darkness step	Decay & discharge of recovery	Blue shift *(1nm)*	Oxidation & discharge of recovery mechanism
	Subsequent Light Exposure	Recovery	Initial red shift *(1nm)*, Blue shift *(Varies)*	Photooxidation, light-mediated H_2O passivation

Photooxidation and corrosion of the ZnS shell, which occurs before and concurrently with oxidation of the CdSe core, can explain the fast decay of intensity that occurs immediately upon light exposure. Corrosion of the ZnS shell reduces surface passivation of the CdSe core (where the exciton is located) which decreases quantum yield.[15,17,47] The ZnS shell is in a meta-stable state before illumination due to the large (12%) crystal lattice mismatch between CdSe and ZnS which causes strain to build up at the CdSe/ZnS interface and within the ZnS shell.[17,48] Degradation of the ZnS shell during photooxidation leads to the formation of physical defects as the ZnS shell relaxes that act as nonradiative recombination pathways.[35,36]

This conclusion is supported by the fact that aged CdSe/ZnS QDs (6 months) have a significantly less pronounced initial high quantum yield state and blue shifted emission peak compared to newly synthesized QDs (**Figure A.12**). The disappearance of the initial meta-stable high QY state is caused by slow oxidation and degradation of the ZnS shell while the QDs are stored in solution (air environment). This is bolstered by the fact that aged QDs (with more surface defects) undergo much more recovery upon light exposure, presumably due to there being more defects on the CdSe surface that are temporarily passivated. Decay of QD PL intensity has also been attributed to heating,[54] which in this case could occur due to the continuous light exposure. However, this is unlikely since the area of the QD-polymer film exposed to light shows no measurable increase of temperature over a period of 45 minutes ($\Delta T < 1°C$) (**see Experimental Methods**).

A number of mechanisms have been presented in the literature to explain the reversible recovery of PL intensity such as photo-induced QD surface transformation (caused by heat cycling),[40] light-activated rearrangement of surfactant molecules (caused by light exposure cycling),[38] and light-

mediated adsorption/desorption of H_2O (caused by pressure cycling).[31] Semi-reversible intensity recovery attributed to QD surface transformation (CdSe/ZnS QD solutions and films) is unlikely because it requires deliberate heating above room temperature and localized heating of the QD-polymer film was ruled out in this system. Light-activated rearrangement of ligands is also an unlikely mechanism since this effect is observed in core/shell CdSe/ZnS QD solutions where ligand dynamics are not hindered.[38]

However, the system in this study is a solid QD-polymer film, so the solid polymer matrix surrounding the QDs should hamper the rearrangement of ligands on, and their diffusion to/from, the QD surface. Furthermore, if rearrangement of ligands is the underlying reason for the reversible nature of PL recovery, it is reasonable to assume that the matrix would play an important role. However, PL recovery was observed in two different polymers (poly(methyl methacrylate) and polystyrene) which should interact with the QD ligand differently due to the different side groups.

A general understanding of the physical evolution of each type of QD under light exposure is provided below. When the plain CdSe core QD is exposed to light it experiences surface oxidation and degradation which explains the decay of its intensity and blue shift of its emission. However, it is interesting that the plain CdSe core QDs do not undergo an eventual PL intensity recovery for a number of reasons. First, previous studies have shown that plain CdSe core QDs can undergo PL recovery upon light exposure.[31] Second, the plain CdSe core QDs do not have a protective ZnS shell so they should also interact with surrounding water and experience the light-H_2O passivation mechanism. In this case, the absence of PL recovery could be do there being no

protective shell, which allows for immediate (and eventually massive) degradation of the CdSe core surface due to photooxidation and corrosion. It seems the damage to the CdSe core overwhelms (or hinders) the light-H_2O passivation mechanism. However, it is possible in this case that PL recovery is occurring but that the oxidation and degradation of the CdSe core is so profound that it overwhelms the PL recovery.

For the CdSe/ZnS core/shell QDs, we suggest that oxidation/degradation of the ZnS shell combined with light-mediated adsorption/desorption of H_2O serves as the mechanism behind PL recovery and its reversible behavior. During QD encapsulation in the polymer matrix (spin-casting), water is likely trapped in the QD-polymer film at the QD surface. When light is incident on the CdSe/ZnS QDs, it leads to oxidation/degradation of the 0.5 nm thick ZnS shell and some degradation of the CdSe core, leading to the initial PL decay behavior and blue shifting. However, the degradation of the ZnS shell is offset by H_2O mediated passivation (PL recovery behavior). Because light and H_2O are required for the PL recovery to occur, the PL recovery dissipates when light is removed. However, the disappearance of PL is not immediate, which suggests that the underlying recovery mechanism is due to a chemical reaction at the QD surface that continues briefly after the light is removed. PL recovery can be reinitiated upon light exposure because the H_2O surrounding the QD is encased by the surrounding polymer matrix. The irreversible spectral blue shift can also be explained by this light-H_2O mechanism since the ZnS shell is irreversibly oxidized and corroded, which allows the CdSe QD to also eventually irreversible oxidize and corrode.

In the case of the core/thin graded shell CdSe/$Cd_{1-x}Zn_xSe_{1-y}S_y$ QDs, the graded shell does undergo photooxidation and corrosion upon light exposure. However, the gradient composition of the $Cd_{1-x}Zn_xSe_{1-y}S_y$ shell reduces the radial lattice mismatch between the CdSe core and outer ZnS shell, making the core/graded shell QDs thermodynamically stable even when outer shell surface oxidation occurs. Furthermore, the shell is 1 nm thick, double that of the ZnS shell for the CdSe/ZnS QDs, which prevents the CdSe core from being oxidized and corroded. Therefore, no PL decay is observed and light-mediated adsorption/desorption of H_2O leads to an immediate photoenhancement.

The stable optical properties of the core/thick graded shell CdSe/$Cd_{1-x}Zn_xSe_{1-y}S_y$ QDs support the outlined mechanisms for the core CdSe and core/shell CdSe/ZnS QDs. AS with the thin shell version, upon light exposure the core/thick graded shell CdSe/$Cd_{1-x}Zn_xSe_{1-y}S_y$ QDs likely undergo some degree of surface oxidation and degradation. However, the graded shell is very thick (2.7 nm) which effectively isolates the CdSe core from any changes on the shell surface, preventing blue shifting, PL decay, and PL recovery.

4.4 Conclusions

The evolution of PL from core, core/shell, and core/graded shell green-emitting QDs in QD-polymer films was examined under different light exposure conditions in environments commonly experienced by QD systems. It was shown that the compositional profile/shell thickness of QDs (core, core/shell, core/graded shell) significantly affects how the optical characteristics evolve, with very distinct changes occurring for different QD types. For example, decreasing, increasing,

and stable intensity were all observed, which could be reversible or irreversible depending on QD type. In addition, spectral blue shifting was observed in some instances and not in others.

The distinct response of each type of QD arises from how the core (and shell) material interacts with oxygen, H_2O, and light. For a core CdSe QD, the material confining the exciton is in immediate contact with its surroundings, and thus responds quickly and strongly to external stimuli. However, thin shell QDs (including core/shell CdSe/ZnS QD and thin graded shell $CdSe/Cd_{1-x}Zn_xSe_{1-y}S_y$ QD) have an inorganic barrier that can (initially) isolate the core from the environment but that can eventually degrade leading to competing physical mechanisms and interesting optical behavior. Finally, a thick graded shell in core/graded shell $CdSe/Cd_{1-x}Zn_xSe_{1-y}S_y$ QD provides exceptional protection for the CdSe core, due to the shell thickness and thermodynamic considerations, which leads to very stable optical properties. These results clearly demonstrate the importance of proper compositional design for the QD depending on the requirements of the stable or dynamic photonic system.

These experiments are one of the first comprehensive studies on how QD architecture relates to emission evolution under various external influences, and they provide evidence of the chemical and physical changes underlying this evolution. For example, we are able to dispel the common notion that depositing an inorganic shell on a core QD (to make a core/shell QD) ensures strong isolation from the environment. These results provide significant insight into the various mechanisms at play in QDs of different compositional profile under the conditions often experienced by QD photonic systems. Furthermore, it was demonstrated that both reversible and irreversible mechanisms can be active within a QD at the same time, which can lead to a

decoupling of optical properties that might not be anticipated (reversible intensity changes versus irreversible spectral shifts). This work may serve as a general framework for evaluating quantum dots in future studies, as well as help identify the appropriate QD composition profile for a specific application.

We suggest these results (and the strategies to obtain them) are significant because they are relevant to the majority of scientific studies and technological applications that make use of the emission from QDs. Furthermore, these results are critical to consider when making assumptions about the stability of QD emission (spectral position, FWHM, and intensity). This includes characterization techniques where stable emission is required to obtain meaningful results (for example, the variable strip length method or fluorescence lifetime imaging), and photonic systems where long lifetimes are desired (e.g., QD displays, LEDs, and lasers). Finally, scenarios exist where unstable emission is desired (or required) for the device to function (for example, sensors for light, oxygen, water).

Future studies should examine how to tune the decay-to-recovery behavior of intensity in core/shell QDs by controlling the relevant strength of the decay and recovery emissions. This could include changing shell thickness or interfacial defect concentration. Furthermore, the investigations into QDs with lower (red-emitting) and higher (blue-emitting) bandgaps should be conducted to see if similar relationships exist.

4.5 References (Chapter 4)

[1] Medintz, I.L.; Uyeda, H.T.; Goldman, E.R.; Mattoussi, H., *Nat. Mater.* **2005,** *4,* 435.

[2] Adachi, M.M.; Fan, F.; Sellan, D.P.; Hoogland, S.; Voznyy, O.; Houtepen, A.J.; Parrish, K.D.; Kanjanaboos, P.; Malen, J.A.; Sargent, E.H., *Nat. Commun.* **2015,** *6,* 8694.

[3] Lin, C.H.; Lafalce, E.; Jung, J.; Smith, M.J.; Malak, S.T.; Aryal, S.; Yoon, Y.J.; Zhai, Y.; Lin, Z.; Vardeny, Z.V.; Tsukruk, V.V., *ACS Photonics* **2016,** *3,* 647.

[4] Kim, T.-H.; Cho, K.-S.; Lee, E.K.; Lee, S.J.; Chae, J.; Kim, J.W.; Kim, D.H.; Kwon, J.-Y.; Amaratunga, G.; Lee, S.Y.; Choi, B.L.; Kuk, Y.; Kim, J.M.; Kim, K., *Nat. Photonics* **2011,** *5,* 176.

[5] Kim, B.H.; Onses, M.S.; Lim, J.B.; Nam, S.; Oh, N.; Kim, H.; Yu, K.J.; Lee, J. W.; Kim, J.-H.; Kang, S.-K.; Lee, C.H.; Lee, J.; Shin, J.H.; Kim, N.H.; Leal, C.; Shim, M.; Rogers, J.A., *Nano Lett.* **2015,** *15,* 969.

[6] Gong, X.; Yang, Z.; Walters, G.; Comin, R.; Ning, Z.; Beauregard, E.; Adinolfi, V.; Voznyy, O.; Sargent, E.H., *Nat. Photonics* **2016,** *10,* 253.

[7] Mashford, B.S.; Stevenson, M.; Popovic, Z.; Hamilton, C.; Zhou, Z.Q.; Breen, C.; Steckel, J.; Bulovic, V.; Bawendi, M.; Coe-Sullivan, S.; Kazlas, P.T., *Nat. Photonics* **2013,** *7,* 407.

[8] Carey, G.H.; Abdelhady, A.L.; Ning, Z.J.; Thon, S.M.; Bakr, O.M.; Sargent, E.H., *Chem. Rev.* **2015,** *115,* 12732.

[9] Zhao, L.; Lin**,** Z., *Adv. Mater.* **2012, *24,*** 4353.

[10] He, M.; Qiu, F.; Lin**,** Z., *J. Phys. Chem. Lett.* ***2013, 4,*** 1788.

[11] Jung, J.; Yoon, Y.; He, M.; Lin**,** Z., *J. Polym. Sci.: Polym. Phys.* ***2014, 52,*** 1641.

[12] Zhang, L.; Chen, C.; Li, W.J.; Gao, G.H.; Gong, P.; Cai, L.T., *ACS Appl. Mater. & Interf.* **2016,** *8,* 13187.

[13] Qu, L.H.; Peng, X.G., *J. Amer. Chem. Soc.* **2002,** *124,* 2049.

[14] Qu, L.H.; Peng, Z.A.; Peng, X.G., *Nano Lett.* **2001,** *1,* 333.

[15] Dabbousi, B.O.; RodriguezViejo, J.; Mikulec, F.V.; Heine, J.R.; Mattoussi, H.; Ober, R.; Jensen, K.F.; Bawendi, M.G., *J. Phys. Chem. B* **1997,** *101,* 9463.

[16] Beane, G.A.; Gong, K.; Kelley, D.F., *ACS Nano* **2016,** *10,* 3755.

[17] Jung, J.; Lin, C.H.; Yoon, Y.J.; Malak, S.T.; Zhai, Y.; Thomas, E.L.; Vardeny, V.; Tsukruk, V.V.; Lin, Z., *Angewandte Chemie Intern. Ed.* **2016,** *55,* 5071.

[18] Bae, W.K.; Park, Y.S.; Lim, J.; Lee, D.; Padilha, L.A.; McDaniel, H.; Robel, I.; Lee, C.; Pietryga, J.M.; Klimov, V.I., *Nat. Commun.* **2013,** *4,* 2661.

[19] Walsh, B.R.; Saari, J.I.; Krause, M.M.; Nick, R.; Coe-Sullivan, S.; Kambhampati, P., *J. Phys. Chem. C* **2015,** *119,* 16383.

[20] Cooney, R.R.; Sewall, S.L.; Sagar, D.M.; Kambhampati, P., *J. Chem. Phys.* **2009,** *131,* 164706.

[21] Shaklee, K.L.; Leheny, R.F., *Appl. Phys. Lett.* **1971,** *18,* 475.

[22] Liang, X.W.; Wang, H.L.; Zhu, Y.; Zhang, R.; Cogger, V.C.; Liu, X.; Xu, Z.P.; Grice, J.E.; Roberts, M.S., *ACS Nano* **2016,** *10,* 387.

[23] Rizzo, A.; Mazzeo, M.; Palumbo, M.; Lerario, G.; D'Amone, S.; Cingolani, R.; Gigli, G., *Adv. Mater.* **2008,** *20,* 1886.

[24] Dang, C.; Lee, J.; Breen, C.; Steckel, J.S.; Coe-Sullivan, S.; Nurmikko, A., *Nat. Nanotech.* **2012,** *7,* 335.

[25] Malak, S.T.; Jung, J.; Yoon, Y.J.; Smith, M.J.; Lin, C.H.; Lin, Z.; Tsukruk, V.V., *Adv. Opt. Mater.* **2016,** *4,* 608.

[26] Zucolotto, V.; Gattas-Asfura, K.M.; Tumolo, T.; Perinotto, A.C.; Antunes, P.A.; Constantino, C.J.L.; Baptista, M.S.; Leblanc, R.M.; Oliveira, O.N., *Appl. Surf. Sci.* **2005,** *246,* 397.

[27] Zhang, S.C.; Yu, J.H.; Li, X.G.; Tian, W.H., *Nanotechnology* **2004,** *15,* 1108.

[28] Zimnitsky, D.; Jiang, C.; Xu, J.; Lin, Z.; Tsukruk, V.V., *Langmuir* **2007,** *23,* 4509.

[29] Komarala, V.K.; Rakovich, Y.P.; Bradley, A.L.; Byrne, S.; Corr, S.A.; Gun'ko, Y.K., *Nanotechnology* **2006,** *17,* 4117.

[30] Zimnitsky, D.; Jiang, C.; Xu, J.; Lin, Z.; Zhang, L.; Tsukruk, V.V., *Langmuir* **2007,** *23,* 10176.

[31] Cordero, S.R.; Carson, P.J.; Estabrook, R.A.; Strouse, G.F.; Buratto, S.K., *J. Phys. Chem. B* **2000,** *104,* 12137.

[32] Munro, A.M.; Jen-La Plante, I.; Ng, M.S.; Ginger, D.S., *J. Phys. Chem. C* **2007**, *111,* 6220.

[33] Lee, W.; Kim, H.; Jung, D.-R.; Kim, J.; Nahm, C.; Lee, J.; Kang, S.; Lee, B.; Park, B., *Nanoscale Res. Lett.* **2012,** *7,* 672.

[34] Wang, Y.; Tang, Z.; Correa-Duarte, M.A.; Pastoriza-Santos, I.; Giersig, M.; Kotov, N.A.; Liz-Marzán, L.M., *J. Phys. Chem. B* **2004,** *108,* 15461.

[35] Nazzal, A.Y.; Wang, X.Y.; Qu, L.H.; Yu, W.; Wang, Y.J.; Peng, X.G.; Xiao, M., *J. Phys. Chem. B* **2004,** *108,* 5507.

[36] van Sark, W.; Frederix, P.; Van den Heuvel, D.J.; Gerritsen, H.C.; Bol, A.A.; van Lingen, J.N.J.; Donega, C.D.; Meijerink, A., *J. Phys. Chem. B* **2001,** *105,* 8281.

[37] Zhang, H.; Zhou, Z.; Yang, B.; Gao, M.Y., *J. Phys. Chem. B* **2003,** *107,* 8.

[38] Jones, M.; Nedeljkovic, J.; Ellingson, R.J.; Nozik, A.J.; Rumbles, G., *J. Phys. Chem. B* **2003,** *107,* 11346.

[39] van Sark, W.; Frederix, P.; Bol, A.A.; Gerritsen, H.C.; Meijerink, A., *ChemPhysChem* **2002,** *3,* 871.

[40] Hess, B.C.; Okhrimenko, I.G.; Davis, R.C.; Stevens, B.C.; Schulzke, Q.A.; Wright, K.C.; Bass, C.D.; Evans, C.D.; Summers, S.L., *Phys. Rev. Lett.* **2001,** *86,* 3132.

[41] Oda, M.; Shen, M.Y.; Saito, M.; Goto, T., *J. Luminescence* **2000,** *87–89,* 469.

[42] Shinya, M.; Ceco Danov, D.; Soichiro, S.; Yukio, Y., *Jap. J. Appl. Phys.* **2000,** *39,* 4006.

[43] J.A. Woollam Co. Inc. "Guide to using WVase32." Ch.2, A short course in ellipsometry. **2010.**

[44] Peng, Z.A.; Peng, X.G., *J. Amer. Chem. Soc.* **2001,** *123,* 183.

[45] Bae, W.K.; Char, K.; Hur, H.; Lee, S., *Chem. Mater.* **2008,** *20,* 531.

[46] Bae, W.K.; Nam, M.K.; Char, K.; Lee, S., *Chem. Mater.* **2008,** *20*, 5307.

[47] Qin, H.Y.; Niu, Y.; Meng, R.Y.; Lin, X.; Lai, R.C.; Fang, W.; Peng, X.G., *J. Amer. Chem. Soc.* **2014,** *136,* 179.

[48] Xie, R.; Kolb, U.; Li, J.; Basché, T.; Mews, A., *J. Amer. Chem. Soc.* **2005,** *127,* 7480.

[49] Choi, D.; Pyo, J.Y.; Kim, Y.; Jang, D.J., *J. Mater. Chem. C* **2015,** *3,* 3286.

[50] Smith, A.M.; Nie, S., *Acc. Chem. Res.* **2010,** *43,* 190.

[51] Smith, A.M.; Mohs, A.M.; Nie, S., *Nat. Nanotech.* **2009,** *4,* 56.

[52] Yu, P.; Cardona, M., Fundamentals of semiconductors, physics and materials properties. *4th Ed. Springer,* **2010.**

[53] Franceschetti, A.; Zunger, A., *Phys. Rev. B* **2000,** *62,* 2614.

[54] Valerini, D.; Creti, A.; Lomascolo, M.; Manna, L.; Cingolani, R.; Anni, M., *Phys. Rev. B* **2005,** *71,* 235409.

CHAPTER 5. ROBUST, UNIFORM, AND HIGHLY EMISSIVE QUANTUM DOT–POLYMER FILMS AND PATTERNS USING THIOL–ENE CHEMISTRY

5.1 Introduction

Addition of quantum dots to polymer nanocomposites offers significantly improved function for QD-containing nanocomposites, being able to take advantage of the unique optical and electrical properties of QDs[1] while retaining the versatile bulk mechanical properties of the polymeric matrices.[2] Perfected synthetic techniques have afforded precise control over the QD structure, resulting in superior electronic and optical properties.[3] On the other hand, appropriate monomer selection offers complete control over the underlying polymer matrix and tailorable mechanical properties.[4] The precise engineering of the QD structure allows for increased quantum yield,[5] extended photoluminescence lifetimes,[6] and attenuated effects from non-radiative decay mechanisms.[7] This has led to the utilization of QDs in areas spanning photovoltaics,[8] solar concentrators,[9] gain media,[10] LEDs,[11] photonics,[12] and next generation semiconductor lasers.[13] Encapsulation of QDs in a polymer matrix with uniform distribution and suppressed aggregation, while still remaining challenging, has been demonstrated to not only provide added benefits from the bulk properties of the polymer but also improve QD optical properties.[14] Potential applications of these nanocomposites include advanced photonic parity-time symmetric systems including Bragg reflectors[15] and coupled waveguides,[16] that can display phenomenon like unidirectional invisibility.[17]

Photonic systems, in particular, can benefit greatly from the tunable optical properties of QDs, exhibiting exceptionally high optical gains (a requirement of PT systems) as well as the tailored mechanical properties provided by a polymer matrix, facilitating robust backbones and applicability to a host of planar and non-planar substrates. Similar systems have been developed for a subfield of photonics, optoelectronic systems, in which encapsulation of conductive wires in elastomeric matrices imparts stability, flexibility, and stretchability.[18] The incorporation of QDs into polymer matrices is a particularly important step because it allows for the fabrication of stable and uniform functional materials with low optical losses, offering the ability to vary thickness (submicron-to–microns), relative ease in processing, as well as the controlled incorporation of significant quantities of QD gain medium into a matrix for tunable emission strength.

However, the preparation of dispersed QD-polymer composites is challenging, primarily relating to large-scale phase separation, which results in QD aggregation thus high optical scattering and losses. Recent efforts to develop QD-polymer composites have seen limited success since simple mixing of the two components typically leads to significant QD aggregation and phase separation.[19,20] Wang et. al. recently developed microbubble lasers via simple drop-casting of QD-poly (methyl methacrylate) (PMMA) solutions. Loadings above 50% were achieved however, this methodology is not easily adaptable to patterning, as structures are limited to large shapes.[21] Additionally, although more complex reaction schemes can compromise the valuable properties of the QDs, they have only resulted in inclusion of QDs at very low weight percentages.[22] Specifically, aggregation of QDs typically leads to non-radiative decay mechanisms such as quenching [23] (i.e. Förster resonance energy transfer) as well as optical losses from scattering.[24] In addition, while QD photopatterns of low resolution have been generated utilizing TEM grids as a

mask, a clear scalable approach that allows for the fabrication of high resolution patterns in highly loaded QD-composites have not yet been developed.[25] Ehlert et al. demonstrated QD-polymer composites by grafting polymer brushes onto the QD surface and subsequently mixing with like polymers.[26] A proposed method for combating large QD aggregation and phase separation would be the utilization of a fast crosslinking mechanism that takes place on time scales faster than phase separation of relatively large nanoparticles, thereby minimizing the tendency of QDs to phase separate during film formation. Furthermore, it has been suggested that cross-linking during polymerization can reduce aggregation and energy transfer mechanisms, resulting in enhanced emission in comparison to the non-crosslinked counterparts.[27,28]

Thiol-ene photopolymerization has proven to be a versatile reaction that produces crosslinked networks, [29] occurs rapidly, is highly efficient,[30,31] and is largely insensitive to ambient environments. [29, 32] Given the weak nature of the sulfur-hydrogen bond, a free-radical initiating species will abstract a hydrogen from the thiol precursor. Subsequently, the thiyl radical will efficiently attack an electron deficient terminal carbon-carbon double bond, forming a cross-linked network similar to the vulcanization of rubber.[29,32] The crosslink density of thiol-ene photopolymerization can be readily tailored by formulation, enabling tunability of the thermal and mechanical properties of host matrix,[33,34] leading to potentially robust and flexible networks with uniform distribution of components. Moreover, thiol-ene chemistries come in a variety of mixtures depending on the desired properties, including readily available commercial thiol-ene adhesive mixtures.[35] Typical Norland based adhesives consists of a tri-ene (i.e. 1,3,5-Triallyl-1,3,5-triazine-2,4,6(1H,3H,5H)-trione) and a multifunctional mercapto-ester (i.e. pentaerythritol tetrakis(3-mercaptopropionate)), with a urethane based component, and a benzophenone photoinitiator.[35]

The thiol-ene mechanism has been utilized as a "click" reaction to generate nanoparticle-polymer composites via a "graft from" mechanism where the nanoparticle ligands serve as anchoring sites that participate in the step growth thiol-ene polymerization, producing various cross-linked polymer composites in which the nanoparticles can serve as crosslink sites. [35,36,37,38] For instance, Lü et al. grafted thiolated styrene and phenol onto ZnS QDs, followed by a UV initiated free radical polymerization to form a poly(urethane-methacrylate macromer) composite in which QDs were immobilized in the polymer network, taking advantage of thiol-ene based click chemistry.[39] Similarly, Kim et al. functionalized the surface of QDs with a complex norbornene compound and generated a QD – polymer composite by photopolymerizing the tethered –ene with a multifunctional thiol, however no significant loading was achieved, furthermore micron scale patterns were generated with loading not exceeding 0.2 wt %.[22]

In this work, we explore the photopolymerization of thiol-ene chemistries in the presence of butylamine-capped CdSe/$Cd_{1-x}Zn_xSe_{1-y}S_y$ quantum dots (BA-QDs) to generate highly loaded nanocomposite films and patterns with uniform distribution of QDs and minimal aggregation. We show that the use of crosslinking photopolymerization and QDs with shorter ligands, containing no internal alkene bonds, makes possible the fabrication of homogeneous nanocomposites suitable for optical applications as the polymer network encapsulates the QDs while maintaining strong photoluminescence with minimal optical losses from scattering. While photoluminecense properties typically diminish following ligand exchange, it has been shown in previous work that ligand exchange from oleic acid (OA) to butylamine only lowers the QY from 50% to ~30%, with

some batch to bath variation, maintaining these QDs as strong candidates for high optical gain materials. [40] We suggest that shorter ligands better facilitate thiol-ene crosslinking, as OA possesses an internal alkene, which could potentially interfere with the thiol and –ene crosslinking reaction, as it disrupts the initial stoichiometry. Furthermore, initial experiments utilizing oleic acid showed significant amounts of hazing, suggesting large-scale phase separation.

This approach represents a significant departure from previous attempts in that in this work a chemically and mechanically robust network with tunable properties can be fabricated. BA-QDs are encapsulated within the cross-linked polymer network and phase separation is minimized by utilizing shorter ligands and taking advantage of the rapid photopolymerization process. Furthermore, the addition of QDs, given their high typically high quantum yields, alters the UV reaction in such a way that allows for controlled properties as a function of UV irradiation time, facilitating robust, flexible, and highly emissive composites. This approach results in fabricating a well dispersed, highly loaded polymer-QD composite networks which are robust and solvent-resistant for prospective applications in photonics, waveguides, and QD lasers that are chemically inert and optically stable (intensity and spectral position).

5.2 Experimental Methods

Chemicals and Materials. Norland Optical Adhesive 63 (NOA63) was obtained from Edmund optics. All chemicals were used as received.

Film Preparation. QD films were fabricated by first mixing a QD chloroform solution of a known quantity with an equal volume 10 wt% NOA63 solution in Chloroform and spin-casting at 3000 rpm for 1 min. The film thickness ranged from 250 to 400. Silicon, with a 290− 295 nm thick SiO2 surface layer, was used as a substrate. Films were polymerized using Omnicure X-Cite Series 120Q Mercury vapor arc lamp.

Real Time Fourier Transform Infrared Spectroscopy. FTIR measurements of NOA63 and NOA-BAQD composites were conducted using a Nicolet iS50 FTIR in accordance with a procedure previously described.[54] A known quantity of sample was deposited on a NaCl crystal and dried prior to each run for transmission mode. FTIR spectra were collected in the range of 3200−2450 cm^{-1} with a resolution 8 cm^{-1}. Series spectra were collected every half second. Polymerizations were initiated using a LED lamp (OmniCure LX 500) with a 365 nm wavelength. Samples were irradiated until polymerization was complete, indicated by very negligible change in peaks observed. During each reaction the absorbance peaks corresponding to the vinyl group (3080 cm^{-1}) and thiol group (2570 cm^{-1}) were observed as a function of time. The typical allyl peak (1646 cm^{-1}) was not monitored because the intensity was too low. The conversion ratio was taken as the peak area at time t to the peak area before polymerization began. Experiments were conducted in ambient conditions.

Fabrication of QD Patterns. Briefly, a known quantity of QDs was added to a 2 wt% NOA63 solution in chloroform. Typically a $1cm^2$ cut out of a PDMS stamp was placed on a silicon substrate and a small aliquot of the NOA-BAQD solution was injected next to the stamp to allow capillary forces to pull solution in or the solution was injected on top of the stamp followed by placing of the stamp on the substrate, in accordance with a procedure previously described. Samples were polymerized using an Omnicure X-Cite Series 120Q Mercury vapor arc lamp.

Differential Scanning Calorimetry. The heat flow as a function of temperature of the DIAH-tethered QD sample was measured using a TA Instruments DSC (differential scanning calorimeter) Q200 with hermitically sealed aluminum pans. Samples were analyzed from −50 to 200 °C using a 10 °C/min temperature profile under a constant flow of argon.

Thermogravimetric Analysis. The sample weight as a function of temperature of the composite QD samples was measured using a TA Instruments TGA (thermogravimetric analysis) Q50 with a 100 μL platinum pan. Samples were analyzed from RT to 600 °C using a 10 °C/min temperature profile under a constant flow of argon.

Force−Distance Measurements. Force−distance measurements were performed to analyze the mechanical properties of NOA-BAQD composites, which were freely suspended on the copper-TEM grids with circular aperture size of 10 μm. The deflection sensitivity of the AFM tip was obtained by conducting force−distance experiment on a sapphire substrate. The spring constant of the AFM tip was determined by using the thermal tune method.[41] The radius of the AFM tip was obtained by deconvoluting the images on 20 nm gold nanoparticles.[43] The force−distance curves were obtained with various ramp rates of 0.2, 0.4, 0.6, 0.8, 1.0, 2.0, 4.0, 6.5, and 10 Hz.

X-Ray Diffraction. X-ray diffraction measurements were performed on a X'Pert PRO Alpha-1 diffractometer (PANalytical) using the Cu-$K_{\alpha 1}$ component.

5.3 Results and Discussion

Norland Optical Adhesive 63 utilized in this study consists of a tetrafunctional thiol in a near 1:1 molar ratio with a trifunctional alkene, as well as a photoinitiator.[29] Scheme 5.1 shows the routes which are utilized for fabricating NOA63/BA-QD QD-polymer composites and thiol-ene reaction. As discussed previously, and illustrated in Scheme 1b, upon irradiation with UV light, a free radical is generated on the sulfur, leading to the thiyl readily attacking carbon-carbon double bonds, preferably terminal ones, causing the polymer reaction to proceed very similar to that of a

Scheme 5.1: Schematic showing (a) proposed mechanism for fabrication of thiolene/QD composite and (b) initiation and propagation of thiol-ene

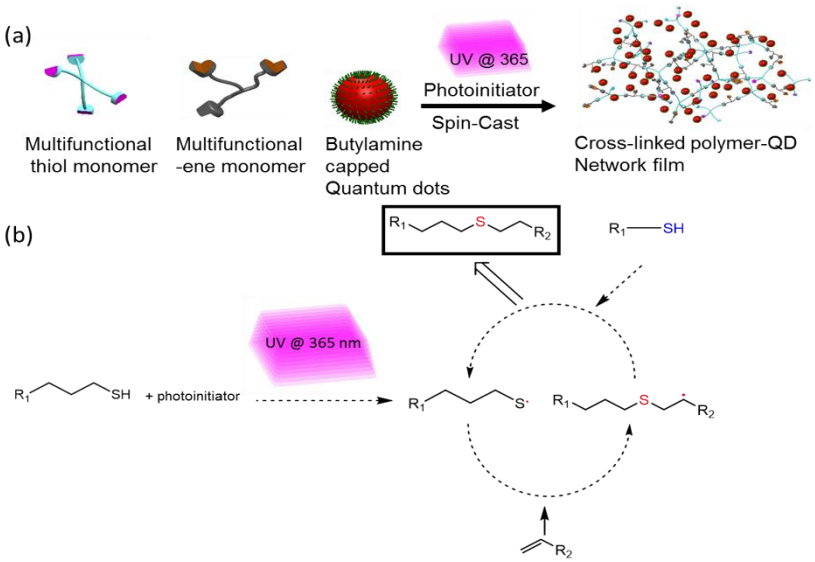

step growth mechanism.[32] Butylamine was used as the ligand for the BAQDs due to its short chain, and the lack of a terminal –ene.

Because the amine functionality attaches to the QD surface, the exposed surface chemistry of the particles is a simple alkane, making the ligand highly unlikely to participate in the thiol-ene reaction. The NOA63 monomer mixture is readily soluble in mildly polar solvents such as chloroform and acetone.[35] Neat NOA63 films were produced by dissolving a known amount of

the adhesive (1 or 5 wt%) in chloroform, and then an aliquot was spincast, followed by degassing and UV irradiation. Neat films show minimal optical scattering and have large scale uniformity, as confirmed by darkfield and brightfield optical imaging (Figure 5.1a & 5.1b). Atomic force microscopy (AFM) confirms smooth surface with microroughness, $R_q \sim 2$ nm for 5 x 5 um^2 surface areas (Figure 5.1).

Similar approach was used to fabricate a uniform QD-polymer nanocomposite. First, a concentrated solution of BA-QDs in chloroform was mixed with a dilute solution (1 or 5 wt%) of NOA63 in chloroform to produce a NOA63-BA-QD solution. Subsequently, films were fabricated by spin casting the concentrated solution of NOA63-BA-QDs on a silicon wafer, followed by degassing, and immediate exposure to UV light for several minutes. Figure B.1 shows TEM images of the BA-QDs with average size of 8 nm and AFM images showing surface roughness of below 4 nm for 25 um^2 surface areas.

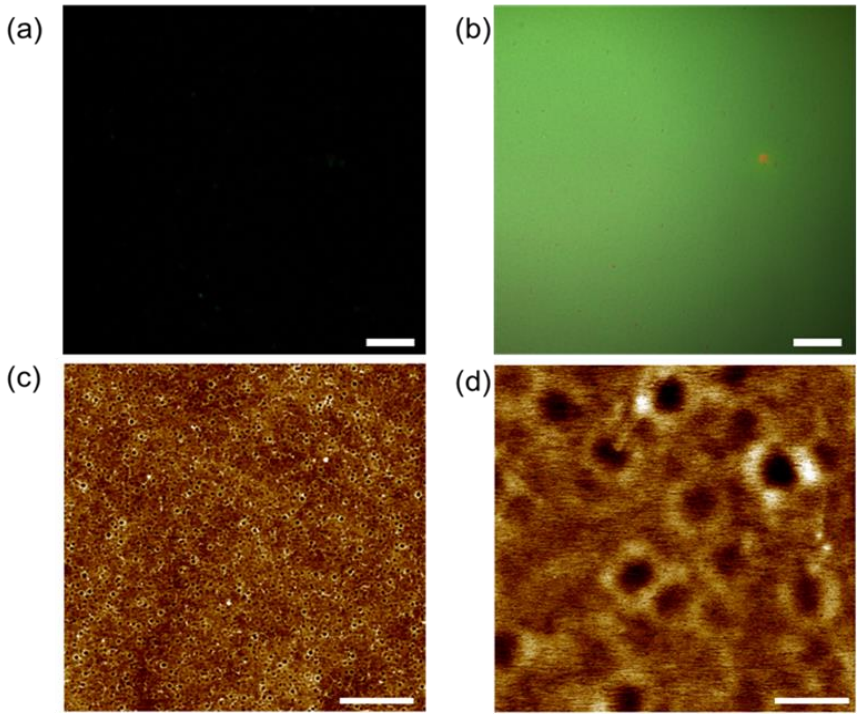

Figure 5.1: Optical imaging of neat NOA63 films showing a) dark field, b) bright field. Scale bars are 50 µm. AFM images c) and d) for a 50 µm and 5 µm scans respectively. Scale bars and height scales for c) are 10 µm and 7 nm respectively, for d) 1 µm and 6 nm respectively.

The fluorescence emission of the unpolymerized NOA-BAQD solution and composite film is similar to that of the neat BA-QDs in solution, with a slight redshift in the peak position and a slight broadening of the full-width at half-max (FWHM) (Figure 5.2a). These changes suggest an energy transfer as caused by a possibly aggregated solution, and a close packed QD film, as well as optical reabsorption due to the overlap of the absorbance and emission states.[42]

Minimal aggregation in the nanocomposite is further confirmed by uniform dark field and SEM

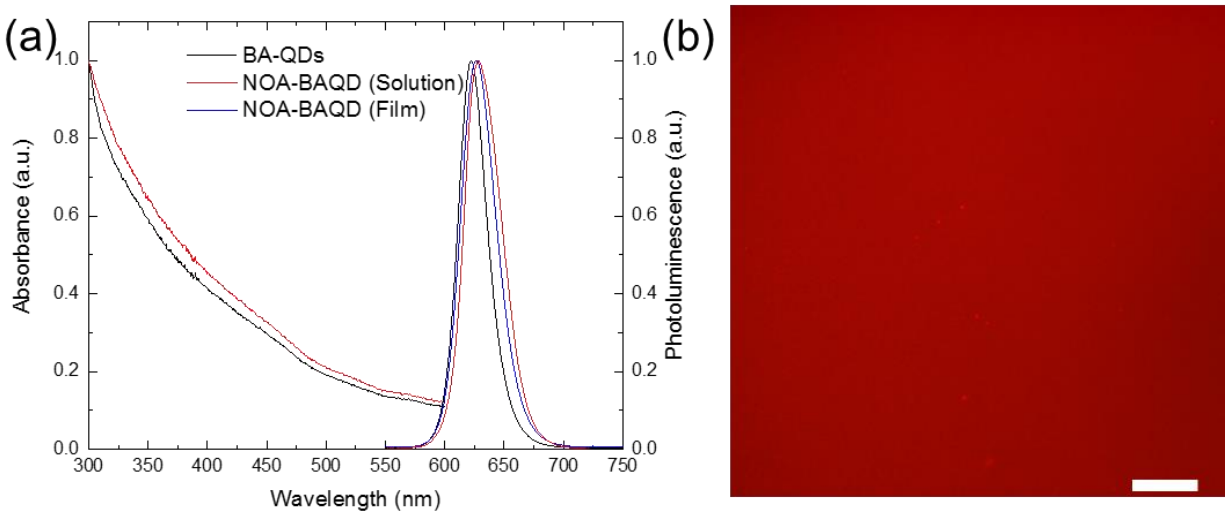

Figure 5.2: (a) Comparison of absorbance from neat BA-QDs and unpolymerized NOA63 with BAQDs in solution and photoluminescence from neat BA-QDs in solution unpolymerized NOA63 with BAQDs in solution and NOA-BAQDs in a closed packed polymer film. A slight increase in absorbance and a small redshift as well as slight peak broadening is noticed from pure QD to composite. 50x fluorescence (b) image of a QD-polymer film showing minimal scattering and uniform fluorescence over large areas. Scale bar – 20 µm.

imaging (Figure B.2). Very little scattering is observed in the dark field image indicating fine QD-polymer mixing and uniformity without QD aggregation at a sub-micron scale and minimal surface roughness. Furthermore, SEM of the film topology shows some possible aggregation or surface roughness of the polymer composite film. Fluorescence imaging shows uniform emission (intensity and color) as well over large regions of the film, thus, confirming the aforementioned conclusion.

Given the sensitivity of QDs to their surrounding environment, the optical properties were further studied to confirm that the close interaction between QD/monomer and QD/polymer did not result in significant alteration of properties. (Table B.1, Figure B.3) Quantum yield measurements on

BAQD and unpolymerized NOA-BAQD shows that no change in QY occurs upon introduction of NOA monomers in solution. Furthermore, comparison of a NOA-BAQD film PL emission relative to a BAQD film shows emission was reduced by half, likely due to volume reduction of QDs present, indicating films still maintain their good optical properties.

5.3.1 Morphology of QD polymer films

Topography and phase AFM scans confirm the uniform nature of the QD-polymer surfaces with uniform distribution of nanoscale features (Figure 5.3). The high resolution AFM image shows well dispersed nanoscale domains of random aggregates of about 200 nm in dimensions. Higher resolution scans indicate the aggregates are composed of spherical QD nanoparticles with apparent dimensions below 40 nm due to dilation by the AFM tip (see inset of Figure 5.3b and d).[43] The RMS roughness of the 500 x 500 nm^2 AFM images is 3.6 nm, indicating very uniform surface nanoscale morphology with minute variation of elevations caused by the presence of the QDs embedded in the polymer matrix.

The heterogeneous nature of the AFM phase image is a clear indication of a multiphase system of nanoscale domains composed of densely packed semiconducting QDs within soft polymer matrix.[44] Phase imaging in AFM can be an effective method for identifying surface properties

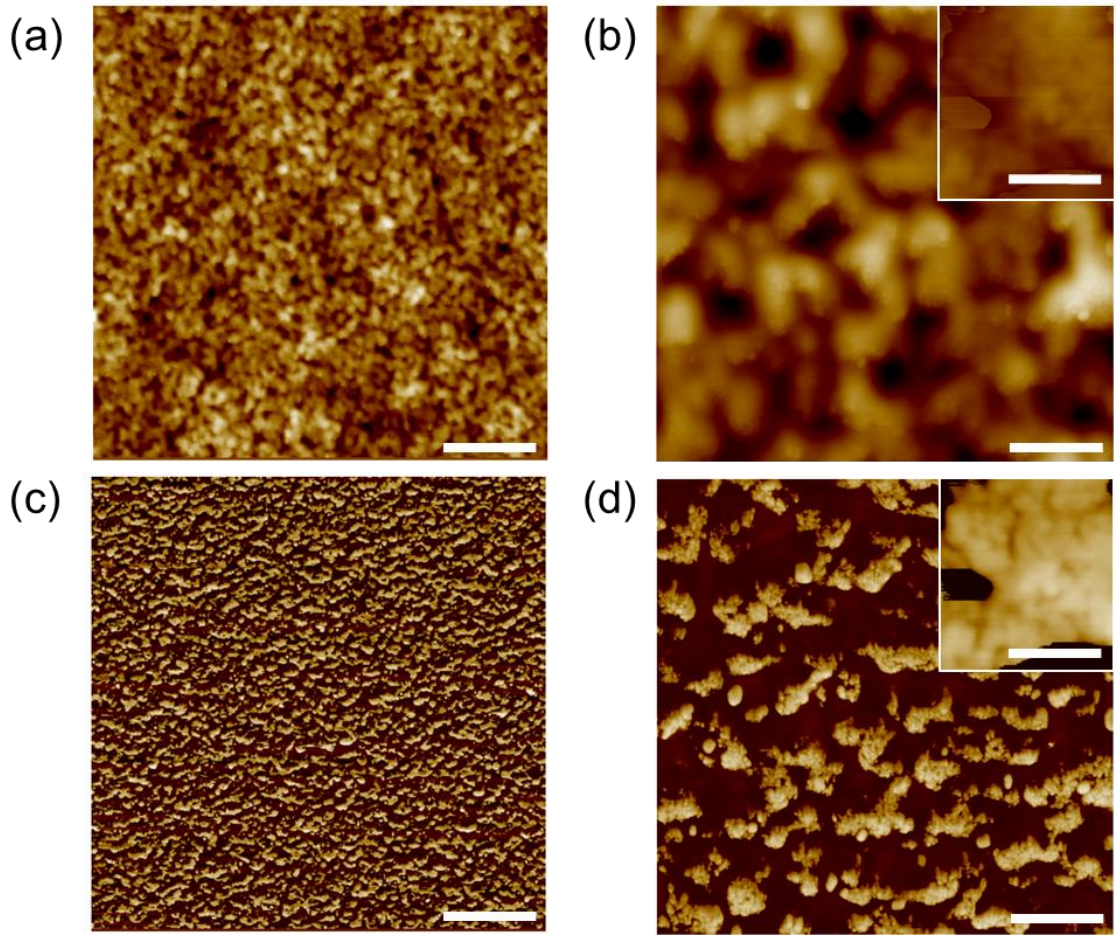

Figure 5.3: AFM topography (a,b) and phase (c,d) images for highly loaded NOA-BAQD films. Scale bars for (a,c) and (b,d) are 2 µm and 400 nm respectively. Height scales for (a) and (b) topography images are 100 nm and 80 nm respectively. Insets show a zoomed in image of NOA-BA-QD film showing QD clusters with scale bar of 100 nm.

such as stiffness[44,45,46] and chemical composition distribution.[44,45,46] The contrast arises in both the attraction (light tapping) or repulsion (hard tapping) modes between the AFM tip and the surface, resulting in a change of the phase of the oscillating cantilever for different materials components.[47] Though the difference in mechanical properties of the two phase system is not immediately known, the bright and dark regions shown in the AFM images suggest areas of glassy (bright) and elastomeric (dark) materials, respectively.[48] This difference suggests that the QD aggregates are surrounded by a soft polymer matrix in these *in-situ* polymerized nanocomposites. Indeed, for polymer nanoparticle composite systems, Ash et al.[49] suggest the formation of

cooperative rearranging regions (CRR) in which nanoadditives can serve as templates for a porous network if there is significant non-wetting at the interface between polymer and additive. We suggest that in our case, the aggregation of the QDs disrupts the percolation of the polymer network, resulting in the creation of "nanoscale void regions" in which the polymer surrounding the QD aggregates is compliant. The aggregation observed in this system is nanoscale and uniformly widespread, and therefore does not significantly increase optical scattering, disrupt light propagation, or lead to variations in film thickness over the substrate. Furthermore, X-ray diffraction (XRD) shows no phase change and crystal lattice distortions of QDs upon their encapsulation with the NOA polymer (Figure B.4).[50] Indeed, all d-spacings and peak width remain unchanged with diffuse halo around 20^{o} indicating amorphous nature of polymer matrix.

5.3.2 Thermal Properties

Next, BAQD-NOA films of varying ratios of BA-QD to NOA63 were analyzed with TGA and DSC to understand how the thermal properties of the composites vary with QD loading (Figure 5.4). The pure NOA film decomposes to nearly zero mass after heating to 600°C indicating complete decomposition of the polymer upon thermal exposure (Figure 5.4a). Pure BA-QD samples show weight loss up to 600°C with >80% of the sample still remaining at this temperature. The initial weight loss is attributed to the organic fraction of the QDs (butylamine ligand has a boiling point of 78°C)[51], although there is still weight loss taking place up to 450°C, this can be attributed to tightly bound ligand leftover from the ligand exchange. The residual mass upon completion of the run at 600°C is due to pure CdSe/$Cd_{1-x}Zn_xSe_{1-y}S_y$ QDs, around 78 wt%, as the boiling point for a bulk semiconductor of this nature is well beyond the experimental

conditions. Similarly, NOA-BAQD sample decomposition begins at 100°C and follows a trajectory between that of the pure BAQDs and pure NOA samples. There is some variation in the thermal stability for the composite samples between 100°C and 300°C, weight loss in this region is typically due to organic content, suggesting minor variations in the amount of organic present. Depending on the concentration of QDs in the composite samples TGA shows decomposition until all polymer is completely removed, leaving behind the pure thermally-stable QD.

DSC shows no detectable T_g or T_m (within the temperature range of experiment) for the neat BA-QD sample, while the NOA polymer has a T_g of ca. 30°C (Figure 5.4b).[52] The T_g of the QD-polymer composite depends on the fraction of QDs in the composite, with the T_g gradually decreasing as more QDs are introduced into the polymer composite. The decrease in T_g is counterintuitive given that the addition of hard semiconducting component to a polymer matrix

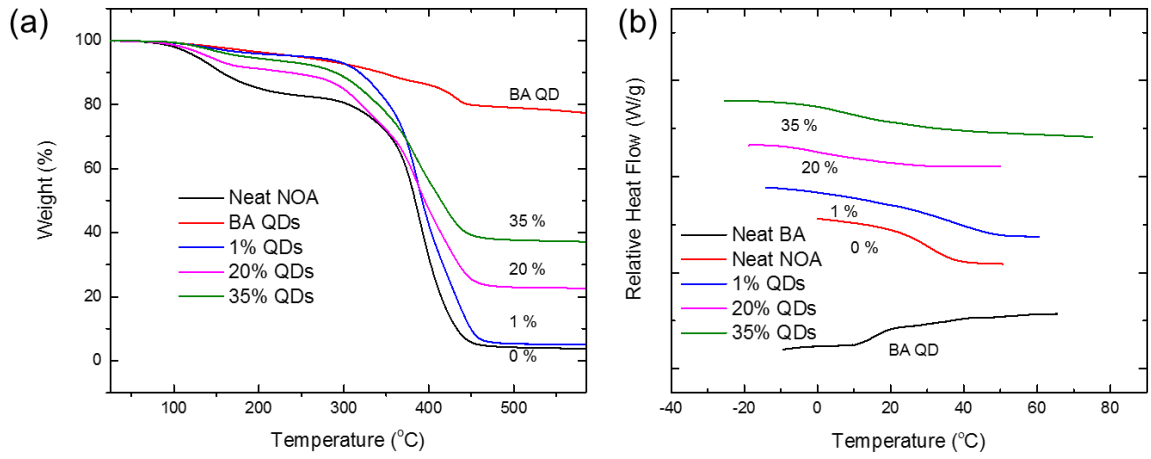

Figure 5.4: TGA (a) and DSC (b) of neat components and NOA-BAQD composite films. TGA confirms loading, while DSC shows significant reduction in T_g values as loading is increased.

typically results in an increase of T_g due to common reinforcing effect with inorganic reinforcing components.[2,53] In contrast, our results suggest that the crosslinking density of the composite

decreases with some type of plasticization effect taking place due to excess organic ligand in the QD system as will be further discussed below.[40]

To understand the crosslink density of the nanocomposite system real time infrared (RTIR) spectroscopy was used to observe the conversion of the vinyl (-ene) and thiol functional groups as a function of irradiation time.[37,54,55,56] Typical RTIR spectra for the NOA and NOA-BAQD composite at various irradiation times can be seen in Figure 5.5a and 5.5b respectively,

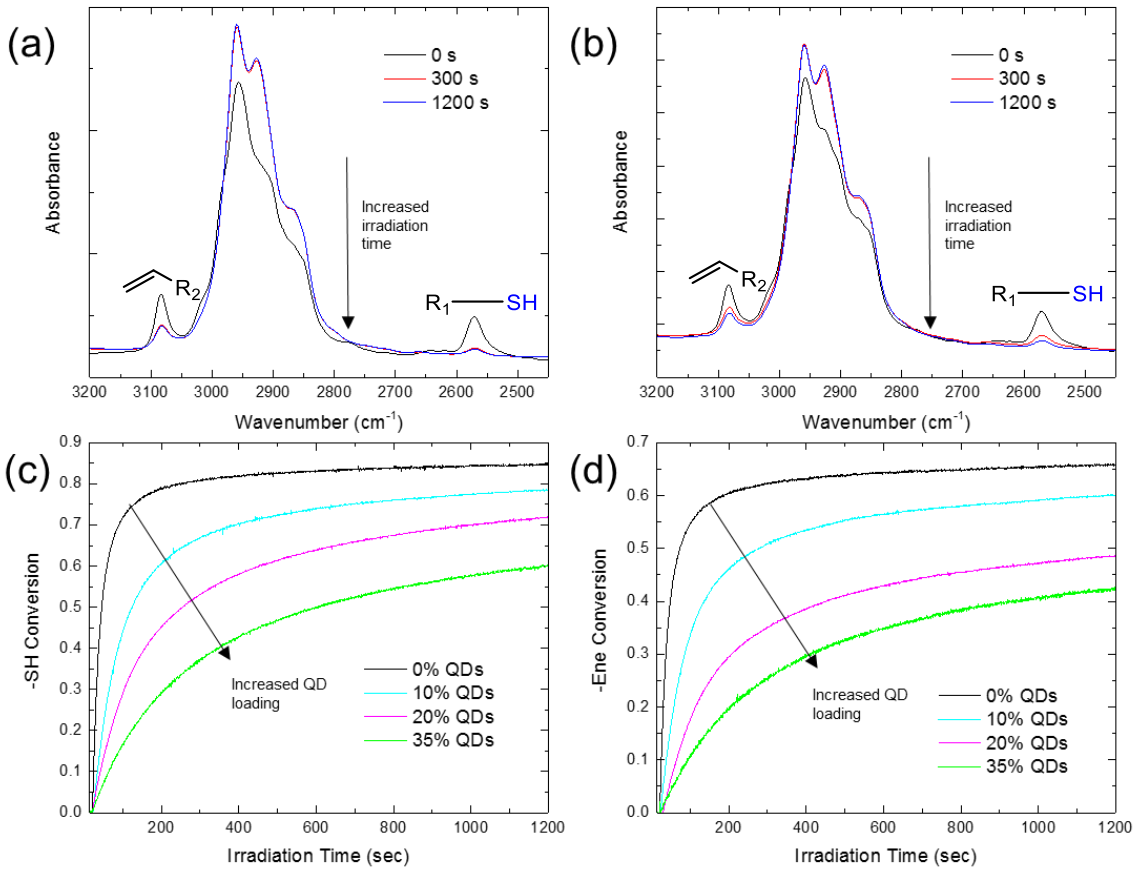

Figure 5.5: Representative time-lapsed FTIR showing reduction in –C=CH$_2$ (ene at ~3080 cm^{-1}) and –SH (thiol at ~2570 cm^{-1}) with more UV irradiation time for both (a) neat NOA 63 and (b) NOA-BAQD composite. Conversion of both (c) –ene and (d) –thiol groups for neat NOA 63 and NOA-BAQD with increasing concentrations of QDs clearly shows suppressed conversions.

emphasizing the –ene peak at ~3100 cm^{-1} and the thiol peak at ~2570 cm^{-1}. The conversion as a function of irradiation time for both thiol and –ene can also be seen in Figure 5c and 5d, respectively.

It can be clearly observed that the intensity of the thiol and –ene peaks is reduced with increased irradiation time (Figures 5.5a and 5.5b). Taking the conversion as the change in area under these specific peaks Figure 5.5c and 5.5d shows a clear trend that the conversion and loading percentage

are inversely proportional. Initially, with the neat NOA the conversion for the thiol and –ene functional groups is near complete after 300 seconds. Notably, the conversion does not reach 100% (the thiol reaching ~85% and –ene reaching ~66% after 1200 seconds), which is due to the dense crosslinked network achieved, as the gel point for typical formulations is ~40%, limiting mobility, and the conversion of both functional groups is not the same.[71] While previously observed systems typically show the –ene being the dominant constituent as a significant amount of –ene monomers can also homopolymerize, but for the current adhesive that is not the case.[55] The specific ally ether used, triallyl isocyanurate, does not possess the ability to homopolymerize,[57] however, high crosslinking densities are still achieved in the neat polymers. Upon addition of QDs significant reduction in conversion/crosslinking occurs. With conversion exceeding 50% for –SH upon addition of 35 wt% QDs.

It is worth noting that similar systems have been investigated, in which functionalized nanoparticles are incorporated into a polymer matrix, and the inclusion of nanoparticles does not typically disrupt the polymerization kinetics, unless the nanoparticles are functionalized with a ligand that can participate in the photopolymerization reaction, or there is a strong affinity between the nanoparticle surface and the functional group of the monomers being used, in this case a thiol or an -ene.[37,58] Specifically, Phillips et al. noted a strong interaction between the thiol-gold surface, limiting the availability of thiols in their particular system to react with –ene monomers.[37] Herein, this is not the case, although it has been shown that thiols will have a strong affinity to the surface of QDs,[59] UV exposure of a tetrathiol, pentaerythritol tetrakis(3-mercaptopropionate), with photoinitiator irgacure 651, in the presence of BA-QDs resulted in no appreciable change in the

thiol peak using FTIR over a period of 15 minutes, suggesting the thiol does not tether to the QD surface.

However, the QD nanoparticles are significant light absorbers, given the typical quantum yield of these QDs around 30% and strong absorption in near-visible range (Figure 5.2).[40] Because the polymerization is initiated using 365 nm light, the QDs absorb a significant quantity of the irradiated light, thereby retarding the reaction. One important thing to note is typical gelation point for similar multifunctional thiol-ene mixtures occurs around 40% conversion, thereafter the polymerization kinetics are severely hindered as a semi-solid has formed, however, significant hampering of reaction kinetics take place well prior to this point upon incorporation of QD components.[57,60]

To further analyze these changes, we used on the absorbance at 365 nm to calculate the fractional absorbance (Figure 5.2).[61] The QDs by themselves absorb about ~39% of the light at this wavelength, while addition of an aliquot of NOA monomer solution making the final solution similar to that of ~10 wt% NOA-BA-QD sample, resulted in a very negligible increase in the amount of light absorbed to ~40%. Furthermore absorbance measurements were done on solutions of varying concentrations in order to calculate the molar absorptivity at 365 nm, which was on the order of 10^6 mol^{-1} cm^{-1} for these particular CdSe based QDs, similar to values previously obtained, suggesting significant attenuation of the light as it travels through the composite film.[62] While it appears that the QDs absorb majority of the irradiated light that is used to initiate the

polymerization of NOA, the reduction in conversion (crosslinks) does not necessarily equate to a reduction in T_g.

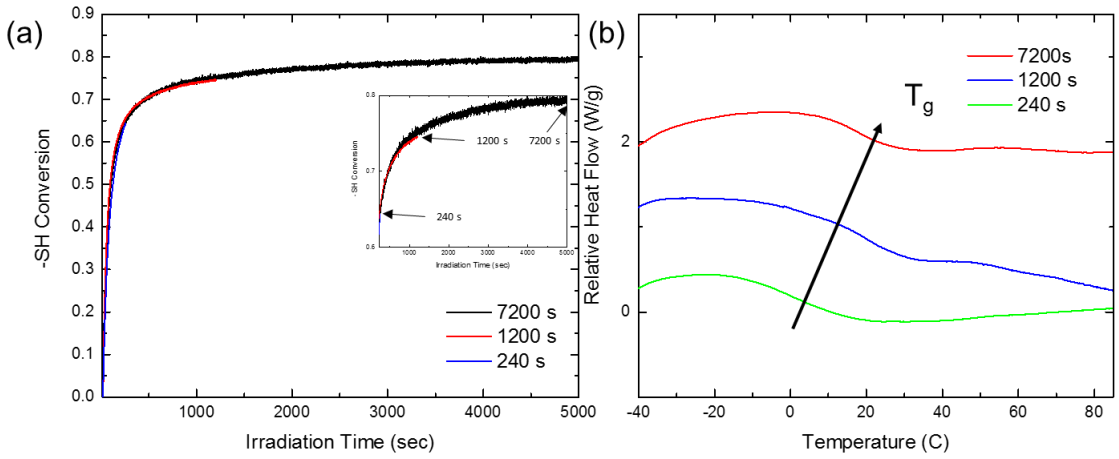

Figure 5.6: (a) Conversion of –thiol groups for NOA-BAQD with 10 wt % QDs at different irradiation times showing the time dependence of the conversion of functional groups (inset shows a zoom in of final conversion) and (b) DSC plots showing the shift in T_g with increased irradiation time.

A reduction in crosslinking density could result in a decreased T_g, however, several other factors can affect the T_g of crosslinked polymers. [63,64] In order to determine the effect of the conversion on the T_g three 10wt % BA-QD-NOA samples were irradiated with UV light for varying times, 240, 1200, and 7200 seconds. Following each exposure, samples were analyzed with DSC to determine the T_g **(**Figure 5.6).

Figures 6a and 6b show the –SH conversion for samples irradiated and the DSC curve for each sample, respectively. While none of the samples reached the thiol conversion of the neat NOA (~85%), the longer the samples were irradiated the higher the conversion, with a maximum conversion of ~80% reached for the sample irradiated for 7200 seconds. Correspondingly, Figure

6b shows an increase in T_g with longer irradiation times. Again the T_g does not recover to that of the neat NOA (30°C for neat NOA vs 20°C 10 wt% sample irradiated for 7200 seconds). Although near complete recovery of the T_g could be observed with longer irradiation times, it is not expected, due to the mismatch in polarity between the monomer constituents and QD ligand.

Indeed, it has been established that a non-wetting interface between a hard surface and a polymer can result in a reduction of T_g as a result of confinement, network disruption, and formation of highly mobile polymer domains at the interface.[65,66,67] As mentioned, Ash et al. performed an in situ free-radical polymerization in which methylmethacrylate monomers were polymerized in the presence of alumina nanospheres capped with a silane capping agent, ranging in size from 17 to 38 nm, to form a polymethylmethacrylate (PMMA)-alumina nanocomposite. A decrease in T_g of nearly 25°C was observed with as little as 0.5 wt% alumina incorporated into the composite system. The reduction in T_g was attributed solely to contributions from the nanoparticles, as removal of the alumina resulted in the T_g returning to that of the neat polymer. Dewetting at the interface between alumina and PMMA results in the nanoparticles creating nanoporosity throughout the composite, causing an overall disruption of the polymer network and an increased number of polymer islands with enhanced mobility near the QD-polymer interface.[49] Similarly, Bansal et al. observed a reduction in T_g for a polymer composite consisting of polystyrene and silica nanoparticles that was dependent on the interparticle spacing.[68] A consistent reduction of T_g was observed as the interparticle spacing was reduced, which was not observed when the surface of the filler was functionalized to better wet the polymer. In the case of the BA-QD-NOA system, though the T_g can be partially recovered with extended irradiation times, there is a permanent decrease in T_g that gets larger as more QDs are added to the system. In accordance with previous

studies the addition of more QDs into the polymer appears to reduce the interparticle spacing, enhance polymer confinement, and create CRRs, resulting in localized nanoscale phase separation in which nanoscale regions of a highly mobile phase exists at the QD-polymer interface. One significant difference in the current system is that the monomer mixture is composed of all crosslinkers, which were initially thought to enhance dispersion.

Demir et. al[69] observed significant enhancement in nanoparticle dispersion in a polymethylmethacrylate (PMMA) matrix upon addition of a difunctional crosslinker. These changes were attributed to difunctional crosslinkers slowing down the diffusion of nanoparticles to form aggregates. While it was envisioned in this study that addition of multifunctional crosslinkers would create a diffusion limited system which would severely limit QD aggregation, there appears to be some incompatibility at the interface between QD and monomers which leads too nanoscale aggregation. It is worth noting that the filler particles can be treated for better wetting with the polymer.

While the current monomer/ligand selection does appear to demonstrate a non-wetting interface, and a T_g that is not completely recoverable, the thermal properties can still be controlled to an extent. The variability of T_g indicates that the polymer composite can be changed from a rigid state to a more soft and flexible state as a function of the irradiation time, while still remaining as a robust, intact polymer composite. To demonstrate the flexible nature of the QD composite films, films were detached from silicon substrates and suspended in fluid and bent with tweezers (Figure S5). Understanding the thermal properties of composite systems enables tailoring of the composite

structure for a given application (i.e. waveguides and lasers), which is particularly important when designing optical systems on flexible substrates.

5.3.3 Kinetics of Polymerization

Further analysis of the RTIR data allowed for more in depth understanding of the polymerization. The rate of propagation, also termed the rate of polymerization, R_p, can be calculated as follows, $R_p = d[M]/dt$, where [M] is the monomer concentration. R_p is typically calculated from the –ene conversion curve by using the initial slope of the conversion data in Figure 5.5d (Table 5.1).[37]

As previously stated, significant retardation of the polymerization rate occurs upon addition of QDs to the system. Assuming a standard photoinitiated polymerization, the rate of polymerization and the rate of initiation, R_i, are proportional, i.e. $R_p \alpha R_i^{0.5}$, with R_i being influenced by a number of things including concentration, efficiency, and light intensity.[70] As was shown earlier, light is significantly attenuated as the concentration of QDs is increased, limiting the amount of light available to initiate the polymerization and form free radicals. Furthermore, using the conversion the reaction order of this composite system was determined.

Table 5.1: Effect of QD Concentration on Rate of Polymerization and Final Conversion of –ene.

Sample	Rate of Polymerization (s^{-1})	Final Conversion %
0 wt %	0.015	66
10 wt %	0.006	60
20 wt %	0.003	48
35 wt %	0.001	42

Assuming an overall first order reaction, being half order in terms of each monomer, log(1-x), where x is the -ene conversion, was plotted as a function of time (Figure 5.7). While majority of the thiol-ene formulations tend to follow a first order reaction rate that does not appear to be the case here. As was previously shown, addition of QDs to the monomer formulation results in a significant decrease in the amount of UV light available for the photoinitiatior to absorb as the QDs are the dominating component. As a result, the polymerization proceeds via a two stages with different rates: the polymerization initially proceeds at one rate and upon reaching the gelation point this rate is severely hindered. It has been reported, the critical gel point for thiol-ene chemistries of this functionality is ~40%, for the neat polymer this is reached within 40 seconds.[71]

In our case, fitting analysis reveals that the polymerization kinetic transitions from one exponential decay to another well beyond 40. For the neat polymer, it appears that an additive of the adhesive could be perturbing the reaction resulting in a non-linear polymerization rate. As QDs are added to the pre-polymer mixture less light is available to be absorbed by the photoinitiator, thereby less

free radicals are generated, resulting in a much slower reaction than what is to be expected from your traditional free-radical, step growth like polymerization.

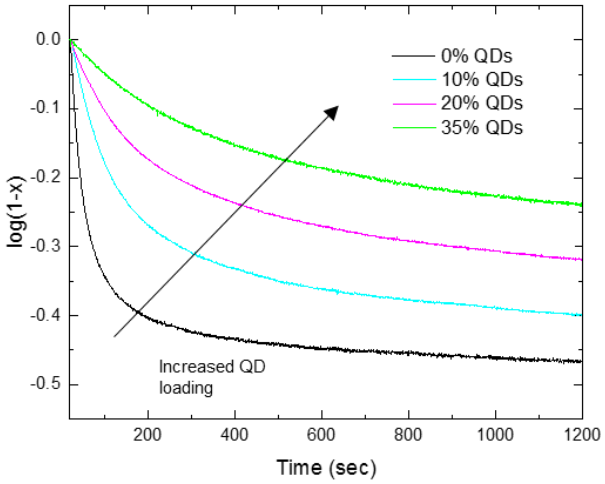

Figure 5.7: Plot of log(1-x) as a function of UV irradiation time showing initial first order reaction kinetics.

5.3.4 Mechanical Properties of QD-polymer films

Force spectroscopy measurements were conducted via an AFM nanomechanical probing to further corroborate the observed change in the thermal and mechanical properties. In this case, force-distance curves were gathered from thin films suspended across a circular aperture in order to calculate tensile elastic modulus in accordance with the well-known approach (Figure 8). [72,73,74,75]

Based on the load-deflection characteristics of the polymer thin films, the elastic modulus of the neat polymer NOA film was found to be 16.4 ± 2.5 GPa, with no significant changes in the

modulus value observed upon addition of 0.5 wt% BA-QDs (Figure 8d). It is worth noting that initial values are higher than that expected for the neat polymer film and can be related to large initial deformation during tip jump-in initial contact.[35] However, above 0.5 wt % QDs there is a drastic threshold like decrease of the modulus down to 5.0 ± 0.52 GPa, with the highest loading measured (33 wt%), the modulus drops even further, to 1.2 ± 0.44 GPa (Figure 8d).

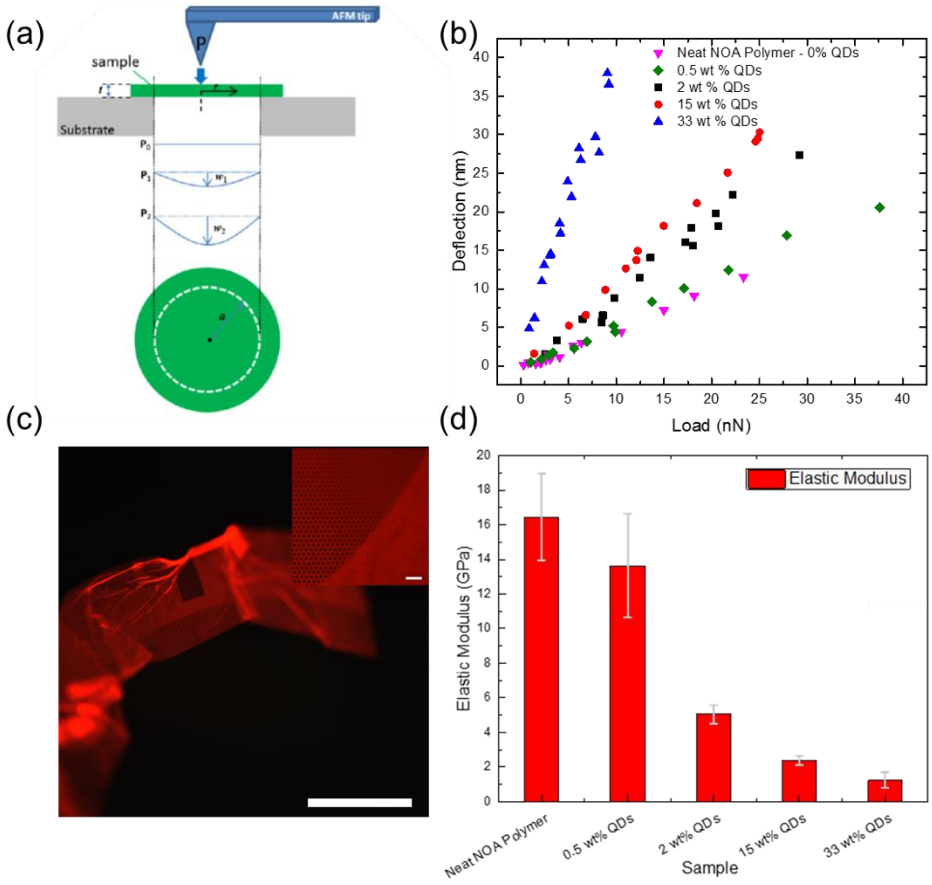

Figure 5.8: Force spectroscopy experimental setup (a) in which a point load is applied to a thin film suspended across a circular aperture using an AFM probe. (b) Representative Force-Distant curves showing difference between highest loaded polymer and no loading. (c) Wrinkled NOA-BA-QD film suspended across the edge of a TEM grid, inset is zoomed in image of composite film on grid. (d) Elastic modulus for films with varying QD loading, measured using force spectroscopy. Scale bars – 50 µm.

Drop in the elastic modulus for polymer composites has been observed in several studies after adding inorganic components. For instance, Bowman et al. showed a clear correlation between glass transition temperature and resulting modulus, depending on the thiol-ene/thiol-acrylate monomer constituents used, with lower T_g's resulting in lower moduli.[33] Herein, the lower the

conversion/crosslinking the lower the T_g. Furthermore it has been shown that increased crosslinking results in enhanced mechanical properties and vice-versa.[76] The continued reduction of elastic modulus with increased loading suggests that the crosslinking density of the polymer matrix is being altered, causing a change in mechanical properties.[33] As was confirmed by FTIR and UV-vis, an increase in QD loading results in a significant portion of the UV light, used to initiate the polymerization, being absorbed by the QDs. Although it has also been shown that a reduction of the Young's modulus in nanocomposites has resulted due in part to the same reason a reduction in T_g is observed, weak interface and in some cases, cavitation at the interface,[28] in this study it appears that the crosslinking plays a significantly larger role.

These results clearly show that the physical properties of the QD-polymer composite vary drastically with QD loading fraction and UV irradiation time with both glass transition and mechanical strength decreasing significantly as a result of adding quantum dots and decreasing crosslinking density and polymerization progression. This approach, thus, can be used to reliably control the mechanical properties of these composite films without requiring the inclusion of additional chemical additives (reinforcing or plasticizing) that could alter the optical properties as caused by suppression of large-scale phase separation in QD-polymer systems.

5.3.5 QD-polymer Film Patterning with Soft Lithography

To demonstrate the feasibility and compatibility of the BA-QD-NOA mixture for making robust and low optical loss waveguide and cavity like structures and patterns, we exploited soft

lithographical approaches. Two patterning methods were utilized here: micromolding in capillary (MIMIC) and microtransfer molding (uTM) (Scheme 5.2).[77]

Scheme 5.2: Soft lithographic techniques exploited in this study: (a) micromolding in capillary (MIMIC) and (b) microtransfer molding (uTM), in which a very dilute monomer solution is used to create patterns on the submicron

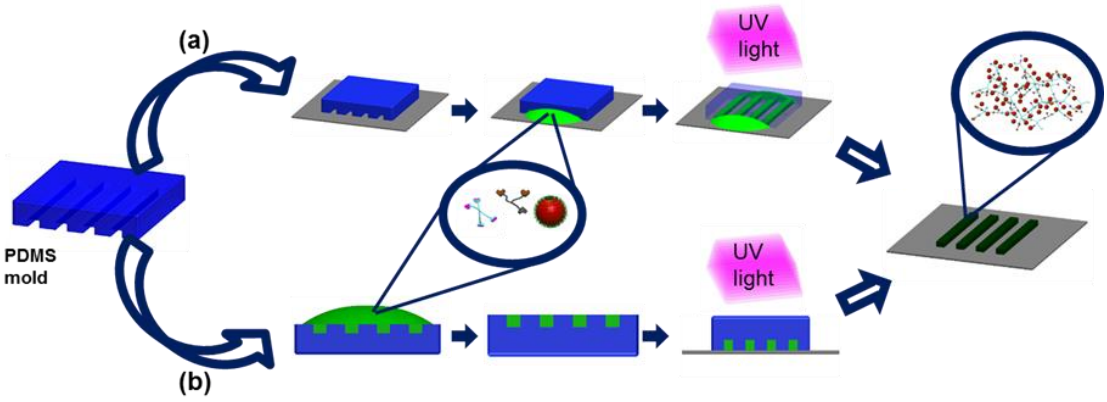

Benefits of these techniques include the ability to fabricate high aspect ratio, sharp featured freestanding patterns, that can be sequentially repeated to produce complex physical patterns. These two techniques are complimentary to each other since they both can be used to generate three-dimensional structures.[77] Given the fluid-like nature of the initial monomer–QD mixture, capillary forces can readily pull the mixture into the columnar structures of polydimethylsiloxane (PDMS) stamps during traditional microprinting.[77,78,79] In this fabrication approach, a PDMS stamp is placed on a substrate (typically a silicon wafer). A drop of a 1 wt% polymer solution with QDs is placed next to the columnar openings of the PDMS stamp, and capillary forces pull the solution into the stamp. Prior to irradiating with UV light, the solution inside the stamp is degassed to remove trapped gasses. Following UV irradiation, the stamp is simply peeled off, leaving behind a QD-polymer composite pattern on the substrate.

In another approach, the monomer-QD solution is instead placed directly on top of the PDMS stamp, followed by capillary forces pulling solution into the recessed regions, and removal of any excess solution (Scheme 5.2b). The polymerization then proceeds as in the previous approach used to produce a thin film. Patterns of neat polymer and polymer-QD composites generated via both techniques can be seen in bright field and fluorescence optical images and AFM scans in Figure 5.9.

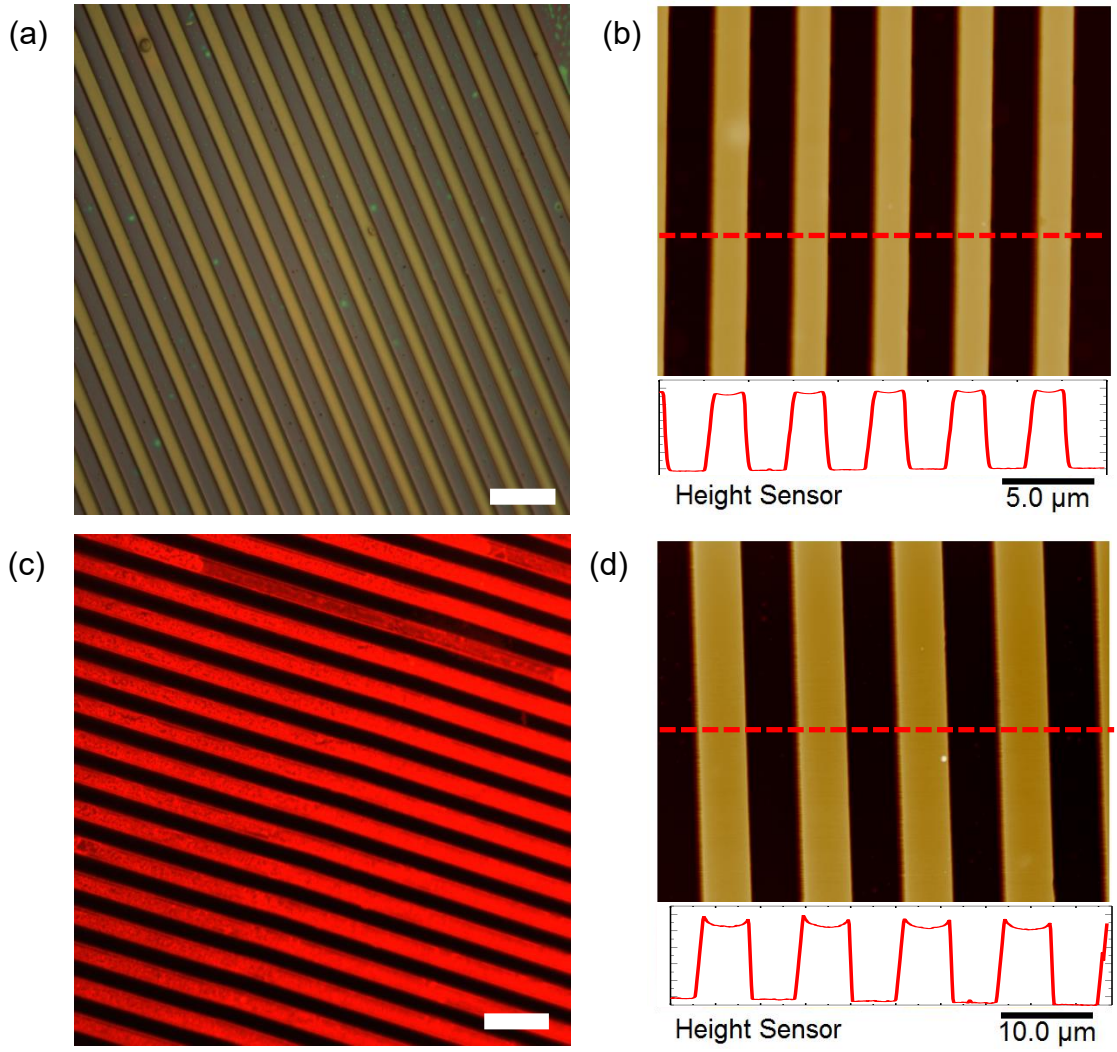

Figure 5.9: Bright-field (a) and AFM topography (b) images of soft lithographic patterns of neat NOA polymer. Fluorescence (c) and AFM topography (d) images of soft lithographic patterns of neat NOA- BAQD polymer composite. Optical image scale bars – 20 µm and AFM max height – 1 µm.

QD-polymer patterns generated here display very sharp sub-micron to micron scale patterns with controlled and consistent physical characteristics (width, height, and spacing) over large surface areas of mm^2. A variety of single layer and multilayers patterns can be fabricated, including strips/waveguides and holes. Multilayer patterns fabricated using both methods in Scheme 5.2, AFM and Fluorescence imaging confirm layered structure and emissive nature. (Figure 5.10)

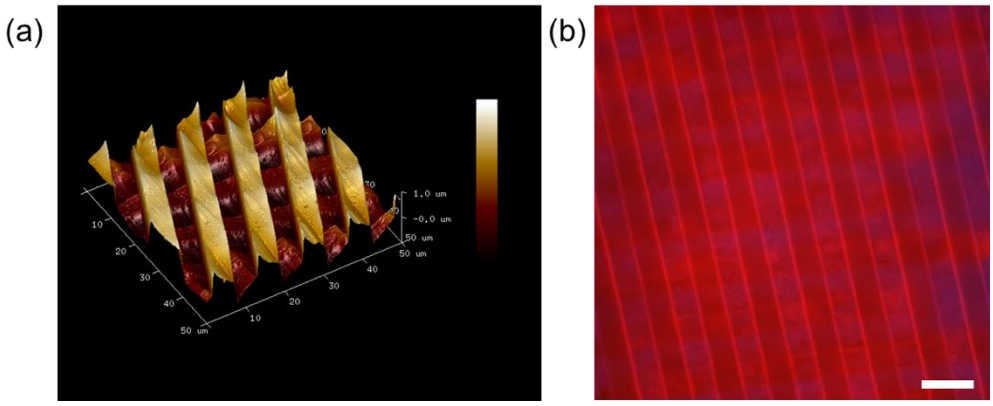

Figure 5.10: AFM scan (a) showing 3D structure prepared using complimentary soft lithography techniques and (b) Fluorescence imaging showing a layered structure consisting of red emitting (lower) and blue emitting (upper) waveguide strips. Scale bar – 20 µm.

5.4 Conclusions

This work has demonstrated a facile technique using thiol-ene chemistry to incorporate QDs into a polymer matrix in controllable and uniform manner with suppressed large-scale aggregation of QDs. Taking advantage of shorter QD ligands with simple alkane backbones makes it feasible to embed QDs within a polymer matrix without noticeable phase separation. The incorporation of QDs into monomer matrix results in reduced and controllable light absorption and, thus, the degree

of crosslinking and polymerization kinetics that allows to adjust the mechanical thermal properties making QD-polymer composite with unusually high QD load (up to 30% instead of common <1%) which are rather flexible and behave as elastomeric-like materials with high optical clarity, low optical losses, and high, uniform photoluminescent emission.

Moreover, we demonstrated that traditional microprinting methods can be applied to the materials in order to fabricate complex 3D highly emissive patterns. Overall, this approach yields highly emissive and optically stable films with minimal optical scattering, due to the nanoscale phase separation, which maintain the optical capabilities of the QDs. The significant reduction in modulus allows for the composite to be formed on nonplanar or flexible substrates, or on its own as a robust freestanding and flexible film. These commercial adhesives are extremely low cost, robust, and offer the ability to tune mechanical and thermal properties via selection of initial monomer chemistry and control of exposure parameters.

5.5 References (Chapter 5)

[1] Talapin, D. V.; Lee, J.-S.; Kovalenko, M. V.; Shevchenko, E. V., *Chem. Rev.* **2010**, *110*, 389.

[2] Sperling, L. H., Introduction to physical polymer science. John Wiley & Sons: 2005.

[3] Jung, J.; Lin, C. H.; Yoon, Y. J.; Malak, S. T.; Zhai, Y.; Thomas, E. L.; Vardeny, V.; Tsukruk, V. V.; Lin, Z., *Angew. Chem., Int. Ed.* **2016**, *55*, 5071.

[4] Li, Q.; Zhou, H.; Hoyle, C. E., *Polymer* **2009**, *50*, 2237.

[5] Greytak, A. B.; Allen, P. M.; Liu, W.; Zhao, J.; Young, E. R.; Popovic, Z.; Walker, B. J.; Nocera, D. G.; Bawendi, M. G., *Chem. Sci.* **2012,** *3*, 2028.

[6] Sonawane, K. G.; Agarwal, K. S.; Phadnis, C.; Sharma, D.; Layek, A.; Chowdhury, A.; Mahamuni, S., *J. Phys. Chem. C* **2016,** *120*, 5257.

[7] Bae, W. K.; Park, Y.-S.; Lim, J.; Lee, D.; Padilha, L. A.; McDaniel, H.; Robel, I.; Lee, C.; Pietryga, J. M.; Klimov, V. I., *Nat. Commun.* **2013**, *4*, 2661.

[8] Chuang, C.-H. M.; Brown, P. R.; Bulovic, V.; Bawendi, M. G., *Nat. Mater.* **2014,** *13*, 796.

[9] Meinardi, F.; McDaniel, H.; Carulli, F.; Colombo, A.; Velizhanin, K. A.; Makarov, N. S.; Simonutti, R.; Klimov, V. I.; Brovellii, S., *Nat. Nanotechnol.* **2015,** *10*, 878.

[10] Lin, C. H.; Lafalce, E.; Jung, J.; Smith, M. J.; Malak, S. T.; Aryal, S.; Yoon, Y. J.; Zhai, Y.; Lin, Z.; Vardeny, Z. V.; Tsukruk, V. V., *ACS Photonics* **2016**, *3*, 647.

[11] Mashford, B. S.; Stevenson, M.; Popovic, Z.; Hamilton, C.; Zhou, Z. Q.; Breen, C.; Steckel, J.; Bulovic, V.; Bawendi, M.; Coe-Sullivan, S.; Kazlas, P. T., *Nat. Photonics* **2013,** *7*, 407.

[12] Malak, S. T.; Jung, J.; Yoon, Y. J.; Smith, M. J.; Lin, C. H.; Lin, Z.; Tsukruk, V. V *Adv. Opt. Mater.* **2016**, *4*, 608.

[13] Maragkou, M., *Nat. Mater.* **2015**, *14*, 1186.

[14] Wood, V.; Panzer, M. J.; Chen, J. L.; Bradley, M. S.; Halpert, J. E.; Bawendi, M. C.; Bulovic, V., *Adv. Mater.* **2009**, *21*, 2151.

[15] Reithmaier, J. P.; Sek, G.; Loffler, A.; Hofmann, C.; Kuhn, S.; Reitzenstein, S.; Keldysh, L. V.; Kulakovskii, V. D.; Reinecke, T. L.; Forchel, A., *Nature* **2004**, *432*, 197.

[16] Ramezani, H.; Kottos, T.; El-Ganainy, R.; Christodoulides, D. N., *Phys. Rev. A* **2010,** *82*, 043803-1.

[17] Lin, Z.; Ramezani, H.; Eichelkraut, T.; Kottos, T.; Cao, H.; Christodoulides, D. N., *Phys. Rev. Lett.* **2011,** *106*, 213901-1.

[18] Song, J.; Li, J.; Xu, J.; Zeng, H., *Nano Lett.* **2014,** *14*, 6298.

[19] Liu, Z.; Sun, Y.; Yuan, J.; Wei, H.; Huang, X.; Han, L.; Wang, W.; Wang, H.; Ma, W., *Adv. Mater.* **2013,** *25*, 5772.

[20] Coe-Sullivan, S.; Steckel, J. S.; Woo, W. K.; Bawendi, M. G.; Bulovic, V., *Adv. Funct. Mater.* **2005,** *15*, 1117.

[21] Wang, Y.; Ta, V. D.; Leck, K. S.; Tan, B. H. I.; Wang, Z.; He, T.; Ohl, C.-D.; Demir, H. V.; Sun, H., *Nano Lett.* **2017,** *17*, 2640.

[22] Kim, C.-H.; Bang, J.-H.; Hong, K. B.; Park, M.-H., *RSC Adv.* **2016**, *6*, 96700.

[23] Resch-Genger, U.; Grabolle, M.; Cavaliere-Jaricot, S.; Nitschke, R.; Nann, T., *Nat. Methods* **2008**, *5*, 763.

[24] Noh, M.; Kim, T.; Lee, H.; Kim, C.-K.; Joo, S.-W.; Lee, K., *Colloids Surf., A* **2010**, *359*, 39.

[25] Wang, Y.; Li, X.; Sreejith, S.; Cao, F.; Wang, Z.; Stuparu, M. C.; Zeng, H.; Sun, H., *Adv. Mater.* **2016,** *28*, 10637.

[26] Ehlert, S.; Stegelmeier, C.; Pirner, D.; Förster, S., *Macromolecules* **2015**, *48*, 5323.

[27] Vaidya, S. V.; Couzis, A.; Maldarelli, C., *Langmuir* **2015**, *31*, 3167.

[28] Raja, S. N.; Luong, A. J.; Zhang, W.; Lin, L.; Ritchie, R. O.; Alivisatos, A. P., *Chem. Mater.***2016,** *28*, 2540.

[29] Kade, M. J.; Burke, D. J.; Hawker, C. J., *J. Polym. Sci. A Polym. Chem.* **2010,** *48*, 743.

[30] Lowe, A. B., *Polym. Chem.* **2010,** *1*, 17.

[31] Chan, J. W.; Hoyle, C. E.; Lowe, A. B., *J. Am. Chem. Soc.* **2009,** *131*, 5751.

[32] Hoyle, C. E.; Bowman, C. N., *Angew. Chem., Int. Ed.* **2010,** *49*, 1540.

[33] Carioscia, J. A.; Schneidewind, L.; O'Brien, C.; Ely, R.; Feeser, C.; Cramer, N.; Bowman, C. N., *J. Polym. Sci. A Polym. Chem.* **2007,** *45*, 5686.

[34] Senyurt, A. F.; Wei, H.; Hoyle, C. E.; Piland, S. G.; Gould, T. E., *Macromolecules* **2007,** *40*, 4901.

[35] https://www.norlandprod.com/adhesiveindex2.html

[36] Khire, V. S.; Benoit, D. S. W.; Anseth, K. S.; Bowman, C. N., *J. Polym. Sci. A Polym. Chem.* **2006,** *44*, 7027.

[37] Phillips, J. P.; Mackey, N. M.; Confait, B. S.; Heaps, D. T.; Deng, X.; Todd, M. L.; Stevenson, S.; Zhou, H.; Hoyle, C. E., *Chem. Mater.* **2008,** *20*, 5240.

[38] van Berkel, K. Y.; Hawker, C. J., *J. Polym. Sci. A Polym. Chem.* **2010,** *48*, 1594.

[39] Lü, C.; Cui, Z.; Wang, Y.; Li, Z.; Guan, C.; Yang, B.; Shen, J., *J. Mater. Chem.* **2003**, *13*, 2189.

[40] Malak, S. T.; Lafalce, E.; Jung, J.; Lin, C. H.; Smith, M. J.; Yoon, Y. J.; Lin, Z.; Vardeny, Z. V.; Tsukruk, V. V., *J. Mater. Chem. C* **2016**, *4*, 10069.

[41] Cook, S. M.; Schäffer, T. E.; Chynoweth, K. M.; Wigton, M.; Simmonds, R. W.; Lang, K. M., *Nanotechnology* **2006**, *17*, 2135.

[42] Kagan, C. R.; Murray, C. B.; Bawendi, M. G., *Phys. Rev.B* **1996**, *54*, 8633.

[43] McConney, M. E.; Singamaneni, S.; Tsukruk, V. V., Polym. Rev. **2010**, *50*, 235.

[44] Sanchez, M. S.; Mateo, J. M.; Colomer, F. J. R.; Ribelles, J. L. G., *Eur. Polym. J.* **2006,** *42*, 1378.

[45] Raghavan, D.; Gu, X.; Nguyen, T.; VanLandingham, M.; Karim, A., *Macromolecules* **2000,** *33*, 2573.

[46] Magonov, S. N.; Elings, V.; Whangbo, M. H., *Surf. Sci.* **1997,** *375*, L385.

[47] Luzinov, I.; Julthongpiput, D.; Malz, H.; Pionteck, J.; Tsukruk, V. V.; *Macromolecules* **2000,** *33*, 1043.

[48] Luzinov, I.; Julthongpiput, D.; Tsukruk, V. V.; *Macromolecules* **2000***, 33*, 7629.

[49] Ash, B. J.; Siegel, R. W.; Schadler, L. S., *J. Polym. Sci. B Polym. Phys.* **2004,** *42*, 4371.

[50] Baranov, A. V.; Rakovich, Y. P.; Donegan, J. F.; Perova, T. S.; Moore, R. A.; Talapin, D. V.; Rogach, A. L.; Masumoto, Y.; Nabiev, I., *Phys. Rev. B* **2003,** *68*, 165306.

[51] Beachell, H. C.; Taylor, H. A., *J. Chem. Phys.***1942**, *10*, 106.

[52] DiOrio, A. M.; Luo, X.; Lee, K. M.; Mather, P. T., *Soft Matter* **2011**, *7*, 68.

[53] Droste, D. H.; Dibenedetto, A. T., *J. Appl. Polym. Sci.* **1969,** *13*, 2149.

[54] Chiou, B.-S.; Khan, S. A., *Macromolecules* **1997**, *30*, 7322.

[55] Cramer, N. B.; Bowman, C. N., *J. Polym. Sci. A Polym. Chem.* **2001**, *39*, 3311.

[56] White, T. J.; Natarajan, L. V.; Tondiglia, V. P.; Bunning, T. J.; Guymon, C. A., *Macromolecules* **2007**, *40*, 1112.

[57] Hoyle, C. E.; Lee, T. Y.; Roper, T., *Polym. Sci. A Polym. Chem.* **2004,** *42*, 5301.

[58] Lee, T. Y.; Bowman, C. N., *Polymer* **2006**, *47*, 6057.

[59] Chen, C.-J.; Chiang, R.-K.; Huang, C.-Y.; Lien, J.-Y.; Wang, S.-L., *RSC Adv.* **2015**, *5*, 9819.

[60] Zhou, H.; Li, Q.; Shin, J.; Hoyle, C. E., *Macromolecules* **2009,** *42*, 2994.

[61] Pfeiffer, H. G.; Liebhafsky, H. A., *J. Chem. Educ.* **1951**, 28, 123.

[62] Gao, X.; Cui, Y.; Levenson, R. M.; Chung, L. W. K.; Nie, S., *Nat. Biotechnol.* **2004**, *22*, 969.

[63] Stutz, H.; Illers, K. H.; Mertes, J., *J. Polym. Sci. B Polym. Phys.* **1990**, *28*, 1483.

[64] Krumova, M.; López, D.; Benavente, R.; Mijangos, C.; Pereña, J. M., *Polymer* **2000**, *41*, 9265.

[65] Ellison, C. J.; Torkelson, J. M., *Nat. Mater.* **2003**, *2*, 695.

[66] Ellison, C. J.; Torkelson, J. M., *J. Polym. Sci. B Polym. Phys.* **2002**, *40*, 2745.

[67] Forrest, J. A.; Dalnoki-Veress, K.; Dutcher, J. R., *Phys. Rev. E* **1997**, *56*, 5705.

[68] Bansal, A.; Yang, H.; Li, C.; Cho, K.; Benicewicz, B. C.; Kumar, S. K.; Schadler, L. S., *Nat. Mater.* **2005**, *4*, 693.

[69] Demir, M. M.; Castignolles, P.; Akbey, U.; Wegner, G., *Macromolecules* **2007**, *40*, 4190.

[70] Lecamp, L.; Youssef, B.; Bunel, C.; Lebaudy, P., *Polymer* **1997**, *38*, 6089.

[71] A. F. Jacobine, *Radiat. Curing Polym. Sci. Technol.* **1993**, *3*, 219.

[72] Timoshenko, S.; Woinowsky-Krieger, S.; Woinowsky-Krieger, S. Theory of Plates and Shells; McGraw-Hill: New York, **1959**; Vol. 2.

[73] Jiang, C.; Markutsya, S.; Pikus, Y.; Tsukruk, V. V., *Nat. Mater.* **2004,** *3*, 721.

[74] Markutsya, S.; Jiang, C.; Pikus, Y.; Tsukruk, V. V., *Adv. Funct. Mater.* **2005,** *15,*771.

[75] Kim, S.; Xiong, R.; Tsukruk, V. V., *Langmuir* **2016**, *32*, 5383.

[76] Gauthier, M. A.; Luo, J.; Calvet, D.; Ni, C.; Zhu, X. X.; Garon, M.; Buschmann, M. D., *Polymer* **2004**, *45*, 8201.

[77] Xia, Y.; Whitesides, G. M., Angew. Chem., Int. Ed. **1998**, *37*, 550.

[78] Ko, H. H.; Jiang, C. Y.; Tsukruk, V. V., *Chem. Mater.* **2005,** *17*, 5489.

[79] Young, S. L.; Gupta, M.; Hanske, C.; Fery, A.; Scheibel, T.; Tsukruk, V. V., *Biomacromolecules* **2012**, *13*, 3189.

CHAPTER 6. COUPLED WHISPERING GALLERY MODE RESONATORS VIA TEMPLATE ASSISTED ASSEMBLY OF PHOTOLUMISCENT MICROSPHERES

6.1 Introduction

Whispering gallery mode (WGM) resonators have been a subject of significant interest over many years due to their potential as microlasing structures. Owing to their relative ease of fabrication, strong optical confinement, high quality factors, and small volume modes, WGM resonators have been intensely pursued in recent years to demonstrate low threshold lasing, directed lasing, and label free detection.[1,2,3] In addition to low threshold lasing, as a result of the light confinement via total internal reflection at the cavity boundary, 99% of light is confined within the cavity, the remaining 1% manifest itself as an evanescent field just outside the cavity extending hundreds of nanometers outside of the circumference of WGM cavities. Small perturbations of this evanescent field can be readily detected, enabling such novel applications as ultra-sensitive label free WGM detectors.[1,4]

Furthermore, interesting coupling phenomena can be observed and exploited by taking advantage of the evanescent field. The field decays with increasing distance, therefore, to experience coupling, cavities need to be in very close proximity of each other, on the order of few hundreds of nanometers or less, to realize overlap of the evanescent fields for advanced applications.[5] Such

coupling phenomena can be the basis for on chip signal processing, wavelength selective amplification, switching, and modulation.[6] Additionally, taking advantage of such interesting phenomenon, researchers have realized low threshold single mode lasing,[7] low-power optical memory,[8] as well as chemical and biological sensors.[4, 9] Of notable interest, coupled micro-ring WGM resonators non-reciprocal light propagation have been fabricated though a multistep, tedious microfabrication process.[7] Colloidal QD paired microdisk resonators in which via spatial pump modulation, parasitic intra-cavity mode splitting was driven into coalescence at an exceptional point due to the evanescent coupling between resonators.[10] While this coupling phenomenon is a very unique and exploitable feature of WGM resonators, achieving efficient coupling between resonators at large scale, well beyond individual unique structures, is quite a difficult feat, often requiring time consuming and low throughput processes such as photolithography, focused ion beam, and electron beam lithography with their own common limitations related to limited resolution and low throughput.[7,11]

One of the most popular WGM resonators, is an ensemble of monodisperse photoluminescent microspheres.[2] In such microspheres light is confined in all directions, enabling ultra-low mode volumes and ultrahigh quality factors.[2] Additionally, the ease of fabrication in a variety of sizes, and simplistic post fabrication modification makes the microspheres quite attractive facile optical components with silica microspheres being most explored to date.[12] Moreover, the surface groups can be utilized for surface modification with metals nanostructures, dyes, and quantum dots.[13, 14] Similarly, polymeric microspheres can be fabricated via emulsion polymerizations for similar purposes.[15, 16] In this case, post modification can be simplified by utilizing swelling using an appropriate solvent and introducing emissive nanostructures.[90]

The unique features of spherical WGM resonators such as their ease to modify, relative monodispersity, uniform surface chemistry, and high stability make them ideal candidates for lasing and sensing applications.[2, 17] For example, Spillane et al. demonstrated ultralow threshold Raman lasing via fiber coupling to 70 um silica microspheres.[18] Similarly, label-free detection was displayed via similar coupling to 50um silica microspheres.[19] As as-synthesized microspheres typically have size variations between 2 and 10%, translating to large shifts in the WGM resonant peaks. With the modest monodispersity there will likely always be dissimilarities from resonator to resonator. However, strong optical coupling between "detuned" spherical cavities still can be observed.[20] Microspheres with larger size deviations showed normal mode splitting, indicating strong coupling.

However, fine tuning of WGM via coupling between neighboring spherical resonators has been seldomly explored. Attempts at microsphere coupling involved micromanipulator setups to change the inter-microsphere distance,[21] and the random assembly of microsphere aggregates in which microspheres closely packed in linear chains and other geometries.[22] Controlling the location of the micromanipulated exciting microfiber, the equatorial WGM plane could be adjusted, thereby displaying control over the coupling distance between neighboring resonators. Controlled coupling was achieved by moving the resonators via an elastomeric substrate,[23, 24] or by control of inter-resonator separation via a piezo-positioner.[25] While coupling was demonstrated in these systems, an ideal system with practical realization would have a more simplistic setup that be readily fabricated in large reproducible arrays more practical implementation.

An exploitable approach to take advantage of variable coupling between neighboring microresonators at larger scale and in facile fashion should involve directed, template-based assembly.[26] It has been shown that the balance of capillary forces and convective transport can be exploited for directed assembly from microsphere suspensions into two-dimensional arrays resulting in opals, inverse opals, and other photonic crystals.[27,28] Furthering these findings, the ability to assemble aggregates of complex geometries was facilitated by exploiting a photolithography derived template.[26,29] Simply by modifying the size and shape of the underlying patterns, controlled aggregates of microspheres have been demonstrated. Additionally, using wrinkled surfaces, depending on the periodicity and height of the wrinkled features, microspheres can be controllably assembled in chain-like structures and patterned via selective deposition in wrinkled trenches.[30]

While these techniques offer quite a unique feat in the assembly of microspheresvto implement such a system to exploit its optical benefits, one important parameter in attempt to achieve coupling between neighboring resonators is the precise placement of resonators, thereby controlling the coupling gap below 400 nm which is difficult to achieve with traditional photolithographical approaches.

6.2 Experimental Methods

Chemicals and materials: Ip-Dip resist was obtained from Nanoscribe GmbH. Rhodamine 6G and ITO glass were obtained from Sigma-Aldrich. Silica Microsphere were obtained from Polysciences.

Nanoscribe 3D two-photon Lithography: Templates were fabricated using a Nanoscribe Photonic Professional GT instrument.[31] Ip-Dip resist was placed on an ITO substrate in the dip in laser lithography (DILL) configuration and Autocad renderings were polymerized onto the substrate using a 780nm laser.[31] The laser was focused onto the substrate using a 63x (NA = 1.4) objective. The patterns were exposed in galvo mode at a rate of 5000 μm/s and a laser power of 30-50%, using a hatching and slicing distance of 0.2 μm. Arrays sizes were typically 140 μm x 100 μm, and generally it takes about 5 minutes to complete the fabrication of each array. Following light exposure, samples were developed by submerging in SU8 developer for 20 minutes, and immediately in isopropyl alcohol for two minutes, and drying under a stream of N_2 gas.

Templated Assembly: Flow cells were fabricated by taking the ITO substrate with the Nanoscribe pattern and lining three edges with ~50 μm thick mylar tape, leaving one edge free of mylar. An unpatterned glass slide was placed on the top of the first substrate and held in place using three binder clips. The binder clips were placed only on the edges where the mylar film was placed. Microspheres were assembled by injecting a dilute aqueous solution of microspheres doped with R6G dye into the open side of the fluid cell. Microspheres were deposited atop predetermined holes as the aqueous suspension evaporated through the fluid cell.[26]

Confocal Microscopy: The samples were placed on a three-dimensional stage under a WiTec confocal Raman microscope (Alpha 300R) with a fiber-coupled Nd:YAG laser ($\lambda = 532$ nm). The beam was focused through a 50× (NA = 0.75) microscope objective onto the sample using a

dichroic mirror. The emission from the sample was collected through the same objective transmitted through the dichroic mirror as well as a notch filter, focused onto a multimode optical fiber and recorded using a 1/2 m spectrometer and CCD array. The spectral revolution of the setup was 0.02 nm.

FDTD Simulations: The LUMERICAL FDTD software package was used to investigate coupling between WGM modes in microspheres of diameter, D = 3.6 μm, as a function of the gap spacing. The refractive index was set to n = 1.46 and a WGM at 609 nm (in vacuum) was simulated. Coupling was investigated by pumping only one of two microspheres, with diameters of D = 3.6 μm, at gap spacings of 400nm and 1000nm, and observing the formation of modes via evanescent leakage in the un-pumped sphere. In all cases, the electric field profiles and spectra were observed in the plane of excitation.

6.3 Results and Discussion

Herein, we demonstrate the ability to precisely assemble photoluminescent microspheres as coupled paired microbead resonators in predefined high-resolution hole templates with controlled gap spacing down to 50 nm as a result of template assisted assembly **(Figure 6.1).** Instead of using the traditional template cavities as "trapping sites", we push the precision of the coupled positioning by using arrays fabricated via 3-D lithography based upon two-photon polymerization writing.[32] Taking advantage of the sub-100 nm resolution of the two-photon writing technology and the ability to fabricate any arbitrary shape, we demonstrated the control of the coupling and microsphere whispering gallery modes based on the proximity of neighboring resonators. Fast (minutes) and facile fabrication of arrays of microresonators provides novel capabilities for photonic integrated technologies, leading to high throughput microlasers and micro-combs.[33]

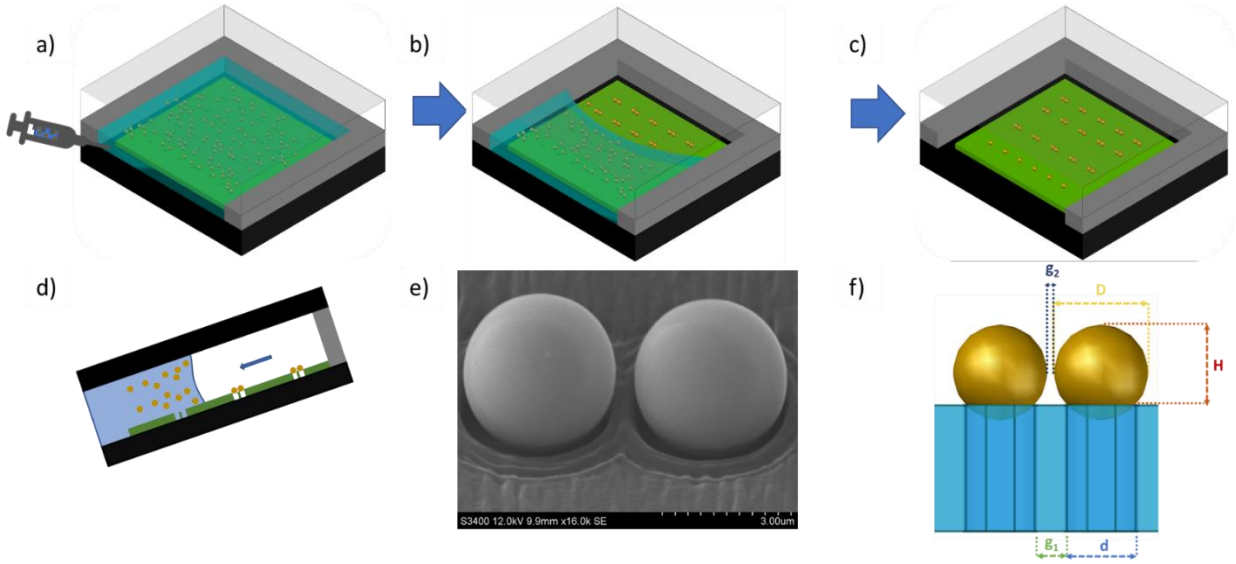

Figure 6.1: Steps of templated assembly in which aqueous suspension is injected into flow cell, as suspension evaporates through the flow cell microsphere are deposited atop predefined cavities. (a-c). Side profile shows microspheres are only partially embedded inside holes (e,f). SEM confirmation Scale bar is 3 µm.

Firstly, a 3D rendering of the pattern of interest is designed for 3D two-photon lithography, with varied gap distances between coupled resonators (see Appendix, Figure C.1). The pattern is then repeatedly fabricated on ITO, followed by exposure to a <0.1 wt. % aqueous suspension of ~3.6 µm microspheres in order to assemble the microspheres (**Figure 6.1**). First an aliquot of an aqueous suspension of microspheres is injected into a fluidic cell. Via capillary forces the solution slowly evaporates through the cell, depositing microspheres atop predefined holes. Based on the predefined geometry of each cavity fabricated via 3D lithography, only one microsphere can assemble into each hole. The entire assembly process is fast, usually completed in a matter of minutes.

Given the microsphere fabrication does typically result in modestly monodisperse microspheres, the template cavities were designed to exclude sizes above 3.6 μm in order to minimize size deviations between neighboring cavities and enhance uniformity of coupled microspheres. Additionally, the template is designed so that the distance between coupled dimers varies from

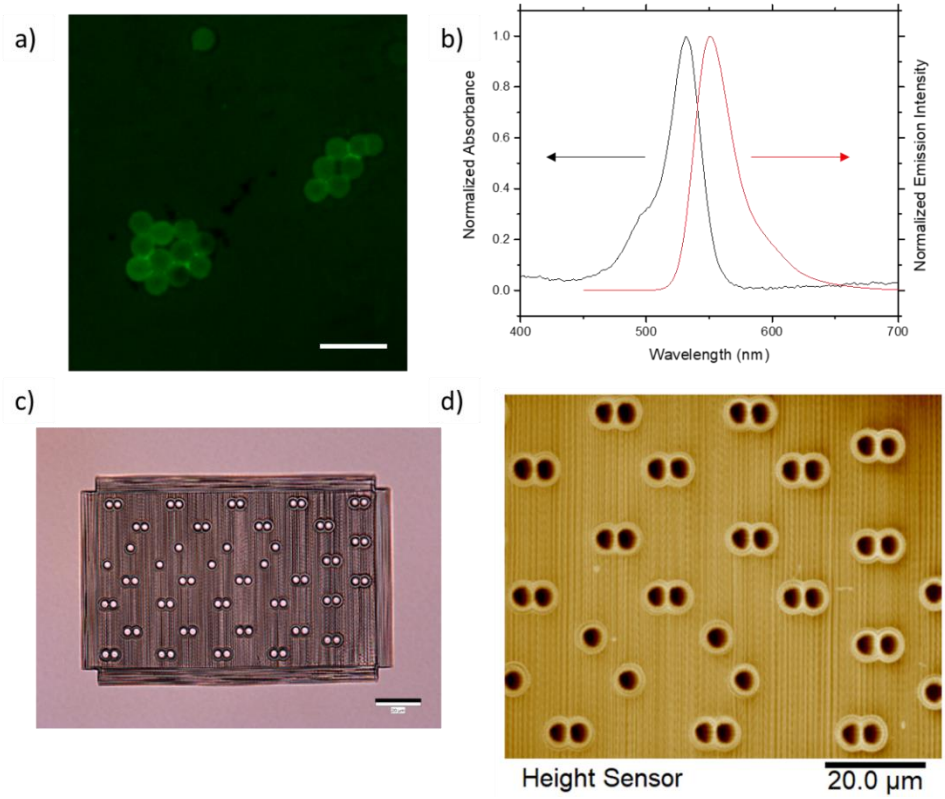

Figure 6.2: Fluorescence of dye-doped microspheres, scale bare is 10 μm (a), absorbance and fluorescence spectrum of doped microspheres (b), brightfield image of template used to assemble microspheres showing monomer and dimer structures (c), touching to hundreds of nanometers and microspheres are trapped in a shallow manner, thus facilitating close distances at their diameter (Figure 6.1) In this design, we can overcome resolution limitation of about 200 nm and push the gap dimension further below, to 50-100 nm (Figure 6.1).

Using a post modification, silica microspheres are decorated with a fluorescent dye, Rhodamine 6G (R6G) by exploring complementary Coulombic interactions mediated by excessive surfactant (**Figure 6.2a**).[34] Strong green emission of the microspheres is close to the selective light absorption at 540 nm and light emission at 550 nm (Figure 6.2a, b). Bright field image of various lithographical patterns for assembling 3.6 um microspheres along with AFM images show high quality of the templates (Figure 6.2) (see other examples in Figure C.2 – C.5). The assembly "yield" calculated by taking the number of holes filled and dividing by the number of initial holes available, is relatively high, at least 75% in most cases even if we use diluted solution to avoid aggregation (**Figure 6.3a**). Therefore, the capillary forces exerted by the liquid slug are enough to selectively remove un-trapped microspheres from the top surface of the template with post-washing.

Since the template cavities are designed to be spherical holes, and there is low surface roughness, the microspheres typically assemble exactly in the center of the cavity (Figure 6.3, Figure C.6a). By taking advantage of 3D writing lithography, not only do we achieve higher resolution than photolithography, but we can push further the resolution by strategic design of the size and shape of cavities. Indeed, SEM imaging of coupled cavities with designed spacing of 50, 200, 350, and

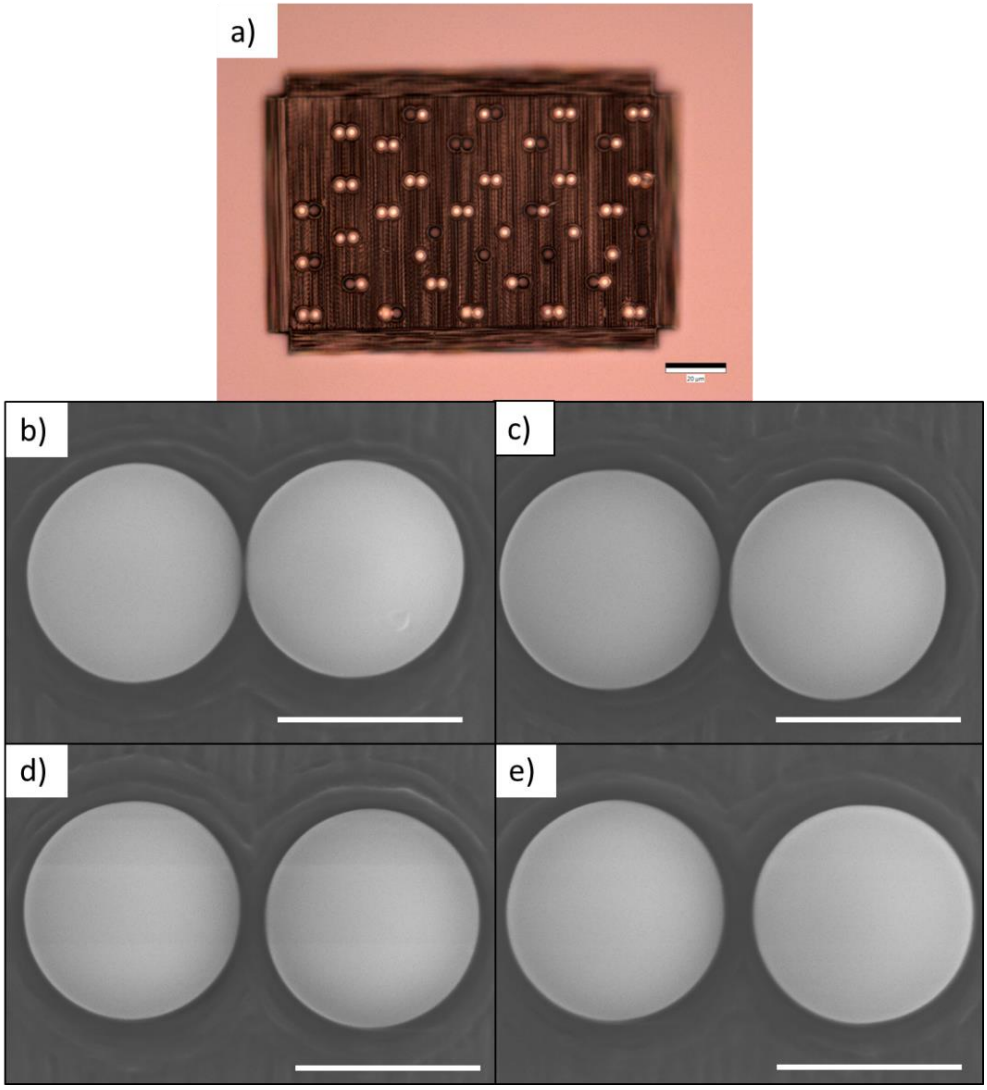

Figure 6.3: (a) Array of coupled microspheres after assembly. Scale bar is 20 µm. Representative SEM images of dimers showing spacing of 50nm (b) 200nm (c) 350nm (d) and 500nm (e). Scale bar is 300 µm

500nm show that while the true spacing is slightly larger than designed, resolution of hundreds of nanometers is still achieved (Figure 6.3b-3e). In most cases, during the templated assembly the microspheres settle in specific positions relative to the neighboring sphere. It is worth noting that, colloidal microspheres are only partially embedded in the template with majority of the microsphere being in the surrounding medium (air) (Figure 6.1 and C.6b). Furthermore, the cavity diameters were designed to be smaller than that of the microsphere in order to sort out microspheres with fitted diameter and elevate the microspheres to sort out micropsheres with larger diameter and "geometrically" reduce minimum gap (Figure 6.1).

Indeed, given the size of the cavity and the approximate diameter of the microsphere, the height

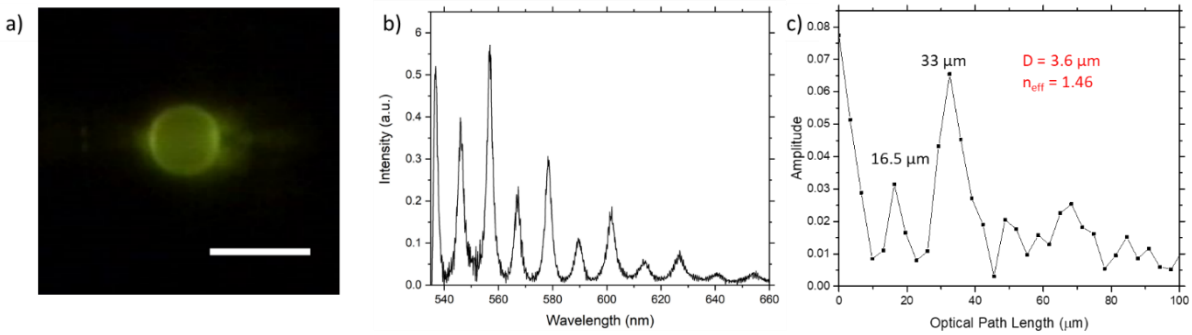

Figure 6.4: (a) darkfield image of microsphere under laser irradiation; (b) spectrum of individual microsphere showing WGM resonant peaks; (c) FFT of wavelength spectrum showing optical path length of resonators.

of the exposed microsphere can be calculated by $H=D/2+\sqrt{((D/2)^2-(d/2)^2}$), where D is the sphere diameter and d is the cavity diameter (Figure 6.1f). Due to the 3D lithography writing limitation, the smallest gap size, g_1, between cavities achievable is around 200 nm (Figure 6.1, Figure C.1a). Thus, taking a microsphere diameter of 3.6 μm, and a cavity diameter of 3.4 μm,

approximately 2.2 μm of the microsphere would be above the level of the substrate, allowing for a much smaller gap between resonators, g_2 (Figure 6.1f). For the example given, for the actual gap size of around 800 nm, the 3.6 μm microspheres will be placed with the 600 nm gap (Figure C.1d). This way, direct placement of microsphere pairs with gap below 100 nm can be realized (Figure 6.2a). Taking this into consideration it is possible to tune the cavity size (depth) and precisely assemble coupled microspheres with interparticle spacing down to sub-50nm resolution thus, overcoming common limitation of 3D writing technology of 200 nm.

To understand the effect of the assembly of the dimers on the coupling behavior, the whispering gallery modes of the microsphere resonators have been investigated via the backscattering imaging using a confocal microscopy with a 0.02 nm spectral resolution (**Figure 6.4a)**. A representative spectrum for a monomer assembled into a template shows a series of intense WGM resonant peaks (Figure 6.4b). Shifts in the peak locations are observed for different microspheres, typically $\leq$ 5nm, likely due to deviations in the sphere diameters. The quality factor, $\lambda/\delta\lambda$, where λ is the resonant wavelength (e.g., 566 nm) and $\delta\lambda$ is its linewidth (2 nm), is close to 300, in good agreement with those reported earlier for silica spheres of similar size.[21]

By converting the WMG spectra to reciprocal space with the Fourier transformation, it is possible to calculate the optical path length $\Delta l = n_{eff}\pi D$ for this microsphere (Figure 6.4c).[3] Taking the distance between the first and second Fourier harmonics, an optical path length is calculated of 16.5 μm and effective refractive index, n_{eff} is estimated to 1.46. These values correspond to the expected values for pure SiO_2, indicating that the fields of the WGMs are contained within the individual microspheres.[35]

Next, by analyzing WGM modes, the resonant positions for first order mode (quantum number q=1, where q is the number of intensity maxima displayed in the radial direction), can be approximated based on the equations for transverse electric (TE) and transverse magnetic (TM) fields, respectively:[36]

$$\lambda_{TE} \approx \frac{2\pi R\sqrt{\varepsilon\mu}}{\nu + 1.85576\nu^{1/3} - \frac{1}{\mu}\sqrt{\frac{\varepsilon\mu}{\varepsilon\mu - 1}}} \tag{6.1}$$

$$\lambda_{TM} \approx \frac{2\pi R\sqrt{\varepsilon\mu}}{\nu + 1.85576\nu^{1/3} - \frac{1}{\varepsilon}\sqrt{\frac{\varepsilon\mu}{\varepsilon\mu - 1}}} \tag{6.2}$$

where ε and μ are the dielectric constant and permeability, respectively and υ is the angular mode number, m, plus ½ (m+1/2). In the case of dielectric silica microspheres, μ = 1. $\sqrt{\varepsilon\mu}$ is represented by the refractive index of the material (1.46) and a radius, R, of 1.77 μm.

The analysis shows that TM modes are suppressed, as they are typically more confined, in addition there are large contributions from the broadband fluorescence. The free spectral range (FSR),

dictating the separation between adjacent modes can be approximated by $\delta\lambda = \lambda^2/2\pi nR$, in this particular system, using 609 nm as the wavelength position, the FSR is approximately 23 nm, in good agreement with what is observed in the spectrum of the individual microsphere (Figure 6.4b).

Furthermore, the formation of WGM resonant peaks was simulated with finite difference time domain (FDTD) modeling for individual microsphere as excited by a pulsed source and the electric field is simulated (see Figure C.7). Comparison of the experimental results and simulations shows the formation of two sets of modes with similar spacing (compare Figure 6.4b and Figure C.7b). In the simulation results, the TM modes seem to be much weaker, nearly suppressed, likely due to the position of the detector as well as the confinement of TM modes.

Following assembly of the microbeads into the predefined cavities, individual and coupled microspheres with controlled gap spacing were analyzed to understand how the change in gap distance effects the coupling behavior of neighboring resonators (**Figure 6.5)**. While the laser irradiates only one sphere, scattering from the laser spot, as well as leakage from the sphere results in the excitation of both microspheres. Depending on the location of the incident beam, a high intensity light spot arises on the opposite side of the sphere and into the neighboring sphere,

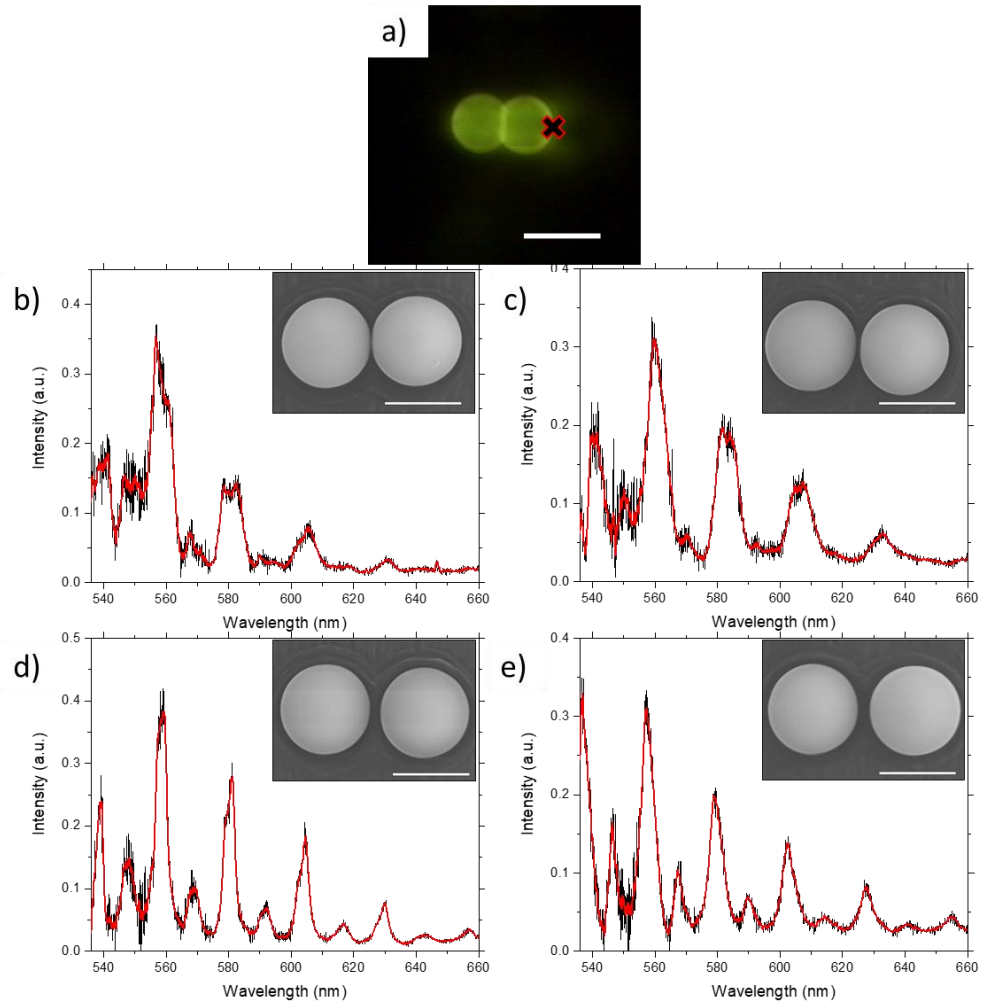

Figure 6.5: Coupled dimer WGM formation following excitation on one end: (a) nominal dimer spacing of 0 nm (b), 200nm (c), 350nm (d), and 500nm (e). Inset shows SEM for each respective dimer. Scale bars of optical and SEM images are 5 and 3 µm, respectively.

suggesting lasing behavior (Figure 6.5a).[37]

Under these excitation conditions, and given the size of the cavities used, only first order mode (q=1) typically due to the generally low-quality factors of resonators of this size.[38] With this realization it becomes easier to identify coupling between modes, without any interference between neighboring modes of higher order. When WGM resonators are in close proximity of one another, such that the evanescent fields can interact, it is expected that coupling will result in mode splitting of resonant peaks.[39]

Similar to the classical case of identical pendulums coupled via a spring, eigenmodes can be observed in two cases: when the pendulums swing in phase with each other and when they swing alternatively towards and away from one another. The mode splitting is mainly due to the coupling of the systems, resulting in the oscillating at a slower rate when in phase, and slightly faster when out of phase. In optical resonators this is manifested as normal mode splitting in coupled harmonic oscillators which results in the formation of bonding and antibonding modes.[21,40]

Starting at direct touching of microsheperes (near 0 nm separation) coupling between neighboring microsphere resonators manifests itself in splitting of the major resonance peaks, with a $\Delta\lambda \approx 4$nm (Figure 6.5b). For larger spacing, mode splitting is observed as well (Figure 6.5d-f). However, the splitting appears smaller, $\Delta\lambda \approx 3$ and 1.5 nm for spacing of 200 nm and 350nm, respectively, nearly diminishing for microsphere pairs with the largest gap distance of 500 nm. If mode splitting is larger than the FWHM of the original peaks for individual micrpspheres the strong coupling

regime is observed.[20] Given the initial δλ in the case of the monomer of approximately 2 nm, as the gap distance is increased it appears as though the mode splitting decreases, suggesting a transition from the strong coupling regime to the weak coupling regime.

To futher corroborate these findings, FDTD analysis was used to characterize mode coupling between microsphere pairs (**Figure 6.6**). To monitor the coupling, only one microsphere of the pair was pumped, while the mode profiles of both microspheres are visualized. Figures 6a and 6b shows microsphere pairs for different gaps. Under these conditions, mode coupling can clealry be observed in both cases, as the mode from the pumped sphere leads to the fromation of WGMs in the un-pumped sphere. Moreover, spectral analysis shows that strong mode splitting is observed when microspheres are near touching (with $\Delta\lambda \approx 4$nm) and shows a near exponential decay to zero as the gap spacing aproaches 1000 nm (individual microsphere) which is in good accord with

experimental trends. The splitting obtained in simulations may decrease more slowly than experiment as the optical loss from the templates has not been included (Figure 6.6c). Finally, the splitting of every mode, which was observed in the experimental studies also appears in the simulation (Figure 6.6d and Figure C.8).

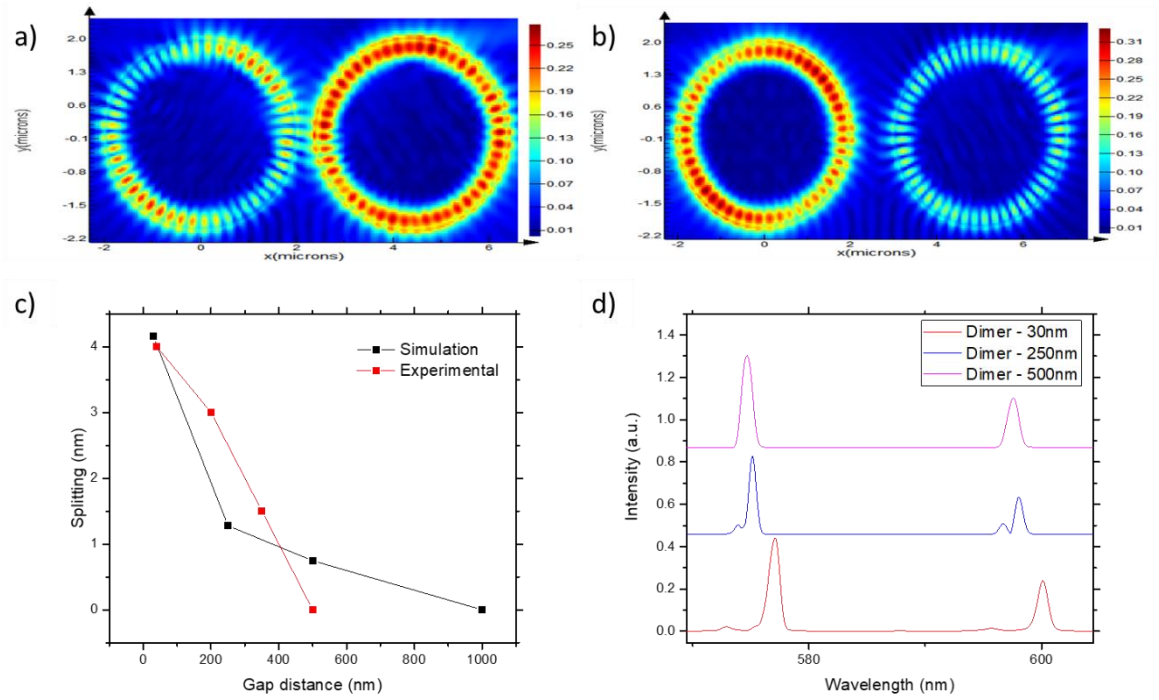

Figure 6.6: FDTD analysis showing modal coupling a distance of 400 nm(a) and 1000 nm (b), mode splitting vs gap distance plot showing exponential decay of splitting (c) and representative spectra for near touching and 1000 nm gap (d).

It is important to note that, traditionally, for coupled resonator systems in which identical resonators are placed side by side and both excited, their degeneracy is broken, which gives rise to the mode splitting.[40] For example, mode splitting has been demonstrated for uniformly pumped microring resonators, causing mode splitting of each respective resonant mode. Coincidentally, when the pump is witheld from one of the resonators, the resulting spectrum changes significantly.

Single-mode lasing is achieved in which the lossy resonator (in which there was no pumping) serves as a suppresing mechanism for unwanted mode operation.[7] Similarly, the ability to probe the resonant modes of undoped microspheres of various configurations has been demonstrated.[22] By coupling light via a side-coupled tapered fiber, various linear and more complex microsphere geometries can be excited to investigate their spectral signature in which the number of split modes was dependent on the number of microspheres. Additionally, controlled coupling, which was demonstrated by the placement of the tapered microfiber, resulted in control of the coupling strength. Similarly, excitation of the fluorescent dye embedded in the microspheres results in the excitation of both resonant modes, and splitting which is strongly influenced by the resonator coupling.

6.4 Conclusions

In summary, we demonstrated coupled microsphere pairs in which the gap can be controlled down to sub-50 nm, well exceeding the achievable precision demonstrated to date. By taking advantage of the facile and fast directed assembly on high-resolution 3D writing lithography templates, we demonstrated a high degree of control over the microsphere placement in an large array template. Additionally, by using the cavities as trapping sites, we further control the spacing between coupled dimers by leaving majority of the microsphere resonator exposed thus, further overcoming the 200 nm resolution limit for initial templates and initiate coupling of WGM modes. Coupling-induced mode-splitting trends were confirmed by FDTD simulations.

Such systems can be instrumental to demonstrate such phenomenon as PT-symmetry breaking at large scale, taking advantage of the precise placement of microresonators as tunable coupling is critical for such systems. Additional work should focus on analyzing the lasing thresholds, directional lasing, and sensing behavior of the coupled microresonators, with a particular focus on microspheres doped with quantum dots, to take advantage of their absorption and emission tunability via size, allowing for tunable excitation, in addition to their high photoluminescence and stability.

6.5 References (Chapter 6)

[1] Yang, S.; Wang, Y.; Sun, H., *Adv. Opt. Mater.* **2015**, 3, 1136.

[2] Vahala, K. J., *Nature* **2003**, 424, 839.

[3] Lin, C. H.; Zeng, Q.; Lafalce, E.; Smith, M. J.; Malak, S. T.; Jung, J.; Yoon, Y. J.; Lin, Z.; Vardeny, Z. V.; Tsukruk, V. V., *Adv. Opt. Mater.* **2017,** *5*, 1700011.

[4] Vollmer, F.; Arnold, S., *Nat. Methods* **2008**, 5, 591.

[5] Wangsness, R. K., *Electromagnetic Fields*, 2nd Edition,Wiley, Hoboken, NJ 1986.

[6] Choi, J. M.; Lee, R. K.; Yariv, A., *Opt. Lett.* **2001,** *26*, 1236.

[7] Hodaei, H.; Miri, M.-A.; Heinrich, M.; Christodoulides, D. N.; Khajavikhan, M., *Science* **2014**, 346, 975.

[8] Hill, M. T.; Dorren, H. J. S.; de Vries, T.; Leijtens, X. J. M.; den Besten, J. H.; Smalbrugge, B.; Oei, Y.-S.; Binsma, H.; Khoe, G.-D.; Smit, M. K., *Nature* **2004**, 432, 206.

[9] White, I. M.; Oveys, H.; Fan, X.; Smith, T. L.; Zhang, J., *Appl. Phys. Lett.* **2006**, 89, 191106.

[10] Lafalce, E.; Zeng, Q.; Lin, C. H.; Smith, M. J.; Malak, S. T.; Jung, J.; Yoon, Y. J.; Lin, Z.; Tsukruk, V. V.; Vardeny, Z. V., *Nat. Commun.* **2019,** *10*, 561.

[11] Peng, B.; Özdemir, Ş. K.; Rotter, S.; Yilmaz, H.; Liertzer, M.; Monifi, F.; Bender, C. M.; Nori, F.; Yang, L., *Science* **2014,** *346*, 328.

[12] Stöber, W.; Fink, A.; Bohn, E., *J. Colloid Interface Sci.* **1968**, 26, 62.

[13] Pastoriza-Santos, I.; Gomez, D.; Pérez-Juste, J.; Liz-Marzán, L. M.; Mulvaney, P., *Phys. Chem. Chem. Phys.* **2004**, 6, 5056.

[14] Gómez, D. E.; Pastoriza-Santos, I.; Mulvaney, P., *Small* **2004**, 1, 238.

[15] Shim, S.-E.; Cha, Y.-J.; Byun, J.-M.; Choe, S., *J. Appl. Polym. Sci.* **1999**, 71, 2259.

[16] Han, M.; Gao, X.; Su, J. Z.; Nie, S., Nat. Biotechnol. **2001**, 19, 631.

[17] Vollmer, F.; Arnold, S., *Nat. Methods* **2008,** *5*, 591.

[18] Spillane, S. M.; Kippenberg, T. J.; Vahala, K. J., *Nature* **2002,** *415*, 621.

[19] Vollmer, F.; Arnold, S.; Keng, D., *Proc. Natl. Acad. Sci. U. S. A.* **2008,** *105*, 20701.

[20] Kanaev, A. V.; Astratov, V. N.; Cai, W., *Appl. Phys. Lett.* **2006,** *88*, 111111.

[21] Mukaiyama, T.; Takeda, K.; Miyazaki, H.; Jimba, Y.; Kuwata-Gonokami, M., *Phys. Rev.*

Lett. **1999,** *82*, 4623.

[22] Li, Y.; Abolmaali, F.; Allen, K. W.; Limberopoulos, N. I.; Urbas, A.; Rakovich, Y.; Maslov, A. V.; Astratov, V. N., *Laser Photonics Rev.* **2017**, 11, 1600278.

[23] Ashili, S. P.; Astratov, V. N.; Sykes, E. C. H., *Opt. Express* **2006**, 14, 9460.

[24] Huang, F.; Baumberg, J. J., *Nano Lett.* **2010**, 10, 1787.

[25] Ilchenko, V. S.; Gorodetsky, M. L.; Vyatchanin, S. P., *Opt. Commun.* **1994**, 107, 41.

[26] Yin, Y.; Lu, Y.; Gates, B.; Xia, Y., *J. Am. Chem. Soc.* **2001,** *123*, 8718.

[27] Ozin, G. A.; Yang, S. M., *Adv. Funct. Mater.* **2001,** *11*, 95.

[28] Norris, D. J.; Arlinghaus, E. G.; Meng, L.; Heiny, R.; Scriven, L. E., *Adv. Mater.* **2004,** *16*, 1393.

[29] Xia, Y.; Yin, Y.; Lu, Y.; McLellan, J., *Adv. Funct. Mater.* **2003,** *13*, 907.

[30] Lu, C.; Möhwald, H.; Fery, A., *Soft Matter* **2007,** *3*, 1530.

[31] Bückmann, T.; Stenger, N.; Kadic, M.; Kaschke, J.; Frölich, A.; Kennerknecht, T.; Eberl, C.; Thiel, M.; Wegener, M., *Adv. Mater.* **2012,** *24*, 2710.

[32] Olszyna, M.; Debrassi, A.; Üzüm, C.; Dähne, L., *Adv. Funct. Mater.* **2019,** *29*, 1805998.

[33] Pasquazi, A.; Peccianti, M.; Razzari, L.; Moss, D. J.; Coen, S.; Erkintalo, M.; Chembo, Y. K.; Hansson, T.; Wabnitz, S.; Del'Haye, P.; Xue, X.; Weiner, A. M.; Morandotti, R., Phys. Rep. **2018**, 729, 1.

[34] Mubarekyan, E.; Santore, M., *Langmuir* **1998,** *14*, 1597.

[35] Polson, R. C.; Vardeny, Z. V.; Chinn, D. A., *Appl. Phys. Lett.* **2002,** *81*, 1561.

[36] Oraevsky, A. N., Whispering-gallery waves. *Quantum Electron.* **2002,** *32*, 377.

[37] Serpengüzel, A.; Küçükşenel, S.; Chang, R. K., *Opt. Express* **2002,** *10*, 1118.

[38] Weller, A.; Liu, F. C.; Dahint, R.; Himmelhaus, M., *Appl. Phys. B: Lasers Opt.* **2008,** *90*, 561.

[39] Thompson, R. J.; Rempe, G.; Kimble, H. J., *Phys. Rev. Lett.* **1992,** *68*, 1132.

[40] Rakovich, Y. P.; Donegan, J. F.; Gerlach, M.; Bradley, A. L.; Connolly, T. M.; Boland, J. J.; Gaponik, N.; Rogach, A., *Phys. Rev. A: At., Mol., Opt. Phys.***2004,** *70*, 051801.

CHAPTER 7. ROBUST LASING MODES IN COUPLED COLLOIDAL QUANTUM DOT MICRODISK PAIRS USING A NON-HERMITIAN EXCEPTIONAL POINT

7.1 Introduction

Non-Hermitian Hamiltonians are used to describe open quantum systems that exchange energy with their environment.[1,2,3,4] In contrast to their closed, Hermitian counter-parts, the family of eigenvalues may be complex, with the imaginary part describing the growth or decay of the amplitudes of the associated eigenfunctions. A surge in interest in Non-Hermitian formalisms and experimental model systems has been fueled by the unusual behavior associated with exceptional points (EP), which are non-Hermitian analogues of quantum degeneracies, where both the real and imaginary eigenvalues coalesce.[2,3] EPs occur at points in the complex parameter space of eigenvalues that is controlled by the strength of the imaginary potential and coupling between two or more modes. Not limited to quantum systems, these concepts have been largely explored in classical optical systems, including those based on Parity-Time symmetry[5,6], that include microwave and optical microcavities[7,8,9,10], waveguides[11,12], and photonic crystals[13,14]. Several counter-intuitive and novel optical phenomena have been realized in these studies, including reversed pump-dependence in lasers[14,15,16,17], unidirectional light propagation[18,19] and topologically-driven state exchange[8,9,10,20]. Circular microcavities laser such as that support whispering-gallery modes (WGMs) have been an exceptionally fruitful platform in which to study and utilize the physics of EPs including the demonstration of selective mode-filtering in PT-symmetric coupled cavities[21] to enforcing single-mode operation in microlasers[22,23] and the ability to implement high degrees of chirality and directionality[24,25] to WGMs which has enabled the

realization of lasers producing beams with orbital-angular momentum[26] and the elimination spatial hole burning[27], all on a micro-chip scale.

These initial observations have impressively demonstrated the power of utilizing EPs to control the behavior of the related Non-Hermitian systems. However, these implementations have so far relied on precisely designed and well-controlled material systems to achieve the desired performance. The sensitivity of the EP to the implemented values of index of refraction, optical gain and loss, and the coupling between modes requires all of these parameters to be simultaneously maintained, and only limited attention has been given to the robustness of the EP in the presence of disorder such as thermal modulation or structural imperfection. Being elementary in nature, most applications have involved only two interacting modes. Expanding the flexibility of these materials and architectural requirements is a necessary step in order to obtain more general platforms for utilizing the phase-change-behavior of non-Hermitian optics.

It is desirable to develop more flexible materials systems for photonics, particularly for micro-photonics and on-chip photonics. These include the solution based, chemically tunable materials such as π-conjugated polymers, hybrid perovskites and colloidal quantum dots. In particular, colloidal quantum dots (CQDs) are nanosized semiconductor particles that possess large optical cross-sections such as stimulated emission and absorption. The emission of CQDs can be tuned to cover a wide spectral range from ultra-violet to infrared regions by simply changing their size or composition, providing flexibility to the design of advanced photonic systems that requires lasing emission at specific wavelength[28]. These properties make CQDs a promising photonic

component that need be studied and developed for future lasing applications. In addition, the ease-of-fabrication can be utilized to create micro-cavities made of solution-processable CQDs by using standard lithographic techniques and a wide variety of substrates.[29] This shows processing advantages over more commercially mature technology based on inorganic semiconductor alloys and multiple quantum wells that are grown via high-vacuum film processing and strict requirements of lattice-matching. It is an interesting question as to whether Non-Hermitian photonics may be implemented on a less exacting platform such as the CQDs.

In the present work we investigate WGMs from microdisk cavities formed from robust crosslinked assemblies of core/alloyed-shell $CdSe/Cd_{1-x}Zn_xSe_{1-y}S_y$ CQDs fabricated by a scalable lithographic process. The majority of the microdisks studied here exhibit WGM-splitting associated with local defects on the disk circumference, which are a natural result of the high-throughput, flexible design approach. Despite this, we demonstrate here localization/delocalization phase-change behavior in near-field-coupled pairs of microdisks. A study of the emission spectra from microdisk pairs reveals that actively pumped interacting microlasers produce spectra more robust against the appearance of mode-splitting. By spatial variation of gain and loss in the coupled microcavity pairs, we show that the removal of the localized parasitic modes originates from their coalescence at an exceptional point of the non-Hermitian multi-mode system. In particular, we show that the intra-cavity mode splitting can be driven into coalescence through inter-cavity coupling in the presence of gain/loss variation. This phenomenon may potentially be used to circumvent some of the inherent obstacles in using solution-based semiconductor materials for lasing and improve the quality of laser emission by reducing the number of parasitic modes in the output.

7.2 Experimental Methods

Chemicals and Materials

1,7 diaminoheptane (DIAH, 98%) and ethyl lactate was obtained from Sigma Aldrich. Toluene and heptane were obtained from BDH Chemicals. CYTOP was obtained from AGC Chemicals. NR 71-3000p photoresist was purchased from Futurrex. All chemicals were used as received.

Microdisk Fabrication.

Fabrication of QD microdisks includes several steps. First, a low refractive index layer of CYTOP (n = 1.34) was deposited on the silicon wafer (n = 3.44) in order to provide light confinement within the QD cavities. CYTOP solution was spun cast on the substrate with a spin speed of 2500rpm for 3 minutes. A subsequent baking at 100℃ for 30 minutes was performed. This process was repeated two times to achieve film thickness of 1.5 μm. A short oxygen plasma etch (5 seconds) was performed to improve the wettability of the CYTOP surface for the deposition of the negative photoresist (NR 71-3000p). Ethyl lactate was added to the negative resist NR71-3000p solution to dilute it to one third of the original concentration provided by the company. The diluted resist was spun cast on the CYTOP/silicon substrate (3000 rpm for 1 minute). The cast film was subsequently soft baked at 165℃ for 5 minutes and exposed to 365 nm with a dosage of 123mW. The exposed film was then post-baked at 100℃ for 5 minutes and developed by soaking in RD6 developer for 5 sec. After the development, the film was rinsed with water and dried by blowing with air. The QD microdisks were fabricated by spin casting butylamine-capped QD

solution (in heptane) of ~3-6 mg/mL at 1000 rpm for 1 minute onto the polymer pattern. The cast layer was subsequently immersed in 0.1M diaminoheptane solution in methanol for 1 minute and rinsed with methanol 2 times while spinning at 3000 rpm for 1 minute. The above process was repeated multiple times to achieve the desired thickness. The polymer pattern was subsequently removed by soaking in acetone while sonicating for 3-10 seconds. The characterization of gain properties of films was previously described.[30]

Optical Characterization.

The samples were placed on a three-dimensional stage under a home-built confocal micro-photoluminescence set-up. The excitation source was provided by a the second harmonic (532nm) of a solid-state pulsed laser based on Nd:YAG delivering 7ps pulses at a repetition rate of 200Hz. The beam was focused through a 40x (NA=0.65) microscope objective onto the sample using a dichroic mirror (550nm long-pass). The emission from the sample was collected through the same objective transmitted through the dichroic mirror as well as an additional 550nm long-pass filter, focused onto a multimode optical fiber and recorded using a 1/2m spectrometer and CCD array. The spectral revolution of the setup was 0.2nm. Alternatively, a camera was placed in the emission path to collect PL images of the disks. The beam size was set to with an iris a 50μm in diameter.

FDTD Modelling

Resonator coupling strength was calculated using Lumerical Mode Solutions. The model was based on the real QD system, with a stack of 5 layers: Si (3 μm)/ SiO2(292 nm)/ CYTOP(1.5 μm)/

QD(varied thickness)/ air(5 μm). The power confined in the QD layer was integrated by using the option of power and intensity integration.

7.3 Results and Discussion

To fabricate CQD microdisk lasers, we have adopted a facile one-pot method to synthesize high quality compositional gradient core/alloyed-shell QDs with an average size of 7.5 ± 0.8 nm (Fig. 7.1a, upper) (see Methods for detailed synthesis procedure). The gradient shell helps to significantly suppress the Auger recombination, which has been the main obstacle to achieve lasing in CQD films in the past. We then utilize a hybrid top-down and bottom-up approach that we previously developed to fabricate the microdisk laser arrays[29] (details described in Methods). In brief, this approach combines standard photolithography that provides up-scalability and precise control of spatial distribution to these CQD assemblies, as well as layer-by-layer deposition to integrate tiny CQDs into photoresist-templated trenches along with the crosslinking of ligands to enhance the mechanical integrity. An SEM image of the resulting microdisk structure is shown in the lower image of Fig. 7.1a.

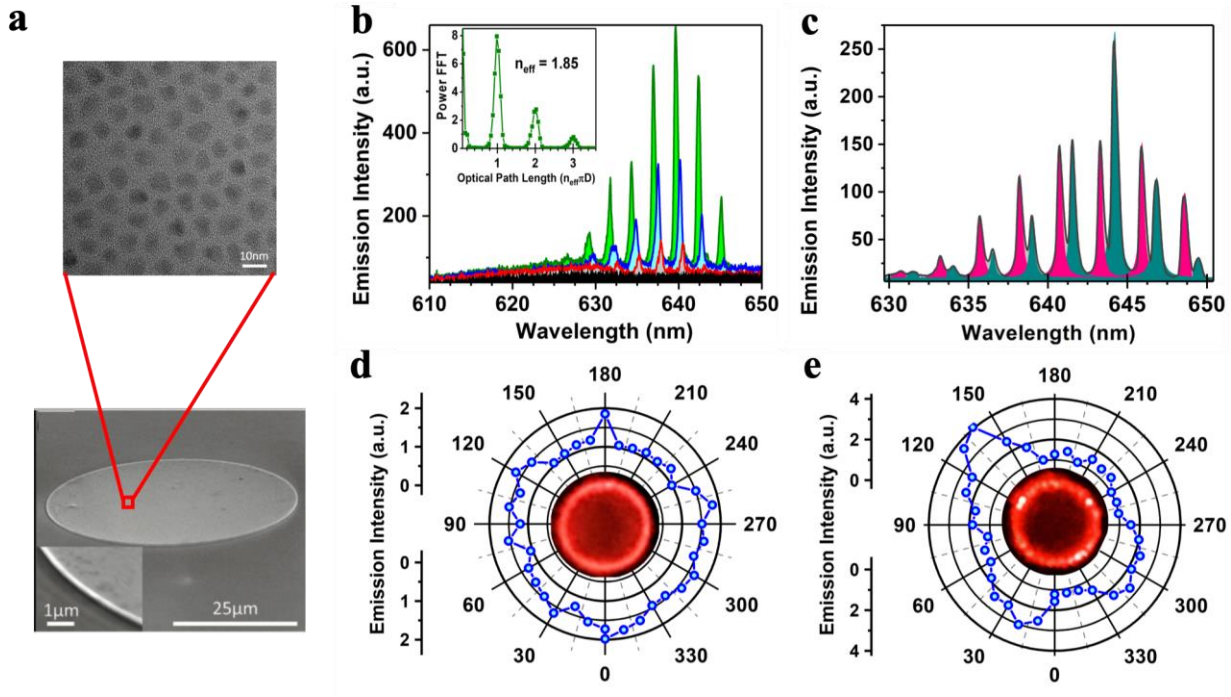

Figure 7.1: Emission characteristics of isolated microdisk resonators. a, (upper) TEM micrograph of oleic acid-capped CdSe/$Cd_{1-x}Zn_xSe_{1-y}S_y$ QDs. (lower) SEM image of a microdisk, inset shows the resonator boundary. b, Laser emission spectra from a microdisk pumped at various intensities: 16 μJ/cm^2 (black), 29 μJ/cm^2 (red), 66 μJ/cm^2 (blue), 116 μJ/cm^2 (green). The inset shows the FFT of the emission spectrum vs. the optical path length $n_{eff}\pi D$, where n_{eff}=1.85 is the effective mode index and D=25 μm. c, Laser emission spectrum from a different microdisk that contains a defect, pumped at 116 μJ/cm^2. The different shaded regions are Lorentzian fits to the two laser modes series. d, Collection-angle dependence of the emission in the plane of the microdisk in (b) with fluorescent image at the center. e, Same as in (d) but for the spectrum shown in (c).

Figure 7.1b shows the spectral evolution of the laser emission from an exemplary microdisk with increasing pump intensity. At low intensity, only a broad photoluminescence band (FWHM ~ 25 nm) is observed, displaying a peak near 630 nm. Above the threshold intensity of 29 μJ/cm^2, narrow laser modes emerge from the PL spectrum (Supplementary Figure D.1). The free-spectral range is $\Delta\lambda \approx 2.6$ nm and well described by the formula for WGM's, namely $\Delta\lambda = \lambda^2/n_{eff}(\pi D)$ where n_{eff} is the effective mode index and D is the disk diameter (D = 25 ± 1 μm). By converting

the spectral units to μm^{-1} and taking the Fourier transform, we extract a series of harmonics of the optical path length $n_{eff}(\pi D)$ (inset), giving the effective index n_{eff} = 1.85 ± 0.05 which is in agreement with the $CdSe/Cd_{1-x}Zn_xSe_{1-y}S_y$ CQD film refractive index (n = 1.86 ± 0.05) determined by ellipsometry.[30,31] In Fig. 1d, we show the angular dependence of the laser emission in the plane of the microdisk, which is isotropic, signaling a homogenous intensity distribution along the microdisk circumference. Additionally, the fluorescent image of the disk under lasing condition shows that the field amplitude is predominantly located along the perimeter.

In contrast, in Figure 7.1c we present the emission spectra from another microdisk of the same size. In this case we are able to resolve two sets of modes, each having $\boldsymbol{\Delta\lambda}$ = 2.6 nm. The additional set of modes is split-off from the other WGM modes by ~0.8 nm. The linewidths of all modes are comparable (~ 0.5 nm) and the splitting does not vary much with increasing pump fluence. In the fluorescent image of Figure 7.1e it is seen that a few particularly bright spots have now appeared on the microdisk circumference.

Microscopic characterization reveals that these bright spots are due to fabrication defects (Supplementary Figure D.2). These defects then act as asymmetric scattering centers that increase out-coupling in the vertical direction giving them their bright appearance. In addition, we see that the defects strongly disrupt the emission isotropy, leading to strong directionality of the emission diametrically across from the defects. Atomic force microscopy has been used to investigate the formation of possible defects during fabrication (Supplementary Figure D.3). There are generally

two types of defects in our microdisks that can induce the obtained mode-splitting. The first type is the small QD aggregates that forms near the disk circumference. These aggregates may originate from the imperfections that exist in QD solutions, which act as seeds to affect the drying process. The second type of defects is difference in circumference height due to inhomogeneous drying. Both type of defects may act as localized perturbations that can introduce asymmetric back-scattering between clockwise (CW) and counter-clockwise (CCW) WGM propagation, lifting the degeneracy between them. This degeneracy lifting has been widely discussed in the context of nanoparticle sensing, where the mode-splitting is employed to register the detection event[32].

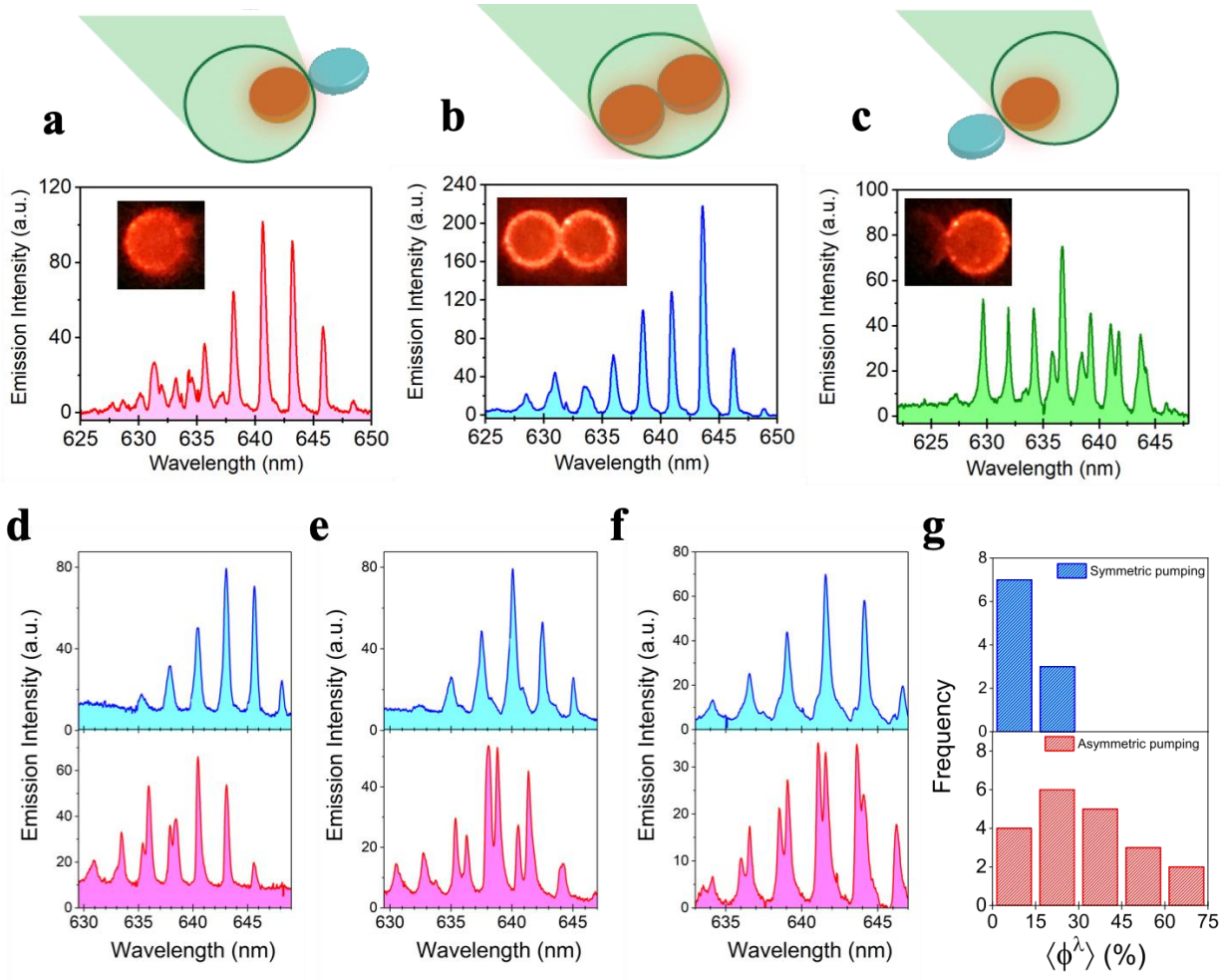

Figure 7.2: Emission characteristics of coupled pairs of microdisk resonators. a-c, Laser emission spectra from a coupled microdisk pair, where the pair is placed at different locations in the pump beam spot, such that only the left or right microdisk is pumped a, and c, or the pair is pumped evenly, b, as illustrated schematically above each plot. The insets show the fluorescent image from the microdisks in each case. d-f, Laser emission spectra from three different microdisk pairs pumped at 116 μJ/cm^2. In each figure the spectrum from the evenly pumped pair (upper) is compared to a spectrum from the asymmetric pumping scheme (lower). The evenly pumped pair consistently shows a reduction in mode-splitting compared to the asymmetric case. g. Frequency distribution of the spectrally averaged modal splitting parameter, $\langle\phi\rangle$, (defined in Eq. (7.1)) for the symmetric (upper panel) and asymmetric pumping schemes (lower panel).

Considering the various phenomena that have been displayed in the non-Hermitian coupled WGM resonators, it is interesting to consider to what degree these interactions may be preserved in the

presence of disorder. This information is imperative if such effects are to be eventually employed in a broad range of photonic applications. We therefore took to the investigation of coupled-pairs of our CQD micro-resonators fabricated from facile, scalable process. The spacing between the two microdisks was 396 ± 20 nm apart (Supplementary Figure D.4), which is less than the emission wavelength and should provide adequate evanescent coupling between the WGM of the two microdisks. In Figure 7.2(a-c), we show the emission spectra obtained when the pair is placed at the center of the beam spot, so that both individual microdisks are pumped evenly (Figure 7.2b), and when the left or right disks are pumped exclusively (Figure 7.2a, c). This configuration resembles the PT-symmetric laser system that was theoretically proposed[21] and experimentally demonstrated to achieve selective mode-filtering[22]. In all three cases we see a distinct laser emission spectrum, and we particularly note the appearance of mode-splitting in Fig. 2c when only the right disk is pumped. It is therefore surprising that the emission spectrum of the evenly-pumped pair shows no trace of the mode-splitting in the same spectral region (Figure 7.2b). This is in stark contrast to the majority of single, isolated microdisks whose spectra contain parasitic mode-splitting (Supplementary Figure D.5). These results suggest that the coupling between the microdisks in the pair is helpful in reestablishing spectral purity in the laser emission spectrum.

In Figure 7.2(d-f) we demonstrate that *this phenomenon is robust*. It is observed in numerous samples in which at least one of the microdisks exhibits mode-splitting during the asymmetric pumping condition. To facilitate comparison over a large number of coupled-microdisks, we define an empirical parameter, ϕ^{λ} to quantify the splitting between individual broken-degeneracy WGM mode-pair,

$$\phi^{\lambda} = \frac{2|\lambda_1 - \lambda_2|}{\Delta\lambda} \tag{1.3}$$

Where λ_1 and λ_2 are the peak wavelengths and the wavelength splitting is normalized by half the free spectral range $\Delta\lambda$. We then take the average, $\langle\phi^{\lambda}\rangle$ of all mode-pairs in the spectrum (see Supplementary Figure D.5). Figure 6.2g shows the frequency distribution of, $\langle\phi^{\lambda}\rangle$ obtained from both the symmetric and asymmetric pumping configurations. Indeed, the wide variability of the emission from asymmetrically pumped pairs, which echoes the variation in the emission spectrum of isolated microdisks (Supplementary Figure D.5), collapses to a narrower distribution with significantly reduced parasitic mode-splitting when the pair is pumped evenly. The results show that the coupling between microdisks in the presence of symmetric gain consistently corrects the sample variability that naturally results from a scalable, high throughput fabrication procedure for micro-photonic elements such as these. As we show below, this is possible due to the presence an exceptional point in the Hamiltonian of the system that provides a channel through which intra-cavity mode splitting can be modulated through inter-cavity coupling.

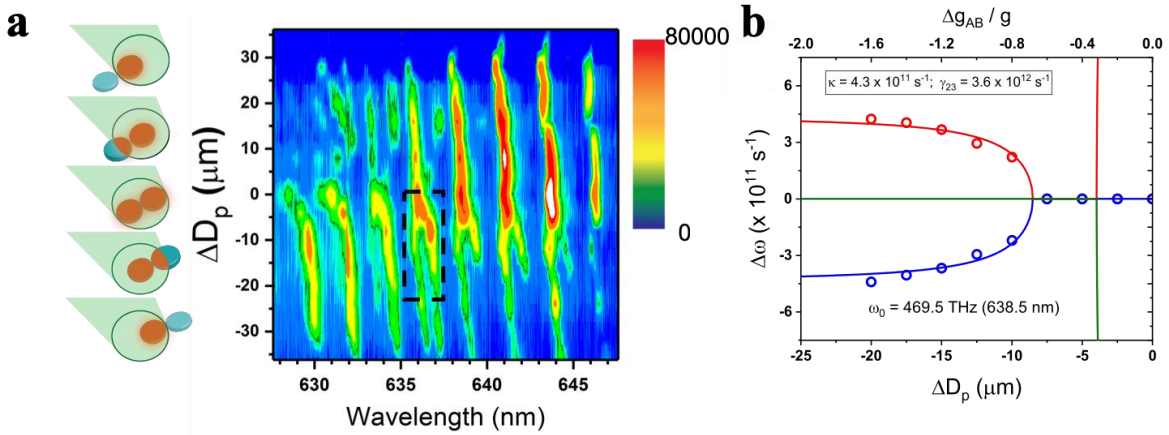

Figure 7.3: Laser emission behavior of microdisk pair under gain variation, where a microdisk having a defect is coupled to another microdisk lacking of defects. a, False-color contour plot of the emission intensity vs. wavelength and relative distance, ΔD_p between the center of the pair to the center of the beam spot, as the pair is shifted through the pump beam spot, which is schematically illustrated on the left. As the microdisk pair nears the center, the split modes merge as clearly seen for several mode pairs in the range of 635-645 nm. b, Mode splitting in the defected microdisk vs. ΔD_p as obtained from the dashed-boxed region in (a). The solid lines are eigenvalue dynamics as a function of the gain differential Δg_{AB} between the coupled microdisks in a three-mode Hamiltonian (see text) that shows coalescence of the intra-cavity modes in the defected microdisk due to the gain variation between the coupled microdisks. The model parameters are indicated.

A detailed look at this behavior is provided by an examination of the laser emission modes under the application of spatial gain variation (Figure 7.3). In these measurements, the microdisk pair is swept through the pump beam spot incrementally. The offset between the pump spot and the pair center, which we call ΔD_p, then becomes a proxy for the gain/loss variation, $\Delta g_{AB} = g_B - g_A$ between the two microdisks, where we refer to the microdisk that shows parasitic splitting as microdisk A with gain, g_A and its neighbor microdisk B with gain, g_B. As seen in Figure 7.3a, when ΔD_p is large and negative, only microdisk A is pumped, and clear mode-splitting can be observed in the laser emission spectrum. Then as the pair of coupled microdisks is moved towards

the center of the excitation beam spot and gain is added to microdisk B, we find that the localized intra-cavity modes gradually move closer in frequency and eventually coalesce near but not quite at the center. This is very surprising, as these modes are localized in microdisk A and gain/loss differential does not change between them. Here, the application of gain to microdisk B modulates the splitting between the parasitic defect modes of microdisk A through the evanescent coupling between the two microdisks.

To understand this behavior in more detail, we consider solution to the eigenvalue problem described by the following Hamiltonian:

$$\widehat{H} = \begin{pmatrix} \boldsymbol{\omega'_1 + \mathrm{i} g_A} & \boldsymbol{\kappa} & \boldsymbol{\gamma_{13}} \\ \boldsymbol{\kappa} & \boldsymbol{\omega'_2 + \mathrm{i} g_A} & \boldsymbol{\gamma_{23}} \\ \boldsymbol{\gamma_{13}} & \boldsymbol{\gamma_{23}} & \boldsymbol{\omega'_3 + \mathrm{i} g_B} \end{pmatrix} \tag{7.4}$$

Where $\omega'_{i=1,2,3}$ are the real parts of the eigenfrequencies in the absence of coupling and $g_{i=1,2,3}$ are the imaginary parts, where we set $g_1 = g_2 = g_A$, and similarly we set $g_3 = g_B$ for the mode 3 in microdisk B. κ is used to represent the intra-disk coupling between CW and CCW modes in microdisk A (modes 1 and 2), whereas γ_{i3} describes inter-disk coupling of i^{th} mode of microdisk A to the mode 3 of microdisk B (see Figure 7.4a). This is an extension of the 2x2 Hamiltonians often considered in Non-Hermitian systems, where an interaction exists between one mode from each resonator.[22] In our case the defect-induced mode-splitting produces a scenario in which three modes interact, and the resulting Hamiltonian is 3x3. In order to simulate the portion of the spatial

gain variation experiment in which ΔD_p increases from -25μm to zero we keep g_A constant, $g_A = g$ (microdisk A is entirely covered by the pump beam) while sweeping g_B from $-g$ to g (microdisk B goes from unpumped to completely pumped). Thus, Δg_{AB} ranges from $-2g$ to zero.

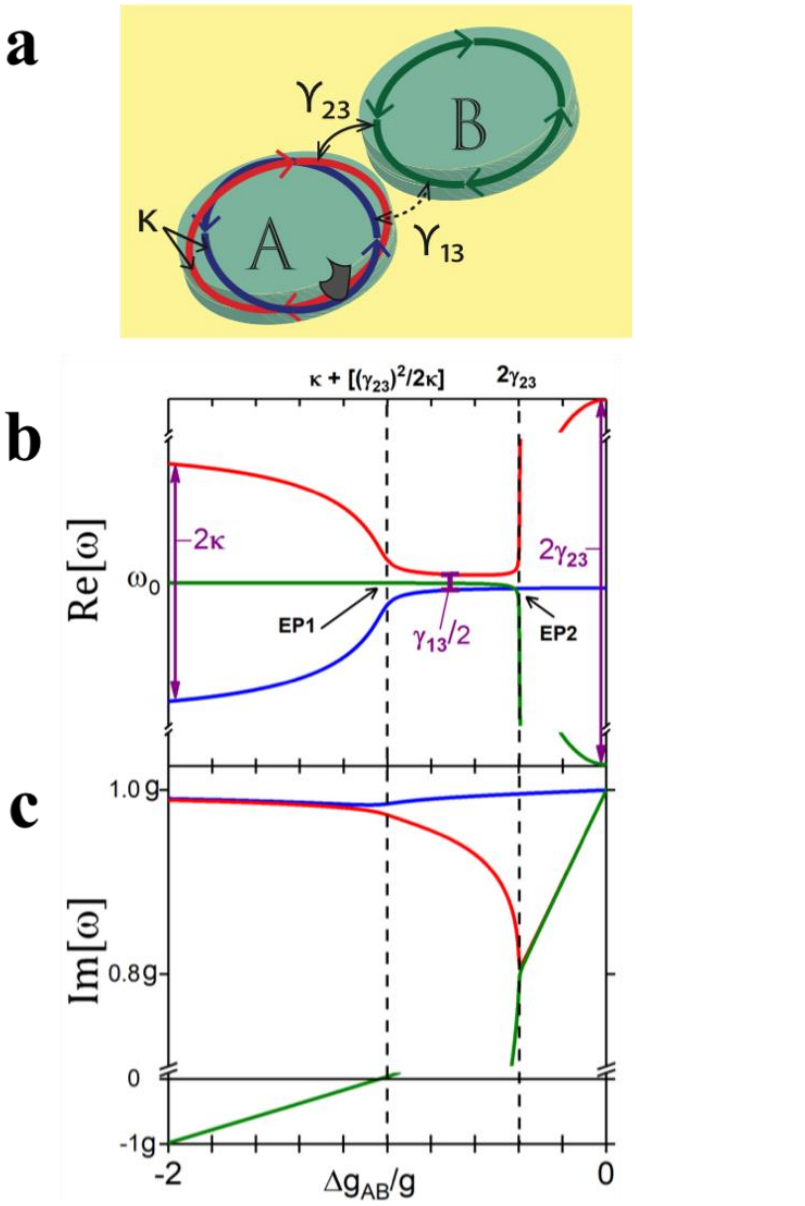

Figure 7.4: Calculated eigenvalue dynamics associated with the three-mode system that describes the mode-splitting coalescence obtained in the experiment. a, Schematic diagram of the modes considered and parameters governing their interaction. For microdisk A, a defect on the circumference induces splitting between CW and CCW WGM modes due to their mutual asymmetric backscattering determined by the parameter κ. These two modes can then couple to the degenerate modes in microdisk B through the inter-disk coupling parameters, γ_{13} and γ_{23}. We consider the case for which $\gamma_{23} \ll \kappa \ll \gamma_{13}$. b and c, Real and Imaginary parts of the eigenvalues of the 'three-mode Hamiltonian' vs. the normalized gain differential, $\Delta g_{AB}/g$ between microdisks A and B. The dashed lines indicate the locations of the exceptional points EP_1 and EP_2. The limiting values of the eigenvalue splitting and the locations of the EPs in Δg_{AB} are given in terms of κ, γ_{13} and γ_{23}.

Considering the boxed region in Figure 7.3a, the experimentally observed phenomenon of intra-cavity mode coalescence can be satisfactorily replicated as demonstrated in Figure 7.3b. The simulations show a typical branch root behavior of an exceptional point that is the origin of the observed coalescence. By setting $\omega'_1 = \omega'_2 = \omega'_3 = \omega_0$, where ω_0 is the average frequency of all three modes, the splitting at large Δg_{AB} is determined by the intra-cavity mode coupling κ. The values of ω_0, g, and κ are then taken from experiment,[24] leaving only γ_{23} and γ_{13} as free parameters. As discussed below, the key to the observation of the coalescence of intracavity modes is the existence of a large coupling anisotropy, $\gamma_{23} \gg \gamma_{13}$, with an exact EP obtained in the limit $\gamma_{13} \to 0$. Similar agreement is obtained between the experimental results and the model for each of the modes for which the coalescence is observed by adjusting the coupling term γ_{23} (Supplementary Figure D.6).

We have analyzed the Hamiltonian in detail to extract the characteristic behavior of the eigenvalues (Supplementary Figures D.7-9). Shown in Figure 7.4b, it is seen that when the absolute value of the gain differential $|\Delta g_{AB}|$ is large, the modes are localized in respective disks and the splitting is determined by the intra-cavity coupling factor of microdisk A taking a value of 2κ. As $|\Delta g_{AB}|$ decreases, the splitting is reduced, showing the square root dependence on Δg_{AB} that is the signature of EP behavior [2,3]. At the particular value $\Delta g_{AB} = [\kappa + (\gamma_{23})^2/2\kappa]$ the eigenvalue splitting collapses to $\gamma_{13}/2$. Thus, when $\gamma_{13} = 0$, the eigenvalues coalesce and the point corresponds to an EP, denoted as EP1. In accordance, the imaginary parts of modes 1 and 2 bifurcate and mode 2 becomes more lossy. Note the remarkable implications of this result, as also shown in the experiment, that *the observed splitting of intra-cavity modes of microdisk A depends on the gain applied to microdisk B.* As $|\Delta g_{AB}|$ decreases further, another transition occurs when $\Delta g_{AB} = 2\gamma_{23}$, denoted as EP2. At this point the real parts of the eigenfrequencies are repelled by

the inter-cavity interaction and the frequency splitting becomes $2\gamma_{23}$. Meanwhile the imaginary parts of eigenvalues 2 and 3 coalesce at this point. This transition is similar to the typical transition between PT-symmetric and PT-broken phases studied in other systems.[19,22] From our model we conclude that the coalescence of intracavity-modes and resulting purification of the laser spectrum results from a natural asymmetry between γ_{23} and γ_{13}.

7.4 Conclusion

The higher-dimensionality of parameter space involved in our coupled resonator system may be useful for nanoparticle sensing applications. It has been demonstrated that a WGM resonator interacting with two judiciously oriented particles may prepare the system at an EP, providing enhanced sensitivity for detection of a third, 'target' particle.[33, 34, 35] Since in our case, the coalescence of modes depends on the gain differential with a 'third-party', this phenomenon may provide an alternative module capable of using an EP for particle detection with increased sensitivity. The coupled-resonator system may be more appealing from an application design point of view due to its simpler implementation and because it does not add additional extrinsic loss. Alternatively, it should be possible to utilize the exceptional point behavior to remove unwanted parasitic modes of individual microcavities in coupled resonators. The applied gain differential could be used as a knob to fine tune the quality of the emission spectrum. Implementation of EPs for this purpose can be particularly welcome benefit for semiconducting photonic materials such as CQD's and π-conjugated polymers, helping to mitigate the trade-off of disorder and instability that comes with their processing advantages.

7.5 References (Chapter 7)

[1] Moiseyev, N. *Non-Hermitian Quantum Mechanics* (Cambridge Univ. Press, Cambridge, 2011).

[2] Heiss, W. D. *J. Phys. Math. Gen.* **2004**, 37, 2455.

[3] Berry, M. V. *Czechoslov. J. Phys.* **2004**, 54, 1039.

[4] Bender, C. M. *Rep. Prog. Phys.* **2007**, 70, 947.

[5] Bender, C. M.; Boettcher, S. *Phys. Rev. Lett.* **1998**, 80, 5243.

[6] El-Ganainy, R., Makris, K. G., Christodoulides, D. N., Musslimani, Z. H. *Opt. Lett.* **2007**, 32, 2632.

[7] Dembowski, C. *Phys. Rev. Lett.* **2001**, 86, 787.

[8] Dembowski, C. *Phys. Rev. E*. **2004**, 69, 056216.

[9] Lee, S.-B. *Phys. Rev. Lett.* **2009**, 103, 134101.

[10] Gao, T. *Nature* **2015**, 526, 554.

[11] Guo, A. et al. *Phys. Rev. Lett.* **2009**, 103, 093902.

[12] Rüter, C. E. *Nat. Phys.* **2010**, 6, 192.

[13] Zhen, B. *Nature* **2015**, 525, 354.

[14] Weimann, S. *Nat. Mater*. **2017**, 16, 433.

[15] Liertzer, M. *Phys. Rev. Lett.* **2012**, 108, 173901.

[16] Brandstetter, M. *Nat. Commun.* **2014**, 5, 4034.

[17] Peng, B. *Science* **2014**, 346, 328.

[18] Feng, L. *Nat. Mater.* **2013**, 12, 108.

[19] Peng, B. et al. *Nat. Phys.* **2014**, 10, 394.

[20] Doppler, J. *Nature* **2016**, 537, 76.

[21] Miri, M.-A., LiKamWa, P., Christodoulides, D. N. *Opt. Lett.* 2012, 37, 764.

[22] Hodaei, H., Miri, M.-A., Heinrich, M., Christodoulides, D. N., & Khajavikhan, M. *Science* **2014**, 346, 975.

[23] Feng, L., Wong, Z. J., Ma, R.-M., Wang, Y. & Zhang, X. *Science* **2014**, 346, 972.

[24] Kim, M., Kwon, K., Shim, J., Jung, Y., Yu, K. *Opt. Lett.* **2014**, 39, 2423.

[25] Peng, B., *Proc. Natl. Acad. Sci.* **2016**, 113, 6845.

[26] Miao, P., *Science* **2016**, 353, 464.

[27] Zhang, Z., *ACS Photonics* **2018**, 5, 3016.

[28] Gaponik, N., Hickey, S. G., Dorfs, D., Rogach, A. L., & Eychmüller, A. *Small* **2010**, *6*, 1364.

[29] Lin, C. H. *Adv. Opt. Mater.* **2017**, 5, 1700011.

[30] Lin, C. H. *ACS Photon.* **2016**, 3, 647.

[31] Malak, S. T. *J. Mater. Chem. C* **2016**, 4, 10069.

[32] Zhu, J. *Nat. Photon.* **2009**, 4, 46.

[33] Zhu, J., Özdemir, S. K., He, L., Yang, Y. *Opt. Express* **2010**, 18, 23535.

[34] Wiersig, J. *Phys. Rev. Lett.*, **2014**, 112**,** 203901.

[35] Chen,W., Özdemir, S. K., Zhao, G., Wiersig, J., Yang, L. *Nature* **2017**, 548, 192.

[36] Bae, W. K., Char, K., Hur, H., Lee, S. *Chem. Mater.* **2008**, 20, 531.

[37] Jung, J. *Angewandte Chemie* **2016**, 128, 5155.

CHAPTER 8. GENERAL CONCLUSIONS AND BROADER IMPACT

8.1 General conclusions and discussion

Overall, the research in this dissertation focused on understanding the fundamentals of light-matter interactions occurring at each level of photonic sources: individual nanoparticles and assembled composite nanostructures, individual and coupled optical resonators, and template assembled individual and coupled optical resonators. Specifically, we focus on how architecture of QDs can affect optical properties of local assemblies of nanostructures. Next, focusing on core, alloyed shell QDs, we considered the effect of ultrafast crosslinkable UV polymerization on developing a polymer support matrix, with particular attention paid to the ligand chemistry, and achieving optimal QD loading with minimal phase separation. Additionally, we investigated how emissive components, such as organic dyes and QDs, assemble onto support resonators such as silica and polymer microspheres, and their subsequent assembly into templates, and resulting optical properties. Finally, we sought to understand how the gain/loss modulation of optically active cavities controls the light propagation characteristics leading to Parity-Time symmetric optical systems.

This research work provides a scientific framework which demonstrates a comprehensive approach which can be applied to designing hybrid photonic systems, ranging from individual nanoparticles and nanostructures to coupled nanocomposite structures, that require control of light-matter interactions resulting in unique optical properties such as enhanced emission, lasing, coupling, and modulated optical mode activity. Major themes of the present work include:

1. Examined, measured, and investigated the PL behavior of various QDs in local assemblies in order to develop frameworks to control the optical activity of these nanostructures;
2. Developed facile polymerization schemes to control the spatial distribution of QDs to control light-matter interactions in these nanocomposites, aiming to utilize these controlled interactions to design novel flexible photonic systems;
3. Utilized unique assembly techniques to achieve large scale arrays of optical resonators. Additionally, taking advantage of resonator assembly on a template to achieve controlled coupling between neighboring cavities in order to realize interesting phenomenon such as PT-symmetric and supersymmetric arrays;
4. Refined microfabrication techniques to assemble individual and coupled microcavites and approaches to tailor the gain/loss contrast of cavities to alter the evanescent coupling within optical cavities, aiming to discover novel optical phenomena for designing novel photonic systems.

Specific issues and challenges addressed in this study were as follows:

1. Identified framework for evaluating dynamic photoluminescence properties of QDs of various core-shell architectures, providing tunability in emission properties based on light exposure and support matrix.
2. Examined how thiol-ene polymerizations affect the dispersion of QDs in polymer matrix to assure minimal phase separation and optimal dispersion. Additionly, the effect on properties such as QD loading, refractive index, Young's modulus, and PL intensity was investigated.

3. Examined the efficacy of silica and polymer microsphere support matrices to assemble emissive materials, including QDs and organic dyes, and furthermore investigated assembly of photoluminescent microspheres in two photon lithography derived templates and their resulting emission and coupling behavior, pushing the spatial resolution, leading to controllable light-matter interactions including light propagation, mode numbers and spacing, as well as mode splitting.
4. Finally, utilized spatial modulation of optical pump to control light-matter interactions via intra and inter-cavity coupling, including evanescent coupling leading to coalescence of defect optical modes by altering the gain/loss contrast in localized regions.

Specifically, optical properties of individual colloidal QDs with different core-shell architectures generated from synthetic chemistry were monitored in our first study. It has been widely known that the shell of QDs imparts stability to the QD optical properties, with appropriate geometry and interfacial smoothing resulting in suppressed re-absorption, reduced Auger recombination, and tunable stokes shift and emission. Unstable QDs with no shell or no smoothing of the interface between core and shell result in variable emission properties that can be activated and deactivated based on light exposure conditions. **Importantly, these QDs showed dynamic photoluminescence properties (decay and recovery of emission), providing a framework for understanding/evaluating stability of QDs.**

Next, we sought out to develop an emissive QD nanocomposite material that was mechanically robust, chemically inert, free standing, and flexible capable of meeting the demands of next generation photonics materials. By taking advantage of thiol-ene chemistry, an ultra-fast, inert, and proven crosslinking polymerization mechanism we successfully fabricated composites films

with **QD loadings >30 wt. %, resulting in highly emissive films with minimal aggregation**, ideal for systems requiring high optical gains. In addition, we studied the polymerization kinetics, further demonstrating a relationship between thiol and -ene conversion and the resulting mechanical properties of the nanocomposite films, with **highly loaded films resulting in a modulus of ~1 GPa, characteristic of reinforced elastomeric materials**. Finally, we demonstrated the feasibility of using thiol–ene chemistry with soft-imprint lithography, fabricating QD loaded waveguides and resonators. Our results demonstrated one of the **highest loaded, mechanically stable and robust QD-polymer nanocomposites** that is readily compatible with patterning techniques to generate photonic systems.

We then examined methodologies to fabricate large scale arrays of photonic systems. Starting with one of the most widely studied WGM resonators, the microsphere, due to its intrinsically high-quality factor and mode volume. First, we refined methods to decorate microspheres with emissive components including QDs and organic dyes while still maintaining solubility in various aqueous and organic solvents. Taking advantage of the sub-500nm resolution of 3D lithography we fabricated templates to then assemble individual and coupled microsphere resonators. Though limited by the resolution of 3D lithography (>200nm), **novel design of the template afforded us the ability to push the resolution below 200nm, to achieve as low as sub 50nm gap spacing between neighboring resonators.** Therefore, we demonstrated the ability to control the coupling between neighboring resonators based on the controlled gap spacing, a necessity for realizing advanced optical phenomenon such as PT-symmetry and supersymmetric arrays.

Finally, by taking advantage of a microfabrication approach involving photolithography, we successfully demonstrated the ability to **develop hybrid individual and coupled resonators with sub-500nm gaps between microdisks.** Furthermore, spatial modulation of the optical pump was

utilized to alter the gain/loss values of coupled microdisks. Intra-cavity mode coupling was experienced due to scattering from inherent defects, formed during the solution-based synthesis mechanism, which was further controlled by simply **altering the gain/loss contrast between cavities to achieve coalescence where the gain/loss contrast was modulated to meet the coupling strength between cavities**.

8.2 Significance and Broader Impact

Photonic local assemblies and structures comprised of emissive component such as QDs, in addition to robust polymer matrices, high quality factor resonators, and high-resolution patterning of coupled optical cavities has the potential to make significant technological advances. These materials are poised to impact areads including PT-symmetry to realize single mode lasing and unidirectional light flow, ultra-sensitive detection, ultra-high resolution displays, in addition to next generation computers providing a potential breakthrough for machine learning and artificial intelligence. As previously mentioned, this research specifically focused on understanding local assemblies of nanostructures, lithography derived individual and coupled photonic cavities, and template-assembled individual and coupled microsphere cavities. To summarize the scientific and technological approaches utilized herein were tailored in order to understand how light-matter interactions can be controlled by using and further exploiting synthetic chemistry, lithography derived large-scale assembly of microscopic cavities, ultrafast UV-crosslinking polymerization schemes, cavity size/geometry, optical pumping modulation, and templated assembly of microsphere resonators.

With the wide range of QD applications, a thorough understanding of the QD compositional profile and the effect on optical properties is essential, allowing for tailored properties based on QD profile. In our initial study we sought to thoroughly understand the effect of different QD core/shell architectures on the resulting optical properties under different light exposure conditions. While studies have investigated the effects of various environmental conditions of QD dynamic PL behavior, few studies have focused on the semi-reversible emission behavior. This work provided a comprehensive study and general framework for evaluating dynamic photoluminescence properties of QDs, whether stable or variable emission is required. It was determined that the

response of the QD arises from the how the core interacts with the surrounding environment. Demonstrating the importance of QD composition when determining the end application, and further providing insight into the various enhancement/reduction mechanisms at play under various common environmental exposure conditions. While stable emission is generally desired, QD core/shell architecture comprised of a sharp interface resulting in the dynamic decay to recovery behavior could be quite advantageous for sensors involving light, water, or air.

Next, in understanding the demands for next generation QD materials, it is critical to consider the need for more robust and stable optical components which can be readily integrated into flexible matrices and materials. We focused on developing a robust and inert support matrix for highly loaded and emissive quantum dot nanocomposites. Most studies in literature that take advantage of polymeric host matrix usually fabricate a composite by simple mixing of the two components, typically resulting in formation of local aggregates. While others have demonstrated success utilizing more complex reaction schemes, **loadings are typically extremely low, not exceeding 1%. Here we reported the fabrication of one of the highest loaded QD nanocomposites, exceeding 30 wt. %,** by taking advantage of QDs with much shorter ligands (butylamine) in comparison to traditional longer ligands (oleic acid or hexadecylamine), resulting in highly emissive films and structures. Of major significance, **due to the efficient polymerization scheme, aggregation was severely retarded**, making the composite materials ideal for systems requiring high optical gains in addition to light guiding and emitting composites, in which QD aggregation, leading to optical scattering and losses, can be detrimental. Further, by exploiting thiol-ene chemistry, an ultrafast, UV crosslinking polymerization that takes places in ambient conditions, we achieved a **nanocomposite with tunable mechanical properties**. We observed an inverse relationship between QD loading and thiol and -ene conversion, as well as the elastic modulus of

the material, achieving a modulus as low as ~1 GPa with the highest QD loading, similar to reinforced elastomeric materials, in contrast to usually observed stiff and brittle materials under these loading conditions. Our findings are **important in the design of robust, flexible, and free-standing nanocomposite advanced photonic systems in which mechanical stability and chemical inertness is a necessity for durable, long lasting flexible optical components.**

Furthermore, we also studied individual and coupled microsphere resonators, demonstrating precise spatial arrangement via templated assembly. Microspheres were particularly of interest due to their inherently high-quality factor and mode volume, and ease of fabrication and post modification. Specifically, we decorated microsphere resonators of various size and polymeric materials with emissive components ranging from organic dyes to QDs. Similar to some of our previous studies, it was demonstrated that the mode activity varied with microsphere resonator size. Additionally, by taking advantage of 3D lithography with ~200nm resolution, we fabricated templates to assemble microsphere resonators. While limited by the 200nm resolution, **unique design of the template afforded us the ability to achieve sub-100nm spacing between neighboring resonators, a feat that would be otherwise difficult to achieve with conventional lithography methods.**

Traditional systems investigating the coupling of microspheres typically involve the use of micromanipulators or the random assembly or microspheres. While the simplicity is sufficient for bench scale testing and understanding coupling phenomenon, given the ultra-high quality factors of microsphere resonators, their incorporation into next generation optical components is inevitable, requiring readily intergrateable assembly techniques. Herein we demonstrate the facile assembly of microspheres into individual and coupled resonators for advanced photonic systems. While it was initially suggested that relief structures used in templated assembly were simply

trapping sites for microspheres, in which holes needed to be at least half the height of the microsphere, our unique design provided a framework for achieving coupled optical resonators, with little to no interference from the underlying template, achieving sub-100nm spacing. As a result of the facile assembly technique and novel system design, **strong coupling was achieved between microsphere dimers with sub-100nm spacing**, pushing the resolution of the 3D lithography instrumentation. **Strong coupling was confirmed via optical pumping, demonstrating large mode splitting which lessened as gap distances were reduced.** Such unique designs involving coupled photonic systems are critical for realizing advanced optical systems in which strong evanescent wave coupling is necessary, such as PT-symmetry and supersymmetric arrays for realizing controllable lasing.

Additionally, large scale arrays are advantageous for advanced photonic systems in which high throughput is necessary such as for detectors and sensing, far exceeding the capabilities of EBL. With WGM resonators having a potentially significant impact on fields such as sensing and detection, microsphere array formation with precise control of location based on templated assembly should prove to be extremely useful. **Unlike traditional mask-based lithographies, 3DL does not require a mask, meaning any arbitrary structure can be developed, potentially leading to very complex arrays for photonic systems.** It is envisioned that such a system, in which an arbitrary 3D template can be fabricated, would be compatible with assembly other optical resonators, including microcylinders, and serve as an ideal support for study and manipulation of microcapsules or Janus particles.

Finally, as mentioned above, large scale array assembly is critical for realizing on chip implementation of optical mircoresonators. To further demonstrate large scale robust lasing arrays, we take advantage of a hybrid microfabrication method involving photolithography to achieve

individual and coupled microdisks assemblies. To demonstrate such phenomenon as PT-symmetry it is generally required to pattern alternating layers of gain/loss. **Herein by spatially modulating the optical pump we impart gain/loss contrast in the coupled resonator system.** Intracavity coupling results from scattering from defects formed during cavity fabrication from colloidal, solution based QDs. This coupling is the result of breaking of the degeneracy of the individual cavity. Clockwise and counterclockwise mode propagation results in mode splitting, which is driven to coalescence by spatial modulation of optical pump and simultaneously exciting both cavities. **This work demonstrates the first example in which colloidal QDs were used to achieve such advanced optical phenomenon such as directional lasing and PT-symmetry. Furthermore, the novel approach, exploiting the intra-cavity coupling, provides a unique mechanism for mode suppression and taking advantage of some of the pitfalls associated with colloidal QDs such as severe aggregation leading to excessive scattering and optical losses.**

Materials based on resonant behavior, in which the evanescent field is critical for achieving coupling or ultra-sensitive detection, have had a tremendous impact on fields including acoustics, as well as radio and microwave frequencies. Suggesting that the impact on optics is still in its infancy. In the coming years, many other applications will emerge ranging from biological and optical sensing to frequency combs and super symmetric arrays for high power and efficient lasing.

8.3 General Acknowledgements

Primary financial support of this work is acknowledged from the Air Force Office of Scientific Research FA9550-14-1-0037 (Synthetic Photonics Multidisciplinary University Research Initiative). Additionally, I would like to acknowledge the Science, Mathematics and Research for Transformation (SMART) scholarship funded by OSD-T&E, Defense – Wide/PE0601120D8Z National Defense Education Program (NDEP)/BA-1, N00244-09-1-0081. QD synthesis was conducted by Prof. Lin's group and confocal micro PL measurement were conducted by Prof. Vardeny's group.

8.4 Dissemination of work

This research work has resulted in 16 scientific publications and 5 oral presentation at national meetings.

8.4.1 Publications

Primary Publications:

1. Lafalce, E.; Zeng, Q.; Lin, C. H.; **Smith, M. J.;** Jung, J.; Yoon, Y.; Lin, Z.; Tsukruk, V. V.; Vardeny, Z. V., Control of Whispering Gallery Modes and PT-symmetry Breaking in Colloidal Quantum Dot Microdisk Lasers with Engineered Notch Implants, In Preparation

2. **Smith, M. J.;** Zeng, Q.; Lafalce, E.; Yu, S.; Zhang, S.; Vardeny, Z.V.; Tsukruk, V. V., Coupled Whispering Gallery Mode Resonators via Template Assisted Assembly of Photoluminescent Microspheres, *Adv. Funct. Mater.*, Submitted

3. Lafalce, E.; Zeng, Q.; Lin, C. H.; **Smith, M. J.;** Malak, S. T.; Jung, J.; Yoon, Y.; Lin, Z.; Tsukruk, V. V.; Vardeny, Z. V., Robust Lasing Modes in Coupled Colloidal Quantum Dot Microdisk Pairs Using a non-Hermitian Exceptional Point. *Nat. Commun.,* **2019**, 10: 561

4. **Smith, M. J.;** Lin, C. H.; Yu, S.; Tsukruk, V. V., QD Composite Materials: Synthesis, Functionalization and Microfabrication for Light Management Application. *Adv. Opt. Mater.* **2019**, 7, 1801072

5. **Smith, M. J.;** Malak, S. T.; Jung, J.; Yoon, Y. J.; Lin, C. H.; Kim, S.; Lee, K. M.; Ma, R.; White, T. J.; Bunning, T. J.; Lin, Z.; Tsukruk, V. V., Robust, Uniform, and Highly Emissive Quantum Dot–Polymer Films and Patterns Using Thiol–Ene Chemistry. *ACS Appl. Mater. Interfaces* **2017,** *9*, 17435.

6. Zeng, Q.; Lafalce, E.; Lin, C. H.; **Smith, M. J.;** Malak, S. T.; Jung, J.; Yoon, Y.; Lin, Z.; Tsukruk, V. V.; Vardeny, Z. V., Spectral and Directional Properties of Elliptical Quantum Dot Microlasers. *Journal of Photonics for Energy,* **2018**, 8, 032218-1.

7. Lin, C. H.; Zeng, Q.; Lafalce, E.; **Smith, M. J.;** Yu, S.; Yoon, Y.; Chang, Y.; Jiang, Y.; Lin, Z.; Vardeny, Z. V.; Tsukruk, V. V., Large-Area Lasing and Multicolor Perovskite Quantum Dot Patterns. *Adv. Opt. Mater.* **2018**, 6, 1800474

8. Lin, C. H.; Zeng, Q.; Lafalce, E.; **Smith, M. J**.; Malak, S. T.; Jung, J.; Yoon, Y. J.; Lin, Z.; Vardeny, Z. V.; Tsukruk, V. V., Large-Scale Robust Quantum Dot Microdisk Lasers with Controlled High Quality Cavity Modes. *Adv. Opt. Mater.* **2017**, *5*, 1700011.

Other Related Publications:

9. Zhang, S.; Panikkanvalappil, S. R.; Kang, S.; **Smith, M. J.;** Yu S.; El-Sayed, M.; Tsukruk V. V. Modulation of Photonic Cavity Modes by Nanostructured Plasmonic Resonator. *ACS Photonics.* **2019**, *Submitted*

10. Xiong, R.; Yu, S.; **Smith, M. J.**; Zhou, J.; Krecker, M.; Zhang, L.; Nepal, D.; Bunning, T. J.; Tsukruk, V. V.; Assembling Carbon Quantum Dot on Nanocellulose Whiskers: Nanocobs for Programmable Chiral Luminescent Biophotonic Materials, *Angewandte Chemie,* Submitted.

11. Zhang, S.; Yu, S.; Zhou, J.; Ponder Jr., J. F.; **Smith, M. J.**; Reynolds, J. R.; Tsukruk, V. V.; Heterogeneous forward and backward scattering modulation by polymer-infused plasmonic nanohole arrays. *J. Mater. Chem. C,* **2019**,7, 3090.

12. Malak, S. T.; Liang, G.; Thevamaran, R.; Yoon, Y. J.; **Smith, M. J.;** Jung, J.; Lin, C. H.; Lin, Z.; Thomas, E. L.; Tsukruk, V. V., High-Resolution Quantum Dot Photopatterning via Interference Lithography Assisted Microstamping. *J. Phys. Chem. C* **2017,** *121*, 13370.

13. Malak, S. T.; **Smith, M. J**.; Yoon, Y. J.; Lin, C. H.; Jung, J.; Lin, Z.; Tsukruk, V. V., Programmed Emission Transformations: Negative-to-Positive Patterning Using the Decay-to-Recovery Behavior of Quantum Dots. *Adv. Opt. Mater.* **2017**, *5*, 1600509.

14. Malak, S.; Lafalce, E.; Jung, J.; Lin, C. H.; **Smith, M. J.**; Yoon, Y. J.; Lin, Z.; Tsukruk, V. V.; Vardeny, Z., Enhancement of Optical Gain Characteristics of Quantum Dot films by Optimization of Organic Ligands. *J. Mater. Chem. C* **2016**, *4*, 10069.

15. Lin, C. H.; Lafalce, E.; Jung, J.; **Smith, M. J.;** Malak, S. T.; Aryal, S.; Yoon, Y. J.; Zhai, Y.; Lin, Z.; Vardeny, Z. V.; Tsukruk, V. V., Core/Alloyed-Shell Quantum Dot Robust Solid Films with High Optical Gains. *ACS Photonics* **2016,** *3*, 647.

16. Malak, S. T.; Jung, J.; Yoon, Y. J.; **Smith, M. J.;** Lin, C. H.; Lin, Z.; Tsukruk, V. V., Large-Area Multicolor Emissive Patterns of Quantum Dot–Polymer Films via Targeted Recovery of Emission Signature. *Adv. Opt. Mater.* **2016,** *4*, 608

8.4.2 Presentations

1. Malak, S.T.; **Smith, M.J.;** Jung, J.; Yoon, Y.J.; Lin, C.H.; Lin, Z.; Tsukruk, V.V.; Decay-to-Recovery Behavior and on–off Recovery of Photoluminescence Intensity from Core_Shell Quantum Dots. *Materials Research Society Conference*, Spring **2018**.

2. Malak, S.T.; **Smith, M.J.;** Yoon, Y.J.; Lin, C.H.; Jung, J.; Yu, S.; Lin, Z.; Tsukruk, V.V.; Programmed Emission Transformations: Negative-to-Positive Patterning Using the Decay-to-Recovery Behavior of Quantum Dots. *Materials Research Society Conference*, Spring **2018**. Best poster nominee

3. **Smith, M.J.;** Malak, S.T.; Jung, J.; Yoon, Y.J.; Lin, C.H.; Kim, S.; White, T.; Bunning, T.; Lin, Z.; Tsukruk, V.V.; Utilizing thiol-ene click chemistry to fabricate highly photoluminescent QD patterns for advanced photonic devices. *Materials Research Society Conference*, Spring **2016**.

4. **Smith, M.J.;** Malak, S.T.; Jung, J.; Yoon, Y.J.; Lin, C.H.; White, T.; Lin, Z.; Tsukruk, V.V.; Utilizing Thiol ene Click Chemistry to Fabricate Highly Emissive QD Films and Patterns for Polymer Based Optical Systems. *12th National Graduate Polymer Conference*, Summer **2016.**

5. **Smith, M.J.;** Malak, S.T.; Jung, J.; Yoon, Y.J.; Lin, C.H.; White, T.; Lin, Z.; Tsukruk, V.V.; Utilizing Thiol ene Click Chemistry to Fabricate Highly Emissive QD Films and Patterns for Polymer Based Optical Systems. *Georgia Tech, Materials Science & Engineering Competition* **2016**.

APPENDIX A. (DECAY-TO-RECOVERY BEHAVIOR AND ON−OFF RECOVERY OF PHOTOLUMINESCENCE INTENSITY FROM CORE/SHELL QUANTUM DOTS SUPPORTING DATA)

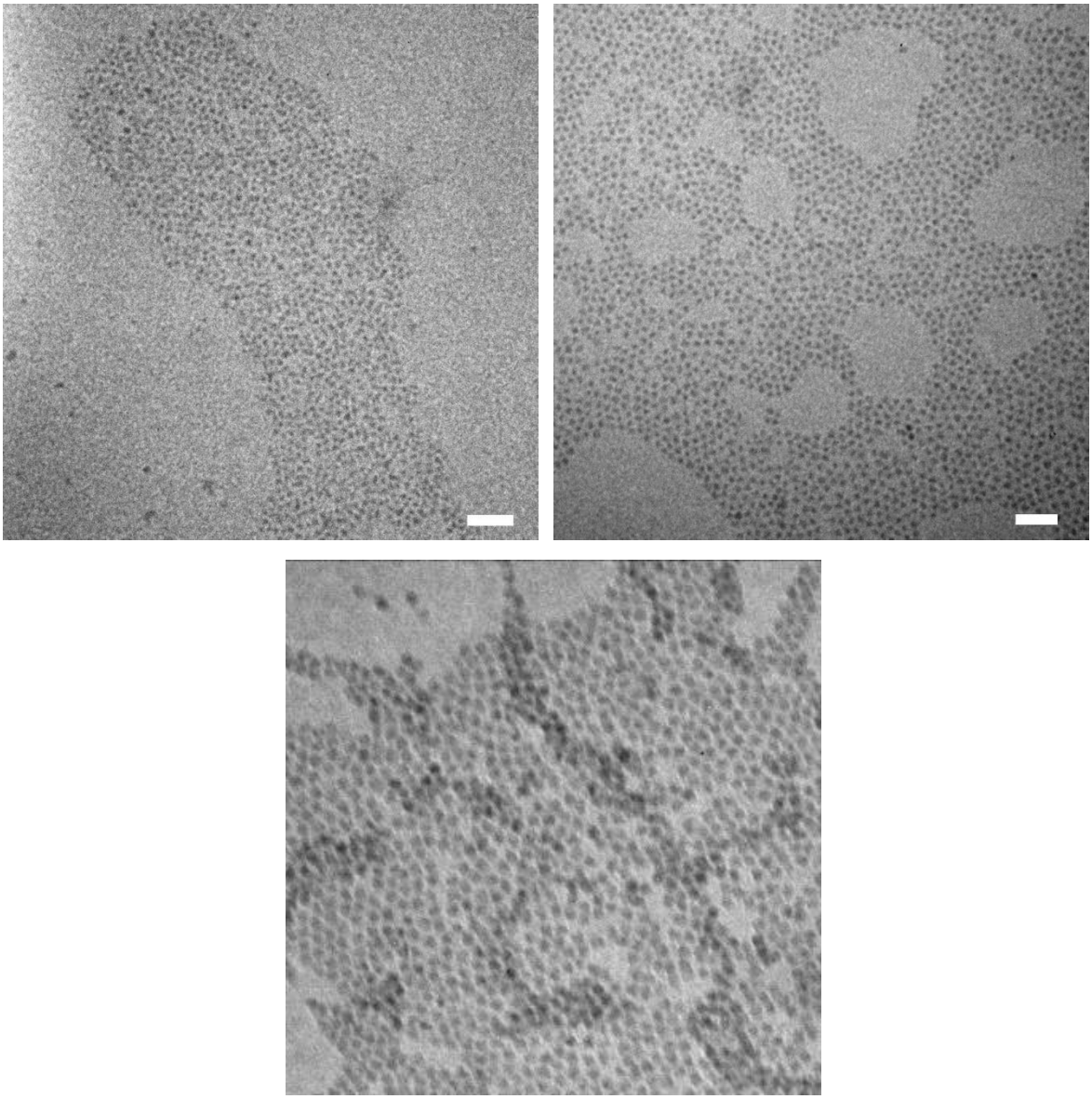

Figure A.1: TEM micrographs of (a) CdSe/ZnS core/shell, (b) thin CdSe/Cd1-xZnxSe1-ySy core/graded shell, and (c) thick CdSe/Cd1-xZnxSe1-ySy core/graded shell QD. Scale bars are 25nm for all images.

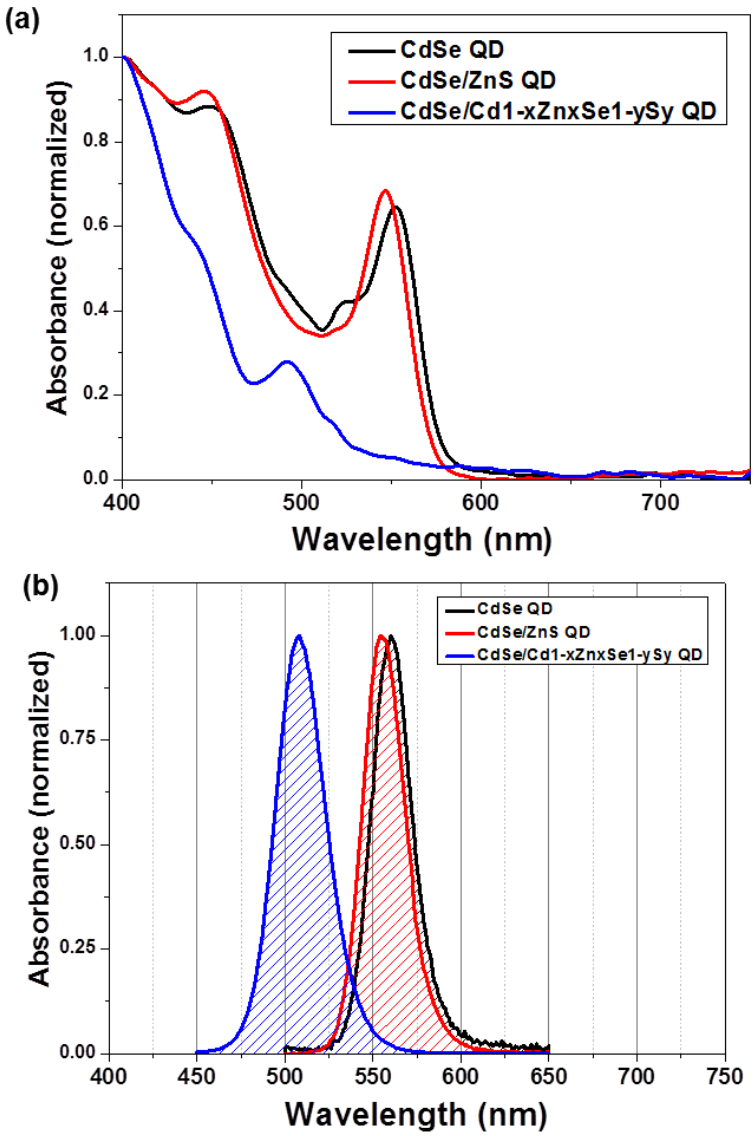

Figure A.2: UV-vis absorbance and photoluminescence of each type of QD design (core CdSe QD, core/shell CdSe/ZnS QD, and core/graded shell CdSe/$Cd_{1-x}Zn_xSe_{1-y}S_y$ QD).

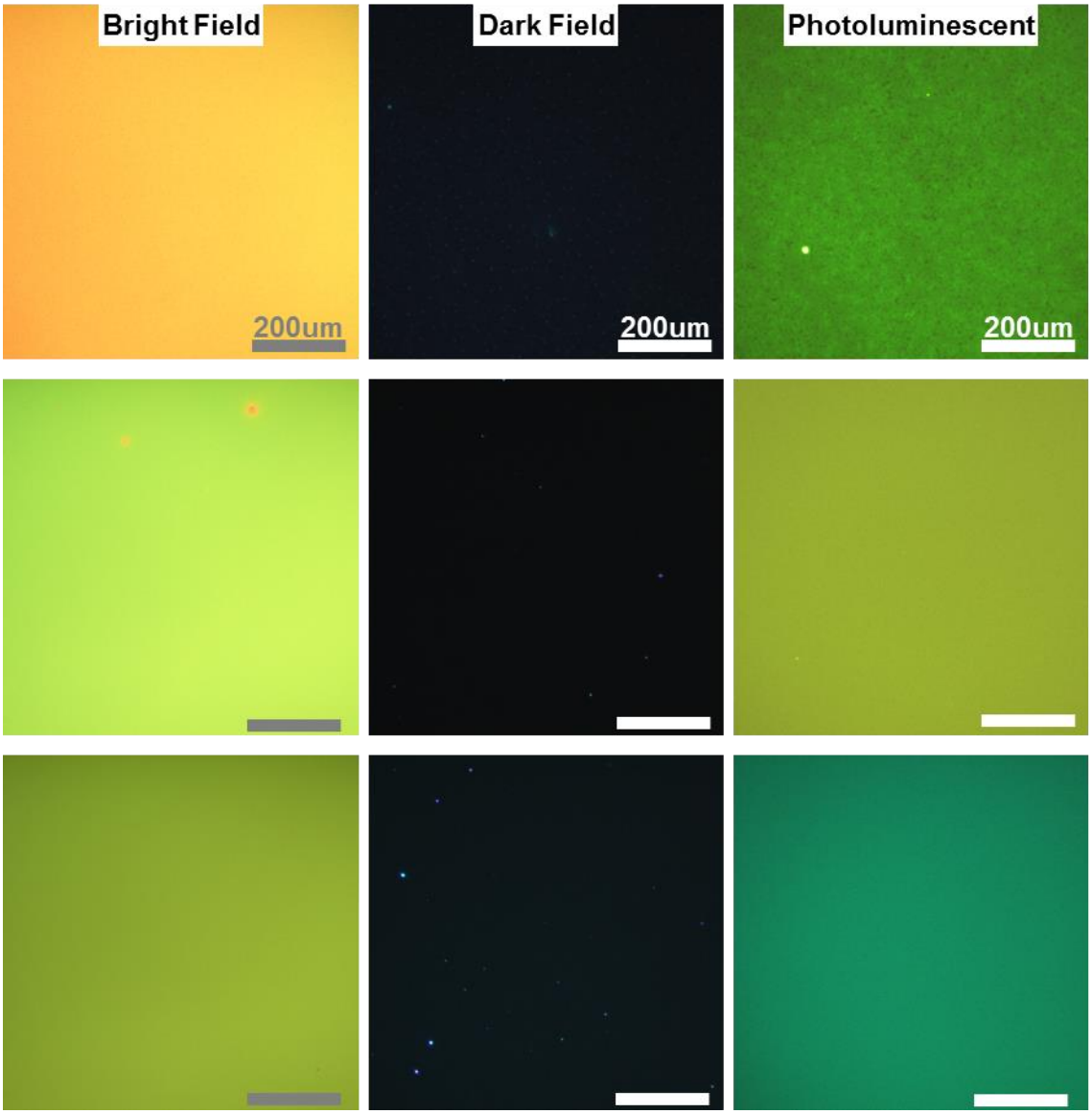

Figure A.3: Bright field (column 1), dark field (column 2), and photoluminescence (column 3) imaging of QD-PMMA films with each type of QD design (core CdSe QD, row 1)(core/shell CdSe/ZnS QD, row 2) (core/graded shell CdSe/$Cd_{1-x}Zn_xSe_{1-y}S_y$ QD, row 3). All scale bars are 200 um.

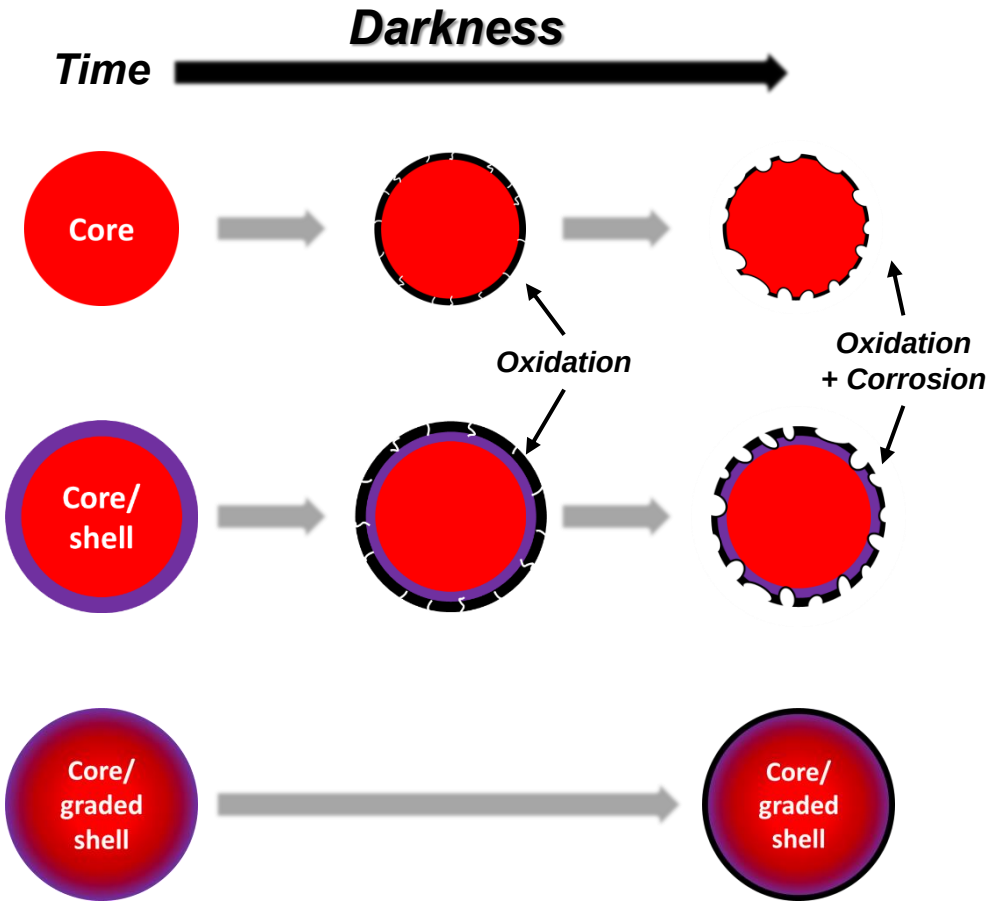

Figure A.4: The proposed physical evolution of each type of QD (CdSe core, CdSe/ZnS core/shell, and CdSe/$Cd_{1-x}Zn_xSe_{1-y}S_y$ core/graded shell) in darkness (air) over a period of 45 minutes (organic ligand not shown for clarity).

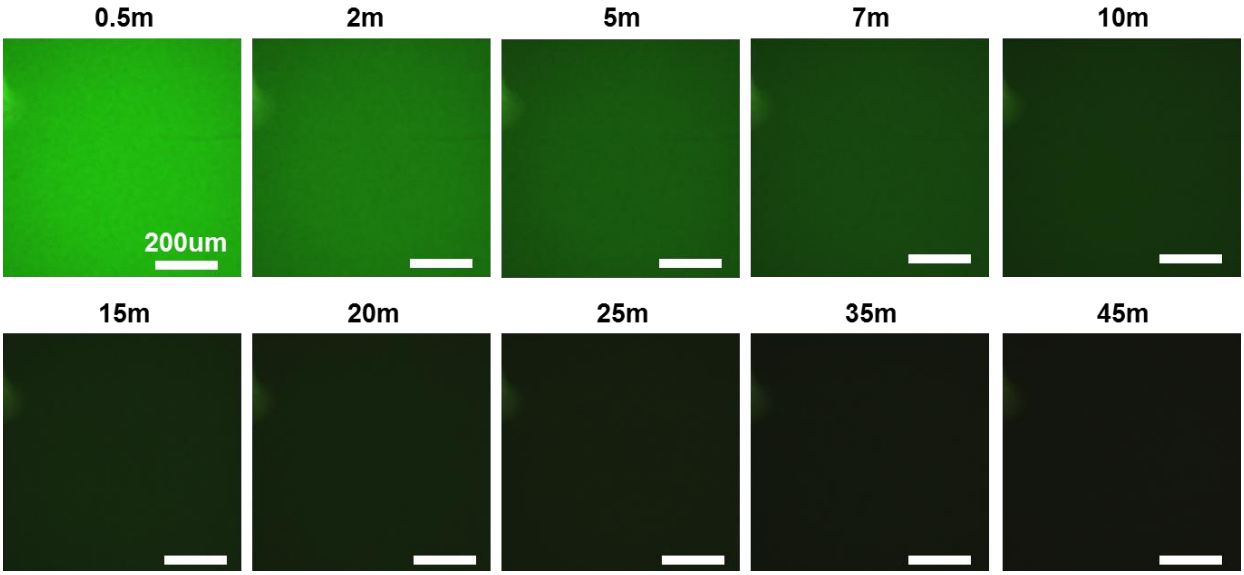

Figure A.5: PL imaging of an unstable plain core CdSe QD-PMMA film under continuous light exposure for 45 minutes (blue: 450-490 nm, 22.5 mW). All scale bars are 200 um.

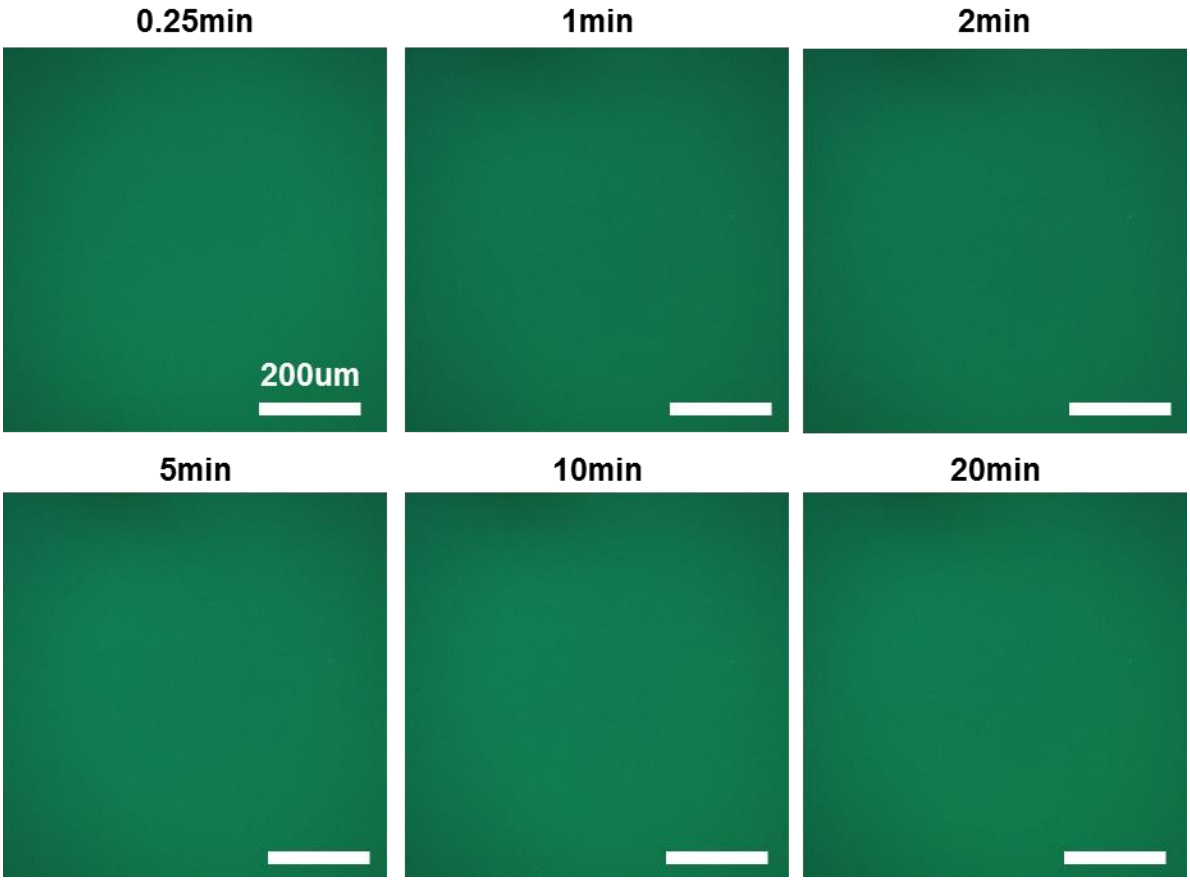

Figure A.6: PL imaging of a stable CdSe/$Cd_{1-x}Zn_xSe_{1-y}S_y$ core/graded shell QD-PMMA film under continuous light exposure for 20minutes (blue: 450-490 nm, 25 mW). All scale bars are 200 um.

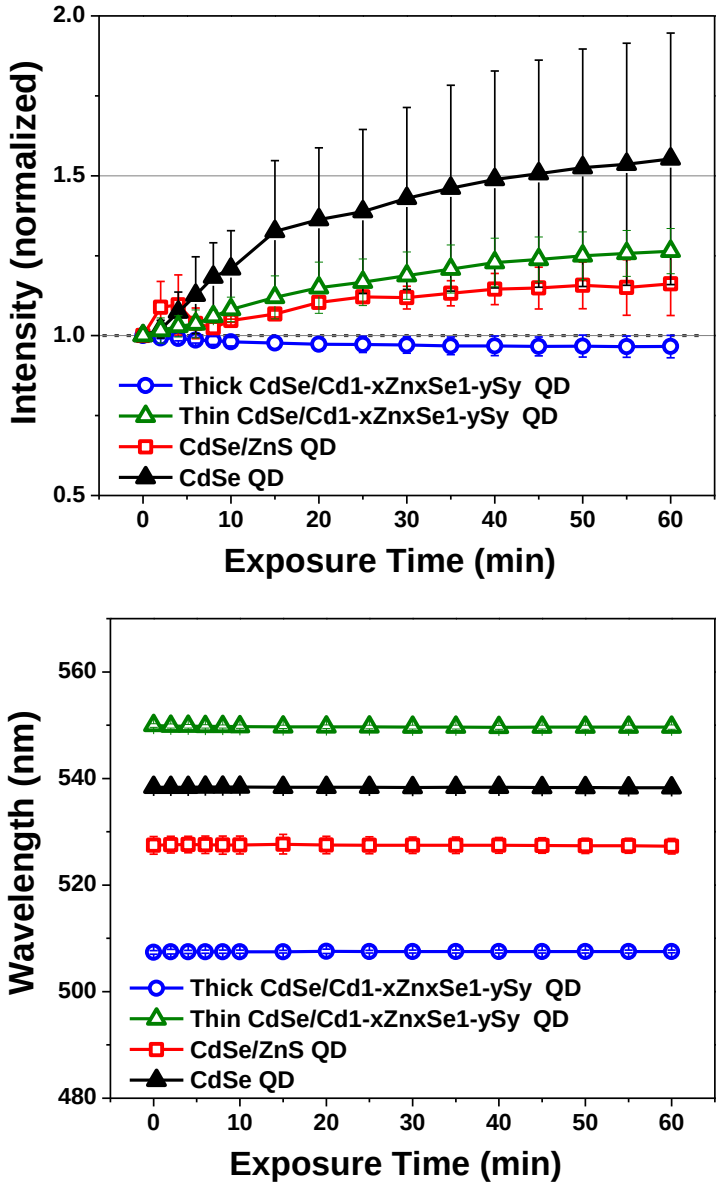

Figure A.7: Evolution of the (a) PL intensity and (b) PL peak position of each QD solution (core CdSe, core/shell CdSe/ZnS, or alloyed core/graded shell CdSe/$Cd_{1-x}Zn_xSe_{1-y}S_y$ QDs) under continuous light exposure (blue: 450-490nm, 1.9mW).

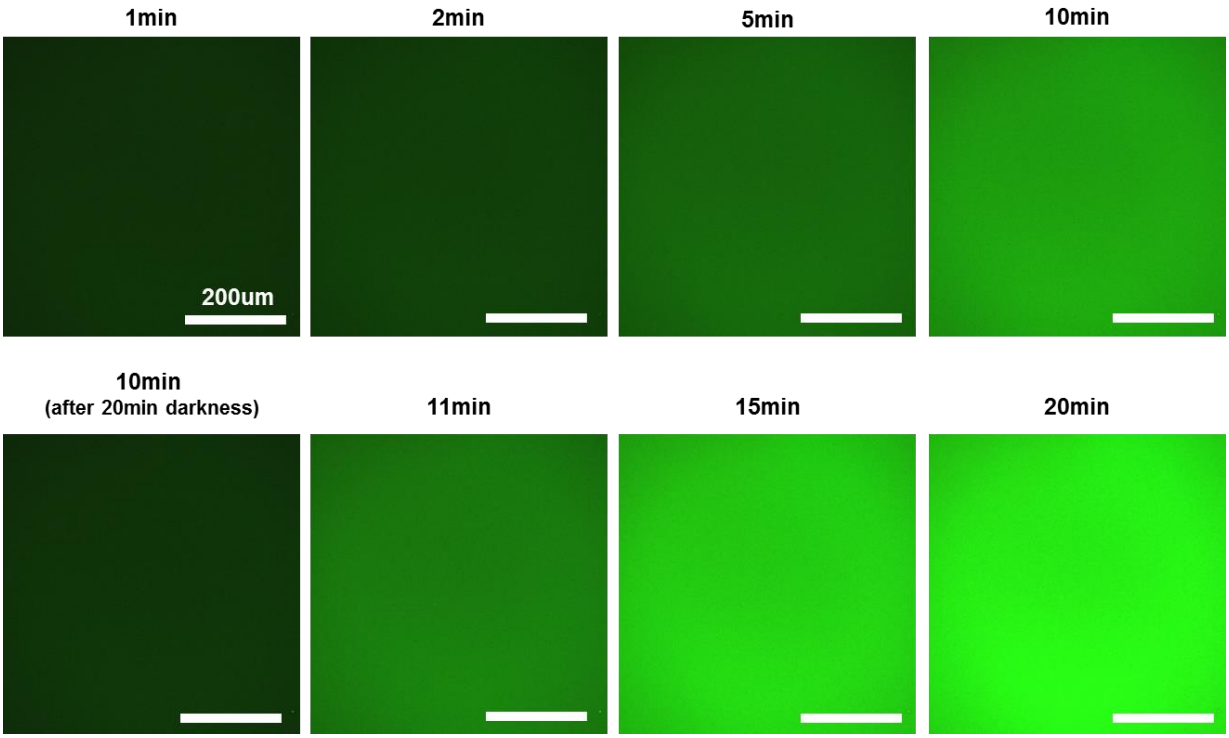

Figure A.8: PL imaging of an unstable core/shell CdSe/ZnS QD-PMMA film under an exposure-darkness-exposure light cycle (blue: 450-490 nm, 19.9 mW). All scale bars are 200 um.

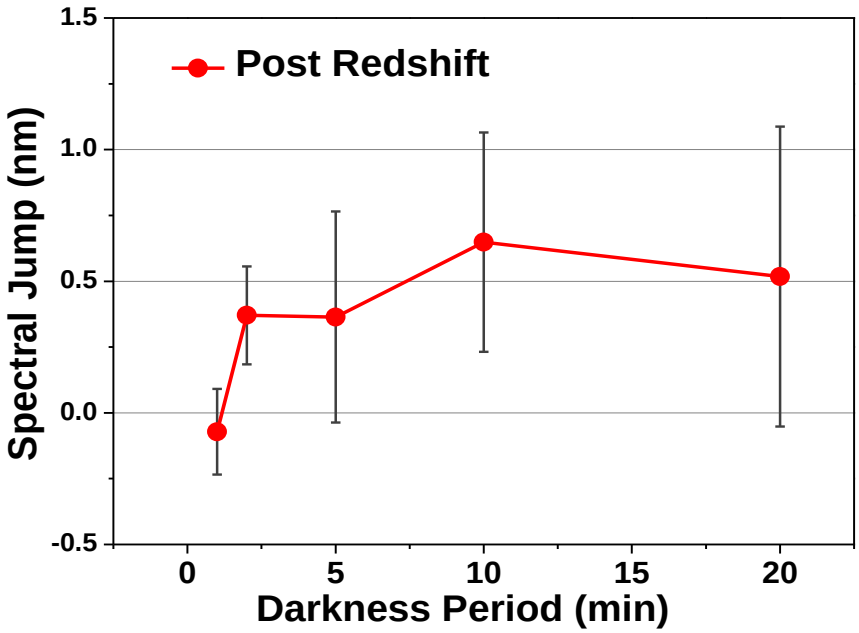

Figure A.9: Spectral red-shift of CdSe/ZnS QDs (in polymer film) that occurs immediately upon re-exposure to light during a light-darkness-light exposure cycle.

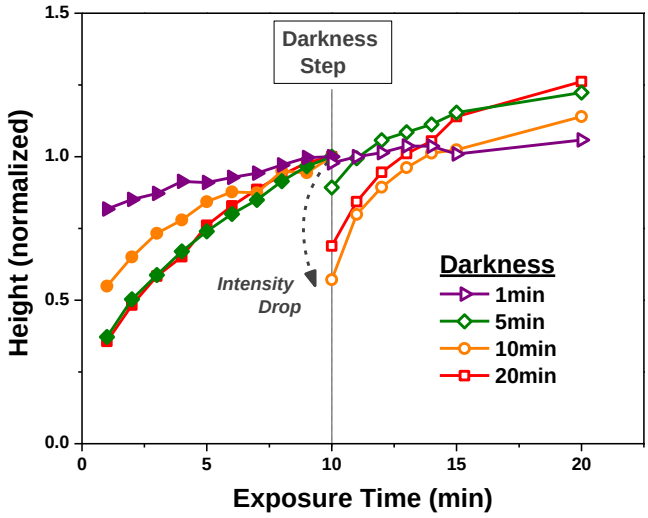

Figure A.10: Examination of how periods of darkness affect the PL intensity of thin shell CdSe/$Cd_{1-x}Zn_xSe_{1-y}S_y$ core/graded shell QDs exposed to light (exposure: 450-490nm)(QD-PMMA films). PL intensity decay dip for different periods of darkness (10 min into light exposure regime).

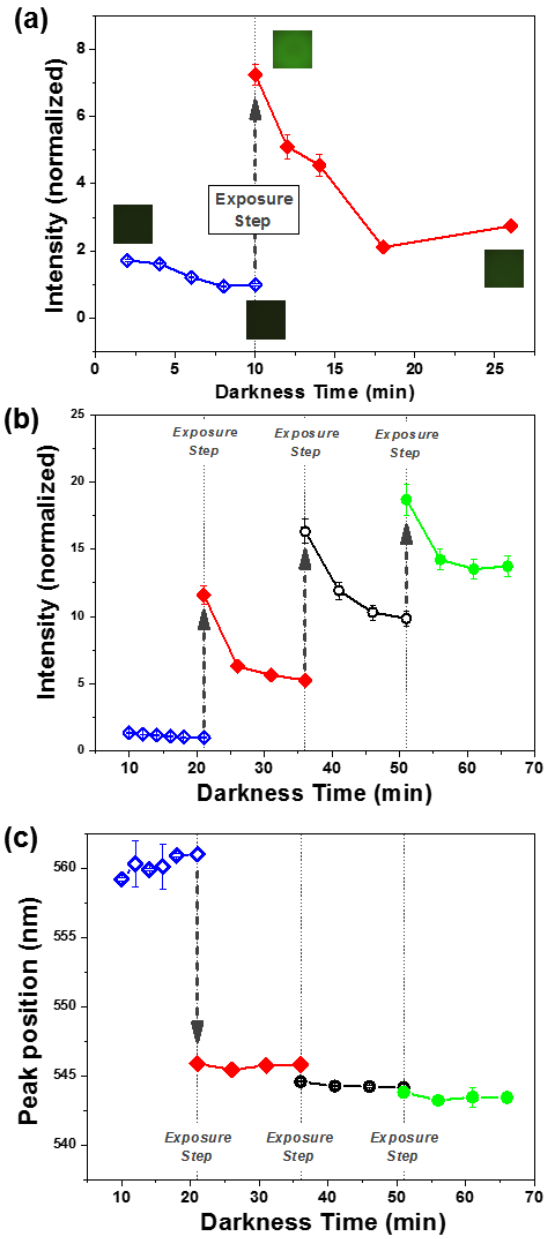

Figure A.11: Examination of the discharge-charge effect observed upon darkness and light exposure steps for a CdSe/ZnS QD-PMMA film. (a) The evolution of PL intensity during a darkness-exposure-darkness trial (a 10-min exposure period) (blue light: 450-490 nm, 26.5 mW). -The (b) PL intensity and (c) PL spectral position during cycling of darkness-exposure-darkness (an 11-min exposure period) (blue light: 450-490 nm 25.3 mW).

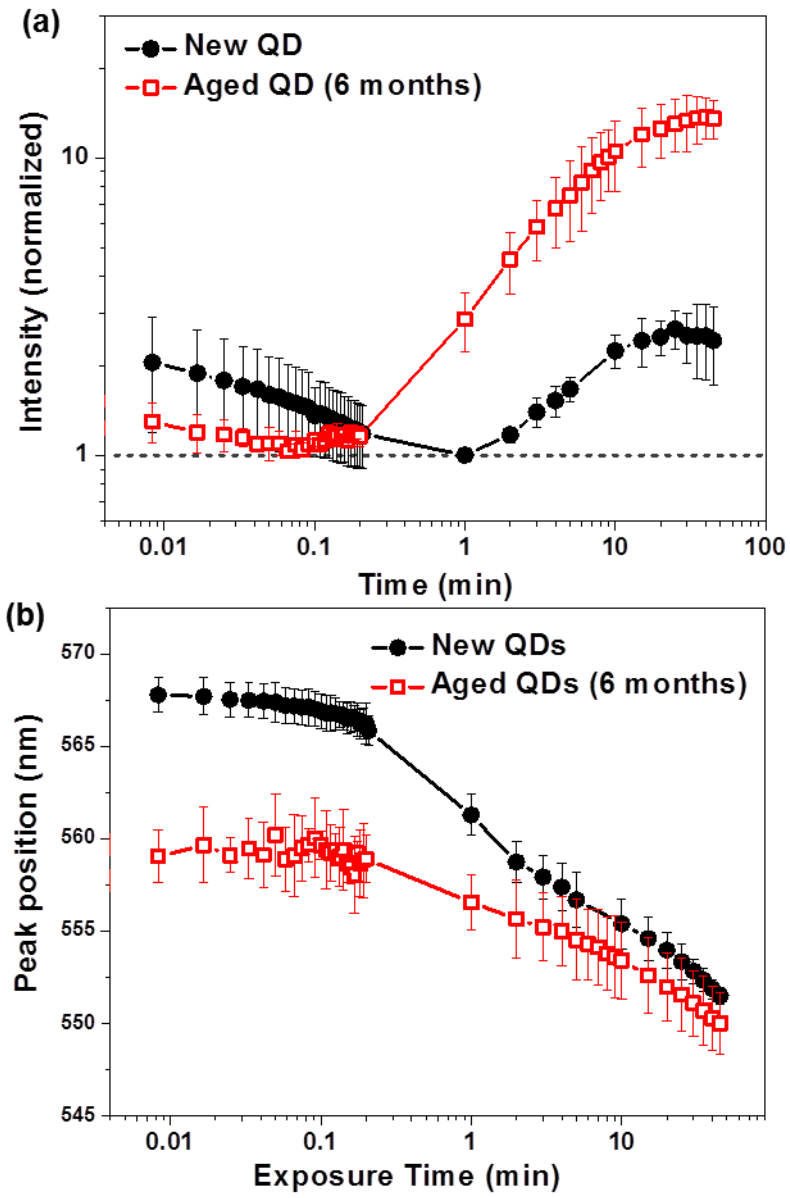

Figure A.12: Evolution of the (a) PL intensity and (b) spectral position of QD-polymer films under continuous exposure (blue: 450-490 nm, 24-28 m) with either recently synthesized or aged (6 months) unstable core/shell CdSe/ZnS QDs.

APPENDIX B. (ROBUST, UNIFORM AND HIGHLY EMISSIVE QD FILMS AND PATTERNS USING FAST POLYMERIZATION WITH THIOL-ENE CHEMISTRY SUPPORTING DATA)

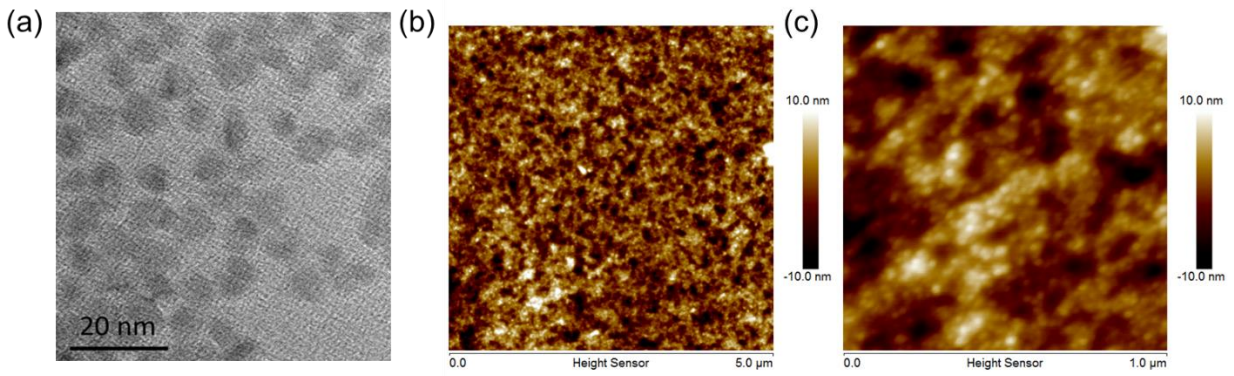

Figure B.1: (a) TEM image of the BA-QDs with average size of 8 nm, and AFM images showing surface roughness of <4 nm for (b) 5 um^2 and (c) 1 um^2 scan size for neat butylamine QD films.

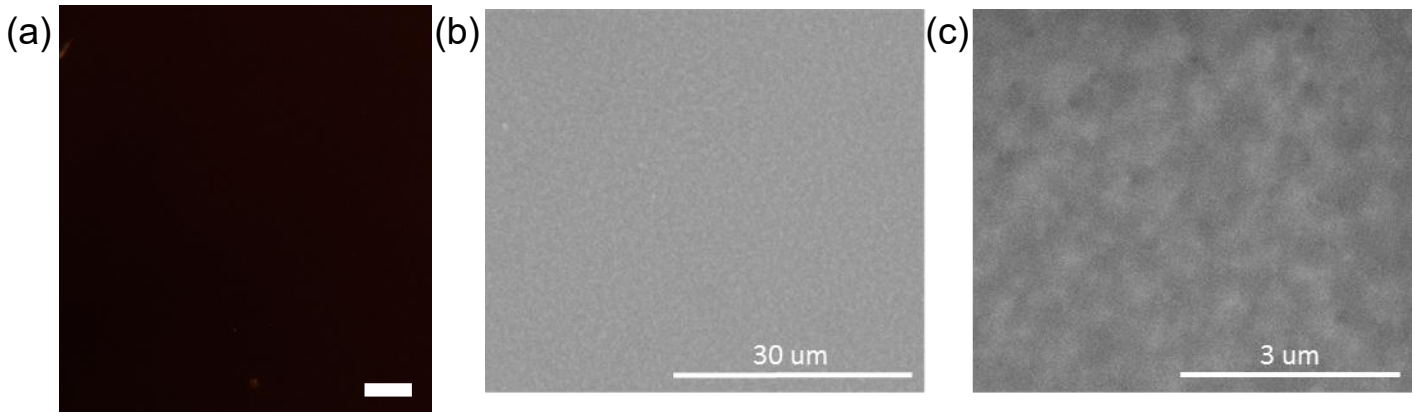

Figure B.2: (a) 50x dark field image of a QD-polymer film showing minimal scattering. Scale bar – 20 µm. (b),(c) SEM of composite film showing minimal aggregation.

Table B.1: Comparison of Optical Properties of QD Solutions.

	OAQD	BAQD	NOA-BAQD
QY	50%	18-30%	18%
Emission Position (nm)	624	622	628

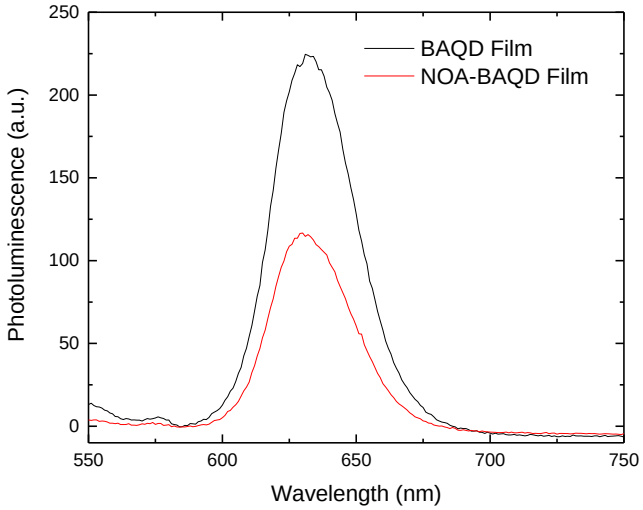

Figure B.3: Relative PL emission of pure BAQD film and NOA-BAQD film showing slight reduction in PL intensity following composite film formation.

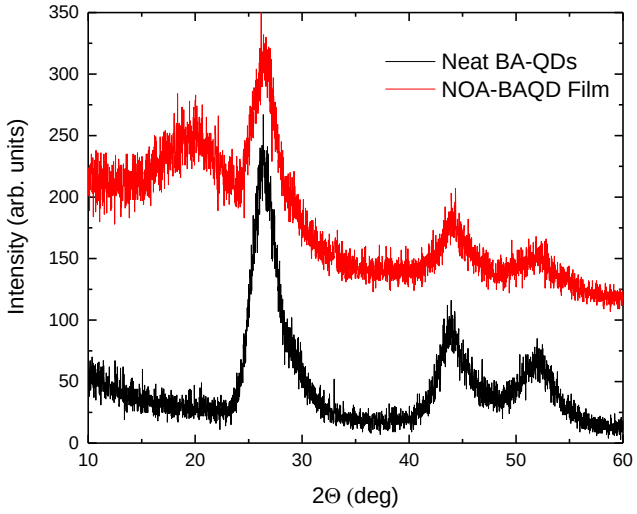

Figure B.5: XRD showing crystal lattice of CdSe based QDs before and after incorporation

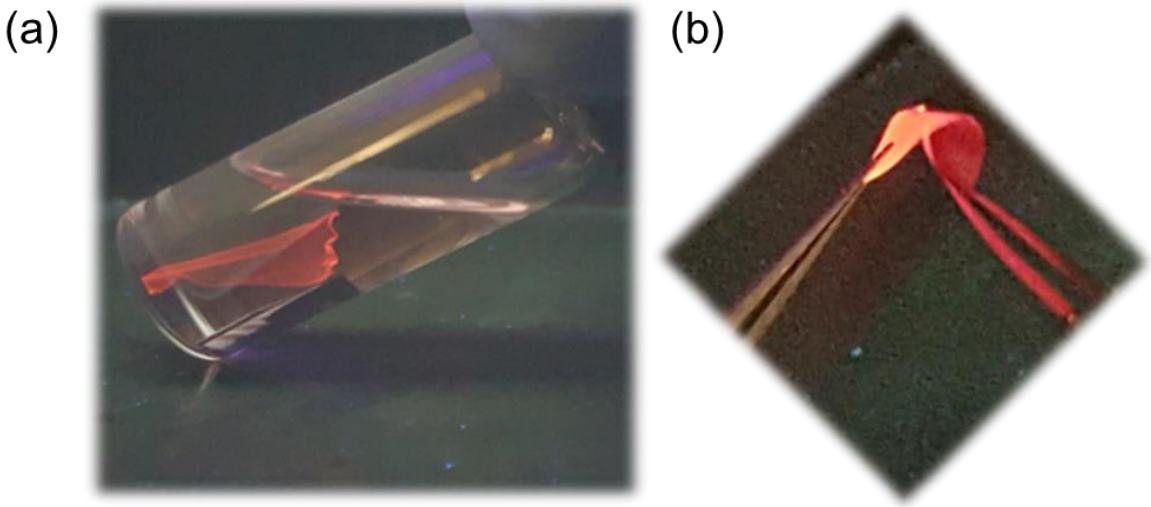

Figure B.4: Freely standing NOA-QD composite film suspended in chloroform (a) and being bent between tweezers (b) under UV illumination.

APPENDIX C. (COUPLED WHISPERING GALLERY MODE RESONATORS VIA TEMPLATE ASSISTED ASSEMBLY OF PHOTOLUMINESCENT MICROSPHERES SUPPORTING DATA)

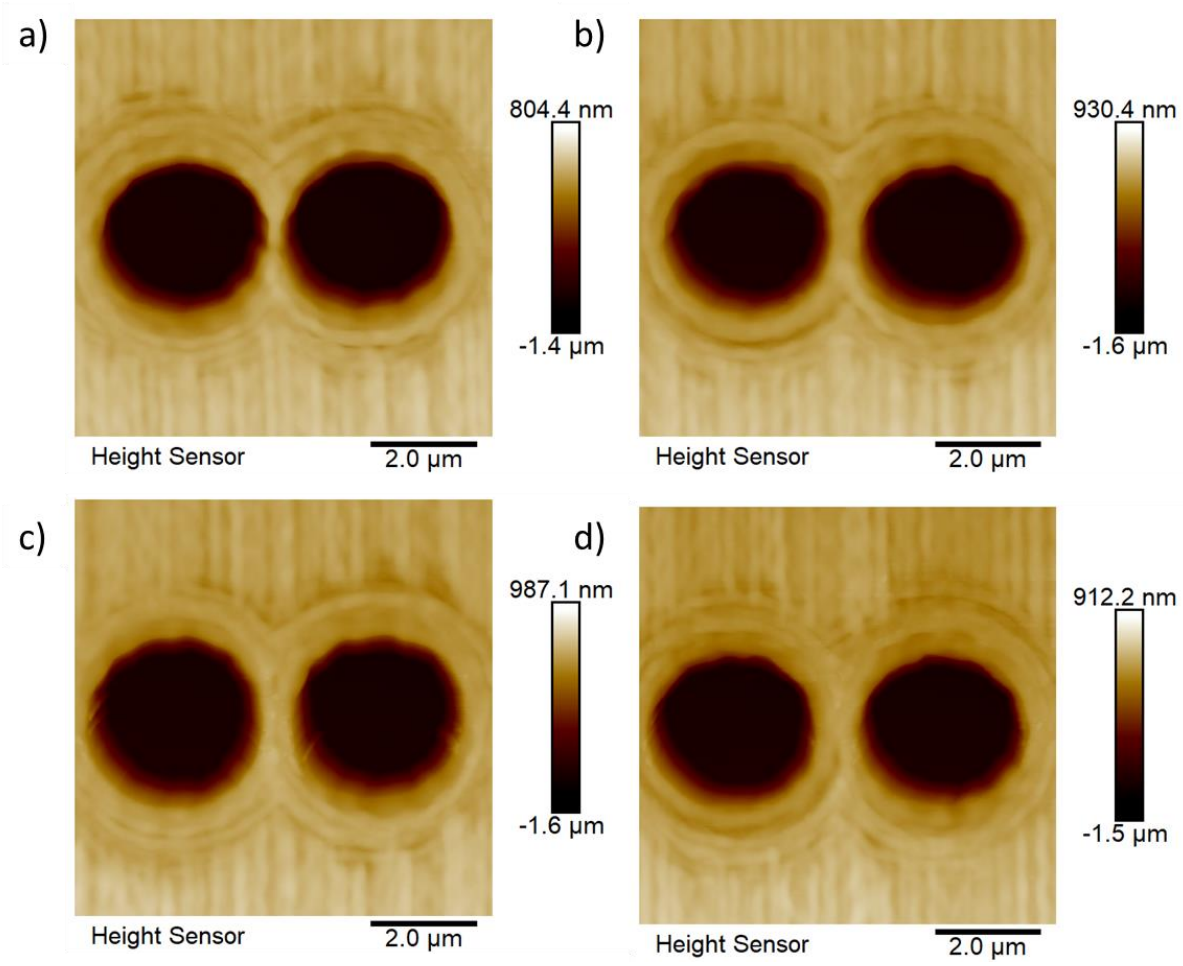

Figure C.1: AFM scans showing coupled cavities for dimers designed with nominal resonator spacing of 0 nm (a), 200nm (b), 350nm (c), and 500nm (d).

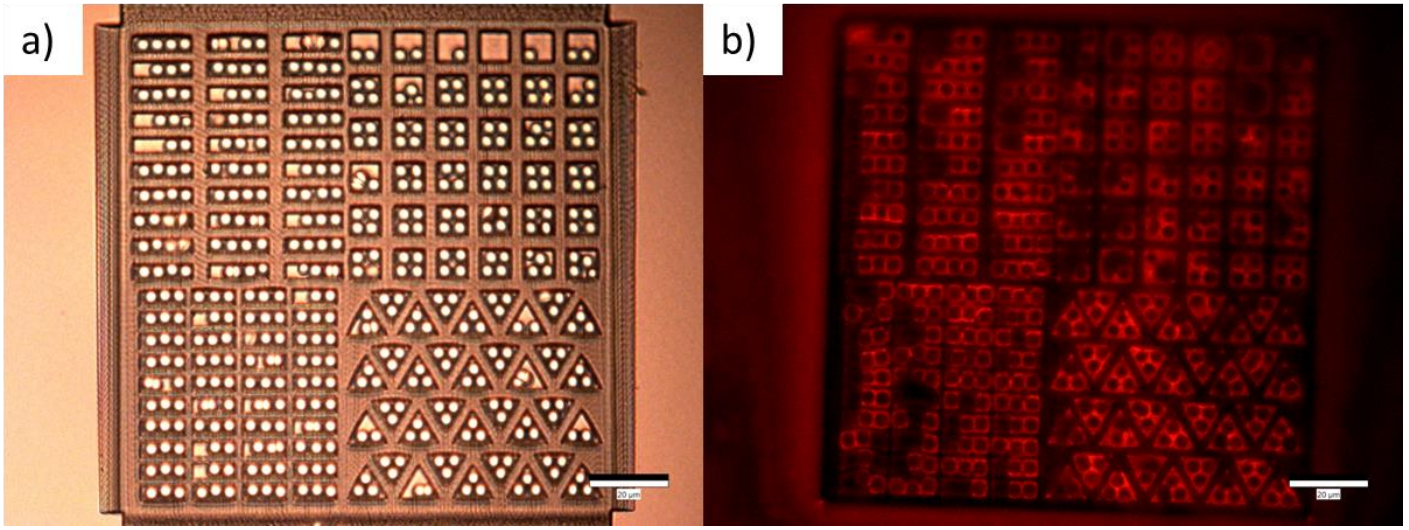

Figure C.3: Optical images showing coupled cavities of various geometries for microspheres of ~4 µm (a) and (b). Scale bars are 20 µm.

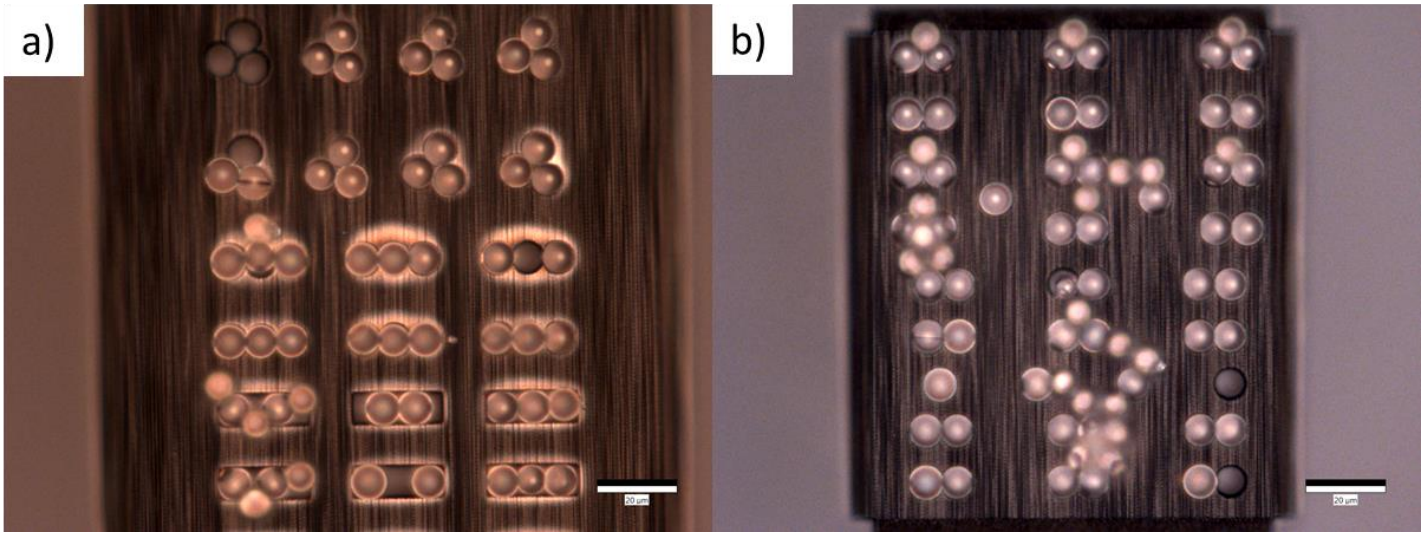

Figure C.2: Optical images showing coupled cavities of various geometries for microspheres of ~8 µm (a) and (b). Scale bars are 20 µm.

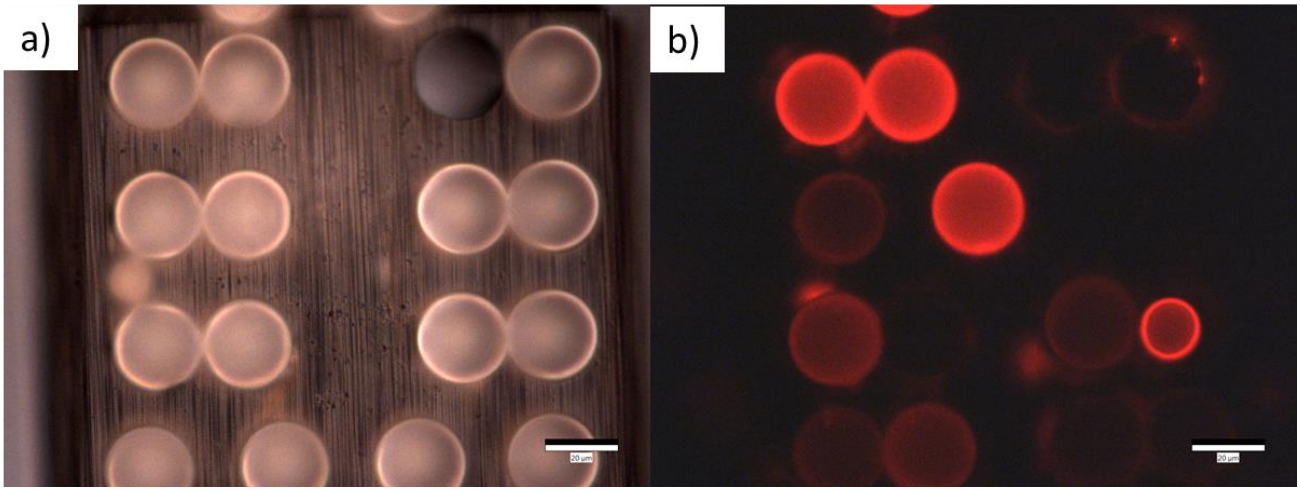

Figure C.5: Optical images showing coupled cavities of various geometries for microspheres of ~25 µm (a) and (b). Scale bars are 20 µm.

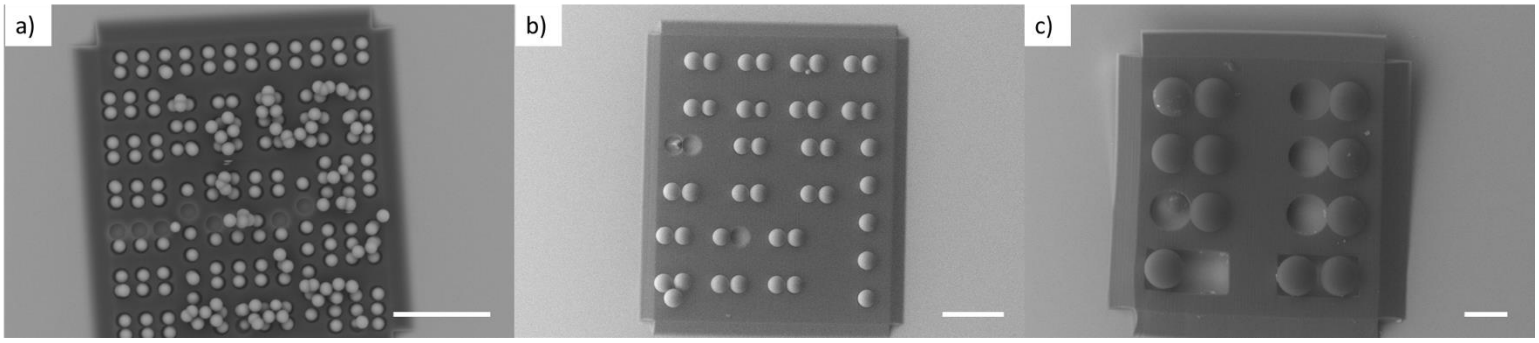

Figure C.4: SEM images showing coupled cavities for microspheres of ~4 µm (a), ~8 µm (b), and ~25 µm (c). Scale bars are 25 µm.

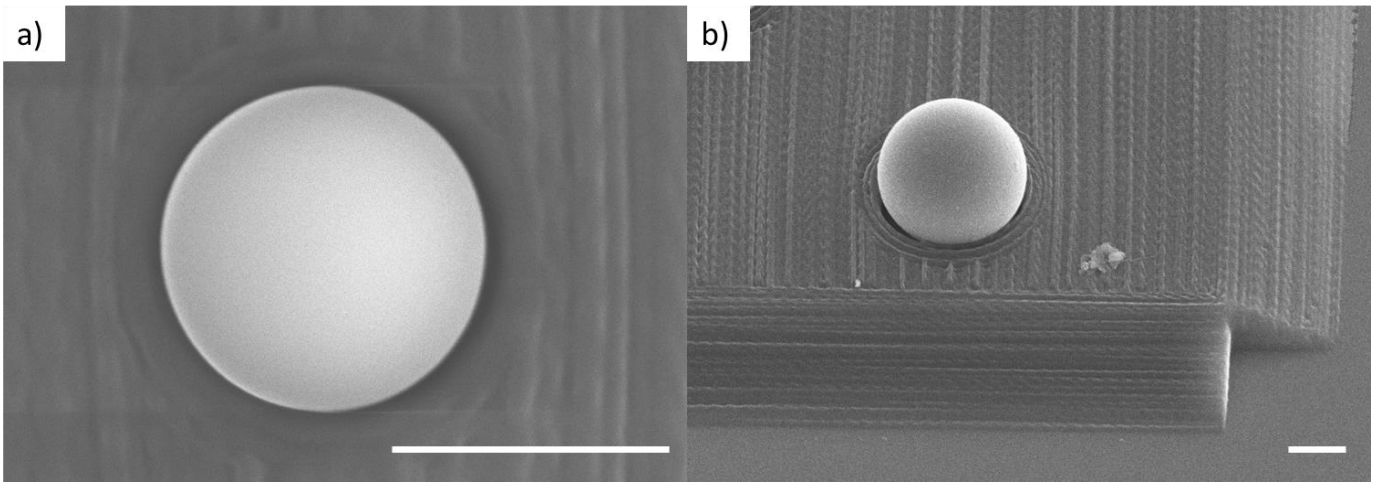

Figure C.6: Additional SEM characterization showing the precise assembly of microsphere into the center of a cavity (a) and 45° tilted SEM for a larger microsphere to further highlight placement (b).

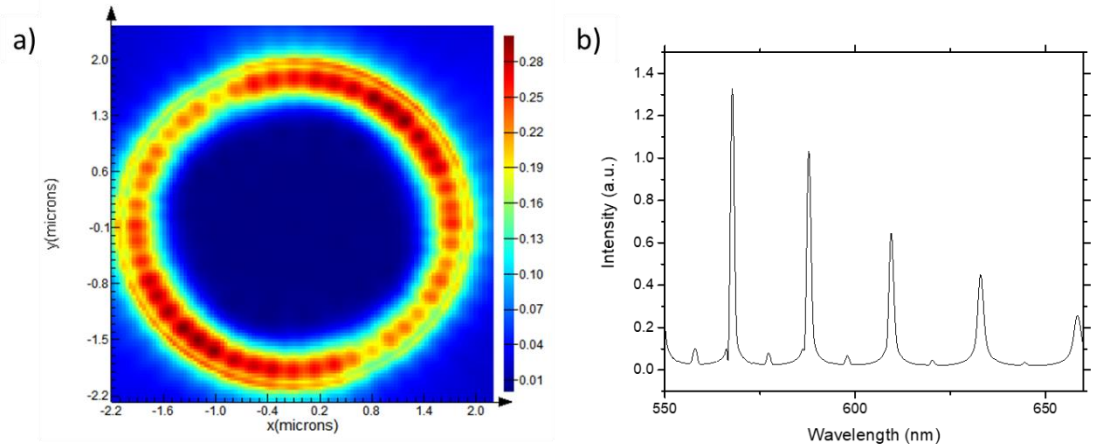

Figure C.7: Modal profile for individual microsphere (a) and WGM spectrum(b).

APPENDIX D. (ROBUST LASING MODES IN COUPLED COLLOIDAL QUANTUM DOT MICRODISK PAIRS USING A NON-HERMITIAN EXCEPTIONAL POINT SUPPORTING DATA)

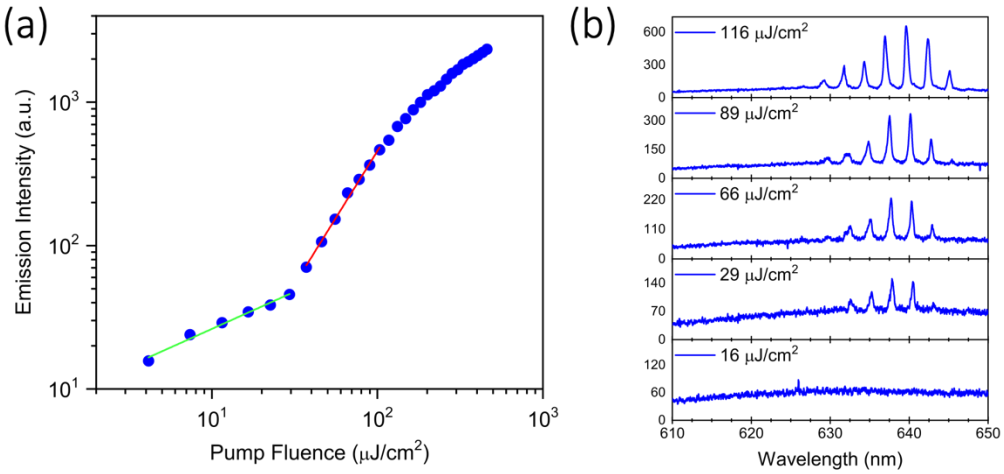

Figure D.1: (a) Light-light curve for an isolated microdisk. The green line indicates the region of sub-linear increase where only spontaneous emission is observed. The red line indicates the super-linear increase above threshold that corresponds to the observation of cavity modes. (b) Emission spectra at different levels of pump fluence. The cavity modes become apparent at a fluence of 29 μJ/cm^2.

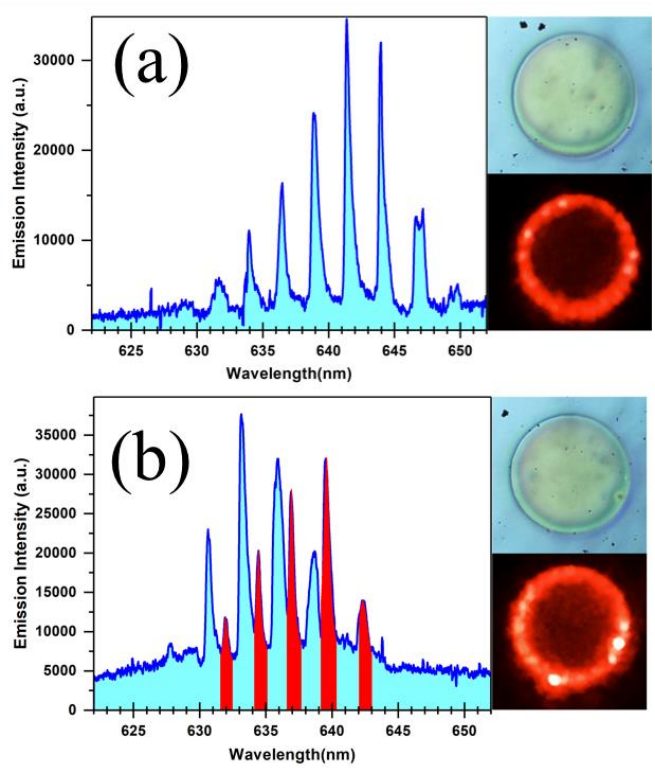

Figure D.2: Comparison of (a) disk lacking defects and (b) disk with defects. Left panels show the emission spectrum. Top right panel is the optical microscope image; bottom right panel is the fluorescent image under lasing conditions. The red shaded regions in (b) are Lorentzian fits to the laser modes, emphasizing the two sets of modes.

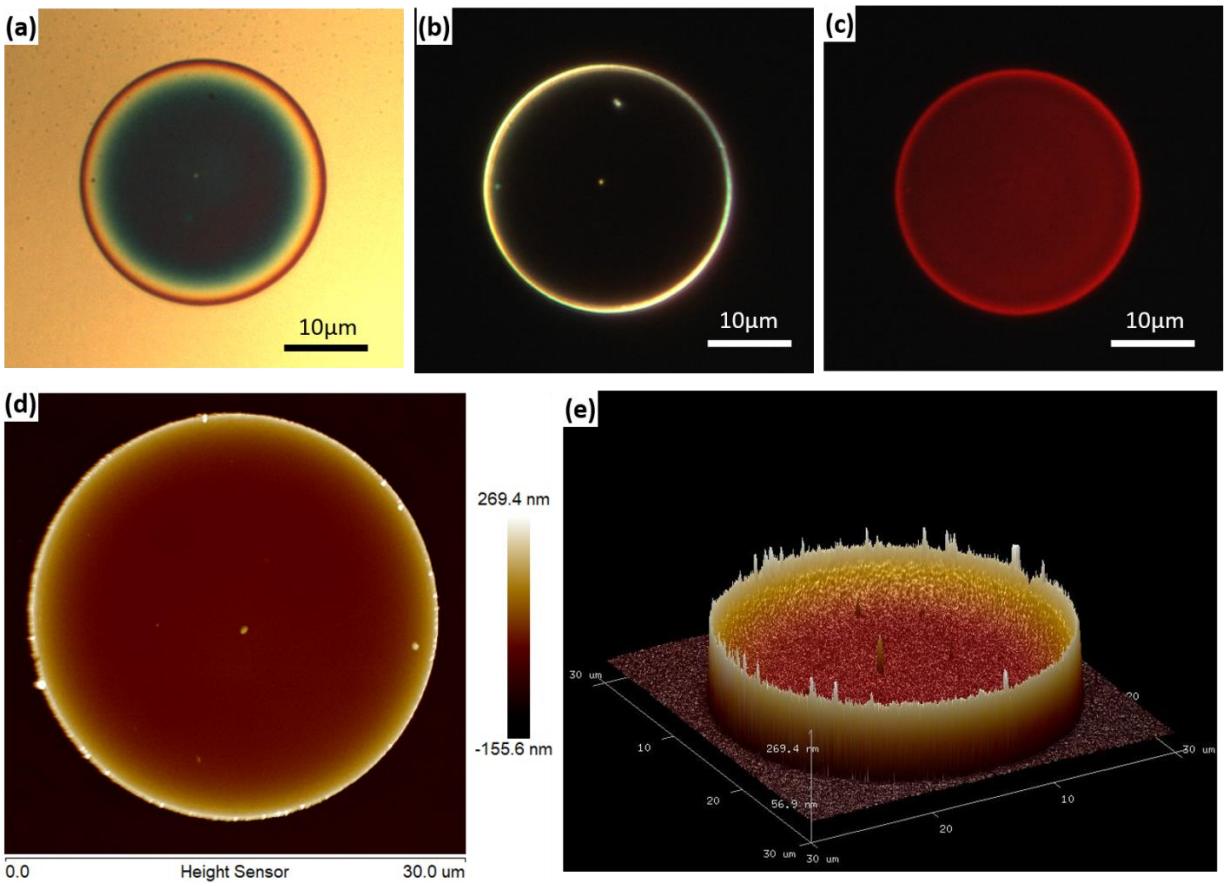

Figure D.3: (a) Bright field, (b) dark field, and (c) photoluminescence microscopic imaging of microdisk with diameter of 25 µm. (d) AFM topographical image (top-view) and (e) 3D projection of microdisk with defects formed near circumference.

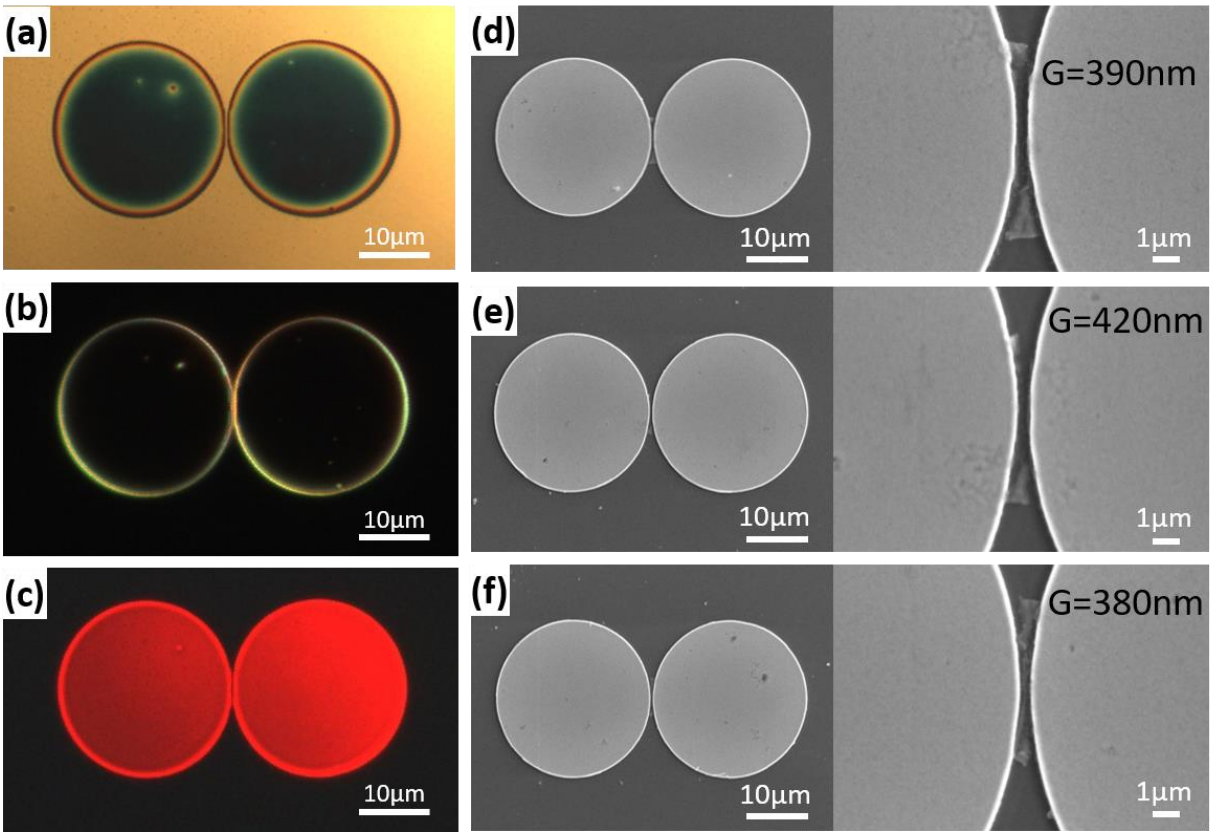

Figure D.4: (a) bright field, (b) dark field, and (c) photoluminescence microscopic imaging of coupled microdisks with disk diameter of 25 μm. (d), (e), (f) SEM images of 3 sets of coupled microdisks.

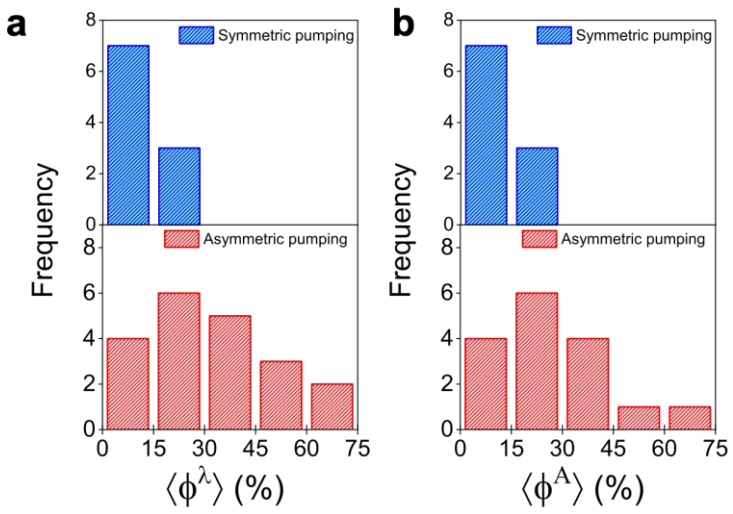

Figure D.5: Frequency distribution of the spectrally averaged modal splitting parameters, $\langle \phi^{\lambda} \rangle$ and $\langle \phi^{A} \rangle$ for microdisks pairs. In each case the top panel shows the splitting parameter from the symmetrically pumped pair while the bottom panel shows that for asymmetric pumping of one disk of the pair.

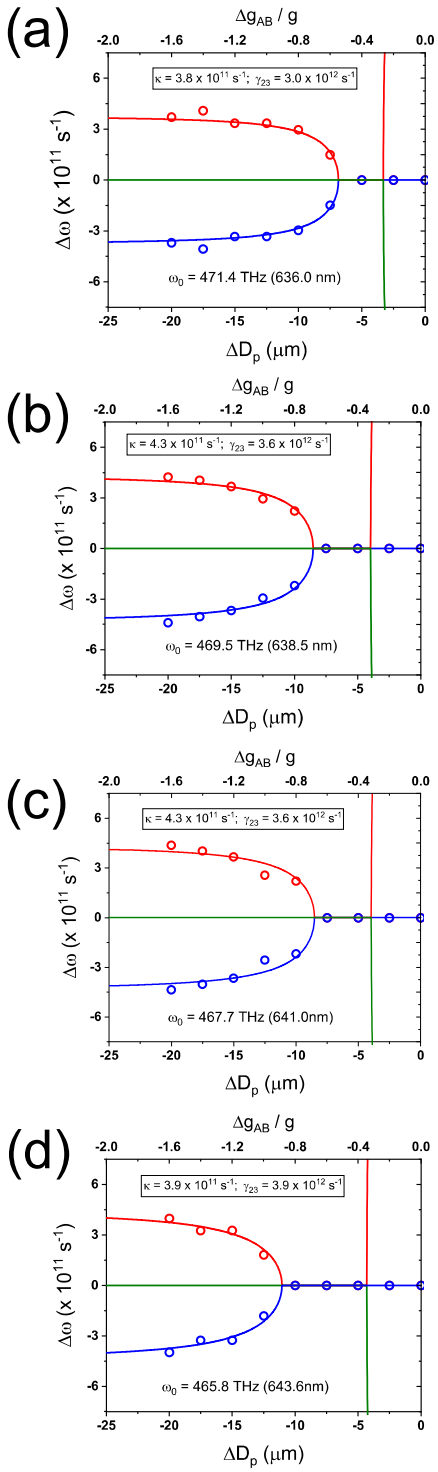

Figure D.6: Comparison of the experimental peak positions from Fig. 7.4a to the model simulations. The excellent fit validates our model.

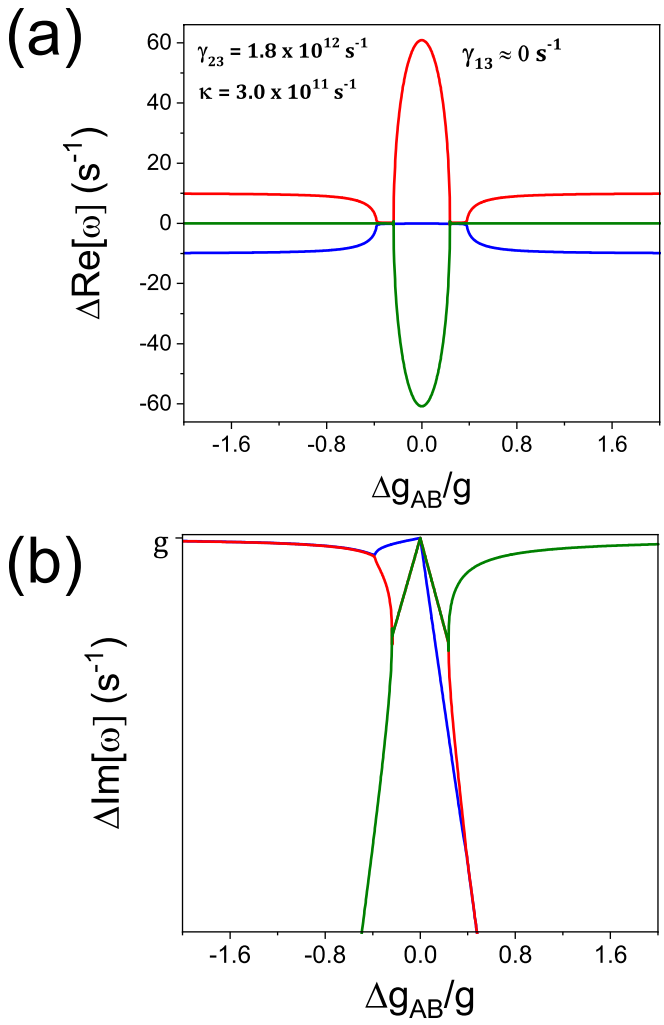

Figure D.7: (a,b) Real and Imaginary eigenfrequencies shown over the full range of the Δg_{AB} parameter space. The behavior is symmetric in the real frequency splitting, whereas only mode 3 will lase while modes 1 and 2 become lossy at large positive Δg_{AB}, as expected.

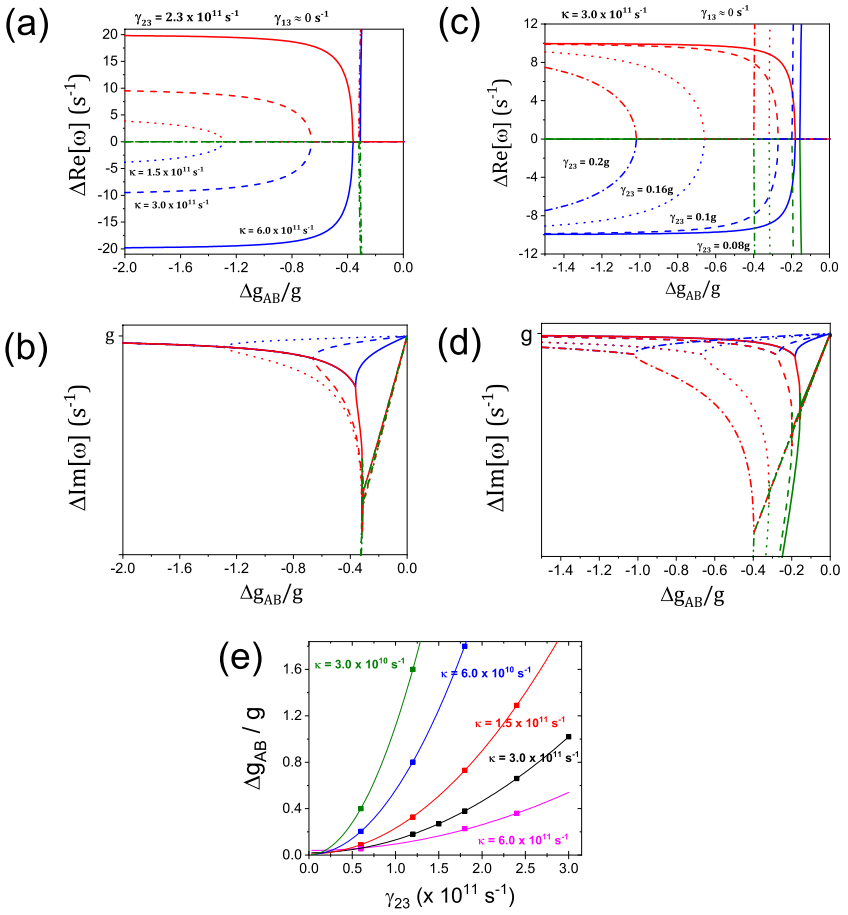

Figure D.8: Eigenfrequencies vs. Δg_{AB}. (a,b) Real and imaginary part of the eigen frequencies ω_1 (blue), ω_2 (red), and ω_3 (green), vs. the gain differential Δg_{AB} for different values of κ with γ_{23} and γ_{13} fixed. (c,d) Same as in (a,b) but for different values of γ_{23} with κ and γ_{13} fixed. (e) Point in Δg_{AB} where EP1 occurs vs γ_{23} for different values of κ. The solid lines are show the family of solutions of the form $\Delta g_{AB} = [\kappa + (\gamma_{23})^2/2\kappa]$.

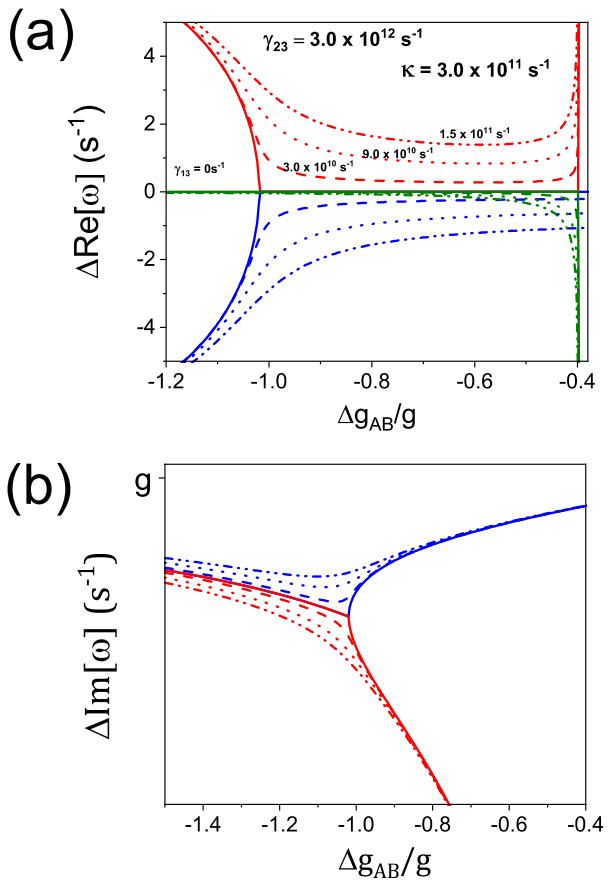

Figure D.9: (a,b) Real and Imaginary eigenfrequencies vs. Δg_{AB} with both γ_{23} and κ held constant for different values of γ_{13}.

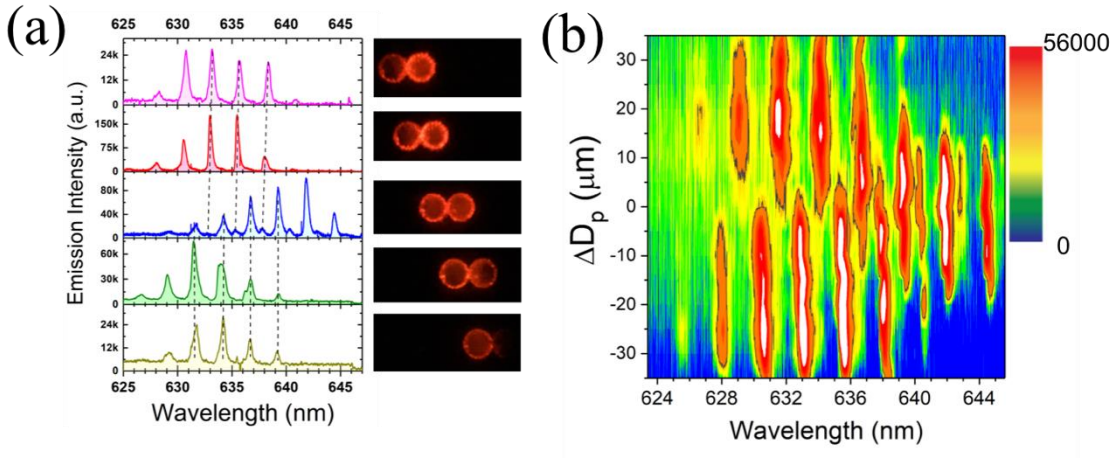

Figure D.10: Effects of spatial gain variation of coupled microdisk resonators without defects. (a) Emission spectra from a coupled microdisk pair as the pair is shifted through different locations relative to the pump beam spot, as illustrated schematically to the left of each spectrum. The corresponding fluorescent images are shown to the right of each spectrum. (b) False-color contour plot of the emission intensity vs emission wavelength and the relative distance between the center of the pair to the center of the beam spot, ΔD_p.

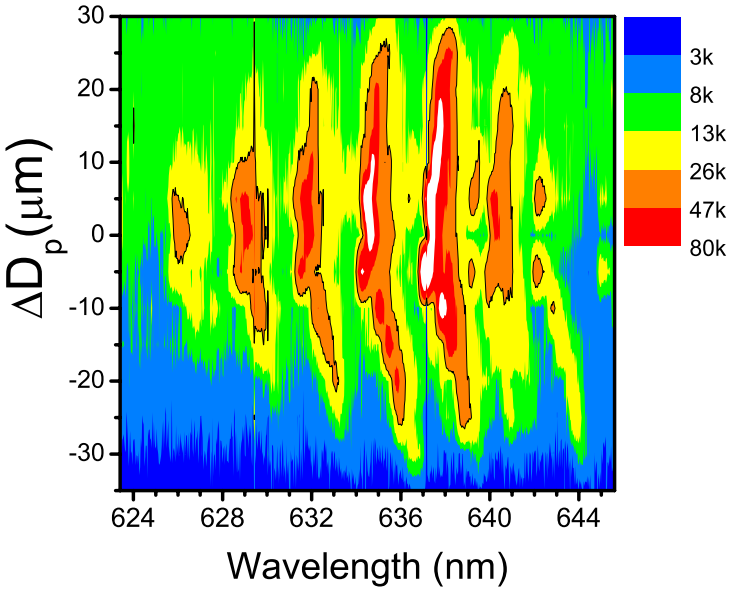

Figure D.11: Effects of spatial gain variation of single microdisk. False-color contour plot of the emission intensity vs emission wavelength and ΔD_p.

VITA

MARCUS JAMES DALEJUAN SMITH

Marcus James Dalejuan Smith was born in Dayton, Ohio on June 17th, 1985 to Ronnie and Jean Smith. He attended elementary through high-school in Dayton, attending Fairview Elementary, Resurrection Middle School, and finally Chaminade Julienne Catholic High School. Marcus earned his B.S. in Electrical Engineering with a minor in Business Administration from the University of Dayton in 2008. Immediately following this he pursued his MS in Materials Science and Engineering at the same university from 2008 to 2010. Upon completion of his MS degree he accepted a position with the Department of Defense (DoD) – Air Force Research Laboratories (AFRL) as a Materials Engineer working in the Aerospace Systems Directorate – Fuels and Energy Branch. Following a few years of employment with AFRL, Marcus was motivated to pursue his PhD and received full funding when he was awarded an internal fellowship through the DoD Science, Mathematics, and Research for Transformation (SMART) program. He was accepted into Georgia Institute of Technology in the Fall of 2014, where he studied under the guidance of Professor Vladimir V. Tsukruk. As a graduate student at Georgia Tech Marcus was an active member of the Black Graduate Student Association (BGSA) and volunteered for many recruitment efforts with both the Center for Engineering Education and Diversity (CEED) and Institute Diversity - OMED. Once finished with his PhD in the Spring of 2019, Marcus will return to AFRL to continue his career as a DoD civilian, where he has aspirations to be in the Senior Executive Service (SES).